

# Nonlinear Frequency Conversion in III-Nitride Doubly Resonant Photonic Crystal Cavities

Présentée le 8 août 2023

Faculté des sciences de base  
Groupe SCI SB RH  
Programme doctoral en physique

pour l'obtention du grade de Docteur ès Sciences

par

**Jun WANG**

Acceptée sur proposition du jury

Prof. F. Mila, président du jury  
Prof. R. Houdré, directeur de thèse  
Prof. H. Benisty, rapporteur  
Prof. M. Galli, rapporteur  
Dr R. Butté, rapporteur



# Acknowledgements

The accomplishment of this thesis cannot be achieved without the tremendous support of my research team and my friends. First, I would like to express my sincere gratitude to my supervisor prof. Romuald Houdré. He is a great supervisor and friend, who spent a great amount of time and patience guiding me not only in academia but also in many other aspects. He provided me with a high degree of freedom when making research plans and he was always available for help in all forms.

Then, I would like to thank my ex-colleagues Mohamed Sabry, Rita Therisod, and Ian Rousseau for training me on nanofabrication and characterization techniques. And special thanks to Rita, who spent a lot of time training me in the clean rooms and taught me all details of fabrication.

I would like to thank my collaborators prof. Nicolas Grandjean and Dr. Jean-François Carlin from the Laboratory of Advanced Semiconductors for Photonics and Electronics (LASPE) of EPFL, Dr. Momchil Minkov from Stanford University, and prof. Matteo Galli, prof. Dario Gerace, Dr. Marco Clementi, and Andrea Barone from the University of Pavia for academic collaboration. Every one of them shared with me the best ideas, knowledge, and skills in their domain.

I would like to thank Zdenek Benes, Joffrey Pernollet, Patrick Alain Madliger, Didier Bouvet from Center of MicroNanoTechnology (CMi), and Nicolas Leiser, Yoan Trolliet, Damien Trolliet from III-V cleanrooms, for technical support of clean room nano-fabrication. I would like to thank Dr. Arnaud Magrez from Crystal Growth Facility and Fabienne Bobard from Interdisciplinary Centre for Electron Microscopy (CIME) for technical support of characterization. I would like to thank Gilles Grandjean, Claude Amendola, Virgile Cavin, Daniel Clément, Adrien Grisendi from the mechanical workshop of the Institute of Physics (IPHYS), José Grandjean from the electrical workshop of IPHYS, and André Fattet from the mechanical workshop of the Institute of Chemical Sciences and Engineering (ISIC) for technical support of mechanical and electrical fabrication.

I would like to thank Florence Hagen and Primo Locatelli from the IT department of IPHYS as well as members from Scientific IT & Application Support (SCITAS) and IT Support Service Desk for software and hardware support.

## Acknowledgements

---

I would like to thank Diane Pellet, Anh Eymann, Nadja Dekumbis, and Yvette Gallay for administrative assistance and support.

I would like to thank Dr. Raphaël Butté from LASPE for helpful discussions and for the careful review of this thesis.

I would like to thank my friends and colleagues Nicolas Villa and Enrico Tartari for our daily discussions and shared ideas. It was very enjoyable working with them in the same office.

Finally, I would like to thank my friends and colleagues Wei Liu, Yao Chen, Danxuan Chen, Pierre Lottigier, Thomas Weatherley, Johann Stachurski, Hoda Shirzad, Sebastian Tamariz, Camille Haller, Pirouz Sohi, Gordon Callsen, Hezhi Zhang, Junqiu Liu, Sichen Mi, Liu Qiu, Dian Tan, Guanhao Huang, Wen Chen, Chan Cao, Dong Liu, Zhenzhu Meng, Qianhui Yu, Le Yu, Junwen Zou, Junrui Zhang, Tianqi Zhu, Zezhen Pan, Chenglu Miao. It was a great pleasure to meet them in Lausanne and share memories together.

*Lausanne, March 22*

Jun WANG

# Abstract

Nonlinear frequency conversion processes, such as second-harmonic generation (SHG) and spontaneous parametric down-conversion (SPDC), are essential in many applications, including the generation of entangled photons. It's desirable to enhance these processes since the nonlinear effects are generally very small and photonic crystal (PhC) cavities are usually implemented for this purpose thanks to the combination of high quality factors and small footprints. Singly resonant PhC cavities, which support one mode at either the input frequency or the output frequency, are extensively investigated by previous studies, and significant enhancement is observed, while doubly resonant PhC cavities, which support simultaneously one mode at the input frequency and another mode at the output frequency, are not because of the difficulty of designing the two resonant modes, even though the enhancement is supposed to be stronger.

This thesis studies the first design of 2D doubly resonant PhC cavities, realized by implementing a bound state in the continuum (BIC), and investigates its applications in SHG and SPDC. The cavities were fabricated on a III-nitride-on-silicon platform with standard semiconductor techniques and characterized on custom optical setups. The doubly resonant condition was fulfilled through passive lithographic tuning and active strain tuning. The SHG was observed with a high conversion efficiency under continuous wave excitation, which is in good agreement with theoretical predictions. Besides, far-field emission patterns with a donut shape and radial polarization at the second harmonic frequency were observed, which also agrees with the BIC confinement theory. The investigation on SPDC was however limited by the sensitivity of classical photodetectors. Nevertheless, the observation of high-efficiency SHG demonstrated the concept of doubly resonant PhC cavities and marked a cornerstone achievement for nonlinear frequency conversion. The fabrication and optical measurement techniques developed in this thesis could also be valuable for future studies.

**Keywords:** photonic crystals, optical microcavities, integrated photonics, doubly resonant cavities, bound state in the continuum (BIC), nonlinear optics, second-harmonic generation (SHG), spontaneous parametric down-conversion (SPDC), III-nitrides, gallium nitride (GaN).



# Résumé

Les processus de conversion de fréquence non linéaire, tels que la génération de seconde harmonique (SHG) et la conversion paramétrique descendante spontanée (SPDC), sont essentiels dans de nombreuses applications, y compris la génération de photons intriqués. Il est souhaitable d'augmenter ces processus car les effets non linéaires sont généralement très faibles et les cavités à cristal photonique sont généralement utilisées à cette fin grâce à la combinaison de facteurs de qualité élevés et de dimensions réduites. Les cavités à cristal photonique à résonance unique, qui supportent un mode à la fréquence d'entrée ou à la fréquence de sortie, ont fait l'objet d'études approfondies et une augmentation significative a été observée, tandis que les cavités à cristal photonique à double résonance, qui supportent simultanément un mode à la fréquence d'entrée et un autre mode à la fréquence de sortie, n'ont pas été étudiées en raison de la difficulté de concevoir les deux modes résonnants, même si l'augmentation est supposée plus forte.

Cette thèse étudie la première conception de cavités à cristal photonique doublement résonnantes en 2D, réalisée en implémentant un état lié dans le continuum (BIC), et investigate ses applications en SHG et SPDC. Les cavités ont été fabriquées avec des matériaux III-nitrides sur silicium à l'aide des techniques standard des semi-conducteurs et caractérisé par des montages optiques spécialement conçus. La condition de double résonance a été obtenue grâce à un accordage passif lithographique et à un accordage actif par la contrainte mécanique. La SHG a été observée avec une efficacité de conversion élevée sous excitation par ondes continues, ce qui est en bon accord avec les prédictions théoriques. En outre, des motifs d'émission du champ lointain avec une forme annulaire et une polarisation radiale à la fréquence de la deuxième harmonique ont été observés, ce qui est également en accord avec la théorie du confinement BIC. Les études sur le SPDC ont toutefois été limitées par la sensibilité des photodétecteurs classiques. Néanmoins, l'observation de la SHG avec une grande efficacité a permis de démontrer la conception de cavité à cristal photonique doublement résonnante et a marqué une étape décisive dans la conversion de fréquence non linéaire. Les techniques de fabrication et de mesure optique développées dans cette thèse pourraient également être précieuses pour les études futures.

**Mots-clés :** cristaux photoniques, microcavités optiques, photonique intégrée, cavités doublement résonnantes, état lié dans le continuum (BIC), optique non linéaire, génération de second harmonique (SHG), conversion paramétrique descendante spontanée (SPDC), III-nitrides, nitride de gallium (GaN).





# List of Acronyms

<b>Notation</b>	<b>Description</b>	<b>Page List</b>
ADC	analog-to-digital converter	63
AFM	atomic force microscopy	30
AOM	acoustic optical modulator	66
APD	avalanche photodiode	62
BHF	buffered hydrofluoric acid	43
CW	continuous wave	61
DFG	difference frequency generation	20
DI	deionized	43
EBL	electron beam lithography	32
EMCCD	electron multiplying charge-coupled device	62
FDTD	finite-difference time-domain	78
FFT	fast fourier transform	78
FH	first harmonic	21
FOPM	fiber optic power meter	62
FWHM	full width at half maximum	35
GME	guided-mode expansion	12
GPIB	general purpose interface bus	63
HF	hydrofluoric acid	28
HSQ	hydrogen silsesquioxane	27
ICP-RIE	inductively coupled plasma - reactive ion etching	27
IPA	isopropyl alcohol	32
LabVIEW	laboratory virtual instrument engineering workbench	63
MIBK	methyl isobutyl ketone	39
MKS	meter-kilogram-second	5
MOVPE	metalorganic vapour-phase epitaxy	27
NA	numerical aperture	81
NEP	noise-equivalent power	106
NIR	near-infrared	59
NI-VISA	national instruments virtual instrument software architecture	63

## List of Acronyms

---

<b>Notation</b>	<b>Description</b>	<b>Page List</b>
OD	optical density	61
OSA	optical spectrum analyzer	68
PBG	photonic bandgap	3
PDC	parametric down-conversion	21
PEC	proximity effect correction	33
PECVD	plasma-enhanced chemical vapor deposition	27
pH	potential of hydrogen	53
PhC	photonic crystal	3
PM	polarization-maintaining	61
PWE	plane-wave expansion	10
Q-factor	quality factor	1
RF	radio frequency	40
RIE	reactive ion etching	40
RMS	root mean square	30
RPM	round per minute	30
RS	resonant scattering	71
RS232	recommended standard 232	63
sccm	standard cubic centimeter per minute	38
SEM	scanning electron microscope	55
SFG	sum frequency generation	20
SH	second harmonic	21
SHG	second harmonic generation	21
SPDC	spontaneous parametric down-conversion	21
TE	transverse electric	10
THG	third harmonic generation	22
Ti:sapphire	titanium-sapphire	62
TM	transverse magnetic	10
TMAH	tetramethylammonium hydroxide	51
TMAI	trimethylaluminium	29
TMGa	trimethylgallium	29
USB	universal serial bus	63
VIS	visible	59
ZEP	ZEP520A	27

# Contents

<b>Acknowledgements</b>	<b>iii</b>
<b>Abstract (English/Français)</b>	<b>v</b>
<b>List of Acronyms</b>	<b>ix</b>
<b>1 Introduction</b>	<b>1</b>
<b>2 Background Information</b>	<b>3</b>
2.1 Photonic Crystals and Cavities . . . . .	3
2.1.1 Introduction to Photonic Crystals . . . . .	3
2.1.2 Theory for Photonic Crystals . . . . .	5
2.1.3 2D Photonic Crystals and Photonic Crystal Slabs . . . . .	10
2.1.4 Photonic Crystal Defects and Cavities . . . . .	14
2.2 Nonlinear Optics . . . . .	19
2.2.1 Nonlinear Susceptibility . . . . .	19
2.2.2 Nonlinear Frequency Conversion . . . . .	20
2.3 III-Nitride Materials . . . . .	22
2.3.1 Crystal Structure . . . . .	22
2.3.2 Optical Properties . . . . .	24
2.3.3 Nonlinear Properties . . . . .	25
<b>3 Fabrication of 2D PhC Slabs</b>	<b>27</b>
3.1 Main Fabrication Processes . . . . .	27
3.1.1 Overview . . . . .	27
3.1.2 Crystal Growth and Thin Film Characterization . . . . .	29
3.1.3 Dicing and Cleaning . . . . .	31
3.1.4 Hard Mask Deposition . . . . .	32
3.1.5 Electron Beam Lithography . . . . .	32
3.1.6 Dry Etching of Silica . . . . .	39
3.1.7 ICP-RIE Etching of III-nitrides . . . . .	40
3.1.8 Membrane Release . . . . .	43
3.2 Auxiliary Techniques . . . . .	44
3.2.1 Strain Engineering . . . . .	44

## Contents

---

3.2.2	Deep Etching . . . . .	50
3.2.3	HSQ Technique . . . . .	51
3.2.4	AlN Etching . . . . .	53
3.2.5	PhC Image Analysis . . . . .	55
<b>4</b>	<b>Optical Measurements</b>	<b>59</b>
4.1	Main Optical Setup . . . . .	59
4.1.1	Parts of the Main Optical Setup . . . . .	59
4.1.2	Electrical Connections and Software Controls . . . . .	63
4.1.3	Wavelength Calibration . . . . .	64
4.2	Auxiliary Setups and Techniques . . . . .	65
4.2.1	Ti:sapphire Tunable Laser . . . . .	65
4.2.2	Supercontinuum Source . . . . .	68
4.2.3	Acousto-optic Modulation . . . . .	70
4.3	Resonant Scattering Measurement . . . . .	71
4.4	Fourier Plane Imaging . . . . .	72
<b>5</b>	<b>Doubly Resonant PhC Cavities</b>	<b>75</b>
5.1	Overview . . . . .	75
5.2	Cavity Design . . . . .	76
5.3	Cavity Modes . . . . .	78
5.3.1	Cavity Modes by Simulation . . . . .	78
5.3.2	Cavity Modes in Experiments . . . . .	81
5.3.3	Redshift of Cavity Modes . . . . .	83
5.3.4	Raman Stress Analysis . . . . .	84
5.3.5	Sample Protection with Nitrogen . . . . .	86
5.4	Influence of Cavity Parameters and Lithographic Tuning . . . . .	87
5.5	Influence of Anisotropy and Active Tuning . . . . .	89
<b>6</b>	<b>Nonlinear Frequency Conversion</b>	<b>91</b>
6.1	Overview . . . . .	91
6.2	Nonlinear Frequency Conversion in Doubly Resonant Cavities . . . . .	92
6.3	Frequency Up-Conversion . . . . .	95
6.3.1	Frequency Up-Conversion in Doubly Resonant Cavity . . . . .	95
6.3.2	Doubly Resonance and Detuning . . . . .	96
6.3.3	Second-Harmonic Generation . . . . .	96
6.3.4	Efficiency Calibration . . . . .	98
6.3.5	SH Far-Field Emission . . . . .	100
6.4	Frequency Down-Conversion . . . . .	102
6.4.1	Frequency Down-Conversion in Doubly Resonant Cavity . . . . .	102
6.4.2	Difference Frequency Generation . . . . .	104
6.4.3	Spontaneous Parametric Down Conversion . . . . .	106

<b>7 Conclusions and Perspectives</b>	<b>109</b>
<b>A Appendices</b>	<b>111</b>
A.1 Purcell Effect . . . . .	111
A.2 Doubly Resonant Cavity Design by Gdspy . . . . .	112
A.3 Main Optical Setup Drawing and Element List . . . . .	114
A.4 Alignment of the Main Setup . . . . .	117
A.5 Ti:sapphire Laser Wavelength Nonlinearity Analysis . . . . .	118
A.6 Lock-in Amplification . . . . .	119
A.7 High Order Modes of Doubly Resonant Cavity . . . . .	120
<b>Bibliography</b>	<b>123</b>
<b>Curriculum Vitae</b>	<b>137</b>



# 1 Introduction

Optical micro-cavities based on structural defects in photonic crystals are promising for nonlinear optic applications because of their tight light-confinement capabilities. The strong electric field of the confined mode in the cavity, which is a result of the high quality factor (Q-factor), greatly enhances the nonlinear process and enables nonlinear applications with low-power and continuous-wave light sources. The footprint of the cavity mode, whose size is comparable to the light wavelength, represents one of the smallest among all optical cavities and is promising for on-chip integrated photonic devices. Moreover, the defect mode inside the photonic bandgap modifies the density of states and changes the state transition probabilities, which results in substantial tailoring of optical properties of atoms and molecules in the material.

In nonlinear frequency conversion processes, when a cavity possesses resonant modes at both the input frequency and the output frequency, it benefits from the electric field amplification of the input light and the emission probability enhancement of the output light simultaneously. This kind of doubly resonant cavity is more advantageous than singly resonant cavities and is ideal for nonlinear frequency conversion.

Although photonic crystals exhibit no preference for the material, as long as the material is transparent for the interested wavelength, III-nitrides, namely GaN and AlN, become the material of choice because of the prominent second-order nonlinear susceptibilities and the transparency at both the input and output frequencies.

The main objective of this thesis is to experimentally realize doubly resonant photonic crystal cavities and investigate their applications in the second-order nonlinear frequency conversion processes, including second harmonic generation and spontaneous parametric down-conversion.

The knowledge background of this thesis contains three major domains: photonic crystals and cavities, nonlinear frequency conversion, and material properties of III-nitrides. The experimental work of this thesis contains four major parts: computational simulation of

## Chapter 1. Introduction

---

photonic crystals and cavities, fabrication of photonic crystal cavities, characterization of photonic crystal cavities, and nonlinear frequency conversion experiments.

This thesis contains the following parts:

**Chapter 2** introduces the three parts of the knowledge background of this thesis, with emphasis on a brief review of plane-wave expansion and guided-mode expansion theory for photonic crystals, second-order nonlinear frequency conversion in photonic crystal cavities, and nonlinear properties of III-nitrides.

**Chapter 3** focuses on the nanofabrication techniques and intermediate characterizations of the photonic crystal cavities, with a comparison of the two main fabrication routines with two different lithography resists. Strain mitigation by spring tethers, which greatly improves the stability of the suspended waveguide and the photonic crystal, and other auxiliary techniques are also presented.

**Chapter 4** focuses on the hardware and software of the optical measurement setup. The resonant scattering and Fourier imaging techniques are also described as they are very basic and important for characterizing photonic crystal cavities.

**Chapter 5** introduces the doubly resonant photonic crystal cavities, which represent the first realization of doubly resonant cavities based on photonic crystal slabs, from the design to the fabrication and the resonant scattering characterization. Passive tuning by lithographic parameter scan and active tuning by applying anisotropic strain are presented, which are essential for controlling the detuning of the dual resonances.

**Chapter 6** is devoted to the nonlinear frequency conversion in the doubly resonant photonic crystal cavity. The second harmonic generation was realized successfully with high conversion efficiency and was comprehensively characterized. The spontaneous parametric down conversion was not observed due to the limited sensitivity of the classical photodetector.

**Chapter 7** summarizes the major results of this thesis and gives perspectives accordingly.



## 2 Background Information

This chapter introduces the relevant background information in order to provide a context for this thesis. This chapter consists of three sections: photonic crystals and cavities, nonlinear frequency conversion, and properties of the III-nitride materials.

### 2.1 Photonic Crystals and Cavities

#### 2.1.1 Introduction to Photonic Crystals

Photonic crystals (PhCs) are dielectric optical nanostructures in which the electric permittivity varies periodically with a typical period comparable to the optical wavelength in the material. According to the periodicity, they can be classified into one-, two-, and three-dimensional (1D, 2D, and 3D) PhCs [Fig. 2.1]. One of the most concerned features of PhCs is the **photonic bandgap (PBG)** that prohibits light propagation in all directions, which is analogic to the electronic bandgap in semiconductors. Examples of artificially produced PhCs are distributed Bragg reflectors (or Bragg mirrors, dielectric mirrors) and PhC nanobeams [1] for 1D, PhC slabs [2–4] and PhC fibers [5–7] for 2D, and piles of strips and spheres for 3D [8–11] [Fig. 2.2 (a–d)]. 2D PhC slabs (see section 2.1.3) are mainly discussed in this thesis.

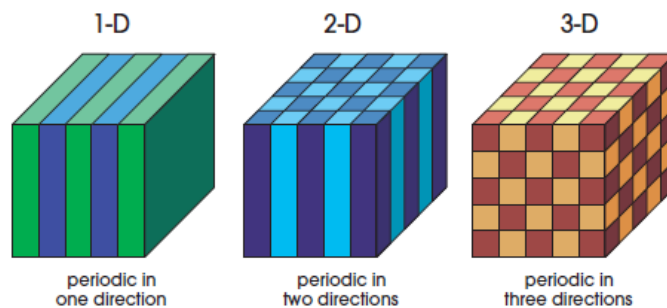


Figure 2.1: Schematic representation of one-, two-, and three-dimensional PhCs (reproduced from [12]). The colors represent different refractive indices.

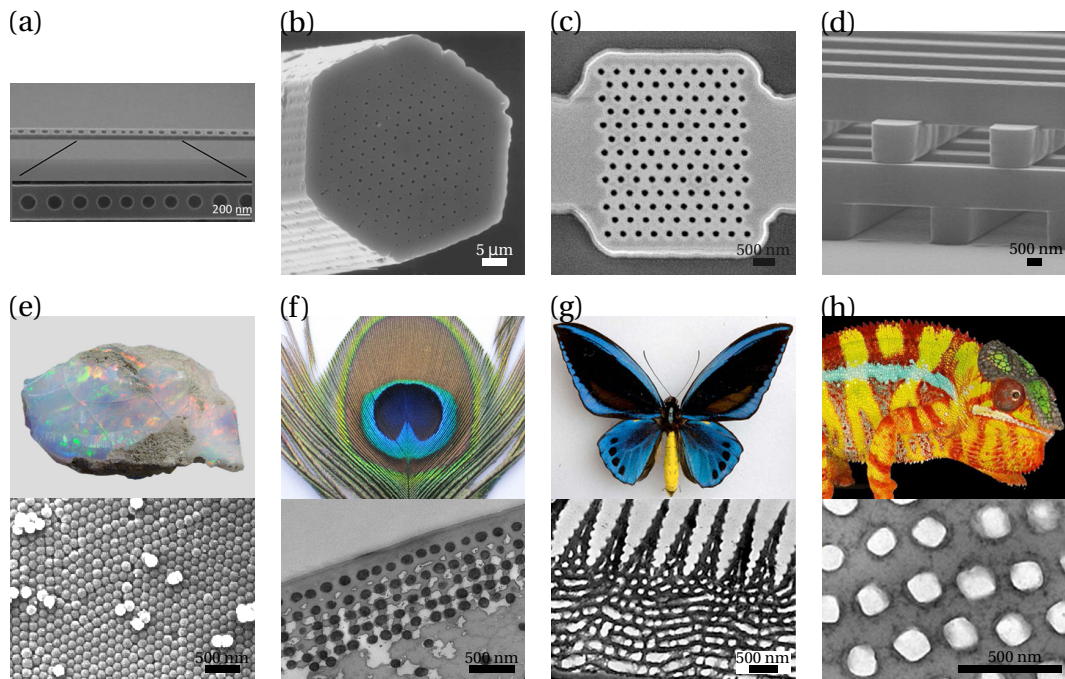


Figure 2.2: Examples of artificial and natural photonic crystals. (a) 1D PhC nanobeam [1]. (b) PhC optical fiber [5]. (c) 2D PhC slab [3]. (d) 3D PhC [9]. (e) Opal [20, 21]. (f) Peacock feather [22]. (g) Butterfly [23]. (h) Chameleon [24].

The concept of PhCs was developed after the publication of two milestone papers by Eli Yablonovitch [13] and Sajeev John [14] in 1987 [15], both concerned high-dimensional periodic optical structures. Yablonovitch's main goal was to engineer the photonic density of states to control the spontaneous emission of materials embedded in the PhC, while John's idea was to use PhCs to affect the localization of light. The periodic dielectric multilayers (e.g., Bragg mirrors) were studied extensively much earlier [16, 17], but without the generalization to high-dimensional cases. The first (3D) PhC with an omnidirectional photonic bandgap was experimentally demonstrated in 1991 in the microwave range [18]. The first 2D PhC was demonstrated in 1996 in the near-infrared range [19], which opened the door for fabricating 2D PhCs by semiconductor techniques. Afterward, the research on PhCs grows exponentially.

PhCs exist in nature but were not recognized before the development of the concept [Fig. 2.2 (e-h)]. First, PhCs occur in minerals like opal, a kind of mineral consisting of piles of silica spheres [25, 26]. More interestingly, PhCs were widely developed and equipped by life forms through natural evolution [27]. Scales of silvery fish [28], tapeta lucida of many vertebrates that cause the eyeshine [29], and eye reflectors of some bivalve mollusks [30] are examples of animal reflectors in which Bragg mirror-like structures enhance light reflections in a broad range of wavelengths. Feathers of some birds [22, 31, 32], scales of butterflies [23, 33], and exoskeletons of some insects [34–36] are examples of structural coloration in which PhC structures enhance light reflection for selected wavelengths. Chameleons were even reported to have active tuning capabilities on their PhC structures [24].

### 2.1.2 Theory for Photonic Crystals

This section introduces some theoretical aspects of photonic crystals, which lead to plane-wave expansion. One can refer to textbooks of electromagnetism [37, 38], solid state physics [39, 40], and photonic crystals [12, 41–43] for more details.

#### Maxwell's Equations in Matter

The most general form of Maxwell's equations in a medium in meter-kilogram-second (MKS) units can be given as follows:

$$\nabla \cdot \mathbf{D} = \rho_f, \quad (\text{Gauss's law}) \quad (2.1)$$

$$\nabla \cdot \mathbf{B} = 0, \quad (\text{Gauss's law for magnetism}) \quad (2.2)$$

$$\nabla \times \mathbf{E} = -\frac{\partial \mathbf{B}}{\partial t}, \quad (\text{Faraday's law}) \quad (2.3)$$

$$\nabla \times \mathbf{H} = \mathbf{J}_f + \frac{\partial \mathbf{D}}{\partial t}, \quad (\text{Ampère's law}) \quad (2.4)$$

where  $\nabla$  is the nabla operator,  $\mathbf{D}$  is the electric displacement,  $\mathbf{B}$  is the magnetic flux density,  $\mathbf{E}$  is the electric field strength,  $\mathbf{H}$  is the magnetic field strength,  $\rho_f$  is the free charge density,  $\mathbf{J}_f$  is the free current density, and  $t$  is time.

The medium can be characterized by the following:

$$\mathbf{D} = \varepsilon \mathbf{E} = \varepsilon_0 \mathbf{E} + \mathbf{P} = \varepsilon_0 \varepsilon_r \mathbf{E}, \quad (2.5)$$

$$\mathbf{B} = \mu \mathbf{H} = \mu_0 (\mathbf{H} + \mathbf{M}) = \mu_0 \mu_r \mathbf{H}, \quad (2.6)$$

$$\mathbf{J}_f = \sigma \mathbf{E}, \quad (2.7)$$

where  $\mathbf{P}$  is the polarization (dipole moment per unit volume),  $\mathbf{M}$  is the magnetization (magnetic dipole moment per unit volume),  $\varepsilon_0$  is the electric permittivity of vacuum,  $\varepsilon$  is the electric permittivity of the material,  $\varepsilon_r$  is the relative electric permittivity of the material,  $\mu_0$  is the magnetic permeability of vacuum,  $\mu$  is the magnetic permeability of the material,  $\mu_r$  is the relative magnetic permeability of the material,  $\sigma$  is the conductivity of the material.

To narrow down the scenario to PhCs made of dielectric materials, the following assumptions are applied for the later sections:

1. The material is isotropic, non-dispersive, lossless, and time-invariant, so that Eq. (2.5) Eq. (2.6) are valid with the permittivity  $\varepsilon_r$  and permeability  $\mu_r$  being real, positive, and not dependent on light frequency or time.
2. The material contains no free charge nor free current:  $\rho_f = 0$ ,  $\mathbf{J}_f = \mathbf{0}$ . This is valid for dielectric materials. For intrinsic semiconductors, the density of free charge or free current is very low, and they can be ignored.
3. The material is non-magnetic:  $\mu_r = 1$ . This is valid for most dielectric materials.

## Chapter 2. Background Information

---

4. The material is generally considered linear when discussing the basic properties of PhCs because the nonlinear effects are relatively small.

### Propagation Equations

In general,  $\mathbf{E}$  and  $\mathbf{H}$  are complex vector functions of both space and time, while the time dependence and the spatial dependence can be separated by expanding the fields into harmonic modes (plane waves):

$$\mathbf{E}(\mathbf{r}, t) = \mathbf{E}_0 e^{i(\mathbf{k}\mathbf{r} - \omega t)} = \mathbf{E}_r e^{-i\omega t}, \quad (2.8)$$

$$\mathbf{H}(\mathbf{r}, t) = \mathbf{H}_0 e^{i(\mathbf{k}\mathbf{r} - \omega t)} = \mathbf{H}_r e^{-i\omega t}, \quad (2.9)$$

where  $\mathbf{E}_0$  is the amplitude of  $\mathbf{E}$ ,  $\mathbf{H}_0$  is the amplitude of  $\mathbf{H}$ ,  $\mathbf{E}_r(\mathbf{r}) = \mathbf{E}_0 e^{i\mathbf{k}\mathbf{r}}$  and  $\mathbf{H}_r(\mathbf{r}) = \mathbf{H}_0 e^{i\mathbf{k}\mathbf{r}}$  are the time-independent part of  $\mathbf{E}$  and  $\mathbf{H}$ , respectively,  $\mathbf{r}$  is the position vector,  $\mathbf{k}$  is the wave number vector.

By inserting Eq. (2.8) and Eq. (2.9) into Maxwell's equations Eq. (2.1)-(2.4), the following equations are obtained:

$$\nabla \cdot [\varepsilon_r(\mathbf{r}) \mathbf{E}_r(\mathbf{r})] = 0, \quad (\text{Gauss's law}) \quad (2.10)$$

$$\nabla \cdot [\mu_r(\mathbf{r}) \mathbf{H}_r(\mathbf{r})] = 0, \quad (\text{Gauss's law for magnetism}) \quad (2.11)$$

$$\nabla \times \mathbf{E}_r(\mathbf{r}) - i\omega\mu_0\mu_r(\mathbf{r})\mathbf{H}_r(\mathbf{r}) = \mathbf{0}, \quad (\text{Faraday's law}) \quad (2.12)$$

$$\nabla \times \mathbf{H}_r(\mathbf{r}) + i\omega\varepsilon_0\varepsilon_r(\mathbf{r})\mathbf{E}_r(\mathbf{r}) = \mathbf{0}, \quad (\text{Ampère's law}) \quad (2.13)$$

By dividing  $\varepsilon_r$  and  $\mu_r$  from Eq. (2.12) and Eq. (2.13), respectively, cross-producting a nabla operator from the left side, and eliminating the complex number  $i$ , the propagation equations are obtained:

$$\frac{1}{\varepsilon_r(\mathbf{r})} \nabla \times \left[ \frac{1}{\mu_r(\mathbf{r})} \nabla \times \mathbf{E}_r(\mathbf{r}) \right] - \frac{\omega^2}{c^2} \mathbf{E}_r(\mathbf{r}) = \mathbf{0}, \quad (2.14)$$

$$\frac{1}{\mu_r(\mathbf{r})} \nabla \times \left[ \frac{1}{\varepsilon_r(\mathbf{r})} \nabla \times \mathbf{H}_r(\mathbf{r}) \right] - \frac{\omega^2}{c^2} \mathbf{H}_r(\mathbf{r}) = \mathbf{0}, \quad (2.15)$$

where  $c = 1/\sqrt{\varepsilon_0\mu_0}$  is the speed of light. The term  $\omega/c$  is known as the wave number  $k$ :  $k = \omega/c = 2\pi/\lambda$ , where  $\lambda$  is the wavelength. Eq. (2.14) and Eq. (2.15) are usually referred to as the **master equations** of propagation.

When the material is not homogeneous, or in general for any arbitrary spatial distribution of permittivity and permeability, the relative electric permittivity and the relative magnetic permeability are scalar fields:  $\varepsilon_r = \varepsilon_r(\mathbf{r})$ ,  $\mu_r = \mu_r(\mathbf{r})$ , where  $\mathbf{r}$  is the position vector. For this reason,  $\varepsilon_r$  and  $\mu_r$  can not be freely moved to the right side of the nabla operator, and they are divided in Eq. (2.12) and Eq. (2.13) before applying the second nabla operator to arrive at Eq. (2.14) and Eq. (2.15).

### Scaling Properties

There are two scaling properties for electromagnetic fields:

1. **Scale with dimension:** when the distribution of the electric permittivity and the magnetic permeability is expanded by a factor of  $\alpha$ :  $\varepsilon'_r(\mathbf{r}) = \varepsilon_r(\mathbf{r}/\alpha)$ ,  $\mu'_r(\mathbf{r}) = \mu_r(\mathbf{r}/\alpha)$ , ( $0 < \alpha < +\infty$ ), the field shape with respect to the permittivity distribution can be maintained as long as the frequency is reduced by a factor of  $\alpha$ :  $\omega' = \omega/\alpha$ .

Take Eq. (2.14) for example, when  $\varepsilon_r(\mathbf{r})$  is substituted with  $\varepsilon'_r(\mathbf{r}) = \varepsilon_r(\mathbf{r}/\alpha) = \varepsilon_r(\mathbf{r}')$  and  $\mu_r(\mathbf{r})$  is substituted with  $\mu'_r(\mathbf{r}) = \mu_r(\mathbf{r}/\alpha) = \mu_r(\mathbf{r}')$ , in order to maintain the field shape, the field  $E_r(\mathbf{r})$  can be substituted with  $E'_r(\mathbf{r}) = E_r(\mathbf{r}/\alpha) = E_r(\mathbf{r}')$  and Eq. (2.14) becomes:

$$\frac{1}{\varepsilon_r(\mathbf{r}')} \nabla \times \left[ \frac{1}{\mu_r(\mathbf{r}')} \nabla \times \mathbf{E}_r(\mathbf{r}') \right] - \frac{\omega'^2}{c^2} \mathbf{E}_r(\mathbf{r}') = \mathbf{0}, \quad (2.16)$$

where  $\omega'$  is the new frequency after expansion, and the nabla  $\nabla$  acts on  $\mathbf{r}$ . On the other hand, Eq. (2.14) is valid with  $\omega$  as long as the nabla acts on the same argument of  $E_r$ ,  $\mu_r$  and  $\varepsilon_r$ :

$$\frac{1}{\varepsilon_r(\mathbf{r}')} \nabla' \times \left[ \frac{1}{\mu_r(\mathbf{r}')} \nabla' \times \mathbf{E}_r(\mathbf{r}') \right] - \frac{\omega^2}{c^2} \mathbf{E}_r(\mathbf{r}') = \mathbf{0}, \quad (2.17)$$

where the  $\nabla'$  now acts on  $\mathbf{r}'$ , and  $\nabla' = \partial/\partial\mathbf{r}' = \partial/[(1/\alpha)\partial\mathbf{r}] = \alpha\nabla$ . By comparing Eq. (2.16) and Eq. (2.17), one can find that  $\omega' = \omega/\alpha$ .

2. **Scale with permittivity:** when the amplitude of the electric permittivity (or the magnetic permeability) is increased by a factor of  $\beta^2$ :  $\varepsilon'_r = \beta^2\varepsilon_r$ , ( $0 < \beta < +\infty$ ), the field shape with respect to the permittivity distribution can be maintained as long as the frequency is reduced by a factor of  $\beta$ :  $\omega' = \omega/\beta$ .

Take Eq. (2.14) for example, when  $\varepsilon_r$  is substituted with  $\varepsilon'_r = \beta^2\varepsilon_r$ , the equation becomes:

$$\frac{1}{\beta^2\varepsilon_r} \nabla \times \left[ \frac{1}{\mu_r} \nabla \times \mathbf{E}_r \right] - \frac{\omega'^2}{c^2} \mathbf{E}_r = \mathbf{0}, \quad (2.18)$$

where  $\omega'$  is the new frequency. By comparing Eq. (2.14) Eq. (2.18), one can find that  $\omega' = \omega/\beta$ . Notice that the scaling on  $\varepsilon_r$  and on  $\mu_r$  can be added up in a serial manner, which is different than the previous scaling property. For instance, if  $\varepsilon'_r = \beta_1^2\varepsilon_r$  and  $\mu'_r = \beta_2^2\mu_r$ , then  $\omega' = \omega/(\beta_1\beta_2)$ .

These two scaling properties are valid in electromagnetic systems with any arbitrary (i.e., not necessarily periodic) distribution of electric permittivity and magnetic permeability. The first property is very useful in practice because the operating frequency of a designed optical structure can be easily tuned by scaling the structure itself. The second property is more difficult to apply in practice because of the difficulty of tuning the permittivity.

### Bloch's Theorem

The master equations Eq. (2.14) and Eq. (2.15) can be written in a general form of **eigenvalue problem**:

$$\hat{O}\mathbf{F} = k^2\mathbf{F}, \quad (2.19)$$

with:

$$\hat{O}_E = \frac{1}{\varepsilon_r(\mathbf{r})} \nabla \times \frac{1}{\mu_r(\mathbf{r})} \nabla \times, \quad (2.20)$$

$$\hat{O}_H = \frac{1}{\mu_r(\mathbf{r})} \nabla \times \frac{1}{\varepsilon_r(\mathbf{r})} \nabla \times, \quad (2.21)$$

where  $\hat{O}$  is the general operator,  $\mathbf{F}$  stands for the electric or magnetic field ( $\mathbf{E}$ , or  $\mathbf{H}$ ), and  $\hat{O}_E$ ,  $\hat{O}_H$  are the corresponding operators. It can be demonstrated that the operator  $\hat{O}$  is Hermitian. Solving the propagation equations turns out to be finding the eigenvalues and eigenvectors of the operator  $\hat{O}$ .

Bloch's theorem states that the eigenvectors  $\mathbf{F}(\mathbf{r})$  of an operator  $\hat{O}$  with a periodic distribution of electric permittivity  $\varepsilon_r(\mathbf{r})$  and magnetic permeability  $\mu_r(\mathbf{r})$  can be expressed in the form of a product of a plane wave term  $e^{i\mathbf{k}\cdot\mathbf{r}}$  and a periodic term  $\mathbf{U}(\mathbf{r})$ :

$$\mathbf{F}(\mathbf{r}) = e^{i\mathbf{k}\cdot\mathbf{r}} \mathbf{U}(\mathbf{r}), \quad (2.22)$$

where  $\mathbf{U}(\mathbf{r})$  stands for the electric or magnetic field ( $\mathbf{E}$ , or  $\mathbf{H}$ ) and possesses the same periodicity as  $\varepsilon_r$  and  $\mu_r$ .

### Fourier Series in 3D

A periodic vector function  $\mathbf{U}$  defined in 3-dimensional space (i.e., a vector field) can be expressed as a Fourier series:

$$\mathbf{U}(\mathbf{r}) = \sum_{\mathbf{G} \in G} \mathbf{C}_U(\mathbf{G}) e^{i\mathbf{G}\cdot\mathbf{r}}, \quad (2.23)$$

where  $\mathbf{r}$  is the position vector,  $\mathbf{G}$  is the reciprocal lattice vector,  $G$  is the set of all reciprocal lattice vectors,  $\mathbf{C}_U(\mathbf{G})$  is the vector Fourier coefficient that corresponds to  $\mathbf{U}$  and  $\mathbf{G}$ :

$$\mathbf{C}_U(\mathbf{G}) = \frac{1}{V} \int_V e^{-i\mathbf{G}\cdot\mathbf{r}} \mathbf{U}(\mathbf{r}) d\mathbf{r}, \quad (2.24)$$

with  $V$  the volume of the first Brillouin zone. A periodic scalar function defined in 3-dimensional space (i.e., a scalar field) can be expressed similarly with scalar Fourier coefficients.

The reciprocal lattice vectors  $\mathbf{G}$  are vectors in the reciprocal space in which the primitive

vectors (i.e., basis vectors associated with a primitive cell)  $\mathbf{b}_j$  are defined as:

$$\mathbf{a}_i \cdot \mathbf{b}_j = 2\pi\delta_{i,j}, \quad i, j \in [1, \dots, N], \quad (2.25)$$

where  $\mathbf{a}_i$  are primitive vectors of the real space,  $N$  is the number of dimensions, and  $\delta_{i,j}$  is the Kronecker delta (i.e.,  $\delta_{i,j} = 0$  if  $i \neq j$ ,  $\delta_{i,j} = 1$  if  $i = j$ ).

The nabla operator acts on a vector Fourier series as:

$$\nabla \times \sum_{\mathbf{G} \in G} \mathbf{C}_U(\mathbf{G}) e^{i\mathbf{G} \cdot \mathbf{r}} = \sum_{\mathbf{G} \in G} [i\mathbf{G} \times \mathbf{C}_U(\mathbf{G})] e^{i\mathbf{G} \cdot \mathbf{r}}. \quad (2.26)$$

### Plane-Wave Expansion (PWE)

According to Bloch's theorem, the electric field and the magnetic field can be expressed in Fourier series:

$$\mathbf{E}_r(\mathbf{r}) = e^{i\mathbf{k} \cdot \mathbf{r}} \sum_{\mathbf{G} \in G} \mathbf{C}_E(\mathbf{G}) e^{i\mathbf{G} \cdot \mathbf{r}} = \sum_{\mathbf{G} \in G} \mathbf{C}_E(\mathbf{G}) e^{i(\mathbf{k} + \mathbf{G}) \cdot \mathbf{r}}, \quad (2.27)$$

$$\mathbf{H}_r(\mathbf{r}) = e^{i\mathbf{k} \cdot \mathbf{r}} \sum_{\mathbf{G} \in G} \mathbf{C}_H(\mathbf{G}) e^{i\mathbf{G} \cdot \mathbf{r}} = \sum_{\mathbf{G} \in G} \mathbf{C}_H(\mathbf{G}) e^{i(\mathbf{k} + \mathbf{G}) \cdot \mathbf{r}}, \quad (2.28)$$

where  $\mathbf{C}_E$  and  $\mathbf{C}_H$  are vector Fourier coefficients given by Eq (2.24).

The term of  $1/\varepsilon_r$  can also be expressed as a Fourier series:

$$\frac{1}{\varepsilon_r(\mathbf{r})} = \theta(\mathbf{r}) = \sum_{\mathbf{G} \in G} C_\theta(\mathbf{G}) e^{i\mathbf{G} \cdot \mathbf{r}}, \quad (2.29)$$

where  $C_\theta(\mathbf{G})$  is a scalar Fourier coefficient similarly given by Eq. (2.24). The term of  $1/\mu_r$  is unity because the material is assumed to be non-magnetic.

By inserting Eqs. (2.27), (2.28), (2.29), into the master equations Eqs. (2.14) and (2.15), and by applying Eq. (2.26) and the non-magnetic assumption ( $\mu_r = 1$ ), one can get:

$$\sum_{\mathbf{G}' \in G} C_\theta(\mathbf{G} - \mathbf{G}') (\mathbf{k} + \mathbf{G}') \times [(\mathbf{k} + \mathbf{G}') \times \mathbf{C}_E(\mathbf{G}')] = -\frac{\omega^2}{c^2} \mathbf{C}_E(\mathbf{G}), \quad (2.30)$$

$$\sum_{\mathbf{G}' \in G} C_\theta(\mathbf{G} - \mathbf{G}') (\mathbf{k} + \mathbf{G}') \times [(\mathbf{k} + \mathbf{G}') \times \mathbf{C}_H(\mathbf{G}')] = -\frac{\omega^2}{c^2} \mathbf{C}_H(\mathbf{G}), \quad (2.31)$$

where  $\mathbf{G}'$  is also a reciprocal lattice vector that is introduced to construct the same term of  $e^{i(\mathbf{k} + \mathbf{G}) \cdot \mathbf{r}}$  on the left side as the right side, and Eq. (2.29) is used by substituting  $\mathbf{G}$  by  $\mathbf{G} - \mathbf{G}'$ .

Eq. (2.30) and Eq. (2.31) are eigenvalue equations in which the eigenvalues  $\omega^2/c^2$  can be determined by diagonalizing the operator matrix for a given value of wave vector  $\mathbf{k}$  in the irreducible Brillouin zone. The operator matrix can be approximated by restricting  $\mathbf{G}$  to a finite set of reciprocal lattice vectors  $G_{\text{approx}}$ , in which  $|\mathbf{G}| \leq G_{\text{max}}$ . A larger  $G_{\text{max}}$  gives higher

accuracy of Fourier expansion at the expense of more computational resources (the number of matrix elements scales with  $(G_{\max})^{2i}$ , where  $i \in \{1, 2, 3\}$  is the PhC dimension). The numerical solution of one of the equations reveals the dispersion relation  $\omega(\mathbf{k})$ , i.e., the band structure, of the PhC. This numerical method is called the **plane-wave expansion (PWE)** method [44, 45] and is suitable for 1, 2, and 3-D infinite PhCs.

### 2.1.3 2D Photonic Crystals and Photonic Crystal Slabs

2D PhCs are PhCs that are periodic in two dimensions and ideally of infinite size in 3D space. Depending on the distribution of the high refractive index region with respect to the low refractive index region, there are mainly two types of 2D PhCs: **PhCs of pillars** and **PhCs of holes** [Fig. 2.4 (a)]. The optical modes in a 2D PhC are classified into **transverse electric (TE)** type if the electric field is parallel to the lattice plane and **transverse magnetic (TM)** type if the electric field is perpendicular to the lattice plane. As a rule of thumb, TM bandgaps are favored in a lattice of isolated high refractive regions (i.e., PhCs of pillars), and TE bandgaps are favored in a connected lattice (i.e., PhCs of holes) [12]. Depending on the symmetry of the periodicity, there are mainly two types of lattices: **square lattices** and **triangular (or hexagonal) lattices** [Fig. 2.3]. PhCs with triangular lattices are favored for generating TE and TM bandgaps simultaneously because they can be regarded as a combination of localized high refractive index islands (spot) connected with narrow bridges (vein) when the radius of the holes is large enough [12].

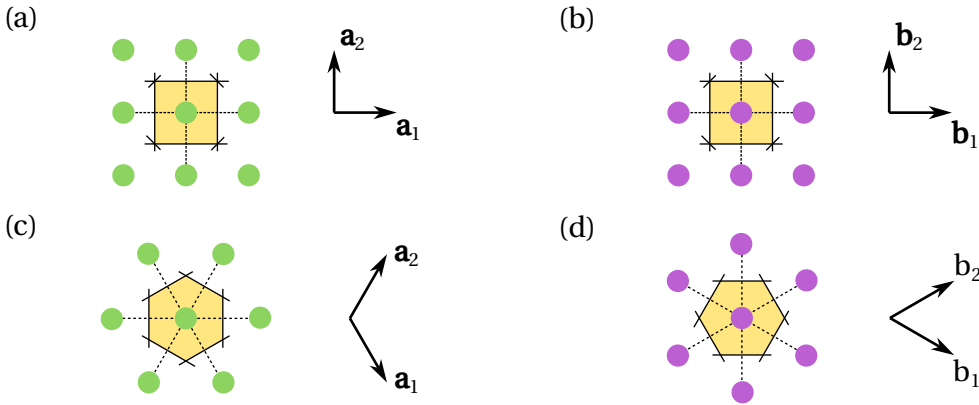


Figure 2.3: Schema of the 2D PhC lattices. Square lattice in (a) real space and (b) reciprocal space. Triangular lattice in (c) real space and (d) reciprocal space. Yellow regions show the Wigner-Seitz primitive cell in real space and the first Brillouin zone in reciprocal space. The primitive vectors are shown accordingly.

The dispersion relation  $\omega(\mathbf{k})$ , i.e., the band structure, of a 2D PhC can be calculated by the PWE method (see section 2.1.2). Fig. 2.4 (b)-(d) shows a series of band structure diagrams for 2D PhCs with a triangular lattice of air holes, calculated with the PWE method [46, 47]. It can be seen that the difference of frequencies for the first and the second band lines (counted from low frequency to high), of type TE (red lines) or TM (blue lines), increases with the



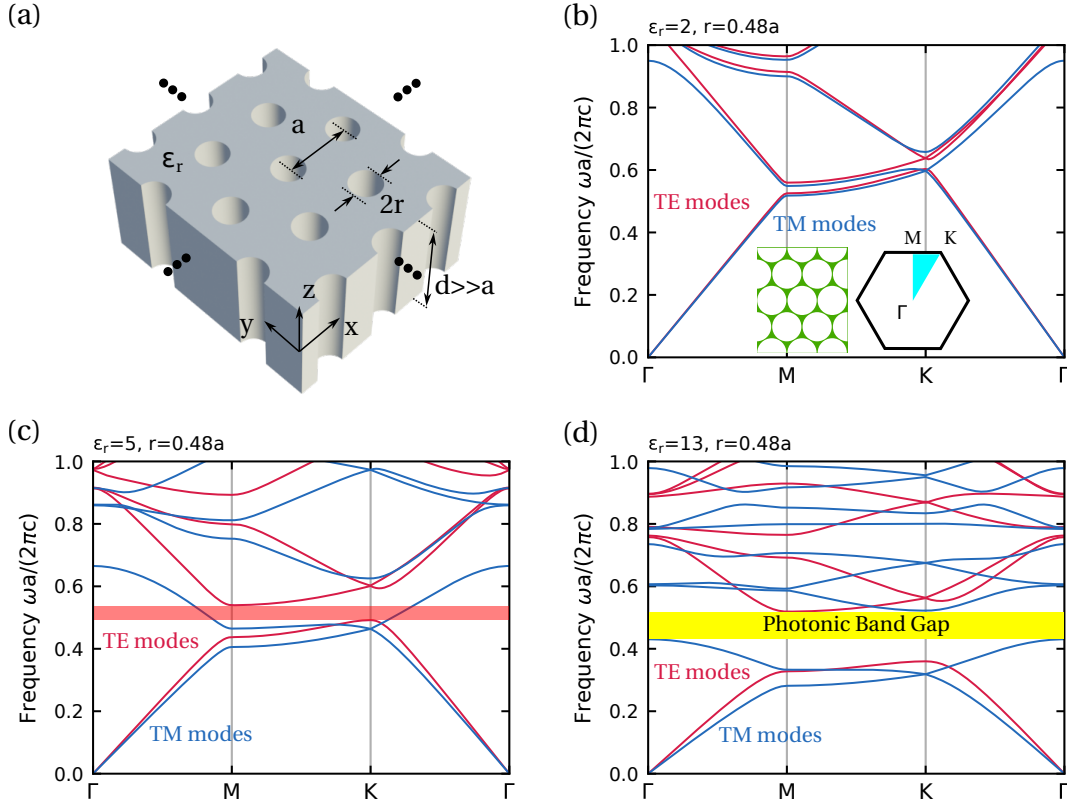


Figure 2.4: Band structure diagrams of 2D hexagonal PhCs with a triangular lattice of air holes, calculated with the PWE method [46, 47]. (a) Schema of the 2D PhC. The relative permittivity of the bulk material is  $\epsilon_r$ , the lattice constant is  $a$ , and the hole radius is  $r$ . (b) Band structure of the PhC slab with  $\epsilon_r = 2$  and  $r = 0.48a$ . The TE modes and the TM modes start to split. Insets show the 2D PhC and its Brillouin zone. (c) Band structure of the PhC slab with  $\epsilon_r = 5$  and  $r = 0.48a$ . The red region shows the photonic bandgap for TE polarization. (d) Band structure of the PhC slab with  $\epsilon_r = 13$  and  $r = 0.48a$ . The yellow region shows the complete photonic bandgap for both TE and TM polarizations. This band diagram should be the same as Fig. 10 in Chapter 5 of [12].

permittivity  $\epsilon_r$  [Fig. 2.4 (b)-(d)], and a **(full) bandgap** is formed between the first and the second TE band lines [Fig. 2.4 (c)], which means TE-polarized light of frequency within this bandgap is prohibited from propagating in any direction in this PhC. When the permittivity  $\epsilon_r$  is further increased, a **complete bandgap** is formed [Fig. 2.4 (d)], which means both TE- and TM-polarized lights of frequency within this bandgap are prohibited from propagating. Notice that when increasing the permittivity, the band lines are generally lowered in frequency, which is resulted from the scaling properties (see section 2.1.2).

In reality, all PhCs are bounded. A 2D PhC is restricted by the bounds along the isotropic direction (i.e., the direction perpendicular to the lattice plane) to a thickness  $d$  and is usually called a **PhC slab** (or slab-PhC) when  $d$  is comparable to or smaller than the lattice constant  $a$  (contrary to, e.g., a PhC fiber) [Fig. 2.5 (a)]. 2D PhC slab is a common form of artificial PhCs due to the convenience of fabrication with anisotropic etching techniques on thin films. Due

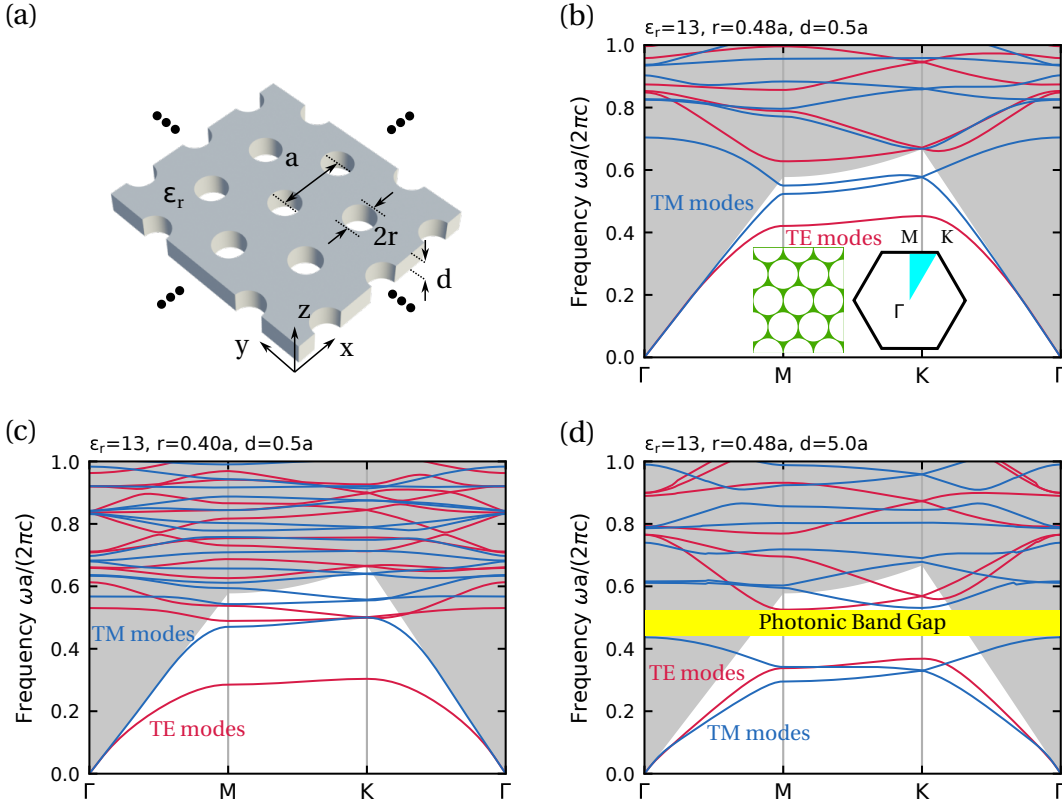


Figure 2.5: Band structure diagrams of 2D PhC slabs with a triangular lattice of air holes, calculated with the GME method [46, 47]. (a) Schema of the PhC slab. The relative permittivity of the bulk material is  $\epsilon_r$ , the lattice constant is  $a$ , the hole radius is  $r$ , and the slab thickness is  $d$ . (b) Band structure of the PhC slab with  $\epsilon_r = 13$ ,  $r = 0.48a$ , and  $d = 0.5a$ . The TE and TM modes are represented by red and blue lines, respectively. The grey region is the light cone. Insets show the 2D PhC and its Brillouin zone. (c) Band structure of the PhC slab with  $\epsilon_r = 13$ ,  $r = 0.40a$ , and  $d = 0.5a$ . TE and TM bandgaps are formed but do not overlap. (d) Band structure of the PhC slab with  $\epsilon_r = 13$ ,  $r = 0.48a$ , and  $d = 5.0a$ . The band structure recovers that calculated by PWE when the slab thickness is large.

to the limited thickness, the dispersion relation of a 2D PhC slab is a mixture of that of an ideal 2D PhC and that of a planar waveguide. The PWE method for infinite 2D PhC can be modified to incorporate the index-guiding effect (similar to total internal reflection) of the planar waveguide, which results in the **guided-mode expansion (GME)** method (described below in this section). The TE and TM modes in 2D PhCs are transformed into quasi-TE and quasi-TM modes in PhC slabs because the electric field is not strictly parallel nor perpendicular to the lattice plane except on the bisection plane of the slab.

Fig. 2.5 (b)-(d) shows a series of band structure diagrams for 2D PhC slabs with a triangular lattice of air holes, calculated with the GME method [46, 47]. Importantly, since the index-guiding effect is not always valid in PhC slabs, the band structure diagrams consist of index-guiding regions (shown in white color) and non-index-guiding regions (also called the light cone, shown in gray color). The light modes in the non-index-guiding regions (also called

in the light cone or above the light line) are **lossy** (or **leaky**) because they propagate in the out-of-plane directions. Comparing Fig. 2.5 (b) to Fig. 2.4 (d), it can be seen that the band structure differs from that of the 2D PhC with the same  $\varepsilon_r$  and  $r$ , and it appears that the band lines are higher in frequency because of the reduced effective permittivity of the slab. Comparing Fig. 2.5 (d) to Fig. 2.4 (d), it can be seen that the band structure recovers that of a 2D PhC when the slab thickness  $d$  is much larger than the lattice constant  $a$ . Comparing Fig. 2.5 (c) to Fig. 2.5 (b), it can be seen that decreasing the hole radius  $r$  effectively lowers the band line frequencies because of the increased effective permittivity. When the hole radius is small enough, the bandgaps of TE and TM polarizations can be formed simultaneously without overlapping [Fig. 2.5 (c)].

### Guided-Mode Expansion (GME)

**GME** [48–51] is a numeric method used for computing the dispersion relations in 2D PhC slabs. It is based on the PWE method while at the same time incorporating the index-guiding effect of the slab. Consider a general case of a 2D PhC of three layers of permittivity  $\varepsilon_1$ ,  $\varepsilon_2$ , and  $\varepsilon_3$ , respectively. The system can be regarded as a planar waveguide when treating the layers as homogenous with an average permittivity  $\bar{\varepsilon}_1$ ,  $\bar{\varepsilon}_2$ , and  $\bar{\varepsilon}_3$ , respectively, with  $\bar{\varepsilon}_2 > \bar{\varepsilon}_1, \bar{\varepsilon}_3$ . The discrete guided modes of the planar waveguide can be indexed by  $\mu = (\mathbf{g}, \alpha)$ , with  $\mathbf{g}$  the in-plane momentum, and  $\alpha$  the mode number. It can be shown that the guided modes are orthogonal so that they can be used as a basis to expand the Bloch modes of momentum  $\mathbf{k}$  of the 2D PhC:

$$\mathbf{H}_{\mathbf{k}}(\mathbf{r}) = \sum_{\mu} \mathbf{C}_{\mu} \mathbf{H}_{\mu}(\boldsymbol{\rho}, z), \quad (2.32)$$

where  $\mathbf{H}$  stands for the magnetic field strength,  $\mathbf{C}_{\mu}$  is the expansion coefficient,  $\boldsymbol{\rho}$  is the in-plane vector. Due to Bloch's theorem, only the modes of momentum  $\mathbf{k} + \mathbf{G}$  contribute to the summation, where  $\mathbf{G}$  is the reciprocal lattice vector. Then the eigenvalue problem equation can be rewritten as:

$$\sum_{\mathbf{G}', \alpha'} \hat{\mathbf{H}}_{\mu\nu} \mathbf{C}_{\mu} = \frac{\omega_{\mathbf{k}}^2}{c^2} \mathbf{C}_{\nu}, \quad (2.33)$$

with the operator:

$$\hat{\mathbf{H}}_{\mu\nu} = \int \frac{1}{\varepsilon(\boldsymbol{\rho})} \left[ \nabla \times \mathbf{H}_{\mu}^*(\boldsymbol{\rho}, z) \right] \cdot \left[ \nabla \times \mathbf{H}_{\nu}(\boldsymbol{\rho}, z) \right] d\boldsymbol{\rho} dz. \quad (2.34)$$

where  $\mu = (\mathbf{g}, \alpha) = (\mathbf{k} + \mathbf{G}, \alpha)$ ,  $\nu = (\mathbf{g}', \alpha) = (\mathbf{k} + \mathbf{G}', \alpha)$ . The coupling of the guided PhC modes to the continuum of radiative modes can be estimated through time-dependent perturbation theory, and the characteristic quality factor can be estimated by  $Q = \omega_{\mathbf{k}}/2\Im(\omega_{\mathbf{k}})$ , where  $\Im(\omega_{\mathbf{k}})$  is the imaginary part of  $\omega_{\mathbf{k}}$  [48].

### 2.1.4 Photonic Crystal Defects and Cavities

Because of the formation of the photonic bandgap, PhCs can be used to confine light in a certain region. To do that, a defect must be created inside a PhC to destroy the periodicity and provide a region to accommodate light modes. The defects are called zero-, one-, and two-dimensional if they accommodate light to propagate in zero, one, and two dimensions, which are referred to as point defects, line defects, and plane defects, respectively. A point defect in a PhC can be considered as a **cavity** in the sense that lights of a range of frequencies are confined in the defect area. A line defect in a PhC can be considered as a **waveguide** in the sense that lights of a range of frequencies can propagate along the defect line. Notice that, in defects based on 2D PhC slabs, the light confinement in out-of-plane directions is accomplished by the index-guiding effect of the slab rather than the photonic bandgap.

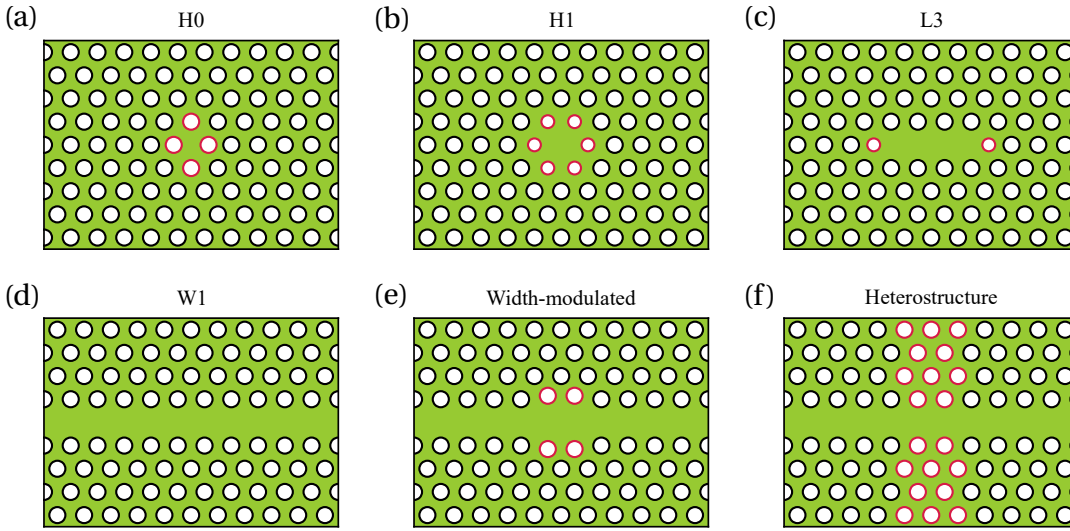


Figure 2.6: Schema of 2D PhC cavities and waveguides. (a) H0 cavity [52]. (b) H1 cavity [53]. (c) L3 cavity [4]. (d) W1 waveguide. (e) Width-modulated cavity [54, 55]. (f) Heterostructure cavity [56, 57]. Red circles indicate the minimum set of holes that are modified in size and position around the cavity.

Several types of cavities and waveguides can be created in PhC slabs by introducing defects: an H0 cavity is created by slightly increasing the distance between two adjacent holes [52] [Fig 2.6 (a)]; an H1 cavity is created by removing one hole [53] [Fig 2.6 (b)]; an L3 cavity is created by removing three holes in a line [4] [Fig 2.6 (c)]. When an entire line of holes is removed, a W1 waveguide is created [58] [Fig 2.6 (d)]. PhC waveguides are not only used for light-guiding [59, 60] as conventional waveguides but also highly interesting in applications of slow light [61–69] since the group velocity ( $v_g = d\omega/dk$ ) can be arbitrarily small for modes close to band edges. Point defects can be created based on a W1 waveguide by slightly modifying the width of the waveguide or by changing the lattice constant in a segment, and these two types are called width-modulated cavity [54, 55] and heterostructure cavity [56, 57], respectively [Fig 2.6 (e) (f)]. The base structures of the cavities are usually modified by changing the hole position, radius, and shape to optimize the cavity for interested quantities,

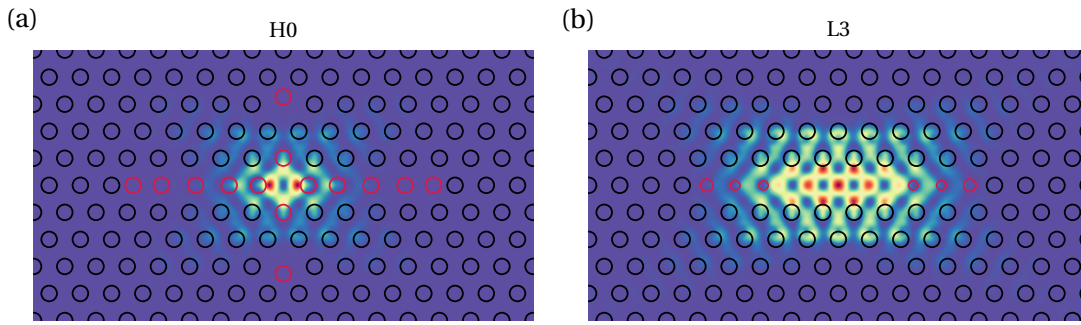


Figure 2.7: (a) Fundamental mode of an H0 cavity, computed by GME. (b) Fundamental mode of an L3 cavity with the same permittivity, slab thickness, and hole radius to lattice constant ratio as in (a). The color map in (a) and (b) shows the electric field square  $E_x^2 + E_y^2$  at the bisection plane of the slab, and the red circles show the holes that are modified in radius and position. The cavity parameters are as from section 5.3.2 in [70].

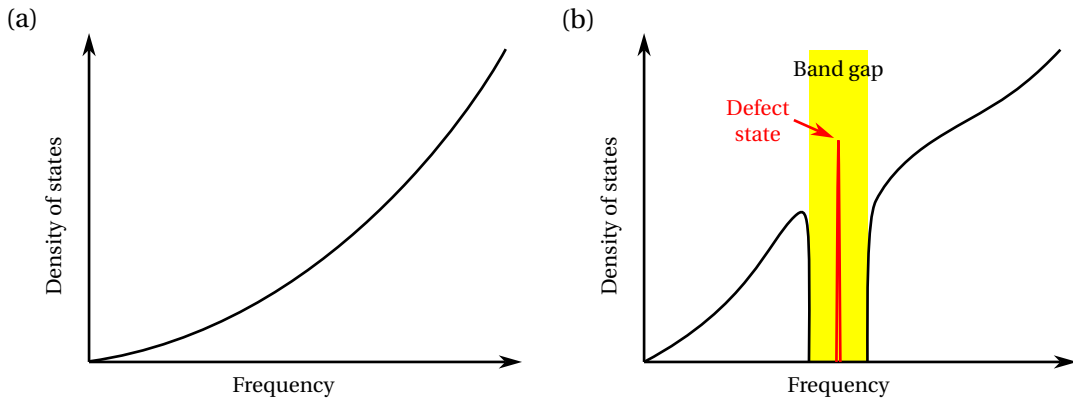


Figure 2.8: (a) Schema of the density of states of a vacuum or a macroscopic cavity with homogeneous permittivity. (b) Schema of the density of states of a PhC cavity.

e.g., the quality factor and the far-field radiative properties.

Since the light confined in a cavity is in the form of a standing wave, its electric field is amplified due to the superposition of wave nodes. High intensity of the electric field in the cavity is desired in applications of nonlinear optics because the strength of nonlinear effects increases with the electric field intensity. Fig. 2.7 (a) (b) shows the electric field distribution in an H0 and an L3 cavity, respectively, for their fundamental modes.

On the other hand, the photonic bandgap and the cavity mode can be used to tailor the spontaneous emission properties of the material. Since no light can propagate in the photonic bandgap, the density of states (or density of modes, defined by the number of modes per frequency or per frequency per volume) is zero in the gap, and the spontaneous emission is suppressed. A cavity mode introduces a defect state in the bandgap and potentially augments spontaneous emission. Fig. 2.8 (b) shows the schema of the density of states of a PhC cavity,

and Fig. 2.8 (a) shows that of a vacuum or a macroscopic cavity with homogeneous permittivity for comparison.

### Quality Factor

The Q-factor is a figure of merit frequently used to characterize PhC cavities (also generally used for other optical and non-optical cavities). The Q-factor of an optical cavity is defined equivalently as the total stored energy divided by the energy dissipated in one oscillation period, the energy decay time divided by the oscillation period, and the resonant frequency divided by the bandwidth of the resonance [71]:

$$Q = 2\pi \frac{E_{\text{total}}}{\delta E}, \quad (2.35)$$

$$= 2\pi \frac{\tau}{T}, \quad (2.36)$$

$$= \frac{f_0}{\delta f}, \quad (2.37)$$

where  $E_{\text{total}}$  is the total energy stored in the cavity,  $\delta E$  is the energy lost per oscillation cycle,  $\tau$  is the energy decay time,  $T = 1/f_0$  is the oscillation period of the electromagnetic field,  $f_0$  is the resonance frequency,  $\delta f$  is the FWHM bandwidth of the resonance. The Q-factor characterizes the ability of light confinement of a cavity. A higher Q-factor is generally desired because the light is better confined, i.e., the bandwidth is sharper, the intensity is higher, the energy lost in an oscillation period is smaller, and the mode lifetime is longer.

There is no theoretical limit for the Q-factor of a PhC cavity, while in experiments, the Q-factor of a PhC cavity is limited by the design of the cavity (including the size of the PhC), the coupling to the input/output channels, the material absorption, and the disorder introduced in the fabrication. The measured Q-factor of a PhC cavity can be written as:

$$\frac{1}{Q_m} = \frac{1}{Q_t} + \frac{1}{Q_c} + \frac{1}{Q_a} + \frac{1}{Q_d}, \quad (2.38)$$

where  $Q_t$  is the theoretically predicted Q-factor for a certain design and simulation volume,  $Q_c$  accounts for the coupling losses,  $Q_a$  accounts for the material absorption, and  $Q_d$  accounts for the scattering losses due to the disorder.

### Modal Volume

The modal volume (or effective mode volume) is another figure of merit frequently used to characterize PhC cavities. The modal volume of a PhC cavity is commonly defined as the spatial integral of the field intensity in the mode, normalized to unity at the field maximum

when considering the Purcell enhancement of the spontaneous emission [72–75]:

$$V_1 = \frac{\lim_{V \rightarrow \infty} \int_V \varepsilon(\mathbf{r}) |\mathbf{E}(\mathbf{r})|^2 d\mathbf{r}}{\max[\varepsilon(\mathbf{r}) |\mathbf{E}(\mathbf{r})|^2]}, \quad (2.39)$$

where  $\varepsilon(\mathbf{r})$  is the electric permittivity,  $\mathbf{E}(\mathbf{r})$  is the electric field strength, and  $V$  is the volume that contains the mode. This definition leads to integral divergence in the general case of leaky cavities but is still widely accepted in computations, provided that the integration is performed in a limited cut-off volume. This definition can be generalized to ensure integral convergence [76, 77].

The modal volume is also defined alternatively as:

$$V_n = \frac{\lim_{V \rightarrow \infty} \left[ \int_V \varepsilon(\mathbf{r}) |\mathbf{E}(\mathbf{r})|^2 d\mathbf{r} \right]^n}{\lim_{V \rightarrow \infty} \int_V [\varepsilon(\mathbf{r}) |\mathbf{E}(\mathbf{r})|^2]^n d\mathbf{r}}. \quad (2.40)$$

where  $n = 2$  when considering Anderson localization, Kerr effect, and two-photon absorption;  $n = 3$  when considering other nonlinear effects such as free-carrier absorption and dispersion.

A smaller modal volume is generally desired because Purcell's factor is inversely proportional to the modal volume [72, 73] (see appendix A.1 for Purcell effect) and because of the similar pursuit of smaller device size in integrated photonics as electronics. One can roughly recognize that the modal volume of the fundamental mode of the H0 cavity is smaller than that of the L3 cavity with the same lattice constant and permittivity [Fig. 2.7 (a) (b)]. PhC cavities generally have the smallest modal volume compared to other kinds of cavities in a dielectric material. In fact, the mode size of PhC cavities is of the order of wavelength in the material, and the modal volume is usually expressed in units of  $(\lambda/n)^3$ , where  $\lambda$  is the wavelength in vacuum, and  $n$  is the refractive index of the material. Some examples of modal volume for common PhC cavities are given in Table 2.1.

Cavity	$V_1 [(\lambda/n)^3]$	$V_2 [(\lambda/n)^3]$
H0	0.42	2.13
L3	0.71	2.90
Width-modulated	1.34	6.02
Heterostructure	1.58	6.07

Table 2.1: Modal volumes of common PhC cavities, adapted from [70].

### Coupling of Cavities

An optical cavity can be coupled to its environment through **ports** (e.g., the semitransparent window of a laser cavity), and the dynamics can be described by the **coupled-mode theory** [38, 78, 79]. The coupling between a single cavity mode and a single port [Fig. 2.9 (a)] can be

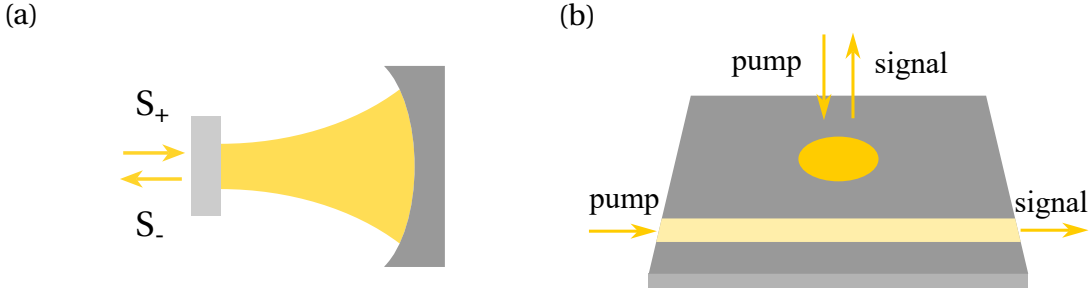


Figure 2.9: (a) Schema of an optical cavity with a single port and single mode. (b) Schema of side-coupling and vertical-coupling of a PhC slab cavity.

described by (chapter 7 of [38]):

$$\frac{da}{dt} = i\omega_0 a - \left( \frac{1}{\tau_0} + \frac{1}{\tau_e} \right) a + \kappa s_+, \quad (2.41)$$

$$s_- = c_s s_+ + c_a a, \quad (2.42)$$

where  $a$  is the complex amplitude of the mode,  $s_+$  is the complex amplitude of the incoming wave,  $s_-$  is the complex amplitude of the outgoing wave,  $i$  is the complex unit,  $\omega_0$  is the resonant frequency,  $1/\tau_0$  is the decay rate due to "internal" loss, i.e., absorption,  $1/\tau_e$  is the decay rate due to "external" loss, i.e., coupling to the port,  $\kappa$  is the coupling coefficient for the contribution of the incoming wave amplitude to the mode amplitude,  $c_s$  and  $c_a$  are coupling coefficients for the contributions of the incoming wave amplitude and the mode amplitude to the outgoing wave amplitude.

The complex amplitude  $a$  is normalized such that  $|a|^2 = W$  with  $W$  the energy of the mode. The complex amplitude  $s_{\pm}$  is normalized such that  $|s_{\pm}|^2 = P_{\pm}$  with  $P_{\pm}$  the power carried by the waves. The decay rate is related to the quality factor as  $\omega_0 \tau / 2 = Q$ . By considering energy conservation and time-reverse symmetry, the coupling coefficients are related as  $\kappa = c_a = \sqrt{2/\tau_e}$  and  $c_s = -1$ . This coupled-mode theory can be generalized to the case of single-mode-multi-port [78] and multi-mode-multi-port [79].

The dynamics of the coupling between the mode and the port are fully described by Eq. (2.41) and Eq. (2.42), from which the reflection, transmission (in the presence of two ports), and other interested quantities can be derived. The resonant frequency  $\omega_0$  and the decay rates  $1/\tau$  can be evaluated by either simulations or experiments for specific cavity designs. Notice that the ports should account for all channels of energy exchange with the environment through electromagnetic waves. For instance, the radiation of the cavity should be considered as outgoing waves in different directions through the correspondent ports.

In applications of on-chip micro-cavities, the cavity is usually coupled to in-plane waveguides (conventional or W1 waveguides) through the evanescent field of the cavity mode [Fig. 2.9 (b)]. Since the introduction of the waveguides modifies the stand-alone cavity design and lowers



the quality factor, a trade-off between the coupling strength and the quality factor is generally considered. On the other hand, when the in-plane cavity exhibits highly concentrated radiation in an out-of-plane direction (usually the normal direction), the cavity can also be excited through free-space beams in that direction. A band-folding technique [80, 81] can be used on PhC cavities to improve the concentration of the radiation, thus the coupling strength, while similarly, it reduces the quality factor.

## 2.2 Nonlinear Optics

Nonlinear optics is a broad topic in optics and is the key to many applications. This section briefly introduces the related aspects, i.e., the nonlinear susceptibility and the second-order nonlinear frequency conversion, and one can refer to textbooks [82, 83] for more details.

### 2.2.1 Nonlinear Susceptibility

In the case of linear optics, the induced polarization scales linearly with the electric field strength [82]:

$$\mathbf{P}(t) = \epsilon_0 \chi^{(1)} \mathbf{E}(t), \quad (2.43)$$

where  $\mathbf{P}$  is the polarization,  $\epsilon_0$  is the permittivity of vacuum,  $\chi^{(1)}$  is the linear susceptibility,  $\mathbf{E}$  is the electric strength,  $t$  is time.

In the case of nonlinear optics, Eq. (2.43) can be generalized:

$$\mathbf{P}(t) = \epsilon_0 [\chi^{(1)} \mathbf{E}(t) + \chi^{(2)} \mathbf{E}^2(t) + \chi^{(3)} \mathbf{E}^3(t) + \dots], \quad (2.44)$$

where  $\chi^{(2)}$  and  $\chi^{(3)}$  are the second and third-order nonlinear optical susceptibilities.

More generally, when considering (anisotropic) dispersion and/or loss, the nonlinear polarization can be expressed as:

$$\mathbf{P}(\mathbf{r}, t) = \sum_n \mathbf{P}(\omega_n) e^{-i\omega_n t}, \quad (2.45)$$

where  $\omega_n$  denotes the frequency involved, and the summation extends over all positive- and negative-frequency components.

The Cartesian components of the second-order nonlinear polarization can be expressed as:

$$P_i(\omega_n + \omega_m) = \epsilon_0 \sum_{jk} \sum_{(nm)} \chi_{ijk}^{(2)}(\omega_n + \omega_m, \omega_n, \omega_m) E_j(\omega_n) E_k(\omega_m), \quad (2.46)$$

where the indices  $i$ ,  $j$ , and  $k$  denote the Cartesian components of the fields (i.e.,  $x$ ,  $y$ , and  $z$ ) independently. The sum notation  $(nm)$  requires that, when performing the summation over  $n$  and  $m$ , the sum  $\omega_n + \omega_m$  should be fixed, which results in 12 permutations over frequency. In general, one needs as many as 324 (complex) numbers to fully describe the  $\chi^{(2)}$  tensor

involving three different frequencies.

Fortunately, because of intrinsic properties, approximations, and symmetry of the medium, far fewer numbers are necessarily needed to describe the nonlinear process:

1. **Reality of the fields:**  $\chi^{(2)}$  with negative frequencies equals the complex conjugate of its counterpart with positive frequencies.
2. **Intrinsic permutation symmetry:**  $\chi^{(2)}$  remains unchanged by a simultaneous interchange of its last two frequency arguments and its last two Cartesian indices.
3. **Assumption of lossless media (full permutation symmetry):** if the media is lossless, then all elements of the  $\chi^{(2)}$  tensor are real numbers, and all frequency arguments can be interchanged as long as the Cartesian indices are interchanged the same way.
4. **Assumption of nondispersive susceptibility (Kleinman's symmetry):** when the involved optical frequencies are much smaller than the lowest resonance frequency of the material system, then the nonlinear susceptibility is considered independent of frequency.
5. **Spatial symmetry of material (crystals):** if the nonlinear medium possesses spatial symmetry (e.g., crystals), many elements of the nonlinear susceptibility tensor cancel out. The form of nonlinear susceptibility of a crystal depends on the point group to which the crystal belongs, and one can refer to the tables as in section 1.5 of [82] and appendix 3 of [83]. An important conclusion is that, for crystals that possess centrosymmetry (inversion symmetry), all elements of the  $\chi^{(2)}$  tensor vanish. Because of this, 11 of 32 crystal classes are excluded from second-order nonlinear optical interactions.

When nondispersive susceptibility ((Kleinman's symmetry) is assumed, a new  $d$ -tensor can be introduced to suppress the frequency arguments:

$$d_{ijk} \equiv \frac{1}{2} \chi_{ijk}^{(2)}, \quad (2.47)$$

and the  $d$ -tensor can be simplified even more by a contracted matrix  $d_{il}$ , where the index  $l$  is determined according to the prescription:

$$\begin{array}{l} jk: \quad 11 \quad 22 \quad 33 \quad 23, 32 \quad 13, 31 \quad 12, 21 \\ l: \quad 1 \quad 2 \quad 3 \quad 4 \quad 5 \quad 6 \end{array} \quad (2.48)$$

where the indices 1, 2, and 3 for  $jk$  are identical to  $x$ ,  $y$ , and  $z$ , respectively.

### 2.2.2 Nonlinear Frequency Conversion

There are a variety of nonlinear processes in a nonlinear photonic material, among which the second-order frequency conversion processes are mainly considered in this thesis. These processes can be classified as sum frequency generation (SFG) and difference frequency generation (DFG) [Fig. 2.10].

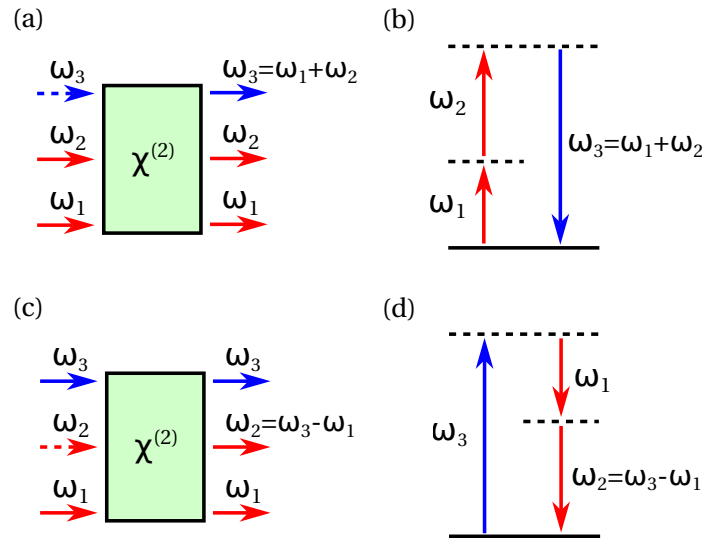


Figure 2.10: Second order nonlinear processes.  $\omega_1 \approx \omega_2 < \omega_3$  is assumed in general. (a) Schema of SFG. Typically there is no input at  $\omega_3$ . (b) Energy level diagram of SFG. (c) Schema of DFG. Typically there is no input at  $\omega_2$ . (d) Energy level diagram of DFG.

SFG is a process in which two light beams (of frequency  $\omega_1$  and  $\omega_2$ ) are sent to the material, and a new light beam ( $\omega_3$ ) is generated with a frequency equal to the sum of the input frequencies ( $\omega_3 = \omega_1 + \omega_2$ ). Second harmonic generation (SHG) can be regarded as a particular case of SFG in which the frequencies of the input beams are identical ( $\omega_1 = \omega_2 = \omega_3/2$ ). In the case of SHG, the generated frequency ( $\omega_3$ ) is referred to as the second harmonic (SH) frequency, and the pump frequency ( $\omega_1 = \omega_2$ ) is similarly referred to as the first harmonic (FH) frequency.

DFG is a process in which two light beams (of frequency  $\omega_1$  and  $\omega_3$ , respectively) are sent to the material, and a new light beam is generated with a frequency equal to the difference of the input frequencies ( $\omega_2 = \omega_3 - \omega_1$ ). This process is also known as parametric amplification since it amplifies the lower-frequency input beam ( $\omega_1$ ). This process is also referred to as parametric down-conversion (PDC) when it is considered as an inverse process of SHG.

Spontaneous parametric down-conversion (SPDC) can be regarded as a particular case of DFG in which only one light beam ((of frequency  $\omega_3$ , the lower-frequency input power at  $\omega_1$  or  $\omega_2$  is zero) is sent to the material, and two new beams ( $\omega_1$  and  $\omega_2$ ,  $\omega_1 + \omega_2 = \omega_3$ ), known as the signal and the idler and are often same or close in frequency ( $\omega_1 = \omega_2$  or  $\omega_1 \approx \omega_2$ ), are generated. SPDC is called degenerate SPDC if the two new beams are of the same frequency ( $\omega_1 = \omega_2$ ), or nondegenerate SPDC otherwise (conventionally, the higher-frequency beam is identified as the signal). Notice that SPDC is a quantum process and generally can not be described by the classical nonlinear theory of DFG. The efficiency is much lower than DFG because of the quantum nature. However, if the signal and idler are resonant in optical microcavities, the process is eventually transformed to classical DFG, and the efficiency is expected to be enhanced.

SFG and SHG, in which the output photon energy is higher than the input photon energy, are also referred to as up-conversion, while DFG and SPDC, in which the output photon energy is lower than the input photon energy, are also referred to as down-conversion.

In nonlinear frequency conversion, two conservation laws are generally valid: energy conservation and momentum conservation. The energy conservation is reflected by the relation of the frequencies, while the momentum conservation is reflected as the phase-matching condition for propagating waves, as in the case of free propagation of light in bulk nonlinear materials or confined propagation of light in waveguides. Because of the normal dispersion of the material, i.e., the refractive index increase with frequency, the phase-matching condition is usually achieved through birefringence with careful polarization controls. The efficiency (i.e., generated power divided by pump power) for up-conversion is proportional to the square of the pump power in the nondepleted condition (i.e., the conversion efficiency is small, and the pump intensity is constant). Otherwise, the Manley–Rowe relations are needed [82, 84]. Near to 100% SHG is theoretically possible and is only limited by the competition from other nonlinear processes such as down-conversion and third harmonic generation (THG). On the other hand, the efficiency for down-conversion is linearly proportional to the pump power, and the values are much smaller than SHG because of the quantum nature of the process (actually, classical nonlinear optics do not allow SPDC to exist).

## 2.3 III-Nitride Materials

### 2.3.1 Crystal Structure

III-nitride compounds are known to exhibit two crystal forms: the metastable cubic zincblende and the hexagonal wurtzite. In electronics and photonics, all III-nitride devices are in the wurtzite form due to their prominent thermostability and growth feasibility. The wurtzite crystal structure belongs to the dihexagonal-pyramidal crystal class (or point group, usually noted as  $6mm$  in Hermann–Mauguin notation, or  $C_{6v}$  in Schoenflies notation). There are different selections of primitive cells and conventional cells, depending on the choice of putting atoms at the center of the cell or the corner [Fig. 2.11 (a)]. It is common to have a primitive cell with atoms at the center of the cell (green dashed rhombus) and a conventional cell with atoms on the corners (red hexagon). The conventional cell of the wurtzite structure [Fig. 2.11 (b)] has the shape of a hexagonal column in which the side length of the bottom hexagon is denoted by a lattice parameter  $a$ , and the height of the column is denoted by a lattice parameter  $c$ , with the relation  $c = a\sqrt{8/3}$ . Each metal atom in the crystal is surrounded by four nitrogen atoms in a tetrahedral shape due to  $sp^3$ -hybridization, and vice versa. The distance between two neighboring metal and nitrogen atoms in the  $c$ -direction is denoted by  $u \cdot c$ , with  $u = 3/8$  the internal displacement parameter. The numerical values of the lattice parameters are listed in Table 2.2.

The crystal vectors can be expressed by using the crystal basis (i.e., the primitive vectors),

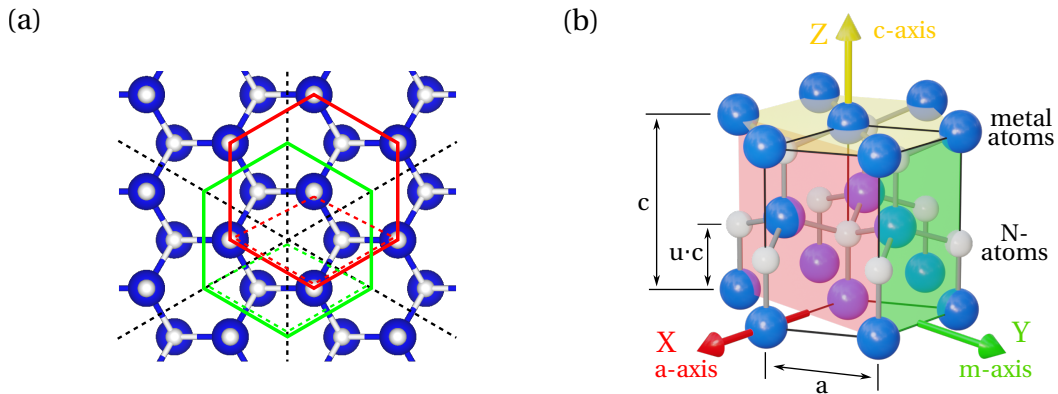


Figure 2.11: (a) Wurtzite III-nitride crystal viewed from the  $c$ -axis. Two different selections of the conventional cell are represented by red and green hexagons. Two selections of the primitive cell are represented by red and green dashed rhombuses, respectively. Cleavage directions of the growth substrate are indicated by black dashed lines. (b) The conventional cell of wurtzite III-nitride crystals. A primitive cell is indicated by black lines.  $a$ -,  $m$ -, and  $c$ -planes are represented in red, green, and yellow, respectively.  $a$ -,  $m$ - and  $c$ -axis, together with their corresponding Cartesian notations  $X$ ,  $Y$ , and  $Z$ , are indicated by arrows of the same set of colors.

Lattice parameter	GaN	AlN	ideal
$a$ [Å]	3.190	3.110	-
$c$ [Å]	5.189	4.980	-
$u$	0.377	0.382	0.375
$c/a$	1.627	1.601	1.633

Table 2.2: Lattice parameters of wurtzite GaN, AlN at room temperature [85].

which is a set of 3 vectors that forms the primitive cell. An example of basis can be given as  $\{\mathbf{a}_1, \mathbf{a}_2, \mathbf{c}\}$ , where  $\mathbf{a}_1, \mathbf{a}_2$  are two of three  $120^\circ$  symmetric vectors on the bottom hexagon of the conventional cell, and  $\mathbf{c}$  is the vector perpendicular to the bottom hexagon. For example,  $[1, 0, 0]$ ,  $[0, 1, 0]$ , and  $[0, 0, 1]$  are three unit vectors expressed using this basis. The crystal planes can be expressed by Miller indices once the basis is selected. For example, the red, green, and yellow planes can be noted as plane  $(2, -1, 0)$ ,  $(0, 1, 0)$ , and  $(0, 0, 1)$ .

Notice that, in cubic crystals, the permuted (swap the position of indices, add or remove the minus sign) vectors and planes experience the same symmetry in the crystal. But this is not valid in hexagonal crystals. For example,  $(0, 1, 0)$  and  $(0, 0, 1)$  are identical planes by symmetry in cubic crystals, but they are obviously different in the wurtzite structure. To better reveal symmetry relations by permutation, the Miller-Bravais notation is introduced.

### Miller-Bravais Notation

The Miller-Bravais notation is typically used for crystal planes [86] in trigonal and hexagonal lattices. Let the Miller indices be  $(h, k, l)$ , and the identical Miller-Bravais indices be  $(H, K, I, L)$ ,

## Chapter 2. Background Information

---

then the conversion relation is given by:

$$(h, k, l) \rightarrow (H, K, I, L) : H = h, K = k, I = -(h + k), L = l, \quad (2.49)$$

$$(H, K, I, L) \rightarrow (h, k, l) : h = H, k = K, l = L. \quad (2.50)$$

Round brackets are used here to indicate crystal planes. As an example, the red, green, and yellow planes are noted as  $(2, -1, 1, 0)$ ,  $(0, 1, 1, 0)$ , and  $(0, 0, 0, 1)$ , from which it can be revealed that these three planes are not the same because one notation can not be permuted from another one.

The Miller-Bravais notation is also used for crystal vectors (i.e., zone axes or Weber symbols) [86], while the conversion relation is non-trivial:

$$[h, k, l] \rightarrow [H, K, I, L] : H = (2h - k)/3, K = (2k - h)/3, I = -(h + k)/3, L = l, \quad (2.51)$$

$$[H, K, I, L] \rightarrow [h, k, l] : h = (3H + K)/2, k = (3K + H)/2, l = L. \quad (2.52)$$

Square brackets are used here to indicate crystal vectors. As an example, the unit vectors  $[1, 0, 0]$ ,  $[0, 1, 0]$ , and  $[0, 0, 1]$  are noted as  $[2/3, -1/3, -1/3, 0]$ ,  $[-1/3, 2/3, -1/3, 0]$ , and  $[0, 0, 0, 1]$ . Notice that the first and the second vectors are in the same permutation class and different from the third one.

### Principal Crystallographic Axes

Alternatively, a crystal structure can also be described by using a Cartesian coordinate system  $o - xyz$ , in which the axes  $x$ ,  $y$ , and  $z$  are referred to as the principal crystallographic axes, and their relation to the symmetry elements of the crystal conforms with the convention [87]. In the case of the wurtzite structure, the  $z$ -axis is aligned with the  $c$ -axis, the  $x$ -axis is aligned with one of the  $a$ -axes, and the  $y$ -axis is perpendicular to the  $x$ -axis and  $z$ -axis. An example of the relation among different notations for directions and planes is specified in Table 2.3.

Conventional name	$a$ -axis	$m$ -axis	$c$ -axis	$a$ -plane	$m$ -plane	$c$ -plane
Miller notation	$[100]$	$[120]$	$[001]$	$(2\bar{1}0)$	$(010)$	$(001)$
Miller-Bravais notation	$[2\bar{1}\bar{1}0]$	$[01\bar{1}0]$	$[0001]$	$(2\bar{1}\bar{1}0)$	$(01\bar{1}0)$	$(0001)$
Cartesian axes	$x$	$y$	$z$	-	-	-

Table 2.3: Directions and planes in the wurtzite lattice under different notations.

### 2.3.2 Optical Properties

The absorption spectrum of semiconductor materials mainly depends on the bandgap, which is derived from the energy-momentum ( $E-k$ ) dispersion relation of the crystal lattice. Band structure calculations for wurtzite III-nitrides show a direct bandgap at the  $\Gamma$ -point, which indicates efficient light-matter interaction without involving phonons and, thus, heating

effects in the crystal. As for the bandgap energy, III-nitride semiconductors cover from the infrared to the deep UV region, with InN at 0.7 eV, GaN at 3.4 eV, and AlN at 6.0 eV. Because of the large bandgap, GaN and AlN show very low absorption until reaching the UV and deep UV range, which brings much convenience for frequency conversion processes without worrying about the high-frequency beam being absorbed by the material.

Because of the built-in polarization, the wurtzite crystal is a uniaxial positive birefringent crystal with its optical axis parallel to the [0001]  $c$ -axis. The optical birefringence is approximately 0.04 in the transparent range [88, 89]:

$$\Delta n = n_e - n_o \approx 0.04. \quad (2.53)$$

The ordinary refractive indices of GaN and AlN at wavelengths of interest are presented in table 2.4. The refractive indices of AlGaIn alloy continuously vary between those of GaN and AlN depending on the relative concentration and can be calculated with empirical equations [90]. The refractive indices are also influenced by the temperature, stress, and crystallinity of the material, whereas the latter two are dependent on the size (or thickness) of the crystal and the growth techniques.

n	GaN	AlN
Ordinary at 775 nm	2.3127	1.9545
Ordinary at 1550 nm	2.2808	1.9407

Table 2.4: Experimental refractive indices for GaN and AlN [90].

### 2.3.3 Nonlinear Properties

The wurtzite structure belongs to the dihexagonal-pyramidal crystal class (usually noted as  $6mm$  in Hermann–Mauguin notation, or  $C_{6v}$  in Schoenflies notation), which lacks inversion symmetry (or central symmetry). Because of this, the negative and positive charge barycenters are separated along the  $c$ -axis, inducing large built-in spontaneous polarization  $P_{sp}$  in the [0001] direction, which gives rise to the piezoelectric effects, and more importantly in this context, to the non-zero second-order nonlinear optical susceptibility [82].

In the  $6mm$  crystal class, the non-vanishing  $\chi^{(2)}$  tensor elements are [82]:

$$\chi_{xzx}^{(2)} = \chi_{yzy}^{(2)}, \chi_{xxz}^{(2)} = \chi_{yyz}^{(2)}, \chi_{zxx}^{(2)} = \chi_{zyy}^{(2)}, \chi_{zzz}^{(2)}, \quad (2.54)$$

where the reference axes,  $x$ ,  $y$ , and  $z$ , are the principal crystallographic axes [83].

## Chapter 2. Background Information

Then the  $\chi^{(2)}$  tensor can be fully expressed as [83]:

$$\chi_{(6mm)}^{(2)} = \begin{bmatrix} 0 & 0 & 0 & 0 & 0 & \chi_{xzx}^{(2)} & \chi_{xxz}^{(2)} & 0 & 0 \\ 0 & 0 & 0 & \chi_{xxz}^{(2)} & \chi_{xzx}^{(2)} & 0 & 0 & 0 & 0 \\ \chi_{zxx}^{(2)} & \chi_{zxx}^{(2)} & \chi_{zzz}^{(2)} & 0 & 0 & 0 & 0 & 0 & 0 \end{bmatrix} \quad (2.55)$$

The non-zero elements of the  $d$ -tensor are  $d_{15}$ ,  $d_{31}$  and  $d_{33}$  and satisfy:

$$d_{15} = d_{31}, \quad d_{31} = -\frac{1}{2}d_{33} \quad (2.56)$$

And the contracted  $d$ -tensor can be expressed as [83]:

$$d_{6mm} = \begin{bmatrix} 0 & 0 & 0 & 0 & d_{15} & 0 \\ 0 & 0 & 0 & d_{15} & 0 & 0 \\ d_{31} & d_{31} & d_{33} & 0 & 0 & 0 \end{bmatrix}, \quad d_{15} = d_{31}. \quad (2.57)$$

The correspondence between  $d$  notation and the  $\chi^{(2)}$  notation can be specified according to relation (2.48):

$$\begin{array}{l} d_{il}: \\ \chi_{ijk}^{(2)}: \end{array} \quad \begin{array}{l} d_{15} \\ \chi_{xzx}^{(2)}, \chi_{xxz}^{(2)} \end{array} \quad \begin{array}{l} d_{31} \\ \chi_{zxx}^{(2)} \end{array} \quad \begin{array}{l} d_{33} \\ \chi_{zzz}^{(2)}. \end{array} \quad (2.58)$$

The refractive indices and nonlinear susceptibilities of interests for GaN and AlN are given in Table 2.5.

	GaN	AlN
$\chi^{(2)}$	$\chi_{zxx}^{(2)} = 5.0 \text{ pm/V}$ $(\pm 10\% \text{ at } 1064 \text{ nm [91]})$ $\chi_{zzz}^{(2)} = -7.6 \text{ pm/V}$ $(\pm 10\% \text{ at } 1064 \text{ nm [91]})$	$\chi_{zxx}^{(2)} < 0.62 \text{ pm/V}$ $(\pm 55\% \text{ at } 1064 \text{ nm [92]})$ $\chi_{zzz}^{(2)} = 15.50 \text{ pm/V}$ $(\pm 55\% \text{ at } 1064 \text{ nm [92]})$ $\chi_{zxx}^{(2)} = 0.4 \text{ pm/V}$ $(\text{sputtered, at } 1064 \text{ nm [93]})$ $\chi_{zzz}^{(2)} = 16 \text{ pm/V}$ $(\text{sputtered, at } 1064 \text{ nm [93]})$
$\chi^{(3)}$	$\chi_{xxxx}^{(3)} = 3.8 \times 10^{-19} \text{ m}^2/\text{V}^2$ $(\text{at } 365 \text{ nm [94]})$	- (no data)

Table 2.5: Experimental nonlinear susceptibilities for GaN and AlN. Note: some ESU (electrostatic units) values in the original reports are converted in MKS units by multiplying a factor of  $(4/3)\pi \times 10^{-4}$  for  $\chi^{(2)}$ , and  $(4/9)\pi \times 10^{-8}$  for  $\chi^{(3)}$  (Eq. 10 in [95]).



## 3 Fabrication of 2D PhC Slabs

This chapter presents the fabrication techniques of 2D PhC slabs. First, the main fabrication workflow, which is mainly inherited and adapted from previous works, is detailed in sequential order. Then, explorations of some auxiliary techniques are reported.

### 3.1 Main Fabrication Processes

#### 3.1.1 Overview

The devices involved in this thesis are mainly of two types: 2D PhC cavities side-coupled to waveguides [Fig. 3.1 (a)] and doubly resonant PhC cavities without side-coupling. In both cases, the PhC slab is suspended in the air to achieve high contrast of refractive indices. The III-nitride layer is etched with  $\text{Cl}_2$  based inductively coupled plasma - reactive ion etching (ICP-RIE) processes, which requires a hard mask with enough resistance.  $\text{SiO}_2$  is the hard mask of choice in this case, and two fabrication routines are developed: the ZEP520A (ZEP) technique and the hydrogen silsesquioxane (HSQ) technique.

The ZEP technique first uses a patterned ZEP layer as a mask to etch a plasma-enhanced chemical vapor deposition (PECVD)-deposited  $\text{SiO}_2$  layer and then uses the patterned  $\text{SiO}_2$  layer as a mask to etch the III-nitride layer. This 2-step etching technique contains mainly the following steps [Fig. 3.1 (b)]:

1. an AlN/GaN thin film of thickness about 200-300 nm is grown on a Si(111) substrate with metalorganic vapour-phase epitaxy (MOVPE);
2. a layer of about 100 nm poly-crystalline/amorphous  $\text{SiO}_2$  is deposited on top of the AlN/GaN layers as a hard mask for III-nitride etching;
3. a layer of about 310 nm ZEP is spin-coated on top of  $\text{SiO}_2$  as a mask for  $\text{SiO}_2$  etching;
4. a pre-designed pattern is written on the ZEP layer with e-beam lithography;
5. the  $\text{SiO}_2$  layer is dry-etched with ICP-RIE, and the pattern is transferred from the ZEP layer to the  $\text{SiO}_2$  layer;
6. the residue of ZEP is removed by wet-etching or dry-etching;

### Chapter 3. Fabrication of 2D PhC Slabs

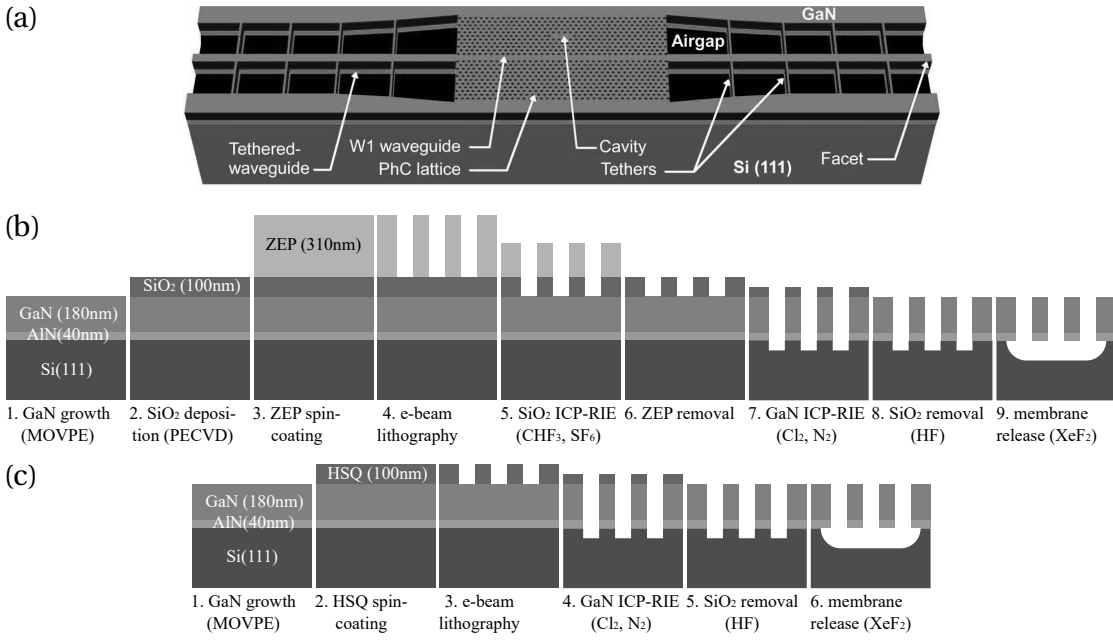


Figure 3.1: (a) Schematic representation of the side-coupling PhC cavity platform (adapted from [96]). The cavity located on the PhC area is side-coupled to a W1 waveguide and then to the tethered waveguide. The PhC part and the waveguides are suspended in the air. (b) Schematic representation of the main fabrication steps of the platform using the 2-step etching ZEP technique. (c) Schematic representation of the main fabrication steps of the platform using the 1-step etching HSQ technique.

7. the AlN/GaN layers are etched by dedicated ICP-RIE, and the pattern is transferred from the SiO<sub>2</sub> layer to the AlN/GaN layer;
8. the residue of SiO<sub>2</sub> is removed by hydrofluoric acid (HF) wet-etching;
9. the AlN/GaN membrane is released from the Si(111) substrate by under-etching Si with XeF<sub>2</sub>, and the suspended structure of AlN/GaN is created.

The HSQ technique (see section 3.2.3) directly uses a patterned HSQ layer as a mask to etch the III-nitride layer since HSQ becomes SiO<sub>2</sub> after electron beam exposure. This 1-step etching technique is simpler than the ZEP technique as the above steps 2-6 are replaced by [Fig. 3.1 (c)]:

2. a layer of about 100 nm HSQ is spin-coated on top of AlN/GaN layer;
3. a pre-designed pattern is written on the HSQ layer with e-beam lithography, and the HSQ layer becomes a patterned SiO<sub>2</sub> layer.

The HSQ technique is generally advantageous over the ZEP technique because: first, it involves fewer steps and makes the fabrication simpler; second, it provides higher resolution because of the high resolution of HSQ itself and smaller distortion during pattern transfer. However, in the case of 2D PhCs, the HSQ technique is much more time-consuming in e-beam lithography (see section 3.2.3). In this thesis, the 2D PhC devices are mainly fabricated with the ZEP technique and the steps are detailed below in sequential order.

### 3.1.2 Crystal Growth and Thin Film Characterization

#### Crystal Growth

The AlN/GaN crystal is epitaxially grown on a Si(111) substrate by MOVPE [97, 98] [Fig. 3.2 (a)]. First, the precursor gases, ammonia ( $\text{NH}_3$ ), trimethylgallium (TMGa) ( $\text{Ga}(\text{CH}_3)_3$ ), and trimethylaluminum (TMAI) ( $\text{Al}_2(\text{CH}_3)_6$ ), together with the carrier gases hydrogen ( $\text{H}_2$ ) and nitrogen ( $\text{N}_2$ ), are transported into a reaction chamber. Then, the metalorganic precursors form complexes with ammonia, and the molecules dissociate at the surface of the substrate because of the high temperature, delivering the desired atoms of Al, Ga, and N. Afterwards, the atoms diffuse on the surface and nucleate to form islands. As more and more atoms are delivered to the surface, the islands grow larger and join together (coalesce) to form steps and layers. Meanwhile, the byproduct of  $\text{CH}_3$  cluster and H atoms form  $\text{CH}_4$ , which is a volatile gas and is pumped out from the chamber. Because of the volatility of the byproduct gas and the stability of the AlN/GaN crystal, the chemical reaction is dominant in one direction. Finally, the film grows along the desired crystal axis when the corresponding crystal plane is matched to the substrate lattice. The overall reaction can be expressed as:

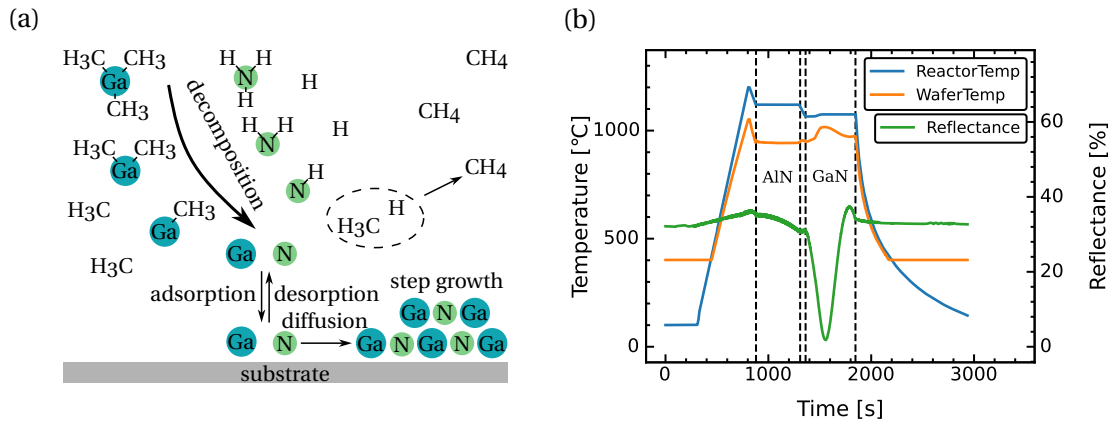
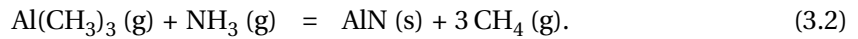
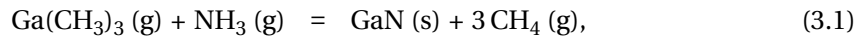


Figure 3.2: (a) Schematic representation of MOVPE growth of AlN/GaN. (b) Temperature and reflectance as a function of time during the growth. The periods for AlN and GaN growth are noted by dashed lines.

To enable epitaxial growth along the  $c$ -axis of the wurtzite crystal, the substrate is desired to match the hexagonal lattice. Sapphire (0001) and SiC (0001) are usually used in this case because of the small lattice difference. However, these substrates are either difficult to fabricate or require complex process techniques in terms of lithography and etching. Alternatively, Si (111) is easy to fabricate, and the processing is compatible with standard silicon techniques [97–99]. The drawback is that the mismatch of lattice constants (lattice mismatch) between Si (111) and GaN (0001) is high, about 17%, which results in a large tensile strain in the film. A larger lattice

mismatch leads to a larger built-in strain, as well as more structural defects, which limits the thickness and quality of the crystal film. Furthermore, the mismatch of thermal expansion coefficients (thermal mismatch) is also an essential factor since the lattice matching should also be considered at high temperatures during the growth [100–103]. In practice, before the growth of GaN, a thin layer of AlN (about 40 nm) is introduced to prevent the formation of Ga-Si eutectics and the associated melt-back etching [98]<sup>1</sup>.

The growth is realized in a dedicated reactor (Aixtron AIX200 RF-S)<sup>2</sup> in which the substrate is mounted horizontally on a spinning stage with a rotation speed of 30 round per minute (RPM). The temperature of the substrate is controlled by the stage and is monitored by both a thermocouple attached to the stage and an infrared pyrometer installed on the top side of the chamber. The thickness of the grown film is monitored by measuring the reflectance of the sample surface. During the growth, the temperature of the stage is firstly raised up to 1200°C with H<sub>2</sub> flow to remove water and adhesion gases [Fig. 3.2 (b)]. Then, the temperature is stabilized at 1120°C with TMAI and ammonia for 428 s, which results in the growth of 37 nm AlN with a growth rate of 0.086 nm/s (5.187 nm/min). Then the temperature is reduced to 1075°C with TMGa and ammonia for 489 s, which results in the growth of 177 nm GaN with a growth rate of 0.362 nm/s (21.718 nm/min). Finally, the precursor gases are turned off, and the substrate is cooled down to room temperature. The temperature measured by the pyrometer slightly differs from that of the thermocouple because the pyrometer measures the surface of the sample while the thermocouple measures the sample stage. The change of emissivity of the sample surface also contributes to the difference.

The wafer with AlN/GaN layers is then stored in a nitrogen box to prevent potential gas adsorption and surface oxidation [104] (see section 5.3.5).

#### Thin Film Characterization

The AlN/GaN/Si(111) sample is usually characterized for film thickness and surface roughness before fabrication. The film thickness was measured by an ellipsometer (J.A. Woollam alpha-SE) along the *x*- and *y*-axis of the wafer and showed a distribution from 217 nm (AlN + GaN) on the center to 180 nm on the border of the wafer [Fig. 3.3 (a) (c)]. Since the sample wafer is spinning at a relatively high speed, the thickness is symmetric around the spin axis, i.e., the center of the wafer. The surface roughness is measured by atomic force microscopy (AFM) (Park Systems XE-100) on the center of the sample for an area of 20×20 μm<sup>2</sup>, by a probe of tip radius 7 nm (Bruker OTESPA-R3) [Fig. 3.3 (b) (d)]. The root mean square (RMS) roughness was measured to be 3.4 nm, and the peak-to-valley difference was about 20 nm.

---

<sup>1</sup>Since the AlN buffer is very thin, and the dislocation density is high, the compression effect of AlN layer is not considered here.

<sup>2</sup>The growth was carried out by Dr. J. F. Carlin in the Laboratory of Advanced Semiconductors for Photonics and Electronics (LASPE).

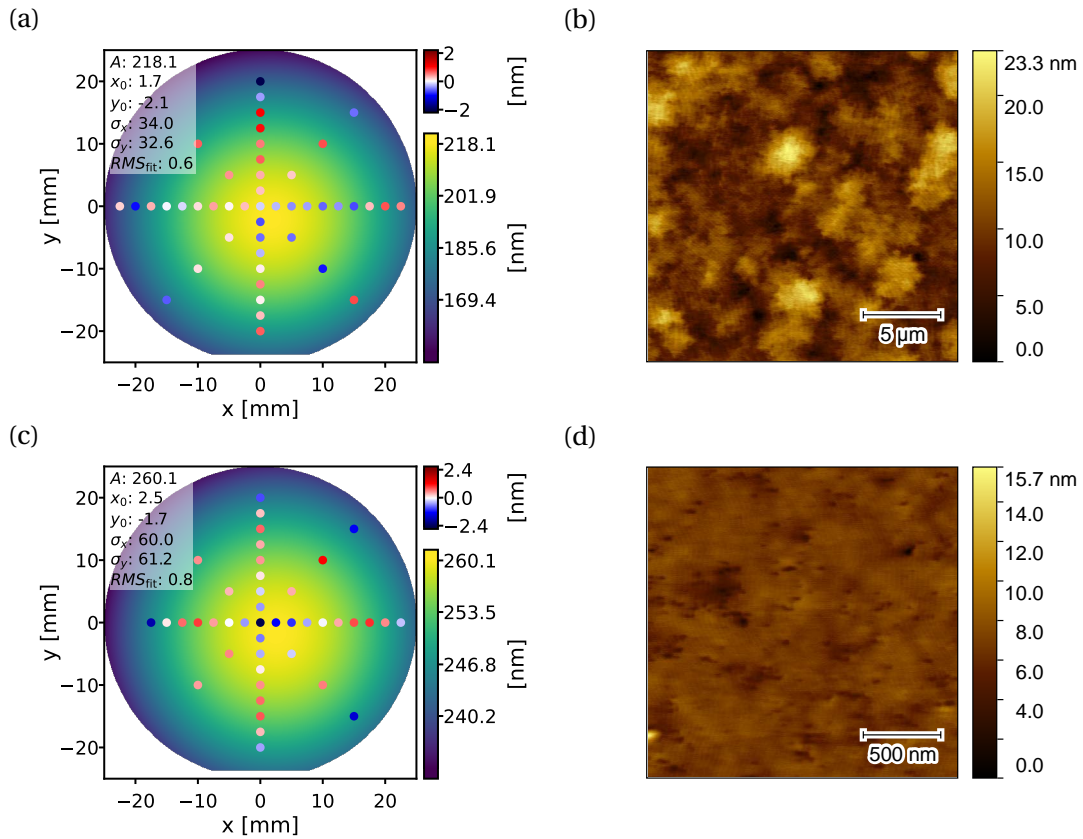


Figure 3.3: (a) Film thickness of an AlN/GaN (37/177 nm) sample measured by ellipsometry. The green disk is the 2D Gaussian fit, and the measured points are shown as scattered points colored by the mismatch from the fitting. (b) Surface morphology of an AlN/GaN (37/177 nm) sample measured by AFM. The field size is  $20 \times 20 \mu\text{m}^2$ , and the RMS roughness is 3.5 nm. (c) Film thickness of an AlN (256 nm) sample measured by ellipsometry. (d) Surface morphology of an AlN (256 nm) sample measured by AFM. The field size is  $2 \times 2 \mu\text{m}^2$ , and the RMS roughness is 0.8 nm. The field size is smaller than (b) because there are no features on a large scale.

### 3.1.3 Dicing and Cleaning

After crystal growth and characterization, the 2-inch Si(111) wafer is diced into small chips at the beginning of fabrication for small-scale production. In the case of mass production, this step is at the end of fabrication.

#### Dicing

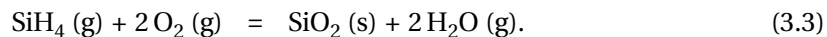
The 2-inch Si(111) wafer is typically diced into chips of size  $5 \times 5$ ,  $10 \times 10$ ,  $15 \times 15$ ,  $20 \times 20 \text{ mm}^2$ . To do that, the wafer is first scribed by a manual or automatic (JFP 100) scriber and then cleaved or broken down. Alternatively, the wafer can be cut by a dedicated circular saw, and in this case, the sample surface needs to be protected by a spin-coated polymer film (e.g., AZ-1512). The  $x$ - and  $y$ -axis of the chip are usually discriminated either by a scribe mark or by a slight difference between chip width and height (e.g.,  $10 \times 11 \text{ mm}^2$ ).

### Cleaning

After dicing, the chips are cleaned up with a standard cleaning process in a fume hood. First, the chips are put in acetone with an ultrasonic bath at 37 kHz (80 kHz for samples with delicate structures) for 5 min. Then, the chips are put in isopropyl alcohol (IPA) with another ultrasonic bath at 37 kHz for 5 min. And finally, the chips are rinsed with IPA and blow-dried with nitrogen gas.

#### 3.1.4 Hard Mask Deposition

A thin layer of Silica ( $\text{SiO}_2$ ) is deposited on top of AlN/GaN layers by PECVD (Oxford Plasmalab System 100 reactor) after dicing and cleaning. First, the sample (typically small chips) is heated up to  $300^\circ\text{C}$  in  $\text{N}_2$  to remove water and other gases. Then the precursor gases of Silane ( $\text{SiH}_4$ ) and Oxygen ( $\text{O}_2$ ) are provided, and plasma is ignited in between the sample holder and the upper electrode. The plasma helps to dissociate  $\text{SiH}_4$  and  $\text{O}_2$  to generate the desired atoms of Si and O. The atoms then bound together on the surface of the sample as the film of  $\text{SiO}_2$  grows up. Meanwhile, the byproduct of  $\text{H}_2\text{O}$  is in the volatile gas phase and is pumped out. The deposition of  $\text{SiO}_2$  does not require lattice matching with the substrate, and the film is amorphous. The overall reaction can be expressed as follows:



The thickness of the deposited  $\text{SiO}_2$  film is measured by interferometry (Sensofar S-Neox). A deposition duration of 110 s results in  $\text{SiO}_2$  thickness of 110 nm (1.0 nm/s) on  $10 \times 10 \text{ mm}^2$  chips. The deposition rate is a bit lower for large wafers because of the larger exposure area and is a bit higher (4% - 8%) near the chip edges. The repeatability of film thickness is precise down to a few nanometers.

#### 3.1.5 Electron Beam Lithography

Electron beam lithography (EBL) is a process using a beam of electrons (e-beam) to change the solubility (exposure) of electron-sensitive films (resist) and then dissolve (develop) unwanted parts in a solvent (developer) to create a patterned mask for etching. It consists of the following steps: layout design, data preparation (including data fracturing, proximity effect correction, and job preparation), resist-coating, exposure, and development.

EBL differs from its counterpart, photo-lithography, because of the very nature of using an electron beam to expose the resist: electrons are negatively charged particles and they repel each other. For this reason, only one beam at a time can be manipulated with high accuracy, resulting in a serial manner of exposure (also called writing in this sense) and the required time scales with the resolution and the area to expose. However, EBL takes advantage of electrons to easily achieve a sub-10 nm resolution without requiring a pre-fabricated mask.

#### Layout Design

Layout design is the process of creating a layout pattern (soft mask) to define the exposure areas. The layout pattern is designed in the GDSII stream format (GDSII) [105], which is a standard binary database format for transferring and archiving 2D graphical design data. It contains hierarchical structures (cells) in which basic geometry elements such as polygons are defined. The format uses internally defined datatypes which makes it platform-independent. The implementation of references significantly reduces the redundancy of the repeating elements and thus improves the efficiency of storage and processing.

There are many software tools (both commercial and open-sourced) with graphical user interfaces for visualizing and creating GDSII files, such as Tanner L-edit, LyoutEditor, KLayout (recommend), etc. Alternatively, there is also the Python package **gdspy** [106] that enables layout creation fully by coding. In this thesis, the side-coupled PhC cavities were designed using both Tanner L-edit (with built-in C++ code) and **gdspy**, the doubly resonant cavities were designed only using **gdspy**, and the GDSII files are visualized with KLayout.

On the layout of side-coupled cavities [Fig. 3.4], the chip size is  $10 \times 10 \text{ mm}^2$ , and the effective writing area is about  $5 \times 5 \text{ mm}^2$ . The effective writing area contains about 100 devices with long waveguides and PhCs (core). The total width of the devices is about 3.2 mm, which is about the minimal size for cleaving and chip handling. The long waveguides are fixed to the bulk by tethers, which could be straight lines or twisted springs (see section 3.2.1). The long waveguides end with a tapered shape for better coupling to lensed (tapered) optical fibers. The core PhC contains a PhC cavity and a W1 waveguide that is connected to the long waveguides on the side. The corners of all features are rounded with a radius of about 200 nm for better mechanical stability.

On the layout of doubly resonant cavities [Fig. 3.5] (see section 5.2), the chip size is  $15 \times 15 \text{ mm}^2$  (or  $20 \times 20 \text{ mm}^2$ ). Since the cavities are not coupled to waveguides, the layout is simpler. The cavities are arranged into groups of thin-arc shapes to scan the thickness of the slab (i.e., the GaN/AlN thin film) since the thickness distribution is symmetric around the center of the wafer (see section 3.1.2). In each thin-arc group, there are about 100 cavities that scan the lattice constant  $a$  and the hole radius  $r$  (10 by 10). The cavities are separated by a distance of 80-150  $\mu\text{m}$  to fully isolate them for proximity effect correction (PEC) (see section 3.1.5) and to ensure each cavity is contained in an individual mainfield of EBL (see exposure part in section 3.1.5). The thin-arc groups are also repeated for redundancy so that there are about 1000 cavities on the chip.

The doubly resonant cavity is created by first defining its grid (with nodes), which is similar to the lattice of the PhC. The grid contains information about the coordinates and the type of each "unit cell" (e.g., holes with different radii and relative shifts). Then, five "unit cells" corresponding to the five holes of different radii are created with elementary shapes. In the case of positive resist (ZEP), the "unit cells" are simply round disks; in the case of negative tone resist (HSQ), the "unit cells" are hexagons with round holes (the negative tone layout can be

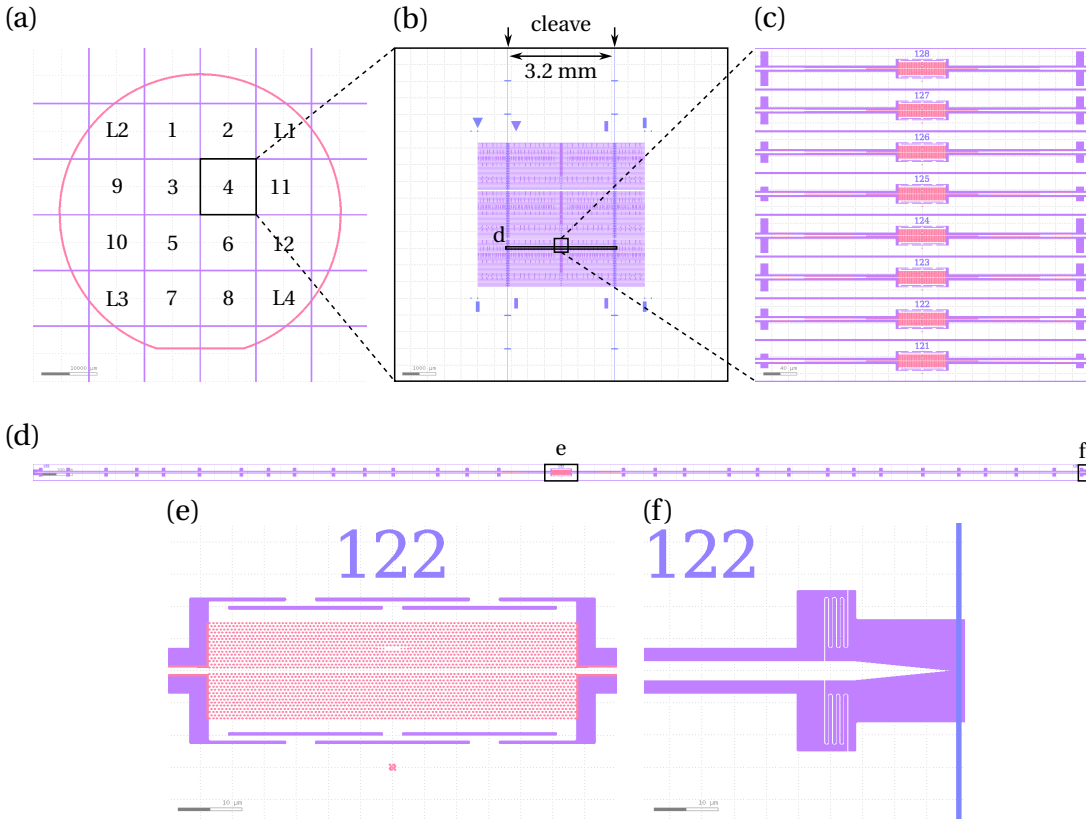


Figure 3.4: Layout design of PhC cavities side-coupled with waveguides. (a) Dicing plan of  $10 \times 10 \text{ mm}^2$  chips on a 2-inch Si(111) wafer. (b) Chip layout of PhCs with side-coupled waveguides. (c) Zoomed view of PhCs. (d) A PhC device with its waveguides. (e) PhC core with an L3 cavity side-coupled to a W1 waveguide. (f) Tapered end of the waveguide.

simply reversed from the positive one by boolean operation but this will result in an arbitrary division of the PhC because of limitation on maximum polygon vertices). Finally, the cavity grid is filled by referencing the "unit cells" to their corresponding locations. A minimized example of doubly resonant cavity design by **gdspsy** is given in appendix A.2.

On both layouts, labels, dose detectors, alignment markers, step measurement windows, laser measurement windows, and other features are optionally added. The labels (text height 4-8  $\mu\text{m}$ ) are shapes etched together with the devices and they help to identify the device under microscopes. The dose detectors are chessboard-like patterns composed of squares of size 250 nm for monitoring the dose level. The step measurement windows are squares of size 100  $\mu\text{m}$  for step measurement by mechanical profilometers. The laser measurement windows are squares of size 250  $\mu\text{m}$  for laser reflectivity tracking during III-nitride etching.

To enable high resolution, the unit of the GDSII files generated by **gdspsy** was set to be  $10^{-9}$  m and the precision was set to be  $10^{-11}$  m. The round shapes are approached by polygons of up to 199 vertices, where the limit is defined by the original version of the GDSII format and guarantees maximum compatibility. The elements on the layout are generally placed on



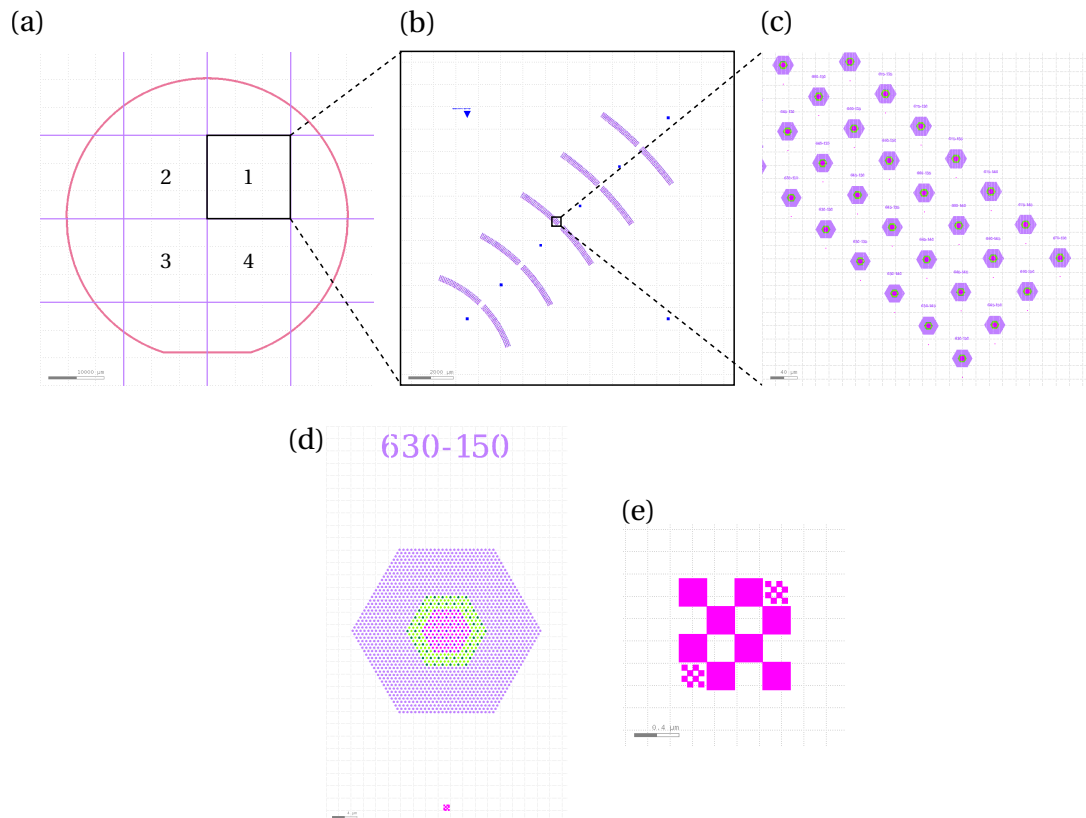


Figure 3.5: Layout design of doubly resonant PhC cavities. (a) Dicing plan of  $15 \times 15 \text{ mm}^2$  chips on a 2-inch Si(111) wafer. (b) Chip layout of doubly resonant PhC cavities. (c) Zoomed view of Cavities. (d) A doubly resonant PhC cavity with its label and dose chessboard. (e) Dose chessboard.

different GDSII layers for different EBL resolutions: the cavities and the dose detectors are on a layer with a fine data fracturing resolution (1-2 nm), the other elements are on layers with coarse fracturing resolutions (5-20 nm).

### Data fracturing

Data fracturing is a basic step that converts the shapes, represented by polygons in GDSII format, to discrete shots of electron beams with appropriate step size, writing order, mainfields, etc [Fig. 3.6 (a)-(c)]. The available software tools for data fracturing are **CATS** and **Beamber**. The step size is the minimum separation of the electron beam shots on the sample surface. It is also roughly the size of fragments that the polygon shapes are fractured into. So the step size represents the resolution of the writing of the electron beams. Notice that the step size is a different concept than the electron beam size. The latter represents the full width at half maximum (FWHM) of the Gaussian distribution of the electron beam on the sample surface and is defined by the focus and the current. There are pre-tested beam sizes recommended for different combinations of step size and exposure dose, and usually, the beam size is

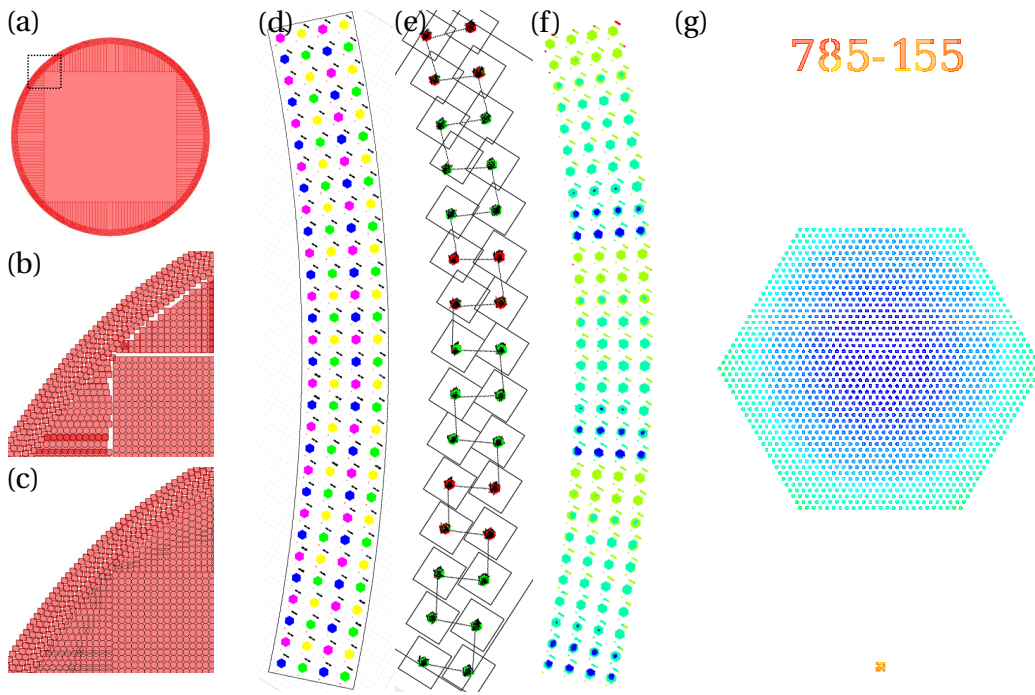


Figure 3.6: Data fracturing and proximity effect correction. (a) Sequential fracturing of a hole in a PhC. The bulk area is fractured as trapezoids that are filled by arrays of successive individual shots, and the sleeve area is fractured as individual shots following the curvature of the edge. (b) Zoomed area of the dashed square in (a) with the resolution the same as the beam step size. (c) Zoomed area of the dashed square in (a) with a higher resolution than the beam step size. (d) Cavities are divided into 4 exposure groups to avoid stitching errors caused by splitting a cavity into different mainfields. (e) Mainfield assignment of a group of cavities. Notice that no cavity is split into different mainfields. (f) Dose map of a group of cavities scanning the cavity parameters after PEC. (g) Dose map of a doubly resonant cavity PEC, with its label on the top and its dose detector on the bottom. High-dose areas are in red and low-dose areas are in blue. Notice that the symmetry of the dose assignment is influenced by the label.

slightly larger than the step size. The fracturing also defines the writing order of the e-beam shots, which can be random for better overall homogeneity or following specific geometries to optimize the local accuracy. Because the e-beam deflection angle is limited, the writing area without moving the sample stage is a small subset of the whole layout and is called the **mainfield**. The translation accuracy of the sample stage is less accurate than the deflection of the e-beam, so stitching errors are generated among mainfields. In data fracturing, the mainfields are adjusted (size and position) to avoid putting critical features on the edges [Fig. 3.6 (d) (e)].

### Proximity Effect Correction

PEC is a correction of the doses assigned to different shots. When a beam of electrons is shot on the sample coated with an e-beam resist, the energy of the electrons is high enough to break the chemical bonds in the resist (in the case of a positive resist, for example, ZEP), which results in an "exposure". Meanwhile, the electrons collide with the atoms. When the collision

is elastic, the electrons are back-scattered by the nuclei of the atom or forward-scattered by the electrons in the atom. When the collision is inelastic, the electrons expel existing electrons out of the atom and create secondary electrons, which propagate randomly. The scattered electrons and the secondary electrons contribute to the exposure of the direct shot area and its proximity, resulting in rounded corners and edges of the mask pattern, and this is known as the **proximity effect**.

To correct the proximity effect, the contribution to the proximity of all the shots is integrated to give an effective dose distribution, and the dose distribution is flattened to the base level by correcting the doses of shots at different locations, which results in higher doses assigned to shots around the edges and the corners. The available software tool for PEC is **Beamer**. In practice, the deposited energy intensity (DEI) distribution (or point spread function (PSF)) of the proximity effect is modeled by two Gaussian functions as [107, 108]:

$$f(r) = \frac{1}{1+\eta} \left( \frac{1}{\pi\alpha^2} e^{-\frac{r^2}{\alpha^2}} + \frac{\eta}{\pi\beta^2} e^{-\frac{r^2}{\beta^2}} \right), \quad (3.4)$$

where  $\alpha$  is the forward-scattering parameter,  $\beta$  is the back-scattering parameter,  $\eta$  is the energy ratio of the back-scattering to the forward scattering, and  $r$  is the distance to the electron incident point. The forward-scattering distribution is assumed to be the same as the Gaussian distribution of the electron beam, and the  $\alpha$  parameter is 0.005  $\mu\text{m}$ . The back-scattering of ZEP/ SiO<sub>2</sub>/III-nitride thin layers on a Si substrate is considered to be the same as the Si substrate, and the  $\beta$  parameter is 33  $\mu\text{m}$ . The energy ratio of the two components  $\eta$  is retrieved from **dose tests** and takes the value of 0.4. Examples of dose assignments are presented in Fig. 3.6 (f) (g).

#### Job Preparation

Finally, the fractured data with PEC is transferred to the EBL system for job preparation. The available software tool is **cjob**, which provides the final arrangement of layout repetitions (dies) on a wafer, a few utilities, and most basically, the base dose and the e-beam selection. The base dose is retrieved from the dose test, and it determines which size (current) of electron beam should be selected by:

$$D_{\text{base}} \left[ \frac{\mu\text{C}}{\text{cm}^2} \right] = \frac{10^3 \cdot I_{\text{beam}}[\text{pA}]}{f_{\text{exp}}[\text{MHz}] \cdot \Delta x^2[\text{nm}]}, \quad (3.5)$$

where  $D_{\text{base}}$  is the base dose (charge per unit area),  $I_{\text{beam}}$  is the electron beam current,  $f_{\text{exp}}$  is the exposure frequency,  $\Delta x$  is the exposure step size. The choice of electron beam currents  $I_{\text{beam}}$  is limited to several predefined values and the exposure frequency  $f_{\text{exp}}$  is limited to up to 50 MHz. When multiple electron beam currents satisfy the above relation, the one that enables the highest exposure frequency is selected.

### Resist Coating

At the beginning of the EBL, a thin layer of e-beam-resist is deposited on the surface of the sample by spin coating. The resist is a material that transforms its solubility in a certain solvent (developer) after being exposed to an electron beam, and it is called positive tone if it transforms from unsolvable to solvable, and negative tone the reverse. In this context, the ZEP photoresist is mainly used. It is a positive tone resist and is widely used because of the high resistance to dry etching techniques and the high achievable feature resolution.

The sample is **activated** by heating up on a hot plate at 180°C for 5 min, or by O<sub>2</sub> plasma treatment (Tepla 300) with 400 standard cubic centimeter per minute (sccm) O<sub>2</sub> at 600 W for 1 min. The activation serves to remove water, adhesion gases, and organic contaminations to enable better adhesion of e-beam-resist on the sample surface. The activation has impacts on the spin curve of resists and the development. The sample is **spin coated** by first dropping the liquid resist on the surface and then spinning the sample at high speed. The resulting thickness of the coated resist is related to the spin speed and the duration, and this relation is referred to as the spin curve. The spin curve is a feature of the resist of fixed concentration and is assumed to be independent of substrate material and location on the wafer. The SiO<sub>2</sub>/GaN/AlN/Si sample is spin-coated 310 nm ZEP (100% concentration) at a speed of 6000 RPM for 60 s. After spin coating, the sample is **baked** at 180°C for 5 min to evaporate the solvent (if it exists) in the resist and to improve the adhesion.

### E-beam Exposure

E-beam exposure is the process of using the electron beam to expose the resist, transforming its solvability. The EBL system (Raith EBPG5000ES) has a similar structure as an SEM but addresses more precision [Fig. 3.7 (a)]. The electrons are generated and accelerated to high energy, typically 100 keV, to have enough energy to transfer the resist and to minimize the focal spot size [Fig. 3.7 (b)]. The electrons then pass through several coils to adjust the deflection and the focus to give a Gaussian intensity distribution at the surface of the sample, where the FWHM is dependent on the current.

During the exposure, the mask pattern is first divided into area blocks called mainfields. The sample stage translates itself to move from one mainfield to another, where a stitching error of 18 nm ( $3\sigma$ ) is introduced. To avoid stitching errors in PhC cavities, each cavity is completely assigned to a mainfield, and in the case of a dense arrangement, the cavities are divided into groups on a different layer so that the mainfields can be correctly assigned [Fig. 3.6 (f)-(g)].

Inside a mainfield, the sample stage is at a fixed position, and the e-beam is moved by an electro-magnetic beam deflector with a maximum deflection of 256  $\mu\text{m}$  and at a frequency of up to 50 MHz. The mainfield is also divided into several subfields to increase writing efficiency and accuracy. The subfield is then divided into trapezoids that are filled by arrays of successive individual e-beam shots. The positioning accuracy of the shots is called exposure resolution,

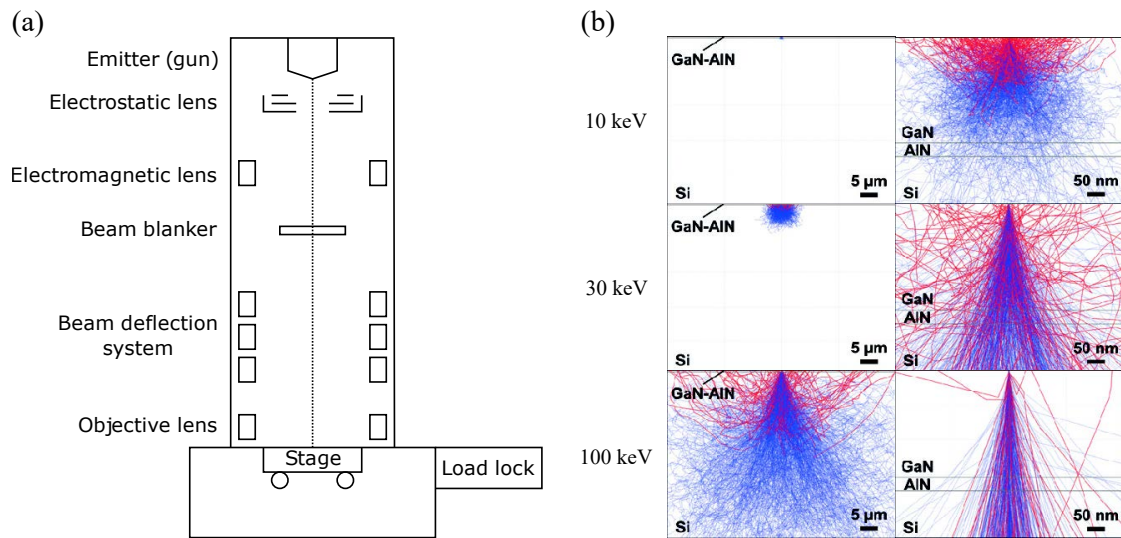


Figure 3.7: (a) Schematic representation of the EBL system (adapted from [109]). (b) Monte Carlo simulations of a 5 nm diameter electron beam of 10, 30, and 100 keV interacting with solids (adapted from [70]). The blue traces are the trajectories of the forward-scattered and secondary electrons, and the red traces are the trajectories of the back-scattered electrons.

and the spacing is called step size. The e-beam is **blanked** during the transition from one trapezoid to another. The system also features a vector scan in which the e-beam is directly deflected to the pattern areas without scanning through the blank areas. The exposure process is highly automated, except that the sample needs to be mounted manually at the beginning with the correct position and orientation.

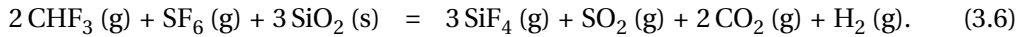
### Development

Development is the process of dissolving the unwanted parts of the resist. The exposed sample is unmounted from the EBL system and is immersed in the n-amyl acetate solution **developer** for 1 min to **develop** (dissolve) the unwanted areas of the resist. The sample is then immersed in a solution of methyl isobutyl ketone (MIBK) and IPA (MIBK:IPA = 9:1) for 1 min to halt the development and is finally rinsed by IPA and blow-dried with N<sub>2</sub> gas. As the development is sensitive to the conditions of the process, the solution, duration, temperature, etc., are kept the same as much as possible to have repeatable results.

#### 3.1.6 Dry Etching of Silica

The pattern in the ZEP layer is then transferred to the SiO<sub>2</sub> layer by ICP-RIE (SPTS Advanced Plasma System, SPTS APS etcher) (see section 3.1.7 for more details on ICP-RIE). The ICP-RIE dry etching utilizes a gas mixture of CHF<sub>3</sub> and SF<sub>6</sub> (at a ratio of 5:1), an ICP power of 950 W, and a chamber pressure of 2 Pa. The sample (wafer) is cooled from the back side by helium (He) flow to a low temperature of 10°C to avoid overheating of the polymer resist. The etching

has no impact on the GaN layer, so a bit of over-etching is possible and is desired to fully open the holes in the SiO<sub>2</sub> layer at the interface with GaN but within the limit of not completely consuming the ZEP resist. The overall reaction can be expressed as:



The sample (2-inch wafer or small chips) is stuck to a 4-inch dummy Si wafer by wax (Quick-Stick Temporary Mounting Wax, melting point 135°C) to be compatible with the etching system and is unmounted and cleaned after etching. Sufficient wax is desired to ensure good thermal contact with the dummy wafer otherwise, the ZEP mask is burnt by the plasma and the heat-releasing etching process. The burnt ZEP not only results in a failure of the etching itself but is also impossible to remove and thus ruins the whole sample.

The relative area of ZEP/GaN with respect to Si of the dummy wafer has an impact on the etching rate because the Si dummy wafer is also etched by the process. 90 s etching results in the pattern transfer from ZEP to SiO<sub>2</sub> for small chips in which the etching rate is about 1.6 nm/s, smaller than that for larger wafers. The selectivity SiO<sub>2</sub>/ZEP is about 2:1, but because of the over-etching, more than 50 nm ZEP is consumed.

The main characterizations for this process are, first, a quick inspection under an optical microscope to make sure the ZEP is not burnt, and second, an SEM image to make sure that the holes in the SiO<sub>2</sub> layer are fully opened. A step measurement by a profilometer on the step marker is optional to make sure that the step is larger than the thickness of SiO<sub>2</sub> so that the ZEP is not completely consumed, but usually, the texture of ZEP can be already identified with optical microscopes or SEM.

After the etching and characterization, the sample is removed from the 4-inch Si dummy wafer by melting the wax. The residue of the wax is cleaned with acetone in an ultrasonic bath. The residue of ZEP is removed by immersing the sample in a dedicated solvent (Microposit Remover 1165) for 12 hours at room temperature. Acetone also dissolves ZEP but is not as efficient as the dedicated solvent, ZEP residue may still remain on the surface even with an ultrasonic bath. Alternatively, the ZEP residue can also be removed by O<sub>2</sub> plasma treatment (PVA Tepla 300 etcher), with a recipe of 400 sccm O<sub>2</sub> flow, 500 W plasma power, for 4 min. Notice that burnt ZEP from CHF<sub>3</sub> and SF<sub>6</sub> dry etching can not be removed by either method.

#### 3.1.7 ICP-RIE Etching of III-nitrides

The pattern on the SiO<sub>2</sub> hard mask is transferred to the GaN/AlN layer by ICP-RIE. Reactive ion etching (RIE) is a typical dry etching technique that uses chemical-active ions in a plasma to etch the target material [Fig. 3.8]. The RIE reactor consists of mainly a pair of parallel-plate electrodes inside a low-pressure chamber. The upper electrode is grounded while the lower electrode is connected through a capacitor to a power supply with alternating voltage (sinusoidal) at a typical frequency of 13.46 MHz (radio frequency (RF)). The electrons of a gas

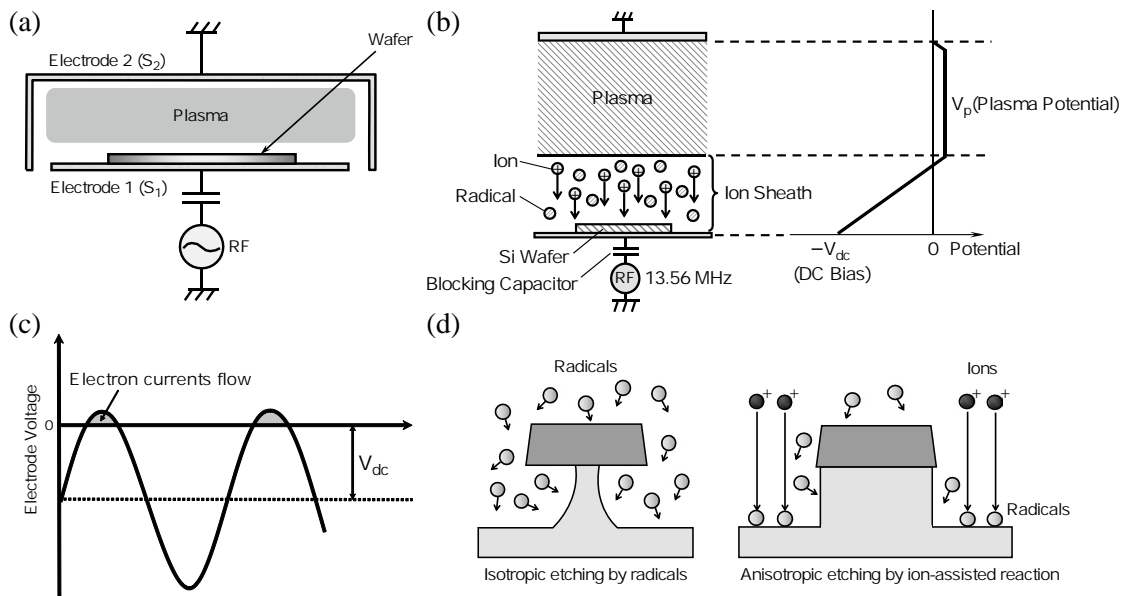


Figure 3.8: Basics of ICP-RIE (adapted from [110]). (a) Schema of the etching chamber. (b) Ion sheath near the lower electrode and the distribution of electric potential. (c) Voltage waveform at the lower electrode. (d) Isotropic etching by radicals and anisotropic etching by the ion-assisted reaction.

atom gain kinetic energy from the electric field, and when the kinetic energy is larger than the ionization energy of the atom, the electrons in the outermost shell are expelled from the atom, and the remaining atom becomes an ion. The expelled electrons are accelerated furthermore by the electric field, and they collide with other atoms to create more expelled electrons in an avalanche. As more and more free electrons and ions are created, the gas exceeds the discharge threshold and becomes plasma. Because the expelled electrons are much lighter than the ions, they follow the oscillation of the electric field and finally collide with the electrodes, while the ions are much heavier, so they remain at almost the same position. The expelled electrons accumulate on the lower electrode because of a blocking capacitor, and the lower electrode is gradually biased to a negative potential bias, denoted as  $-V_{dc}$ . The negatively biased lower electrode then attracts ions, and the bias is mitigated. In a steady state, there is only a small portion in an oscillation period when the lower electrode is positively biased, and the electrons hit the lower electrode. In the rest of the period, ions are attracted to the lower electrode, and the sum of the incremental charge is zero for each period. The region near the lower electrode is called the ion sheath because it contains a normal density of ions but a very low density of expelled electrons. Ions in the ion sheath are accelerated to the lower electrode because of the bias  $-V_{dc}$  and contribute to the etching. The straight vertical trajectory of the ions results in an anisotropic etching profile, which is the key feature for fabricating 2D PhC slabs.

ICP-RIE is an improved version of RIE where the plasma is generated by an additional ICP source with an oscillating magnetic field. The ICP source provides the advantage of a lower ignition threshold and a higher density of the plasma. It also provides the convenience of controlling the ion density and the bias  $-V_{dc}$  separately.

### Chapter 3. Fabrication of 2D PhC Slabs

---

Cl <sub>2</sub> flow	20 sccm
N <sub>2</sub> flow	6 sccm
chamber pressure	1.0 Pa
electrode temperature	25°C
ICP source power	50 W
RF source power	100 W

Table 3.1: Typical etching recipe for ICP-RIE on GaN

In practice, the III-nitride etching is carried out with a dedicated etcher (Sentech SI-500). A typical recipe for etching GaN with SiO<sub>2</sub> mask is shown in Table 3.1. The reactive gas is Cl<sub>2</sub>, and the carrier gas is N<sub>2</sub>. The Cl<sup>n+</sup> ions react with GaN to produce volatile gas. The N atoms provide physical sputtering. The total gas flow mainly determines the pump speed, and it should not be too small so that the byproducts are pumped out quickly without accumulation. The chamber pressure controls the particle density and the mean free path of the ions globally. The lower the pressure, the longer the mean free path of the ions and the higher the etching anisotropy. The electrode temperature is related to reaction conditions and surface diffusion. The ICP source power controls the plasma density and the ion density. The RF source power controls the potential bias  $-V_{dc}$ , and the higher the RF source power, the higher the bias  $|V_{dc}|$ . The system also provides direct control of the bias  $|V_{dc}|$  while the power is automatically calculated. The higher the bias  $|V_{dc}|$ , the higher the kinetic energy and the higher the etching rate, but this may also result in isotropic etching because of the reflection of side walls as well as ion implantation. The chamber pressure and the ICP source power control the density of the ions, and the higher the density, the higher the etching rate.

The etching is stopped automatically by a fixed-time countdown or manually by looking at the real-time reflectivity trace. In the latter case, a square laser tracking window of size  $250 \times 250 \mu\text{m}^2$  is pre-opened in the SiO<sub>2</sub> pattern. A laser at 632.8 nm or 670 nm is shot from above on the area inside the tracking window to measure the reflectivity of the GaN/AlN/Si structure, and the shape of the interference fringe reflects the current thickness of the GaN/AlN layer. The reflectivity becomes constant when the GaN/AlN layer is fully etched. An over-etch into the Si substrate is usually applied to ensure the holes are fully opened at the AlN/Si interface.

The intensity of the reflected light is a result of the interference of the light reflected on the top surface and the bottom surface of the transparent film, so the thickness of the film that corresponds to one period of the reflectivity spectrum is  $d = \lambda/2n$ , where  $n$  is the refractive index. The frequently used values are listed in Table 3.2.

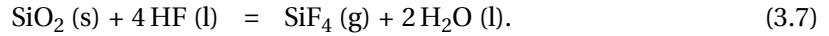
The sample is characterized by a step measurement of the step marker by a mechanical profilometer (alpha-step profilometer). The measured step should be almost twice the thickness of the GaN/AlN layer because of the over-etch.



	$n(\lambda=632.8 \text{ nm})$	$n(\lambda=670 \text{ nm})$	$d(\lambda=632.8 \text{ nm})$	$d(\lambda=670 \text{ nm})$
GaN	2.3779 [111]	2.3666 [111]	133.1 nm	141.6 nm
AlN	2.1496 [112]	2.1465 [112]	147.2 nm	156.1 nm
SiO <sub>2</sub>	1.4636 [113]	1.4628 [113]	216.2 nm	229.0 nm

Table 3.2: Film thickness that corresponds to one period of the reflectivity spectrum.

The residual SiO<sub>2</sub> layer is then removed by HF wet etching:



Typically the sample is immersed in 40% HF for 5 min and then rinsed with deionized (DI) water and blow-dried with N<sub>2</sub> gas. Since the residual SiO<sub>2</sub> layer is very thin, and the reaction is fast, 10% buffered hydrofluoric acid (BHF) for 5 min can also be used.

Then the sample is characterized by a step measurement again to determine the thickness of the SiO<sub>2</sub> residue and to confirm that the over-etch did not consume the SiO<sub>2</sub> mask completely.

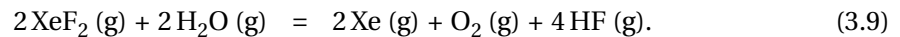
#### 3.1.8 Membrane Release

Finally, the AlN/GaN membrane (film) is released from the Si(111) substrate by xenon difluoride (XeF<sub>2</sub>) gas etching (SPTS Xactix X4 etcher). The XeF<sub>2</sub> gas directly reacts with Si and generates gas phase byproducts that are pumped out from the reaction chamber:



The reaction is heat-releasing, thus to avoid overheating, the XeF<sub>2</sub> gas is injected into the reaction chamber by pulse cycles. The pressure of XeF<sub>2</sub> essentially determines the etching rate, and the duration of each pulse cycle limits the accumulated heat. A recipe of 800 mTorr × 30 s × 10 cycles is generally used but with interruptions every 3-5 cycles for careful checks under an optical microscope to avoid over-etching. Because the pressure is set at the lowest limit of the reactor, and because of the limited sensitivity of the pressure gauges, the pressure control of the system is not highly reliable, so the etching is necessarily stopped and the sample is taken out for inspections from time to time.

The XeF<sub>2</sub> is corrosive to tissues, and it reacts with water vapor in the air to produce HF, which is very toxic, corrosive, and irritant:



So caution is required when handling XeF<sub>2</sub>. The reaction chamber is purged for many cycles with N<sub>2</sub> after sample loading to remove moisture in the chamber and before the sample unloading to remove residual XeF<sub>2</sub>.

## 3.2 Auxiliary Techniques

### 3.2.1 Strain Engineering

The device containing suspended PhCs and waveguides suffers from high residual inner stress and causes the supporting tethers to break in extreme cases [Fig. 3.9] [70]. This section studies the residual stress in the existing platform and proposes an approach of using spring tethers to increase the stability of the suspended platform.

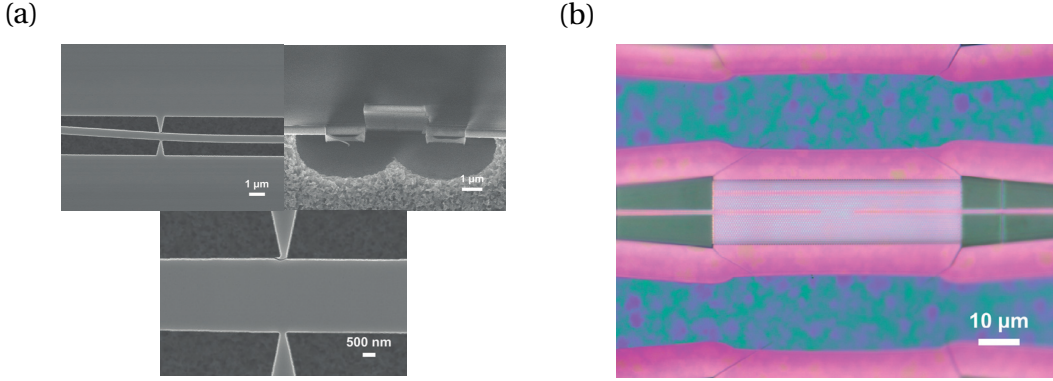


Figure 3.9: (a) SEM images of broken waveguide tethers (adapted from section 4.4.1 of [70]). (b) Optical microscope image of broken PhC (adapted from section 4.4.1 of [70]).

### Estimation of Strain in Suspended GaN Waveguides

If we assume that there is no inner stress at the growth temperature, then

$$L_{\text{GaN}, T1} \frac{a_{\text{GaN}, T2}}{a_{\text{GaN}, T1}} = L_{\text{Si}, T1} \frac{a_{\text{Si}, T2}}{a_{\text{Si}, T1}}, \quad (3.10)$$

where  $T1$  is the room temperature,  $T2$  is the growth temperature,  $L_{\text{Si}, T1}$  and  $L_{\text{GaN}, T1}$  are the length of Si and GaN strips at  $T1$  when fully relaxed,  $a_{\text{Si}, T1}$ ,  $a_{\text{Si}, T2}$ ,  $a_{\text{GaN}, T1}$ , and  $a_{\text{GaN}, T2}$  are the lattice constants for Si and GaN at temperatures  $T1$  and  $T2$ , respectively. By using Eq. (3.10), the strain in the GaN strip at  $T1$  can be expressed as:

$$\epsilon_{\text{GaN}, T1} = \frac{\Delta L_{\text{GaN}, T1}}{L_{\text{GaN}, T1}} = \frac{L_{\text{Si}, T1} - L_{\text{GaN}, T1}}{L_{\text{GaN}, T1}} = \frac{a_{\text{GaN}, T2}}{a_{\text{GaN}, T1}} \frac{a_{\text{Si}, T1}}{a_{\text{Si}, T2}} - 1. \quad (3.11)$$

Young's modulus is defined as:

$$E = \frac{\sigma}{\epsilon} = \frac{F/A}{\Delta L/L}, \quad (3.12)$$

where  $\sigma$  is the stress,  $\epsilon$  is the strain,  $F$  is the force applied, and  $A$  is the cross-section area. The quantitative estimation of strain and related quantities in the GaN waveguide before membrane release is summarized in Table 3.3.

Method	Micro-Raman		Thermal mismatch	
	polycrystalline	single crystal	polycrystalline	single crystal
$E_{xy}$ [GPa]	150	324 [114]	150	324 [114]
$\sigma$ [GPa]	1.5		0.39	0.84
$F$ [N]	$1.58 \times 10^{-3}$		$4.05 \times 10^{-4}$	$8.82 \times 10^{-4}$
$\epsilon$	0.01	0.0046	0.0026	
$\Delta L$ [ $\mu\text{m}$ ]	15.7	7.2	4.1	

Table 3.3: Estimation of strain and related quantities. Numerical values used:  $T_1 = 300$  K,  $T_2 = 1300$  K,  $a_{\text{Si}, T_1} = 5.431/\sqrt{2} = 3.840$  Å [102],  $a_{\text{Si}, T_2} = 5.453/\sqrt{2} = 3.856$  Å [102],  $a_{\text{GaN}, T_1} = 3.189$  Å [101],  $a_{\text{GaN}, T_2} = 3.210$  Å [101],  $E_{\text{GaN}, xy} = 324$  GPa [114],  $A = 350$  nm  $\times$  3  $\mu\text{m}$ ,  $L_{\text{GaN}, T_1} = 1570$   $\mu\text{m}$ .

The stress  $\sigma = 1.5$  GPa was measured by micro-Raman spectroscopy, and the corresponding strain is almost twice the value calculated when solely accounting for thermal mismatch, which is reasonable because the lattice mismatch also adds to the strain. However, the strain analysis at the growth temperature due to lattice mismatch is much more complex, and thus experimental measurements of inner stress are necessary.

It is worth noticing that the gravity force applied to the waveguide is:

$$F_g = \rho_{\text{GaN}}(AL)g = 9.86 \times 10^{-11} \text{ [N]}, \quad (3.13)$$

where the density of GaN  $\rho_{\text{GaN}} = 6100$  kg/m<sup>3</sup> [115] and the gravitational acceleration  $g = 9.8$  m/s<sup>2</sup>. It can be seen that the gravity force is about 7 orders of magnitude smaller than the force induced by strain, and thus it can be safely ignored in the case of daily movements and shocks.

### Spring Tethers

The straight tethers break when the strain-induced deformation exceeds the elastic range of the GaN material. To avoid this, an intuitive way is to increase the length of the tethers and fold them in the form of 2D springs. The 2D spring form reduces the effective elastic constant of the tethers and increases the elastic range to incorporate large deformations, and also decreases the maximum inner stress in the structure.

The first attempt was made by introducing a small rectangular twist in the waveguide tethers. After membrane release, SEM images clearly show the deformation of the spring tethers, and some tethers at the breaking limit are captured [Fig. 3.10 (a)]. The exact geometry and deformation of these tethers were used in finite element simulation (COMSOL) to find the maximum stress in the structure [Fig. 3.10 (b)]. The simulation shows that the maximum stress is dependent on the curvature radius of the joint corners. In the fabrication, the joint corners were simply designed to be rectangular but are self-rounded because of fabrication errors. Then the simulation was adjusted, and it shows that the maximum stress is about 10 GPa for

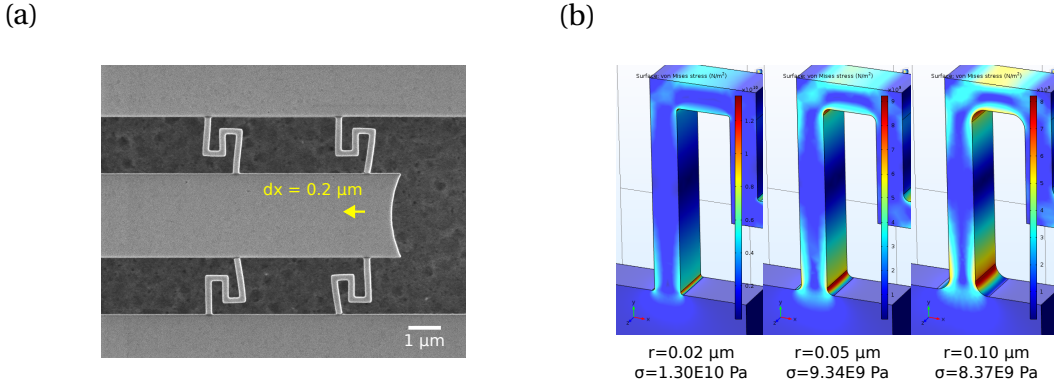


Figure 3.10: Determination of critical stress. (a) SEM of 1-twist square spring tethers with critical deformation. (b) Finite element simulation of the same structure in (a) with different rounding of joint corners to extract the critical stress of about 10 GPa.

a range of curvature radii (using Young's modulus of polycrystalline GaN 150 GPa, Poisson's ratio 0.23, density  $6100 \text{ kg/m}^3$ , and Von Mises stress model). This stress value is regarded as the critical value for the spring design later.

The next step was to design spring tethers that exhibit smaller stress. As pointed out above, the maximum stress is dependent on the curvature of the joint corners, so the joint corners are rounded first, and the curvature radius is set to  $0.4 \mu\text{m}$ . A group of spring tethers with different combinations of twist numbers and main tether lengths are simulated to extract the maximum stress [Fig. 3.11 (a)-(c)]. It shows that the dependence of the maximum stress on the main tether length and the twist numbers exhibits an exponential relation, and a number of combinations are well below the critical stress of 10 GPa. The deformation induced by gravity is also simulated for a spring tether segment (a segment of waveguide plus a pair of spring tethers) of 3 twists and  $8 \mu\text{m}$  main tether length, and the result shows a maximum vertical displacement of 0.25 nm, which can be safely ignored.

The same idea can be applied to the PhC part, where destructive stress is mainly in the direction perpendicular to the waveguide ( $y$ -direction). Different from the tethers for the waveguide, the tethers for the PhC part should be designed to be soft in the  $y$ -direction and rigid in the  $x$ -direction in case the forces applied by the waveguide on the two sides are not balanced. The spring is designed as single ribs [Fig. 3.11 (d) (f)]. The effective elastic constants in the  $y$ -direction of the PhC spring tether and the upper half of the PhC bulk are 183 N/m and  $3.6 \times 10^5 \text{ N/m}$ , respectively [Fig. 3.11 (d) (e)]. The effective elastic constant in the  $x$ -direction of the PhC spring tether and the PhC bulk (when applying a force on the side face of the PhC bulk) is  $2.7 \times 10^4 \text{ N/m}$ . Since the force from the waveguide is applied only on a small area of the W1 waveguide side face, the deformation of the joint part is also studied. The simulation shows that a force of  $1.6 \times 10^{-3} \text{ N}$  deforms the joint part of PhC by up to 140 nm [Fig. 3.11 (f)], which could have a significant impact on the light coupling efficiency to the W1 waveguide.

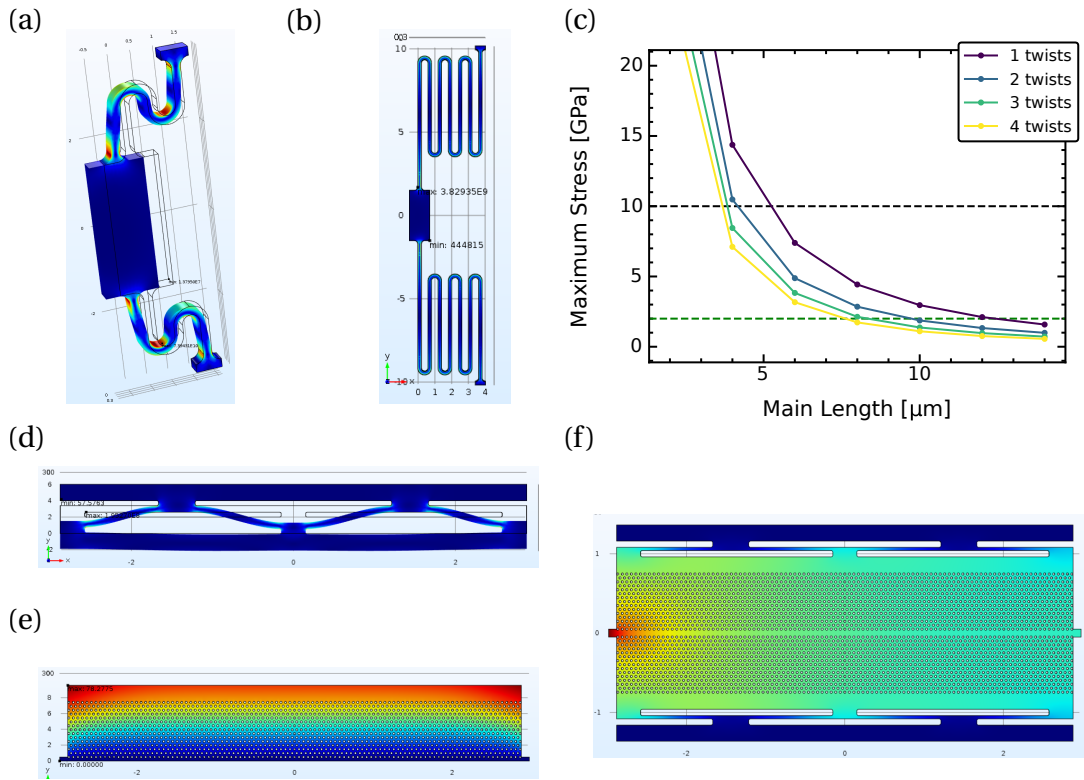


Figure 3.11: Finite element simulations of spring tethers. (a) Finite element simulation of a 1-twist rounded spring. (b) Definition of the main spring length on a 3-twist spring. (c) Dependence of the maximum stress on the main spring length for springs with 1-4 twists. The critical stress is shown by a black dashed line. (d) Simulation of the PhC spring tether when the force is applied in the  $y$ -direction. (e) Simulation of the PhC bulk when the force is applied in the  $y$ -direction. (f) Simulation of the PhC when the force is applied on the waveguide joint.

### Spring Network

Because there are several tens pairs of spring tethers applied to the long waveguide, the whole structure is too large for finite element simulation. To study the strain relaxation of the whole structure, the spring network model was proposed [Fig. 3.12]. The model assumes that the spring tethers and the waveguide are all simple springs, and they form a spring network [Fig. 3.12 (b)]. The left side of the network is fixed (the PhC part is rigid), as well as the right side of each spring tether (attached to the bulk GaN layer). A single stable state of the network can be solved if the elastic constants of each spring segment are known.

The joint point of tether springs and the waveguide can be regarded as a node in the spring

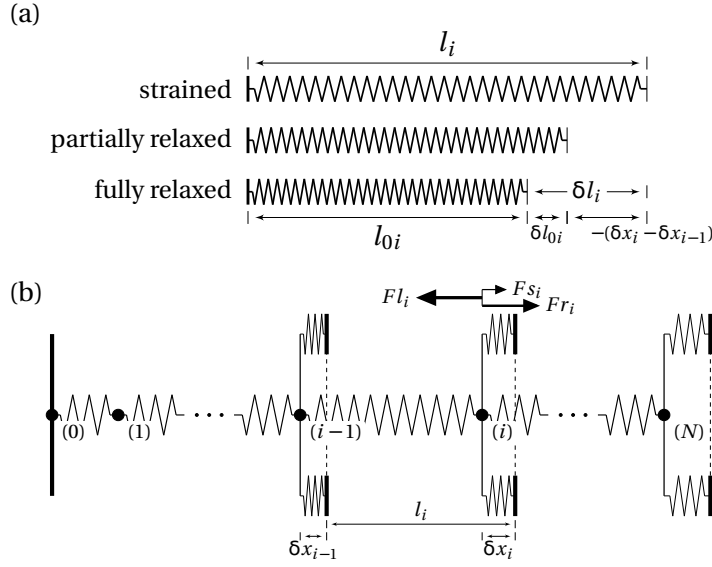


Figure 3.12: Spring network model. (a) Relations of a simple spring at different relaxation states. (b) Spring network with the left side of the main spring and the right side of the tethering springs fixed.

network. The forces applied to a node  $i$  follow the relations:

$$\begin{aligned}
 0 &= Fl_i + Fr_i + Fs_i, \\
 Fl_i &= -k_i(l_i\eta + \delta x_i - \delta x_{i-1}), \\
 Fl_i &= -Fr_{i-1}, \\
 Fs_i &= -ks_i\delta x_i,
 \end{aligned} \tag{3.14}$$

where  $Fl_i$ ,  $Fr_i$ , and  $Fs_i$  are the forces applied by the left waveguide segment, the right waveguide segment, and the spring tethers. For a spring in different relaxation states, there are relations:

$$\begin{aligned}
 \epsilon &= \frac{\delta l_i}{l_{0i}}, \\
 l_i &= l_{0i} + \delta l_i, \\
 \delta l_i &= \frac{\epsilon}{\epsilon + 1} l_i = \eta l_i, \\
 \delta l_{0i} &= \delta l_i + \delta x_i - \delta x_{i-1},
 \end{aligned} \tag{3.15}$$

and there are also boundary conditions:

$$\begin{aligned}
 cFl_i &= -(Fr_i - ks_i\delta x_i) & cFr_N &= 0 \\
 \delta x_{i-1} &= \frac{Fl_i}{k_i} + l_i\eta + \delta x_i & \delta x_0 &= 0 \\
 Fr_{i-1} &= -Fl_i & ks_0 &= ks_1 = 0
 \end{aligned} \tag{3.16}$$

As a summary, in the spring network, there are 3 equations for each node  $i$ ,  $i \in 1, 2, \dots, N$

and 3 unknown variables for each node:  $\delta x_i$ ,  $Fl_i$ , and  $Fr_i$ . The 3N equations were solved numerically by the following algorithm:

1. assign (guess) a value to  $\delta x_N$ ;
2. calculate  $\delta x_{1,1}$  from the first 3 nodes and  $\delta x_{1,2}$  from the last  $3(N - 1)$  nodes;
3. calculate  $\Delta = abs(\delta x_{1,1} - \delta x_{1,2})$ ;
4. repeat the steps above and find  $\delta x_N$  to make  $\Delta$  small enough using binary search.

### Experimental Test of Spring Tethers

The design of waveguide spring tethers and PhC spring tethers was tested in fabrication and turned out to be a success. The large deformation of the spring tethers is easily seen by SEM, and no cracks exist for the whole structure with the appropriate spring parameters. An example is given for a pair of spring tethers of 3 twists and 16  $\mu\text{m}$  main tether length at the end of the waveguide, with a total displacement of  $\delta x_N = 3.1 \mu\text{m}$  [Fig. 3.13 (b)]. The total displacement at full relaxation is  $\delta x_N = 6.9 \mu\text{m}$  (assuming 0.0046 initial strain), and the total displacement given by the spring network is  $\delta x_N = 6.3 \mu\text{m}$ . This suggests that either the initial strain is overestimated or the actual elastic constant of the spring tethers is underestimated. Notice that the elastic constants of the spring tethers may differ from the simulation results because of fabrication errors. Furthermore, the waveguide may not be able to recover the single crystal lattices even if fully relaxed because of the growth defects, the AlN layer, the surface changes, etc. Finite element simulations suggest that the maximum stress in the spring is 0.5 GPa, which is well below the critical value of 10 GPa.

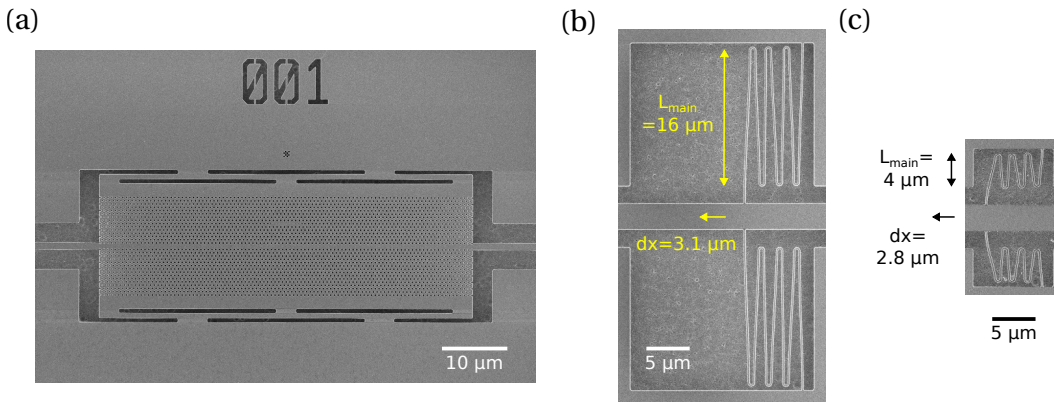


Figure 3.13: Experimental verification of spring tether design. (a) SEM image of the PhC part with spring tethers. (b) SEM image of a deformed 3-twist spring tether pair with the main spring length of 16  $\mu\text{m}$ . Notice that, by design, the ribs of the spring are parallel to each other and perpendicular to the waveguide. (c) SEM image of a deformed 3-twist spring tether pair with the main spring length of 4  $\mu\text{m}$ .

Another example is given for a pair of spring tethers of 3 twists and 4  $\mu\text{m}$  main tether length at the end of the waveguide, which deforms by  $\delta x_N = 2.8 \mu\text{m}$  [Fig. 3.13 (c)]. The total displacement at full relaxation is  $\delta x_N = 7.1 \mu\text{m}$  (assuming 0.0046 initial strain), and the finite element simulations suggest that the maximum stress in the spring is 5.5 GPa, which is still below the

critical value of 10 GPa.

The PhC part of the device protected by spring tethers is also in good shape under SEM [Fig. 3.13 (a)], while the small deformation of 140 nm at the waveguide joint predicted by simulations is not visible at this scale (this deformation should be mitigated due to the relaxation of the spring network).

In summary, the experimental results roughly agree with the finite element simulations and the spring network model. The designed spring tethers reduce the inner stress and thus increase the mechanical stability of the suspended structure. The spring tethers simulation and the spring network analysis provide a way to analyze the strain and stress in the device. The strategy of using spring tethers can be widely used on suspended microstructures to mitigate inner stress.

### 3.2.2 Deep Etching

In the previous fabrication routine, the GaN waveguide was cleaved to make it accessible for side coupling. The waveguide terminal was either flat as it is after cleavage, with low coupling efficiency, or tapered, with high coupling efficiency but low reproducibility because of the uncertainty of the cleavage (section 4.4.2 of [70]), because the guiding scribe should never pass through the waveguide directly).

An intuitive technique to overcome this difficulty is to fabricate deep trenches at the position of the waveguide terminal to guide the cleavage. This requires a pre-fabrication of deep trenches before the fabrication of the PhCs and waveguides. An alignment of the two fabrications (e-beam exposure) is required without extreme alignment precision (an error of a few micrometers can be accepted while the e-beam system can achieve nanometer precision).

The exposure layout of the pre-fabrication contains mainly two vertical lines of 1  $\mu\text{m}$  width for trenches at the waveguide terminals and across the whole chip [Fig. 3.14 (a)]. Several trench width testers, with 10 horizontal bars of width linearly spaced from 200 nm to 2  $\mu\text{m}$ , are overlaid on the main trench lines to investigate the dependence of the trench depth on the trench width. Low-cost photolithography is generally available for the exposure of the pre-fabrication, while in practice, EBL with 20 nm resolution is used for convenience. The fabrication process is adjusted accordingly for deep etching, namely: the  $\text{SiO}_2$  layer thickness is increased to about 1000 nm, the ZEP thickness is increased to 500 nm, the  $\text{SiO}_2$  dry etching duration is increased to 450 s, and the III-nitride dry etching duration is increased to 6000 s.

The e-beam exposure in the second fabrication of PhCs is aligned to the fabricated trenches by  $20 \times 20 \mu\text{m}^2$  square alignment markers with an accuracy of about 50 nm. Before membrane release, the chip is perfectly cleaved along the deep trenches. SEM images of the cross-section view on the trench width testers show that when the trench width is smaller than 1  $\mu\text{m}$ , the trench depth increases with the trench width, and when the trench width is larger than 1  $\mu\text{m}$ , the trench depth is saturated to about 8  $\mu\text{m}$ , and a "W" shape of the trench bottom is visible



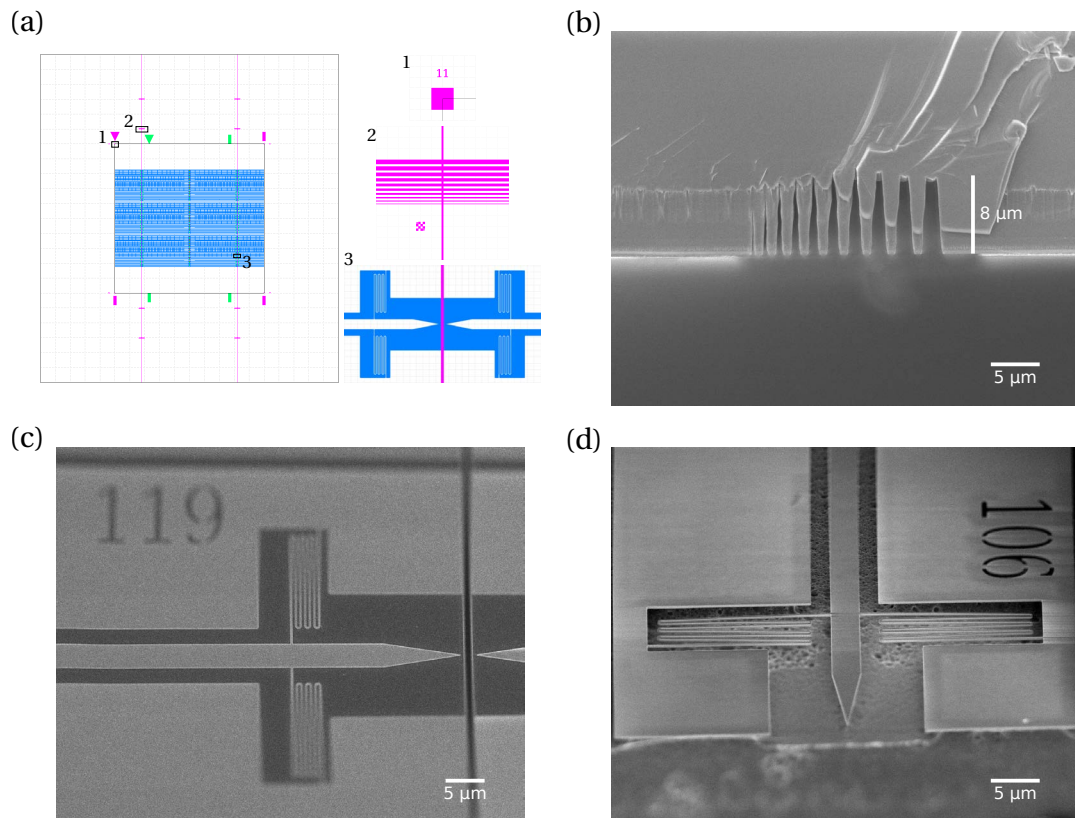


Figure 3.14: (a) Layout design for deep etching. 1-3 shows a  $20 \times 20 \mu\text{m}^2$  square alignment marker, a trench width tester composed of 10 horizontal bars of width linearly spaced from 200 nm to 2  $\mu\text{m}$ , and an example of the waveguide terminal, respectively. (b) SEM of the cross-section of the trench width tester after cleavage. (c) SEM image of the waveguide terminal before membrane release. The deep trench is visible at the tapered tip. (d) SEM image of the waveguide terminal after membrane release.

[Fig. 3.14 (b)]. The waveguide terminals before and after membrane release are also inspected, and a clear termination of the tapered tip is verified [Fig. 3.14 (b)].

### 3.2.3 HSQ Technique

HSQ ( $[\text{HSiO}_3/2]_n$ ) is an inorganic compound used as a negative resist in EUV (Extreme Ultraviolet Radiation) photolithography and EBL [116–118]. When exposed to high-energy electrons or EUV, it cross-links via hydrogen evolution concomitant with Si-O bond crosslinking, which results in a  $\text{SiO}_2$ -like mask non-dissoluble in the developer of Microposit<sup>TM</sup> MF-CD-26 or tetramethylammonium hydroxide (TMAH) ( $\text{N}(\text{CH}_3)_4^+ \text{OH}^-$ ). HSQ provides a very high feature resolution up to sub-10 nm while its reproducibility is relatively lower than ZEP because of the instability of the compound and the high sensitivity to temperature. As discussed in the introduction of this chapter, in this context, the main advantage of HSQ is the high resolution and the simplification of the fabrication process, while the main disadvantage is the much longer exposure time.

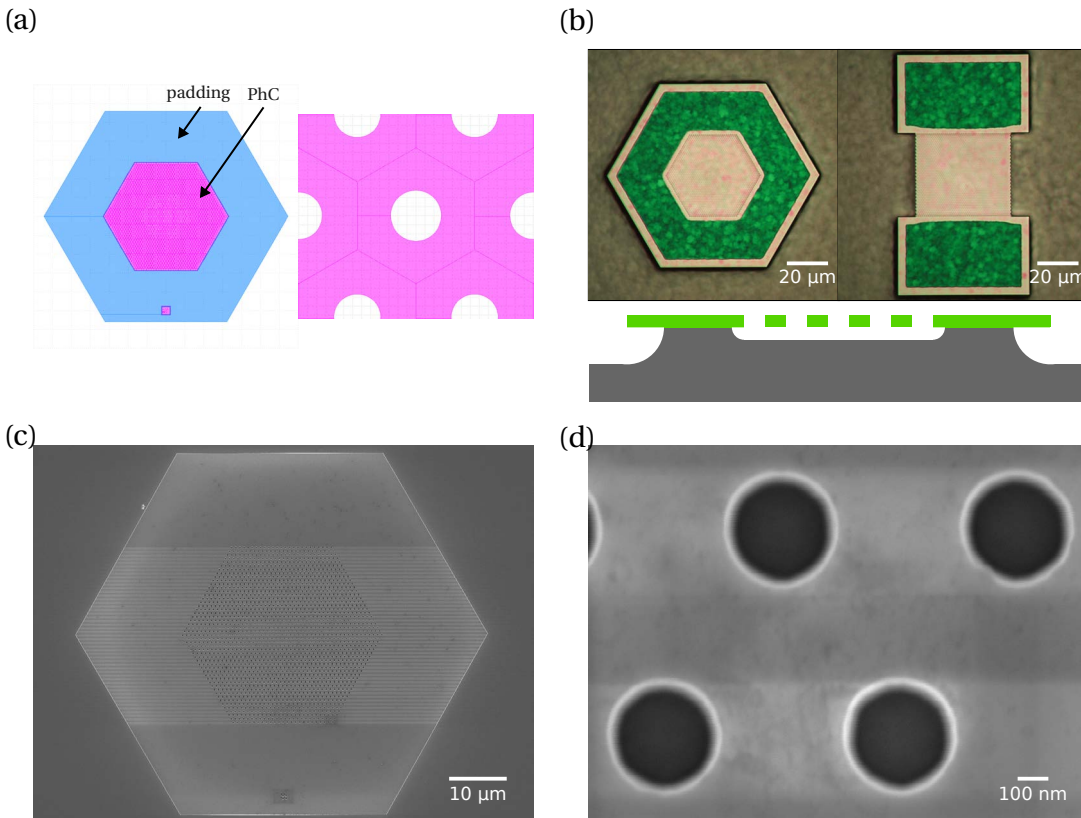


Figure 3.15: (a) Layout design of the negative tone mask for a doubly resonant cavity with hexagonal padding. The PhC part is in pink, and the pad is in blue. The hexagonal tile for a hole is shown on the right. (b) Microscope images of doubly resonant cavities with hexagonal padding and anisotropic rectangular padding after membrane release. A schematic view of the cavity cross-section is shown at the bottom. (c) SEM image of a cavity with hexagonal padding. (d) SEM image of PhC holes fabricated with HSQ technique.

Since HSQ is a negative resist, the mask layout should be inverted accordingly. The intuitive way to invert the layout is to apply a boolean operation to subtract the complementary part of the positive pattern. However, the derived pattern contains many holes, and the vertices number exceeds the limit for a single polygon in the framework of the GDSII standard, which results in an arbitrary partition of the pattern, and the exposure writing order is not controlled. To avoid these, the mask layout is redesigned by filling the doubly resonant lattice with hexagonal tiles (or atoms) with the same hexagon size and different hole sizes [Fig. 3.15 (a)], and the exposure writing order inherits the filling order of the cavity.

Also, because of the negative nature of HSQ, the blank areas among the cavities are too large to expose, and thus only the padding area around the cavity is exposed [Fig. 3.15 (a)]. To save exposure time, the padding area is put on a different GDSII layer than the PhC part for lower exposure resolution. The padding area and the PhC area are combined with a 200 nm overlapping reserved for stitching errors.

In EBL, the GaN/AlN/Si(111) chip surface is first prepared by 10 min O<sub>2</sub> plasma treatment. Then 6% HSQ dissolved MIBK (Methyl Isobutyl Ketone, (CH<sub>3</sub>)<sub>2</sub>CHCH<sub>2</sub>C(O)CH<sub>3</sub>) is spin-coated on top of the GaN/AlN/Si(111) chip with a spin speed of 6000 RPM, which results in about 120 nm HSQ without baking. Then the chip is mounted for e-beam exposure, and the base dose is tested to be about 1600 μC/cm<sup>2</sup>. After exposure, the chip is developed in 25% TMAH for 1 min and rinsed with DI water for about 10 min. Because TMAH is a neurotoxin and a strong base, for safety reasons, the development is carried out in an enclosed wet bench dedicated to this process. The DI water in the rinsing sink is continuously flowing for 30 min once activated, and its resistivity is tracked. The potential of hydrogen (pH) value of the water is confirmed to be neutral at the end of rinsing by ensuring a resistivity value larger than  $\geq 16 \times 10^6 \Omega \cdot \text{cm}$ . The chip is finally blow-dried with N<sub>2</sub> gas. The following fabrication processes are the same as the ZEP technique.

The HSQ technique provides, in general, smoother and more accurate features than the ZEP technique, as can be seen by SEM images [Fig. 3.15 (c) (d)]. However, the price to pay is the longer exposure time because of the larger exposure area and higher exposure dose. In practice, the exposure time of the HSQ technique is ten times longer than the ZEP technique for the same number of devices. The larger exposure area also results in longer data preparation time and larger data files, and in some extreme cases, these become heavy burdens. In optical measurement, the cavities fabricated with the HSQ technique exhibit slightly higher Q-factors which may suggest that the limitation on the Q-factors mainly comes from the roughness on the top and bottom surfaces of the GaN/AlN slab.

### 3.2.4 AlN Etching

The etching of AlN is different than that of GaN because the aluminium (Al) atoms in the material lead to non-ion-assisted etching and the formation of a side-wall protection film, which results in different selectivity and side-wall verticality [110]. The byproduct of AlCl<sub>3</sub> forms a film on the side wall, self-masking the etching and reducing the verticality. The oxygen (O) atoms in the hard mask (SiO<sub>2</sub> or polymers) bound with the Al atoms to form an aluminium oxide film, which also contributes to the self-masking effect.

The pressure of the etching chamber is controlled by a pump throttle through a feedback loop using pressure sensors. The control becomes unstable when the throttle is at a low level, i.e., when the target pressure is too high, or the total gas flow is too small. The variance of pressure induces variable RF bias and etching rate, which is not desired. To avoid this issue, the combination of the total gas flow and the target pressure is tested and selected in the correct range. No noticeable effect is found when changing the electrode temperature from room temperature to 100°C

An example of the tested recipe and conditions are as follows: SiO<sub>2</sub> hard mask thickness 200 nm, AlN thickness 240 nm, Cl<sub>2</sub>/BCl<sub>3</sub>/Ar flow at 30/10/10 sccm, chamber pressure 0.3 Pa, RF bias -400 V, ICP power 100 W, electrode temperature 25°C, total etching time 114 s (manual

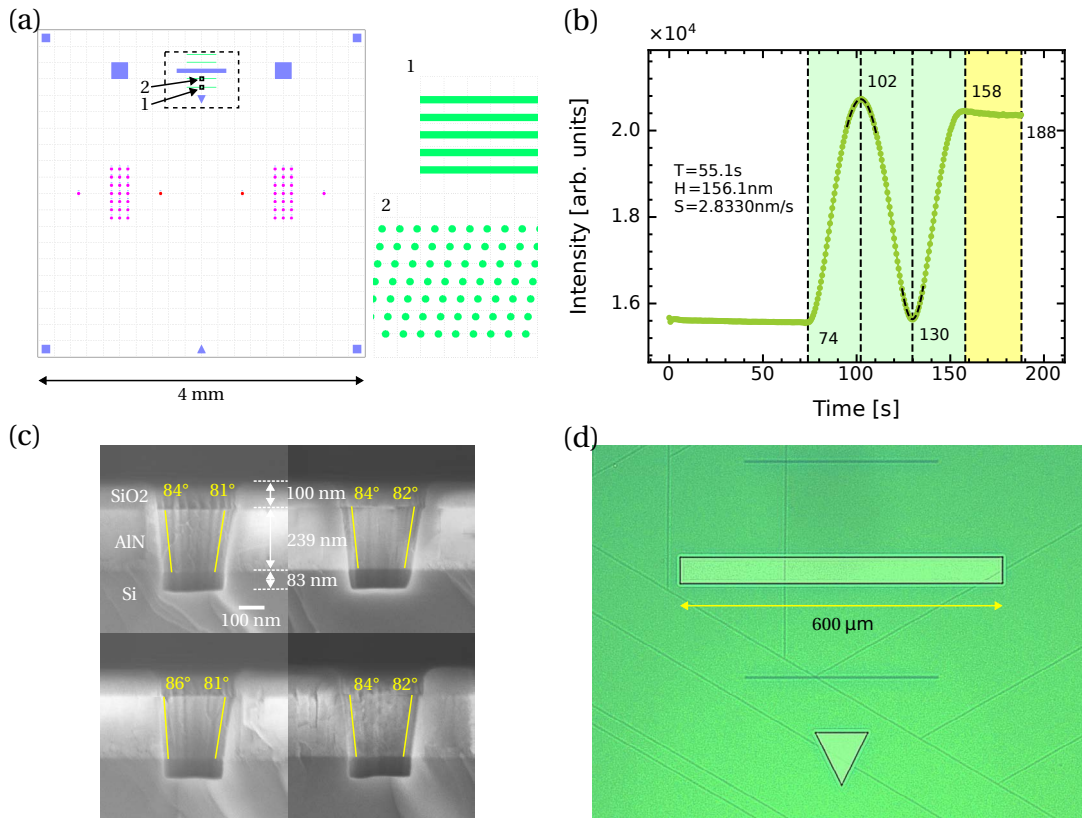


Figure 3.16: (a) Mask layout for AlN etching test. The chip is cleaved vertically in the middle after etching. 1 and 2 are strips and holes for side-viewing. (b) Reflectivity trace during the etching of AlN. Green and yellow regions indicate the etching of AlN and Si, respectively. (c) SEM images of the side view of holes after cleavage. The side wall inclination angle is about 83°. (d) Optical microscope image of the mid-top region, marked by a dashed rectangle in (a), of the chip after ZEP removal. Cracks are visible along the vertical and  $\pm 60^\circ$  directions, which corresponds to the crystallographic axes of wurtzite AlN in *c*-plane.

stop), reflectivity period 55.1 s, AlN etching rate 2.833 nm/s, selectivity SiO<sub>2</sub> : AlN about 1 : 3.2, over-etch into Si 80 nm [Fig. 3.16 (b) (c)].

The etching test mask contains features of strips and holes that provide a cross-section view after cleavage [Fig. 3.16 (a)]. The resulting side wall inclination angle is about 83° [Fig. 3.16 (c)], which is comparable to the result in [119] (80.1°, nickel, Ni used as hard mask), but not comparable to that of GaN. The different angles on the two sides of the holes may be due to the fact that the sample was not mounted parallel to the electrodes (the sample size is small and is glued to a Si dummy wafer with QuickStick wax).

The etching gas composition for AlN is Cl<sub>2</sub>/BCl<sub>3</sub>/Ar with a volume concentration ratio of about 3:1:1. Cl<sub>2</sub> is the main reactive gas, while BCl<sub>3</sub> is added to suppress the formation of aluminium oxide film, and Ar is the main ion source [119]. A larger RF bias (absolute value) results in a higher etching rate but a smaller selection ratio because of the physical sputtering. A higher flow rate of Cl<sub>2</sub> tends to decrease the etching rate because of the BCl<sub>3</sub> self-masking effect.

Self-cracking of the AlN layer is observed during processing [Fig. 3.16 (d)]. The cracks follow the crystallographic axes and are mainly due to the large residual stress from the growth. After long storage, low-density cracks are found on AlN samples. And the crack density increases along with the fabrication steps due to the heating processes involved. Because of the cracks and the non-ideal etching, the device fabrication with AlN was not continued.

### 3.2.5 PhC Image Analysis

The PhC image analysis refers to the analysis of the PhC morphology by applying computational image processing techniques to scanning electron microscope (SEM) or AFM images of the 2D PhC. The images taken during or after fabrication provide not only the PhC profile recognizable by human eyes but also rich statistical information about the PhC, which can be used for comparison with the ideal design to find out, e.g., distortions introduced by fabrication.

The main procedures of PhC image analysis are [Fig. 3.17]: 1. detect the holes in the PhC and extract the positions and sizes; 2. statistical analysis of the hole positions and sizes. The analysis of the hole edge smoothness [120] is also possible but not investigated here.

The edge pixels of the holes are first extracted by Canny's method [121] (algorithm, in OpenCV) and are clustered according to relative distances and connectivity (algorithm, custom). The edge pixel clusters are filtered to exclude defects and are fitted by circles to find the centers and radii. However, the result of this method is strongly dependent on the threshold value given in edge detection and is not robust when the hole edge "illumination" is not isotropic. Because of this, the second step of fine hole detection is applied, and the former one is referred to as coarse hole detection.

In fine hole detection, the image is divided into sub-images containing one hole each by using the hole centers and radii estimated by the coarse hole detection [Fig. 3.17 (a)]. In each sub-image, the hole edge profiles are extracted along several radial directions, and one pixel per profile is selected according to proper edge detection criteria, for example, maximum brightness and matching of a certain shape. A circle is then fitted to the selected pixels to extract the hole center positions and radii again. The hole radii are dependent on the edge detection criteria while the center positions are less influenced. Besides the coarse and fine hole detection methods mentioned above, other hole detection techniques could work as well.

In the hole position analysis, the lattice constant is estimated by finding the most probable value (fitting the frequency histogram by a Gaussian function) of the nearest-neighbor distances (algorithm, in scikit-learn) of hole positions [Fig. 3.17 (c)]. An ideal crystal lattice is generated by using the estimated lattice constant and is translated and rotated to match the extracted hole positions by the iterative closest point algorithm (custom). Finally, the drifts of the hole positions compared to the ideal lattice are calculated [Fig. 3.17 (d)]. The drifts can be also mapped on the original image to show the distortion of the PhC [Fig. 3.17 (d)].

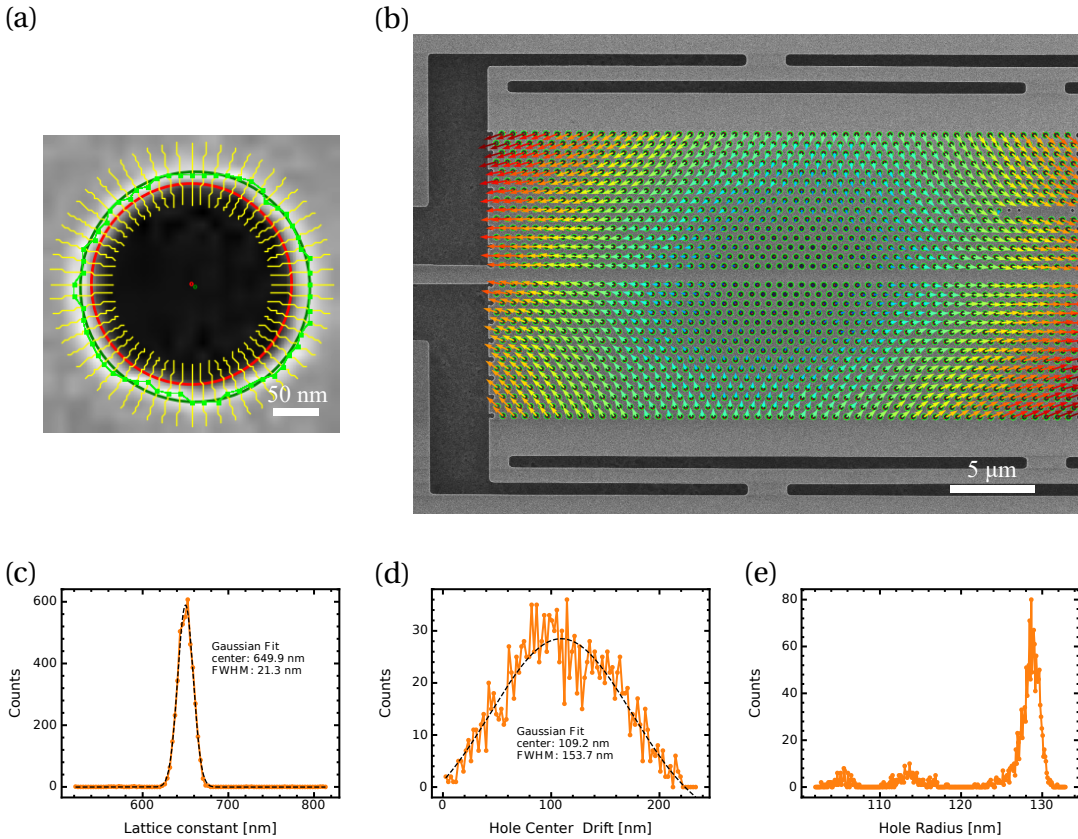


Figure 3.17: (a) Example of a sub-image containing one hole for fine hole detection. The red and green circles represent the coarse and fine fitting of the hole edges. The yellow lines in radial directions are the paths from which the edge profiles are extracted. The light green points represent the selected pixels. (b) Drift map of a suspending PhC. Colored arrows show the drift vectors of holes compared to a perfect lattice. (c) Frequency histogram of lattice constant distribution in (b). (d) Frequency histogram of hole center drift distribution in (b). (e) Frequency histogram of hole radius distribution of a doubly resonant cavity.

In the current example, the drift map shows contraction in the  $y$  direction and expansion in the  $x$  direction of about 1%. However, the distortion on the image may not reflect the real deformation of the PhC because of the accuracy limits of the imaging system, i.e., the image could be deformed itself due to non-perfect calibration of the imaging tool (SEM).

In the hole radii analysis, the radii of the holes are represented by a frequency histogram and are fitted by Gaussian functions [Fig. 3.17 (e)]. In the current example for a doubly resonant cavity, three peaks are visible which corresponds to the different hole sizes in the core, transition, and outer regions of the cavity. Hole roughness analysis is also possible but is highly dependent on image quality and thus not emphasized here.

The computational image analysis shows rich information in PhC images that are not obvious to bare eyes and has great potential in PhC morphology characterizations. However, there are two major limitations. First, the images could be deformed because of the distortion

induced by the imaging system. To solve this issue, an imaging system with better calibration is preferred. If the distortion induced by the imaging system is consistent, a reference sample (e.g., a PhC without membrane release) could be used for calibration or comparison. Second, the extracted hole radii are dependent on the edge detection criteria. To solve this issue, the criteria should be fixed when comparing different samples. An image with a higher resolution is generally preferred due to smaller dependencies of radii on edge detection criteria.





# 4 Optical Measurements

This chapter presents the optical measurement techniques of 2D PhC slabs and cavities. First, the main optical setup is detailed. Then, some auxiliary setups are presented. Finally, frequently used measurement methods, i.e., resonance scattering and Fourier imaging, are introduced.

## 4.1 Main Optical Setup

### 4.1.1 Parts of the Main Optical Setup

The main optical setup [Fig. 4.1] is redesigned based on the existing setup [70]. It consists of five parts: the sample stage and objective, the inspection part (blue beam), the near-infrared (NIR) part (red beam), the visible (VIS)<sup>1</sup> part (green beam), and the side coupling part (bottom). The drawing of the main setup is also available in appendix A.3 with element lists. The setup alignment is briefly introduced in appendix A.4.

#### Sample Stage and Objective

As a typical scenario of optical measurement, the sample, which is essentially a Si chip of size in between  $10 \times 10 \text{ mm}^2$  and  $20 \times 20 \text{ mm}^2$ , is placed horizontally on a sample stage. The sample stage possesses the degree of freedom of pitch and yaw for horizontal alignments and rotation around the  $z$ -axis to control the sample orientation. The sample stage is firmly attached to a piezoelectric module (PI P-611.3 NanoCube) with  $x$ - $y$ - $z$  3-axis translation capability for  $100 \text{ }\mu\text{m}$  range each and with nanometer-scale precision. The piezoelectric stage is then firmly attached to  $x$ - $y$  translational stages with manual micrometer knobs for coarse translation adjustments. The sample stage can be upgraded to a container that encapsulates the sample

---

<sup>1</sup>In this context, NIR mainly refers to the light at around  $1550 \text{ nm}$ , and VIS mainly refers to the light at around  $775 \text{ nm}$ . The range of the visible spectrum is not defined with sharp boundaries. It is typically recognized as  $380\text{-}750 \text{ nm}$  but could extend to  $310\text{-}1100 \text{ nm}$  under optimal conditions [122]. Human eyes see the  $775 \text{ nm}$  light as in red color but with much lower sensitivity than, for instance, green light.

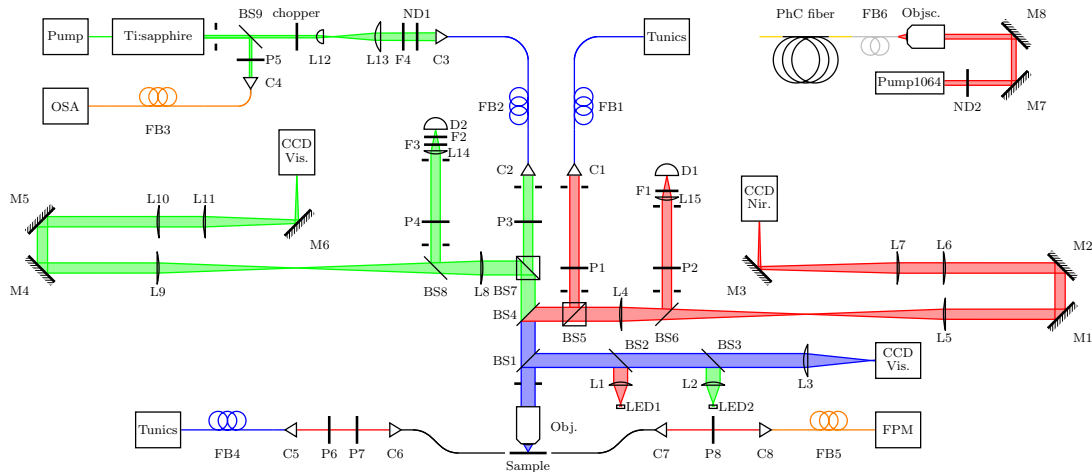


Figure 4.1: Schematic drawing of the main optical setup. It consists of five parts: the sample stage and objective, the inspection part (blue beam), the NIR part (red beam), the VIS part (green beam), and the side coupling part (bottom).

for gas (e.g., nitrogen) protection and bends the sample for strain control (see section 5.5).

A microscope objective is located above the sample to couple light to the sample and to collect the light scattered or emitted from the sample in the vertical direction. The microscope objective is fixed to a mount that provides the degree of freedom for pitch, yaw, and rotation. The mount is attached to a translation stage in the  $z$ -direction to adjust its altitude. The  $z$ -translation stage is then attached to  $x$ - $y$ - $z$  translation stages, together with a mirror (not shown in Fig. 4.1) that redirects the light path from the vertical direction to the horizontal direction. The objective and the mirror can be translated together in  $x$ ,  $y$ , and  $z$ -directions for coupling, while the objective can be translated individually in the  $z$ -direction for focusing.

### Inspection Part

The inspection part [Fig. 4.1 (blue beam)] is designed to visualize the sample. It also assists the focus of the laser beams on the sample surface as well as the alignment of the laser beam to specific locations, i.e., the cavities. The inspection light path is branched from the main light path by a removable beamsplitter (BS1), which is typically a 50% reflection pellicle working in both the VIS and NIR range. The light is sent to an analog camera composed of a CCD array (CCD Vis.) and a replaceable lens (L3). The background illumination for the infrared range is an LED that emits at 1550 nm (LED1), and the illumination for the visible range can be a blue LED or a white light LED (LED2). For simplicity, the illumination lights from the LEDs are quasi-collimated by lenses (L1 and L2) and are sent to the sample by beamsplitters (BS1, BS2, and BS3). The transmission and the reflection of the beamsplitters are selected such that enough light from the LEDs can be reflected toward the sample, and enough light from the sample can pass through to be detected on the CCD array at the same time. The light from the

sample can also be redirected to the infrared camera (CCD Nir.) by two mirrors, which are not shown on the drawing.

### NIR Part

The NIR part [Fig. 4.1 (red beam)] is designed to send and receive light in the NIR range (around 1550 nm).

On the sending side, the NIR excitation laser is injected into the setup through a fiber collimator (C1). After passing through a polarizer (P1), the collimated beam is reflected by a nonpolarizing beamsplitter (BS5) and a short-pass dichroic mirror (BS4) and is sent to the objective (Obj.). The two reflections bring some challenges for the alignment, mainly because the NIR light is invisible and the reflectivity of the dichroic mirror is low for visible light (see section A.4). The excitation light source is typically a continuous wave (CW) tunable laser (Tunics, Yenista Tunics T100-S), which provides a laser beam of power 0.2-5 mW in the 1480-1660 nm range, and it is connected to the main setup by a polarization-maintaining (PM) fiber (FB1). The laser source can be amplified by an Optical Fiber Amplifier (OFA, Amonics series) up to 100 mW in a smaller range (telecommunication C-band, 1530-1565 nm, and L-band, 1565-1625 nm). Alternatively, the in-coupling collimator (C1) also accepts the broad-band supercontinuum light source (see section 4.2.2 for more details).

On the receiving side, the light from the sample is collected by the objective and sent back to the dichroic mirror (BS4) in the collimated form. The light is then redirected by the dichroic mirror to the detection part. After the reflection by a mirror or a beam splitter (BS6), the light is collected by a photodiode (PD, D1, InGaAs sensor, Eosystems DSS-IGA020TC). A tube is attached to the aperture of the PD to block the environmental light and to provide mount positions for an edge-pass filter (F1) with optical density (OD) about 4, a small lens (L15), and a tunable iris. The long-pass filter (F1, edge at 1400 nm, with optical density, or OD, about 5) helps to block light with a wavelength outside the desired range (there is no short-pass filter above 1600 nm available, nor necessary). The lens (L15) helps to focus the collimated light on the small effective area of the PD. The tunable iris is optionally attached to the opening of the tube to select the direction of the incident light more precisely. The PD and the tube are attached firmly together, and they have degrees of freedom of translation in horizontal and vertical directions, although the light coupling is tested not sensitive to the positioning because of the focus lens (L15). A polarizer (P2) is located in front of the PD-tube module as an analyzer, with its polarization direction perpendicular to that of the polarizer (P1). Neutral density (ND) filters can be optionally added in front of the PD or after the collimator (C1) to adapt the power to the desired range.

The light can also be sent to a CCD camera (CCD Nir.) after passing through some lenses and mirrors (L4-L7, M1-M3). This path is long because it enables multiple functions: when L4, L5, and L6 are removed, or only L6 is removed, it can form a normal image of the sample surface; when L5 and L6 are removed, it can form an image of the Fourier plane of the objective; and

## Chapter 4. Optical Measurements

---

when all lenses are on site, it can form an image of the Fourier plane as well as providing room in between L4 and L5 for Fourier space filtering.

The beam splitter (BS6) enables power detection and imaging simultaneously and can be removed or replaced by a mirror if more light is preferred for imaging or power detection, respectively. When light needs to be collected to optical fiber, a fiber collimator can be installed between BS6 and L5 (not shown on the drawing).

### VIS Part

The VIS part [Fig. 4.1 (green beam)] is designed to send and receive light in the VIS range (around 775 nm). It is very similar to the NIR part, except that the design of the elements (e.g., anti-reflection coating) is optimized for VIS light.

On the sending side, the VIS excitation laser is injected into the setup through a fiber collimator (C2). The collimated beam is sent to the objective in a straight line after passing through a polarizer (P3), a beam splitter (BS7), and the dichroic mirror (BS4). The excitation light source is typically a CW titanium-sapphire (Ti:sapphire) tunable laser (see section 4.2.1). Alternatively, the in-coupling collimator (C2) also accepts the broad-band supercontinuum light source (see section 4.2.2).

On the receiving part, the power detector is an avalanche photodiode (APD) (D2, Si sensor, Hamamatsu C4777-01), and there are two edge-pass filters (F2, F3) that form a transparent window of 750-850 nm with the blockage OD about 5. The camera on the VIS side (CCD Vis, Andor iXon Ultra DU-897U-CS0-EXF) is an electron multiplying charge-coupled device (EMCCD) that has very high photon sensitivity (initially prepared for the case of low SHG efficiency).

### Side-coupling Part

The side-coupling part [Fig. 4.1 (bottom)] is inherited from the previous design and is used to measure the NIR transmission of on-chip devices with waveguides, for example, cavities side coupled to W1 waveguides. The excitation laser from the source (Tunics) is guided with a PM fiber (FB4) and injected into a fiber port (C5). After passing through a  $\lambda/2$  waveplate (P6) and a polarizer (P7), the beam is collected by another fiber port (C6) and is sent to a segment of fiber with a tapered end. The tapered end of the fiber works as a micro-lens that facilitates the coupling to the on-chip waveguides. The transmitted light is collected by another segment of end-tapered fiber. After passing through a fiber port (C7), an analyzer (P8), and another fiber port (C8), the light is sent to a fiber optic power meter (FOPM) (ILX Lightwave FPM-8200) through a multimode fiber (FB5). The end-tapered fibers are attached to a stage with  $x$ - $y$ - $z$  translations and pitch and yaw adjustments to enable maximum coupling to the waveguides.

## 4.1.2 Electrical Connections and Software Controls

The digital instruments are connected directly to the computer [Fig. 4.2 (a)]. The cameras and the oscilloscope are connected to the computer via universal serial bus (USB) with their dedicated software drivers. The tunable laser for 1550 nm and the FOPM are connected to the computer via general purpose interface bus (GPIB), and their drivers are managed by national instruments virtual instrument software architecture (NI-VISA). The tunable laser for 775 nm (actually just the actuator controller) is connected to the computer via recommended standard 232 (RS232) and USB, and its driver is managed by NI-VISA. The oscilloscope serves as an analog-to-digital converter (ADC) that converts analog signals from the detectors, e.g., photodiodes and power meters, to the computer. When lock-in detection is needed, a lock-in amplifier (Stanford Research Systems SR510 or SR830) is connected between the detectors and the oscilloscope (see appendix A.6 for lock-in detection).

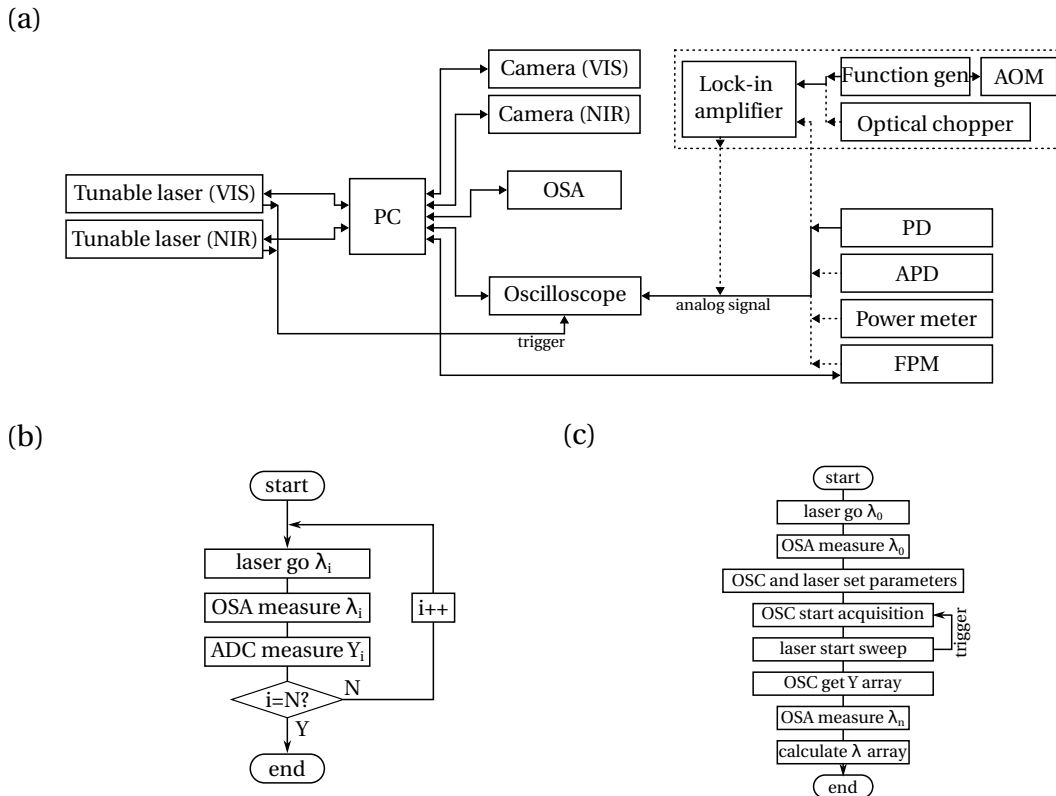


Figure 4.2: (a) Schema of electrical connections of the main setup. (b) Flowchart of point-by-point measurement. (c) Flowchart of sweep measurement (OSC: oscilloscope).

The measurement (data acquisition) is automated by laboratory virtual instrument engineering workbench (LabVIEW). Two types of measurements are mainly employed, the point-by-point measurement and the sweep measurement [Fig. 4.2 (b) (c)]. The point-by-point measurement is very simple and provides an accurate correspondence between the wavelength and the signal. However, it takes a long time since the actuator stops at each data point

(typically 3 point/s without wavelength calibration). The sweep measurement, on the other hand, is very fast (related to the sampling speed of the oscilloscope, 10M points/s at maximum, and the movement speed of the actuator, 100 nm/s at maximum for Tunics, and about 2 nm/s for Ti:sapphire laser), and is accurate enough with an electrical trigger from the actuators to the oscilloscope (The Tunics provides a dedicated trigger output, while for the actuator on the Ti:sapphire laser, the trigger is connected to its power connector pin). The wavelengths are automatically calibrated using the OSA in case of a nonlinear relation between wavelength and actuation. The absolute accuracy of the wavelength given by the OSA is about 1 pm (with maximum wavelength resolution and minimum video bandwidth), while the OSA itself has a 17 pm redshift for its full wavelength range compared to a Xe lamp. This calibration takes a relatively long time (0.5 s) as the OSA takes a spectrum containing the desired signal and fits the peak. A more convenient instrument for wavelength calibration would be a wavemeter.

### 4.1.3 Wavelength Calibration

The repeatability of the output wavelength for the 775 nm range Ti:sapphire laser and the 1550 nm range NIR tunable laser was found to be limited. Wavelength fluctuation of up to 50 pm was observed for the NIR tunable laser after start-ups of the instrument [Fig. 4.3 (a)]. The wavelength accuracy of the Ti:sapphire laser is worse because of the custom actuation. To have spectra that are comparable over time, the wavelength must be calibrated by an absolute reference each time a spectrum is acquired.

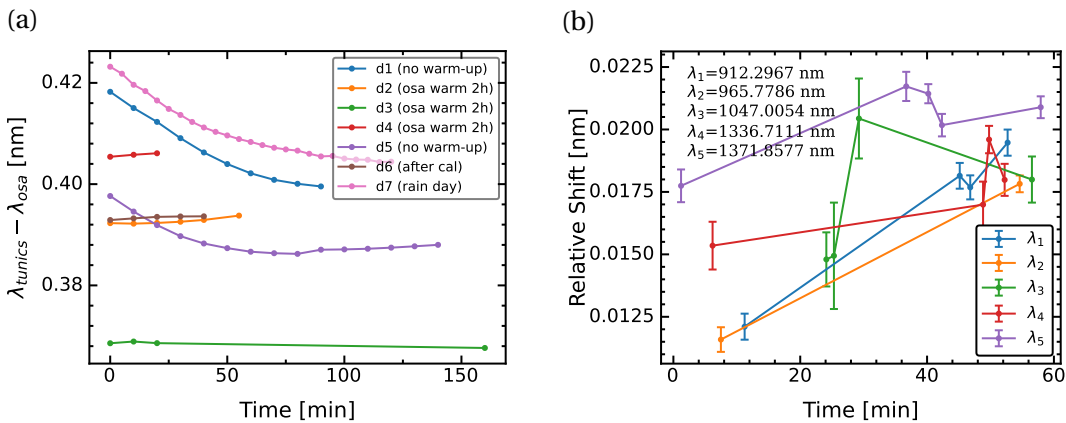


Figure 4.3: (a) Wavelength repeatability at 1550 nm of the tunable laser measured by the OSA. Labels d1-d7 represent measurements on different days after turning on the laser. (b) Relative shift of Ar lamp emission peaks measured by the OSA.

One way to calibrate the wavelength is to bypass a reference beam through a known medium (e.g., hydrogen cyanide, acetylene) and record the absorption spectrum of the medium at the same time as taking the experimental spectrum. Another way to calibrate the wavelength is to bypass a reference beam to an instrument that directly measures the wavelength (e.g., wavemeter, OSA).

A scanning OSA is applied in practice to measure the wavelength. The OSA takes a short spectrum around the expected wavelength range and fits the Gaussian peak to extract the wavelength. The process is automated by the LabVIEW scripts. In order to verify the reliability of the process, an argon (Ar) lamp (Oriel 6030) is used to calibrate the OSA. Although the incoherent light of the Ar lamp is difficult to be coupled in the optical fiber for the OSA, 5 emission peaks can be identified, an average redshift of 17.3 pm was measured, and the red-drift over one hour was about 5 pm [Fig. 4.3 (b)].

## 4.2 Auxiliary Setups and Techniques

### 4.2.1 Ti:sapphire Tunable Laser

#### Ti:sapphire Tunable Laser Assembly

The Ti:sapphire part [Fig. 4.4] provides the tunable CW laser source for excitation in the VIS (775 nm) range. It is composed of a pump laser, a tunable Ti:sapphire (Coherent 890), an optical modulator, and fiber coupling parts.

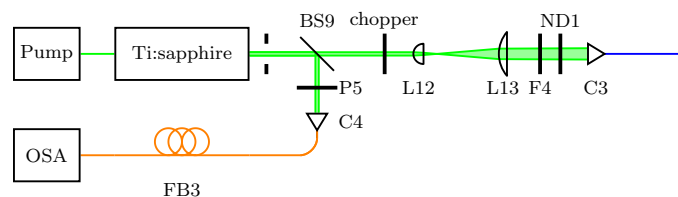


Figure 4.4: Ti:sapphire laser part.

The pump laser (Sprout H-10W) is a CW laser with a maximum power of 10 W at a fixed wavelength of 532 nm. It is internally an Nd: YVO<sub>4</sub> diode-pumped solid-state (DPSS) laser that lases at 1064 nm and uses intra-cavity frequency-doubling to convert the output to 532 nm. The Ti:sapphire laser is detailed in the sections below.

The output beam of the Ti:sapphire laser is linearly polarized in the vertical direction with TEM<sub>00</sub> transverse mode and beam size less than 3 mm in diameter. The beam is expanded by two lenses (L12, L13) to a diameter of about 8 mm and is then coupled to a parabolic reflective fiber collimator (C3) and sent to the main setup through a single mode (780 nm) PM fiber. The expansion of the beam is implemented to enable tighter focus, thus, higher coupling efficiency. The unwanted green pump light is optionally filtered out by a long-pass filter (F4), and the intensity is optionally controlled by an ND filter (ND1) before coupling to the fiber.

Due to the precision limit of the actuator mechanics, the wavelength repeatability is not very high (about 0.2 nm and drifting). The relation between the wavelength and the actuator position is also not strictly linear (see appendix A.5). To compensate for these, a small part (1-5%) of the beam is branched by a beam sampler (BS9), collected by a collimator (C4), and

## Chapter 4. Optical Measurements

sent to the OSA through a multimode fiber to extract the wavelength, where a polarizer (P5) works as an intensity controller.

The beam can be modulated by optical choppers with a 50% duty cycle to 6000 Hz or a 0-50% variable duty cycle to 1000 Hz (depending on the chopper wheel used). Alternatively, the beam can also be modulated by an acoustic optical modulator (AOM) with a variable duty cycle of up to 2 MHz (see section 4.2.3).

### Working Principle

The Ti:sapphire laser has been widely used for short pulse generation since its invention in the 1980's [123–126] because of its wide emission band. It is also used in CW mode as a tunable laser with proper wavelength selection and cavity design, which is the case in this context. The employed Ti:sapphire laser (Coherent 890) operates at a wavelength range of about 730–850 nm with a peak output intensity of more than 300 mW at around 780 nm (with up to 10 W pumping at 532 nm).

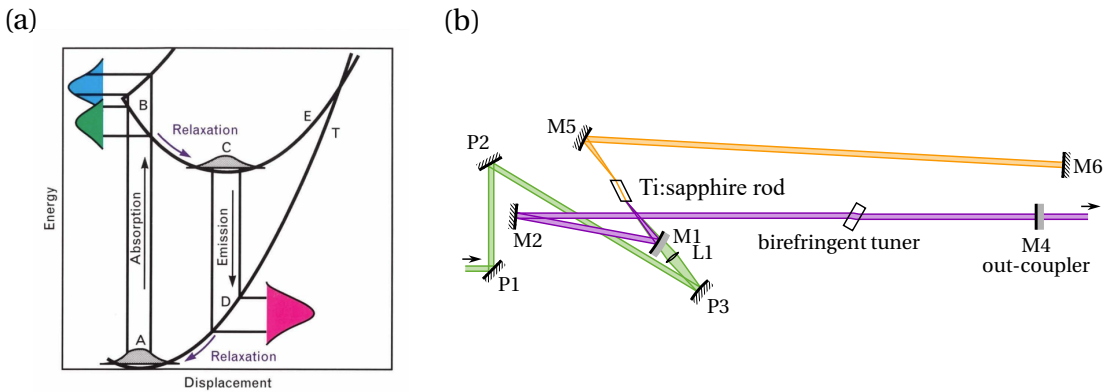


Figure 4.5: (a) Diagram of Ti:sapphire lasing mechanism (adapted form [124]). (b) Schematic drawing of the Ti:sapphire laser cavity.

The gain medium of the laser is a sapphire ( $\text{Al}_2\text{O}_3$ ) crystal doped by titanium (Ti) atoms. A Ti atom replaces the site of an aluminium atom and bounds to six neighboring oxygen atoms, so it appears like a  $\text{Ti}^{3+}$  ion. Five intrinsic energy levels of free  $\text{Ti}^{3+}$  ions are distorted by the cubic electric field of the surrounding oxygen atoms, and they form an excited doublet level (E) and a ground triplet level (T). The energy of these levels is also influenced by the displacement of the  $\text{Ti}^{3+}$  ion inside the oxygen cage. During the lasing process, the  $\text{Ti}^{3+}$  ions on the ground level are pumped to the excitation level by green or blue lasers [Fig. 4.5 (a)]. Then they are quickly relaxed by emitting phonons and displacing themselves in the oxygen cages before reaching the upper lasing level. Then the  $\text{Ti}^{3+}$  ions emit photons in the red and NIR range and reach the lower lasing level with a large energy span. Finally, they return back to the ground level by, again, emitting phonons and displacing themselves. So, effectively, the Ti:sapphire laser works as a four-level system. The emitted phonons are seen as a heating-up, and thus



the sapphire crystal requires efficient heat removal, such as water cooling.

### Structure and Wavelength Tuning

The Ti:sapphire laser cavity is formed by a full reflective mirror (M6) and a semi-transparent mirror (M4), in which a Ti:sapphire rod is placed [Fig. 4.5 (b)]. The 532 nm green pump laser can be injected into the sapphire rod through a concave and dichroic mirror (M1). In theory, the emission of the Ti:sapphire laser covers a wide range of 690-1100 nm. However, this wide range requires different sets of mirrors, and in practice, the range of 730-850 nm can be accessed with a fixed set of mirrors.

The output wavelength is tuned by a wavelength filter installed at Brewster's angle [Fig. 4.5 (b)]. The wavelength filter is typically made of a stack of two quartz birefringent plates (in general 1-3 plates of quartz, or MgF<sub>2</sub> for UV and IR range) and thus is usually referred to as the birefringent tuner<sup>2</sup>. The tuner has a quasi-periodic transmission spectrum, and the peak positions are dependent on the angle between the incident beam and the crystal's main optical axis. Since the birefringent tuner is inside the laser cavity, the unwanted wavelengths experience larger loss and finally below the lasing threshold, and the desired wavelength also becomes the dominant one because the upper and the lower lasing levels are themselves adapted to this wavelength through interactions with phonons.

To tune the transmission peaks, the tuner is rotated along an axis perpendicular to the plates' surfaces by a translational high-precision acoustic actuator (Oriel 18246, with Oriel 18011 controller) attached to a rotating disk that accommodates the birefringent tuner. In practice, there are two regions where the wavelength is linearly tuned by the actuator [Fig. 4.6 (a)], and between these two regions, the laser is randomly hopped to the most probable emission wavelength because the birefringent tuner is at its low transmission position. The direct output power of the Ti:sapphire laser is linearly dependent on the pump power and reaches 350 mW at the maximum pump of 10 W [Fig. 4.6 (b)]. The lasing threshold is about 4 W, depending on the alignment of the pump. The linewidth of the output wavelength is smaller than 40 pm, as measured by the OSA, but could be limited by the resolution of the OSA [Fig. 4.6 (c)]. Mode hopping of the laser, i.e., discrete wavelength under continuous scan, is observed in the wavelength range of 759-762 nm [Fig. 4.6 (d)].

The sapphire rod and the pump laser are cooled by a water-cooling system integrated with the controller of the pump. The air inside the Ti:sapphire laser can also be cooled and purified by a continuous flow of N<sub>2</sub> gas for better stability.

---

<sup>2</sup>A specific type of birefringent tuner is known as the Lyot filter, which also incorporates polarizers to reduce the linewidth of the transmission peak so as to enable higher wavelength selectivity. But this is not the case in this context.

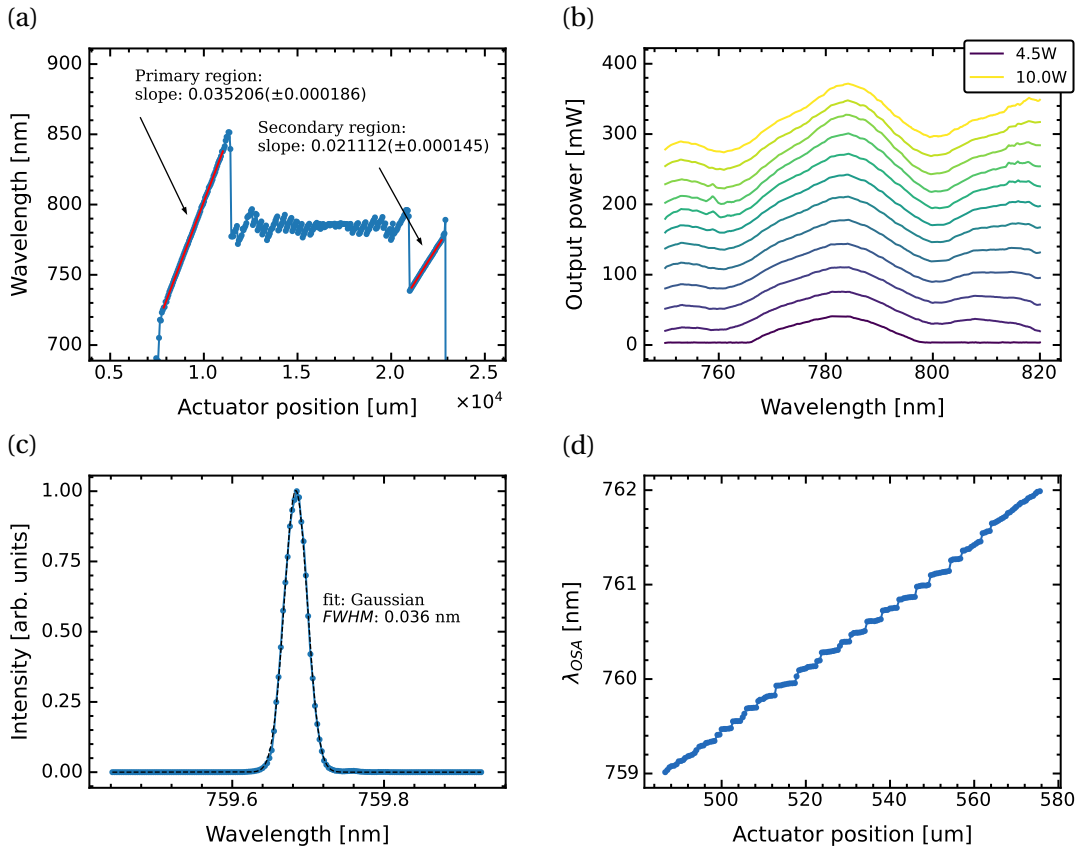


Figure 4.6: Ti:sapphire laser output characteristics. (a) Wavelength dependence on actuator position. The relation is quasi-linear in two regions, where the region on the left provides a larger wavelength range and is primarily used. (b) Direct output power with different pump powers. The lasing threshold is around 4 W, depending on the alignment of the pump. The output power is linearly dependent on the pump power when above the threshold. (c) The output line shape measured by the optical spectrum analyzer (OSA). The line width is limited by the resolution of the OSA. (d) Mode-hopping of the Ti:sapphire laser.

#### 4.2.2 Supercontinuum Source

The supercontinuum source is used for broadband excitations, together with spectrographs. The supercontinuum light is generated inside a PhC fiber pumped by a pulsed laser [Fig. 4.7 (a)]. The pump laser (Pump1064) is a diode-pumped passively Q-switched neodymium-doped yttrium aluminium garnet (Nd:YAG) laser that provides short pulses down to 600 ps at 1064 nm with a peak power of 13 kW and average power of 200 mW. The pump beam is linearly polarized with  $\text{TEM}_{00}$  transverse mode. The pump power can be controlled by a continuously variable metallic ND filter (ND2) with 1-91% (OD 0.04-2.0) transmission. The beam is then reflected by two dielectric mirrors (M7, M8) and coupled to an end-capped single-mode fiber by an objective lens (Objsc). The coupling efficiency from free space to the fiber is about 50% (this may be potentially improved by beam expansion). The end-cap is a small segment of transparent material attached to the facet of a normal single-mode fiber that helps to increase the damage threshold of the fiber by increasing the beam cross-section area at the fiber-air

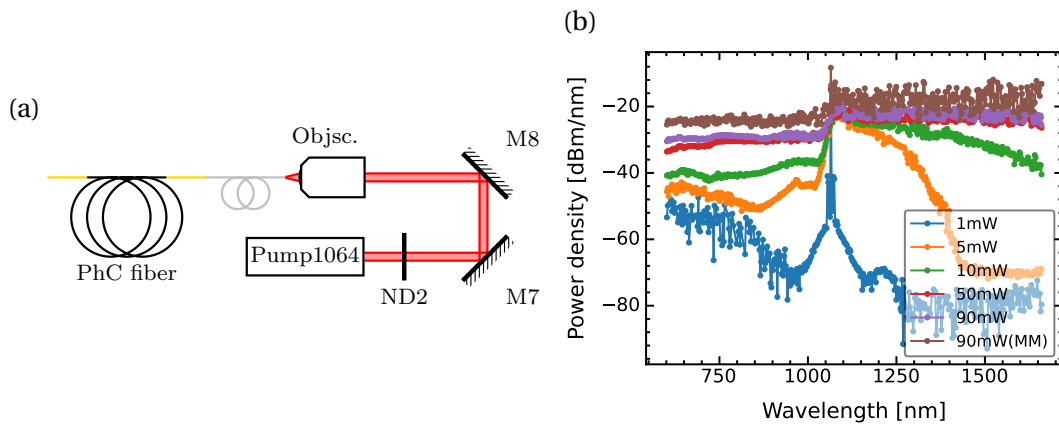


Figure 4.7: a) Schematic drawing of the supercontinuum source. The output is on the left side. b) Output power density of the supercontinuum source with different pump powers (in the end-capped optical fiber), measured by OSA with a single mode fiber (SM, for 1550 nm) connected to the output. The last line represents the same measurement with a multimode (MM) fiber connected to the output.

interface.

The pump is then coupled to the PhC fiber, which is internally a sandwich of a single-mode fiber for 1064 nm for input (HI1060), a segment of the real PhC fiber of several tens of meters, and a single-mode fiber for broadband output (SMF28). The supercontinuum spectrum is generated in the PhC fiber through a series of strong nonlinear processes, and the power is spread continuously in a very large wavelength range. The photonic crystal fiber is a kind of optical fiber for which the cross-section is a photonic crystal cavity that confines the electric field in lateral directions. Because of tight light confinement in the fiber core, photonic crystal fibers exhibit much stronger nonlinearity than normal optical fibers, thus enabling supercontinuum generation under low-power pumping. The supercontinuum output is also pulsed and requires careful operations.

In practice, the power density of the supercontinuum spectrum is around -20 dBm/nm for wavelengths larger than the pump (1064 nm) and -21 dBm/nm for wavelengths smaller than the pump [Fig. 4.7 (b)], measured by the OSA, with 90 mW pump power in the end-capped fiber and with a multimode (MM) fiber connected at the output. The lower power density on the visible side could be the result of either the intrinsic property of the supercontinuum generation or the dispersion of the involved optical fibers. Such measurement could be challenging because the full power of the supercontinuum is difficult to measure, and it may exceed the power limit of the OSA. Thus, optical attenuators are required for safe operation.

The optical elements are installed on a small breadboard enclosed in a box for laser safety considerations. The single-mode fiber ends should avoid direct exposure to air during high-power pumping because the high intensity at the fiber-air interface could potentially damage the fiber core. A multimode fiber or a single-mode fiber with an end cap is usually attached to the output.

### 4.2.3 Acousto-optic Modulation

AOMs are alternatives to optical choppers in lock-in detection. An AOM employs an acoustic wave to periodically change the refractive index in a transparent material and create a Bragg mirror (or thick grating) for light manipulation. The applied free-space AOM (IntraAction AOM-40N) uses an RF signal (provided by its driver) at 40MHz to drive a piezo-electric transducer and generate an ultrasound wave that propagates in a block of dense flint glass (polarization insensitive).

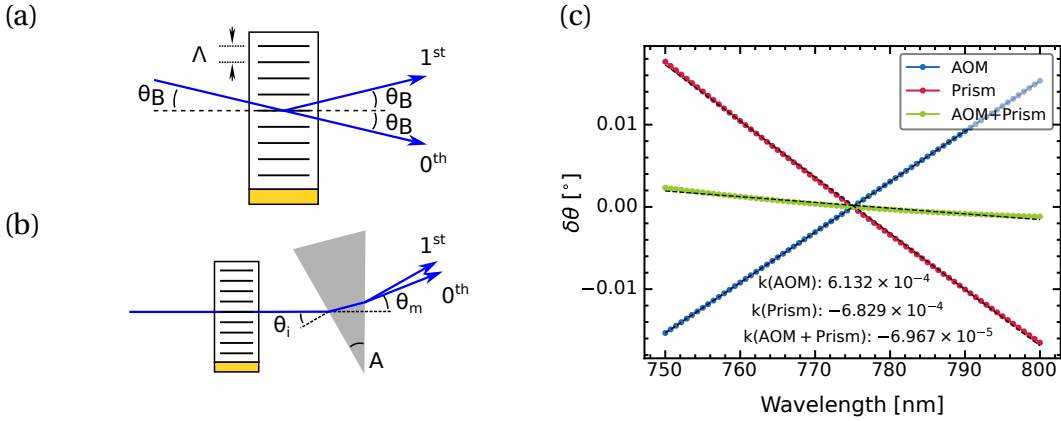


Figure 4.8: (a) Schema of an AOM operated in the Bragg regime. The Bragg angle is exaggerated ( $\theta_B = 0.163^\circ$ ). (b) Schema of dispersion compensation by a prism. The 1<sup>st</sup> order beam is used.  $\theta_B$  is small compared to  $\theta_m$  and  $\theta_i$  ( $\theta_m = 16.052^\circ$ ,  $\theta_i = 23.026^\circ$ ). (c) Calculated relative deflection angle as a function of wavelength for the AOM, the 30° BK7 prism, and the two combined, with the first order diffraction angle of the AOM  $\theta_{+1} = 0.326^\circ$  and the minimum deviation angle of the prism  $\theta_m = 16.052^\circ$ .

There are two operation regimes for an AOM [127–129]: 1. the Raman-Nath regime, in which the incident light beam is parallel to the norm of the acoustic beam, and there are several diffraction orders ( $\dots, -2, -1, 0, +1, +2, \dots$ ); 2. the Bragg regime, in which the incident light beam is tilted by  $\theta_B$  from the norm of the acoustic beam, and there is only one diffracted beam (the 1<sup>st</sup> order, because the others are annihilated by destructive interference). The AOM is operated in the Bragg regime [Fig. 4.8 (a)] for a higher deflection efficiency (fraction of light intensity at the 1<sup>st</sup> order over the incident intensity). The Bragg angle  $\theta_B$  is expressed as (Bragg condition):

$$\theta_B = \arcsin\left(\frac{\lambda_n}{2\Lambda}\right), \quad (4.1)$$

where  $\lambda_n$  is the light wavelength in the glass,  $\Lambda$  is the acoustic wavelength in the glass. By assuming  $\lambda_n = 775 \text{ nm} / 1.5 = 516 \text{ nm}$  and  $\Lambda = 3630 \text{ m/s} / 40 \text{ MHz} = 9.075 \times 10^{-5} \text{ m}$ , the Bragg angle is estimated to be  $\theta_B = 0.163^\circ$ , which is very small. In practice, the yaw of the AOM is fine-adjusted to reach the Bragg regime from the Raman-Nath regime. When the light incident angle is fixed, the deflection efficiency is only dependent on the grating contrast, and thus the acoustic wave intensity and the power of the driving RF signal, which can be modulated by an external electric signal (provided by a function generator, up to 2 MHz bandwidth).

Compared to an optical chopper, the AOM is advantageous for wider modulation bandwidth, small frequency fluctuation, and variable modulation functions. However, its deflection efficiency is lower (<100%, compared to 100% for a chopper). The AOM also changes the frequency of the incident light through Brillouin scattering, but this effect is small and can be safely ignored (for example, 40 MHz acoustic wave results in a wavelength shift of  $8 \times 10^{-5} \text{ nm}$ ).

The dispersion of the diffraction angle can be reduced by one order of magnitude, from  $6.132 \times 10^{-4} \text{ }^\circ/\text{nm}$  to  $-6.967 \times 10^{-5} \text{ }^\circ/\text{nm}$ , by applying a compensation prism [Fig. 4.8 (b) (c)]. The prism is of  $30^\circ$  angle and is made of BK7 glass. It is operated at the minimum deviation regime where the incident and the refracted beams are symmetrical about the axis of symmetry of the prism. The minimum deviation angle is  $\theta_m = 2 \arcsin(n \sin(A/2)) - A = 16.052^\circ$ , where  $A = 30^\circ$  is the prism angle, and  $n = 1.5113$  is the prism refractive index at 775 nm [130]. The incident angle at minimum deviation is  $\theta_i = \arcsin(n \sin(90^\circ - (180^\circ - A)/2)) = 23.026^\circ$ .

### 4.3 Resonant Scattering Measurement

Resonant scattering (RS) is a technique widely used to probe the resonant spectrum of optical microcavities [131]. The cavity is excited by a laser beam from free space, and the reflected light is collected in the same path, which is different from the regime of side-coupling with a waveguide. This technique does not require on-chip waveguides and is suitable for probing 2D PhC cavities.

A general configuration of resonant scattering measurement is shown in Fig. 4.9. A laser beam with a variable wavelength is sent to the sample from the top side and is focused on a 2D PhC cavity by an objective lens. The polarization of the incident beam is controlled by a polarizer (P), and the orientation is along the  $x$ -axis. The sample is rotated such that the far-field polarization of the cavity mode is at  $45^\circ$  with respect to the polarizer. Most of the incident light (with  $x$ -polarization) is directly reflected (nonresonant scattering) by the interfaces of the PhC slab, while a small part contributes to the excitation of the cavity mode. The excited cavity scatters light (resonant scattering) out of the slab with a polarization defined by its far-field mode, which is now at  $45^\circ$  with respect to the  $x$ -axis. The reflected (scattered) light is collected by the same objective lens, reflected by a beam splitter (BS), filtered by an analyzer (A), and collected by a detector. In the simplified scenario, since the analyzer is orthogonal to the polarizer, the direct-reflected light is filtered, and only the light coming from the mode emission passes through.

In a general scenario, the bulk-reflected light and the cavity-scattered light interfere, which is known as Fano interference [132], and results in an intensity spectrum with the Fano lineshape:

$$I(\omega) = A + B \frac{[q + 2(\omega - \omega_0)/\Gamma]^2}{1 + [2(\omega - \omega_0)/\Gamma]^2} \quad (4.2)$$

where  $A$  and  $B$  are constants,  $\omega_0$  is the cavity mode frequency,  $\Gamma$  is the resonance linewidth

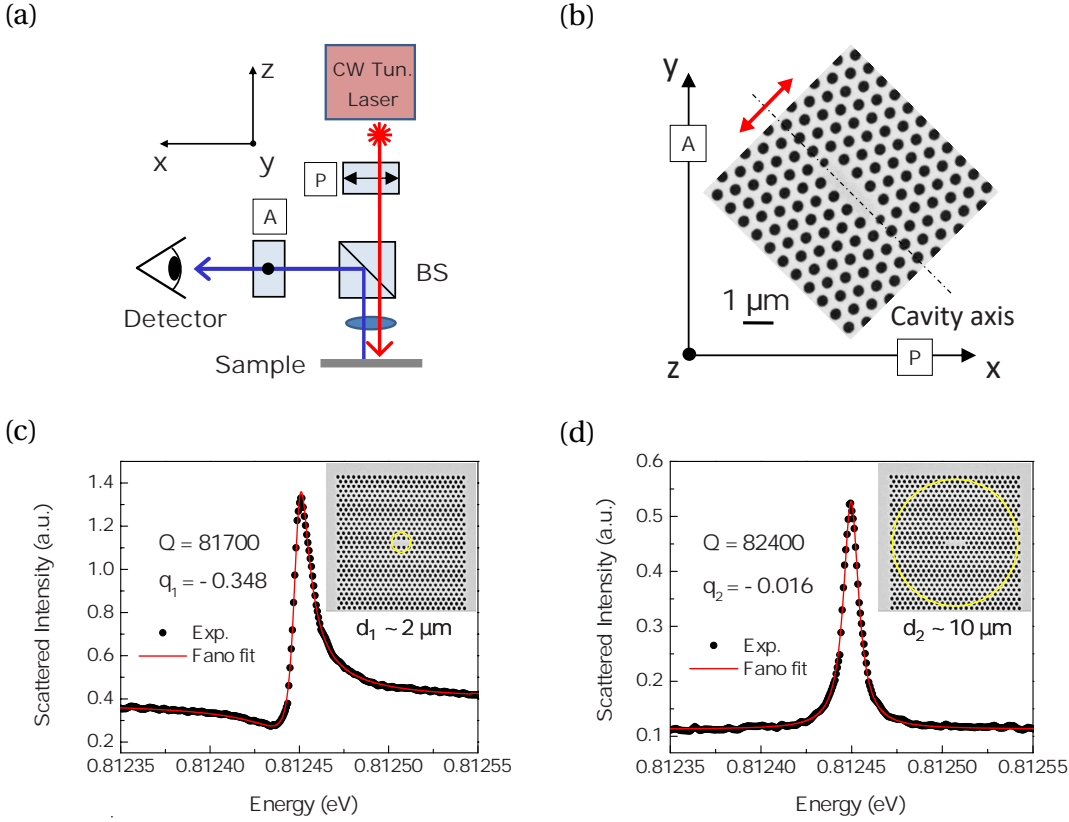


Figure 4.9: Resonant scattering measurement (adapted from [131]). (a) Optical path containing a polarizer (P), an analyzer (A), and a beam splitter (BS). (b) Cavity orientation. The cavity is oriented such that its far-field mode polarization is at  $45^\circ$  with respect to the polarizer and the analyzer. (c) Asymmetric resonance when  $|q|$  is close to one. (d) Reversed Lorentzian resonance when  $|q|$  is much smaller than one.

(FWHM), and  $q$  is a factor that describes the ratio between resonant and nonresonant scattering. When  $|q| \gg 1$ , resonant scattering dominates, and the spectrum lineshape is a Lorentzian function; when  $|q| \ll 1$ , nonresonant scattering dominates, and the spectrum lineshape is a (frequency) reversed Lorentzian function (Fig. 4.9 (d)); when  $|q| \approx 1$ , the resonant scattering strength is comparable to nonresonant scattering, and the spectrum lineshape is strongly asymmetric (Fig. 4.9 (c)).

#### 4.4 Fourier Plane Imaging

Fourier plane imaging is a powerful tool to retrieve the far-field emission pattern of radiative photonic structures. At a fixed wavelength, the light radiation from a photonic structure (PhC cavities, waveguides, etc.) in the upper hemisphere of the sample plane can be regarded as a composition of plane waves of different intensities  $I_i$  and radiation angles  $\theta_i = (\theta_{ix}, \theta_{iy})$  (angle in space) [Fig. 4.10 (a)]. After passing through an objective (a thin lens for simplicity), each plane wave is transformed into a paraboloid wave and is focused on a point  $P_i = (x_i, y_i)$

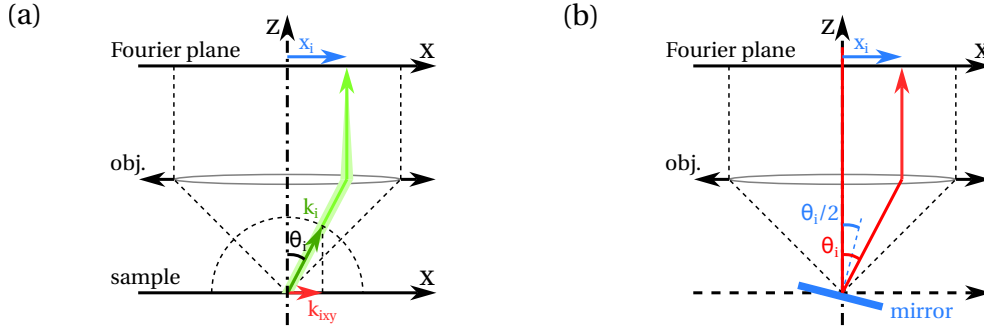


Figure 4.10: Fourier imaging. (a) Schema of basic Fourier imaging. (b) Calibration of  $\theta_i - x_i$  relation using a beam of laser and a mirror.

on the back focal plane (BFP, also called Fourier plane) of the objective. In this way, the different plane wave components are separated and mapped on an image (i.e., far-field image or far-field emission pattern) at the Fourier plane, in which the position of a point corresponds to the radiation angle, and the intensity of the point corresponds to the intensity of the plane wave. The pattern on the Fourier plane is a real image and is captured by an imaging system.

The far-field image can be used to retrieve the radiation angle distribution through calibration of the relation between the radiation angle and the position vector from a reference point on the far-field image. For a PhC structure at a fixed wavelength  $\lambda_i$ , the wavevector in the sample plane  $\mathbf{k}_{i,xy}$  is related to the radiation angle by:

$$\mathbf{k}_{i,xy} = \mathbf{k}_i \sin(\theta_i), \quad (4.3)$$

where  $\mathbf{k}_i$  is the wave vector in 3D space. When sweeping the wavelength and capturing the far-field images at the same time, the dispersion relation between the angular frequency  $\omega_i$  and the in-plane wavevector  $\mathbf{k}_{i,xy}$  can be revealed for the photonic structure. The experimentally measured dispersion relation can be directly compared to the calculated band structure of the PhC, which provides a powerful method for characterizing the fabricated PhC.

On the main setup and taking the NIR part as an example [Fig. 4.1], the light path Sample-Obj-BS4-M1-M2-L7-CCDNir provides the conventional real space imaging of the sample. When doing Fourier plane imaging, a lens L4 is added such that its focus is close to the back focal plane of the objective, and the light path is Sample-Obj-BS4-L4-M1-M2-L7-CCDNir. The Addition of L5 and L6 is inherited from the previous design for the ability of Fourier space filtering in between L4 and L5, and in this case, the light path Sample-Obj-BS4-L4-L5-M1-M2-L7-CCDNir is used for real space imaging while the light path Sample-Obj-BS4-L4-L5-M1-M2-L6-L7-CCDNir is used for Fourier imaging.

The calibration of the relation between the radiation angle and the position vector on the far-field image is done by putting a mirror on the sample stage and tilting it to a series of known angles in  $x$  and  $y$ -directions while capturing the far-field image [Fig. 4.10 (b)].





# 5 Doubly Resonant PhC Cavities

## 5.1 Overview

In SHG and SPDC, the conversion efficiency can be strongly enhanced in doubly resonant cavities, i.e., simultaneously supporting resonant modes at either first- (FH) or second-harmonic (SH) frequencies, respectively [133–136]. In such cavities, nonlinear processes are enhanced by the quality factors ( $Q$ ) of the two modes (i.e., increased temporal confinement), as well as by spatial field confinement. The latter condition additionally requires that a large spatial overlap between the two fields is fulfilled, which generalizes the phase-matching condition in propagating geometries [137]. Doubly resonant conditions have been proposed and experimentally demonstrated in dual period Bragg mirrors [138–140], birefringently phase-matched waveguides [141], geometric dispersion-tuned micro-ring resonators [142, 143], and plasmonic nanoantennas [144]. PhC defect cavities patterned in two-dimensional (2D) slabs, which allow for very tight field confinement in purely dielectric resonators, have been shown to produce significant SHG enhancement in a singly resonant regime at FH [145–153]. However, implementing a doubly resonant condition in PhC slab cavities is a longstanding challenge because the SH frequency range generally lies entirely inside the light cone of the cladding materials, such that efficient confinement in the out-of-plane direction is prevented, not to mention the difficulty of engineering photonic bandgaps around both frequencies to favor the in-plane confinement.

Recently, a theoretical design based on a bound state in the continuum (BIC) opened up a new path for doubly resonant cavities on PhC slabs [154]. The BIC, in the case of a PhC slab, corresponds to the mode that lies inside the light cone but is nevertheless non-radiative, either because of symmetry protection or because of destructive interference between different radiation channels [155–157]. BICs have been theoretically proposed and experimentally implemented to enhance nonlinear generation in singly resonant regimes [158–160]. The doubly resonant PhC cavity design [154] abandoned the commonly-held notion of engineering photonic bandgaps at both FH and SH frequencies. Instead, at SH frequency, a BIC of PhC slab is engineered to provide the out-of-plane confinement, and a heterostructure of

hexagonal lattice is introduced to ensure the in-plane confinement in the absence of a photonic bandgap [161]. On the other hand, at FH frequency, the confinement mechanism is the same as in a conventional singly resonant PhC cavity, i.e., total internal reflection for the out-of-plane confinement and photonic bandgap for the in-plane confinement [151].

The BIC effect in the heterostructure cavity is highly interesting beyond being simply a means to achieve a long-lived mode at SH. In fact, BICs in PhC slabs are associated with a topological charge and are robust to structural modifications [157]. Strikingly, this topological charge manifests itself in the far-field radiation in the vicinity of a BIC in momentum space. Specifically, it was shown that the far-field must be linearly polarized and that, since the emission goes to zero at the BIC, the polarization angle must have a nontrivial winding around it [157]. This has also been demonstrated experimentally [162]. In Ref. [157], it was also proposed that this effect could be used to create vortex beam lasing [163], which can find applications in, e.g., optical trapping [164], light focusing and imaging [163, 165], and communications [166].

By applying the doubly resonant PhC cavity design, highly efficient SHG is experimentally demonstrated in a small-footprint device fabricated in the epitaxially grown highly nonlinear wide-bandgap GaN material. It is also confirmed that the SHG signal is a highly normal-direction concentrated vortex beam with radial polarization. This allows for an extremely high collection efficiency even with a small numerical aperture of the collecting lens, which is different from previous SHG realizations in singly resonant PhC cavities [146, 147, 149, 151]. The main results in this chapter were published in [167].

### 5.2 Cavity Design

The basic structure of the cavity is a 2D PhC made from a hexagonal lattice of air holes in a slab, where the lattice constant is  $a$ , the air hole radius is  $r$ , the slab thickness is  $d$ , and the refractive index is  $n$  [154]. The PhC slab is suspended in air, and external light could be coupled to the cavity from the top side of the slab [Fig. 5.1 (a)]. A heterostructure design is introduced to the PhC slab by increasing the hole radii ( $r_c, r_t, r_o$ ) in three concentric hexagonal regions (core, transition, and outer) whose sizes are defined by the side lengths in units of lattice constant ( $N_c, N_t, N_o$ ) [Fig. 5.1 (b)]. The heterostructure introduces a defect mode inside the photonic bandgap of the outer region at FH frequency, and at the same time, provides a resonant mode at SH frequency in the absence of a photonic bandgap. The out-of-plane confinement is guaranteed by the index guiding of the slab at FH frequency, and by the quasi-BIC at SH frequency [Fig. 5.2]. The Q-factor at FH increases with the sizes of both the core and the outer regions, while the Q-factor at SH increases mainly with the size of the core region from which the quasi-BIC is derived. Although a larger core region results in larger Q-factors at both frequencies, the nonlinear overlap factor decreases with reduced spatial confinement, thus, an optimized core size should be considered to favor a high conversion efficiency.

The far-field emission pattern at FH frequency is engineered with a band-folding technique, which slightly increases the hole radii, with lattice period  $2a$ , by  $\Delta r_c$  and  $\Delta r_t$  in the core and

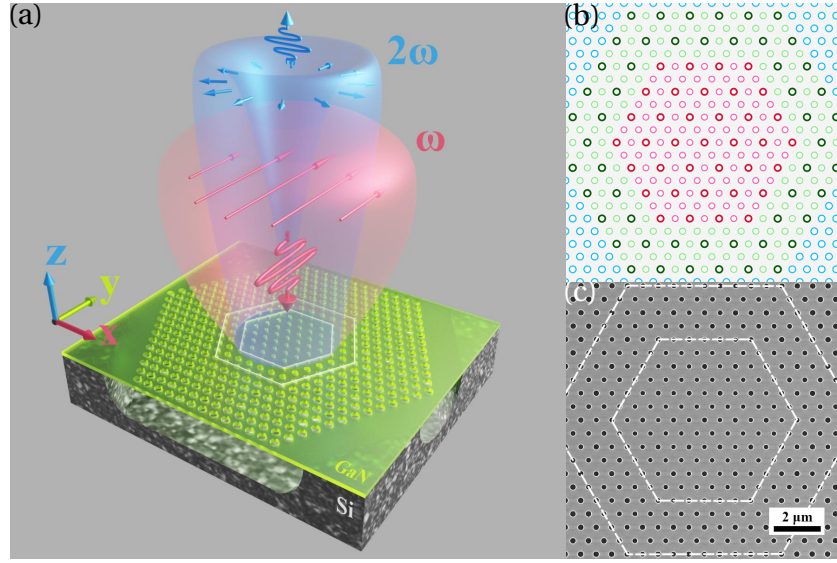


Figure 5.1: Design of doubly resonant cavity (reproduced from [167]). (a) Conceptual rendering of the SHG in a doubly resonant PhC slab cavity under linearly polarized beam excitation. The red and blue lobes represent the far-field intensities of the FH and SH modes, respectively, on the upper side of the slab. (b) Design of a doubly resonant cavity with parameters:  $a = 650$  nm,  $N_c = 6$ ,  $N_t = 4$ ,  $N_o = 14$ ,  $r_c = 130$  nm,  $r_t = 137$  nm,  $r_o = 150$  nm,  $r_{c,inj} = 140$  nm,  $r_{t,inj} = 147$  nm. The core, transition, and outer regions are in red, green, and blue, respectively. The injectors in the core and transition regions are emphasized with crimson and dark green. (c) SEM image of the cavity. The core and transition regions are outlined by white dashed hexagons.

transition regions, respectively. The holes with increased radii are referred to as injectors (or extractors), and their radii are  $r_{c,inj}$  and  $r_{t,inj}$ , respectively. This technique folds the  $k$ -vector components at the Brillouin zone edge to the  $\Gamma$ -point in the reciprocal space, which concentrates the FH emission to the normal direction of the PhC slab and thus increases the in-coupling efficiency of the pumping beam [80, 81], however at the expense of Q-factor at FH.

The resonant modes at FH and SH were designed at wavelengths around 1550 nm and 775 nm, respectively, for which the design parameters are:  $a = 650$  nm,  $N_c = 6$ ,  $N_t = 4$ ,  $N_o = 14$ ,  $r_c = 130$  nm,  $r_t = 137$  nm,  $r_o = 150$  nm,  $r_{c,inj} = 140$  nm,  $r_{t,inj} = 147$  nm,  $d = 214$  nm [Fig. 5.1 (b) (c)]. Theoretical simulations have been performed by three-dimensional finite-difference time-domain (3D-FDTD), in which the refractive indices used were  $n = 2.28$  at FH and  $n = 2.31$  at SH, respectively, to account for material dispersion. The FH mode is predominantly TE-polarized, while the SH mode is predominantly TM-polarized (with respect to the slab plane), and the two are coupled through the  $xxz$  and  $yyz$  components of the GaN second-order susceptibility tensor.

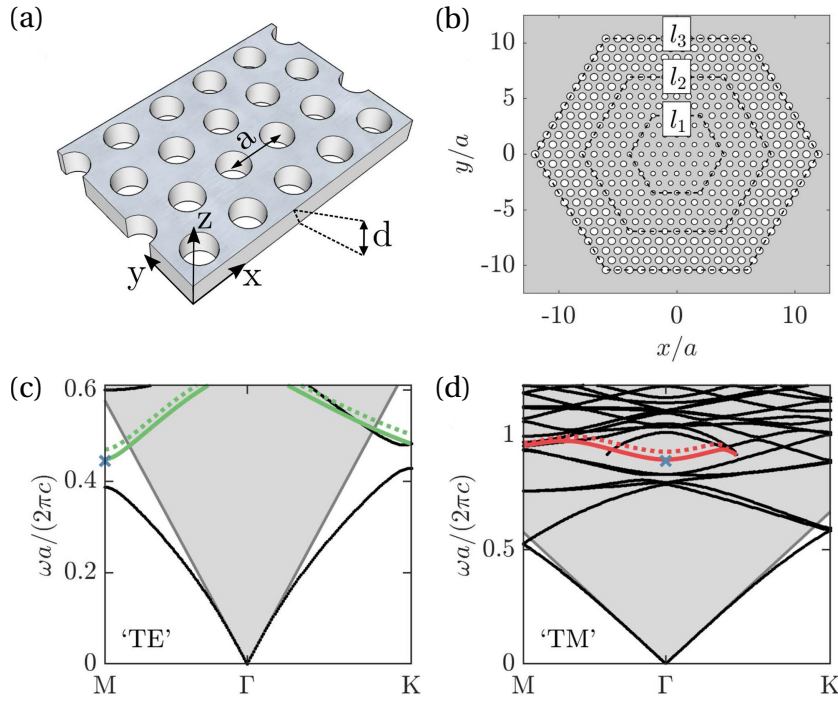


Figure 5.2: Design of the doubly resonant cavity (reproduced from [154]). (a) Schema of a PhC slab of thickness  $d$  with a hexagonal lattice with lattice constant  $a$  of air holes with radius  $r$ . (b) Schema of a heterostructure cavity composed of the core, transition, and outer regions. (c) Photonic bands for the quasi-TE modes for a regular PhC slab with parameters of the core region of the cavity ( $d = 0.28a$ ,  $r = 0.22a$ , and refractive index  $n = 2.32$ ). The light cone is shaded gray. (d) Photonic bands for the quasi-TM modes for the same geometry as in (c), and refractive index  $n = 2.38$ . The green and red lines in (c) and (d) highlight the bands from which the heterostructure mode is derived. The dashed green and red lines show the corresponding bands for  $r = 0.25a$ .

## 5.3 Cavity Modes

### 5.3.1 Cavity Modes by Simulation

The modes of the doubly resonant cavity are explored with finite-difference time-domain (FDTD) simulations (Ansys Lumerical) in both FH and SH frequency ranges. The structure of the cavity is as described in the previous section. The total thickness of GaN and AlN layers is set to 214 nm, and the refractive index is assumed to be  $n = 2.268$  for the whole slab. The mesh of the simulation volume is set with a maximum step of  $a/20$  in the  $x$ - and  $y$ -directions parallel to the slab and  $\lambda/32$  in the  $z$ -direction perpendicular to the slab. The total time (in FDTD) to simulate is around 5-25 ps, while for better resolution of fast fourier transform (FFT) spectra, a longer time (20 ps) is used. To excite all modes in the cavity, a random dipole cloud embedded in the slab is used. To simulate the experimental case where a laser beam is sent to the cavity from the top side, a linearly polarized Gaussian source is used. The simulated spectra, which are the FFT of the electric field  $E(t)$  for an array of sample points on the bisection plane of the slab, are presented in Fig. 5.3. Some examples of the modes are presented in Fig. 5.4 and

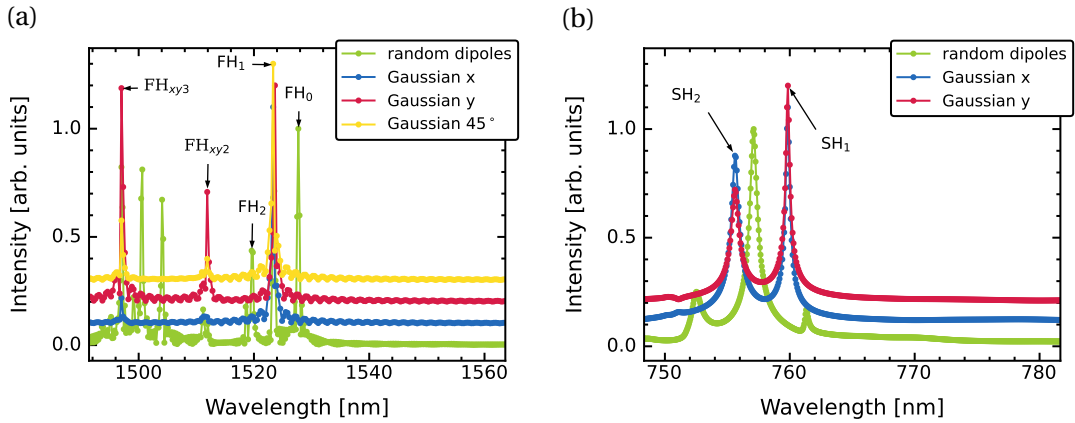


Figure 5.3: Simulated spectra of the cavity with different excitation sources. Random dipoles: a cloud of dipoles of random position, orientation, and phase. Gaussian  $x$ ,  $y$ ,  $45^\circ$ : the Gaussian source propagates from the top in the normal direction of the slab and is centered in the cavity, with  $x$ -,  $y$ -, and  $45^\circ$ -polarizations. (a) Simulated spectra in the FH range.  $FH_{xy2}$  and  $FH_{xy3}$  are the second and third modes excitable by the Gaussian beam. (b) Simulated spectra in the SH range. The redshift of the spectrum for random dipoles might be due to simulation errors.

Fig. 5.5 (see also appendix A.7 for high-order modes).

In the FH range, all modes are of quasi-TE type. The most fundamental mode, which is labeled  $FH_0$ , is only able to be excited by the dipole cloud source. This is because, in the far-field emission pattern, no lobe exists in the normal direction of the slab ( $0^\circ$ ), which means the coupling efficiency from the Gaussian beam to the cavity is very low. The second fundamental mode, which is labeled  $FH_1$ , is able to be excited by a Gaussian beam at any polarization. This is because it is a degenerate mode and can be decomposed as  $FH_{1x}$  and  $FH_{1y}$ , with  $x$ - and  $y$ -polarization in the far-field, respectively. For the far-field pattern, both  $FH_{1x}$  and  $FH_{1y}$  show intense lobes in the normal direction, and the side lobes are very weak because of the injectors/extractors. These two modes enable efficient coupling from the Gaussian source to the cavity, and they are the main resonant modes explored in experiments. The third fundamental mode, which is labeled  $FH_2$ , is again not able to be excited by the Gaussian source because the far-field pattern contains two lobes with  $x$ -polarization but an inversed phase. There are also  $FH_3$  and  $FH_4$  that is close to  $FH_2$  but not easy to excite for the same reason. The second and third Gaussian excitable modes are of much higher order.

In the SH range, all modes are of quasi-TM type. The most fundamental mode, which is labeled  $SH_1$ , can be excited by an  $x$ -polarized Gaussian source when the axis of the beam is moved off the center in the  $x$ -direction. This is because the far field of this mode is a radial polarized donut that contains  $x$ -polarized parts. It can also be excited by a  $y$ -polarized Gaussian source for the same reason. The degenerated second fundamental modes  $FH_{2x}$  and  $FH_{2y}$  can be excited by  $x$ - and  $y$ -polarized Gaussian sources, respectively. Notice that the two lobes in the far field are of the same polarization and phase. The separation in frequency (wavelength) between  $SH_1$  and  $SH_2$  is large so that they are easy to be distinguished in the experiments. The

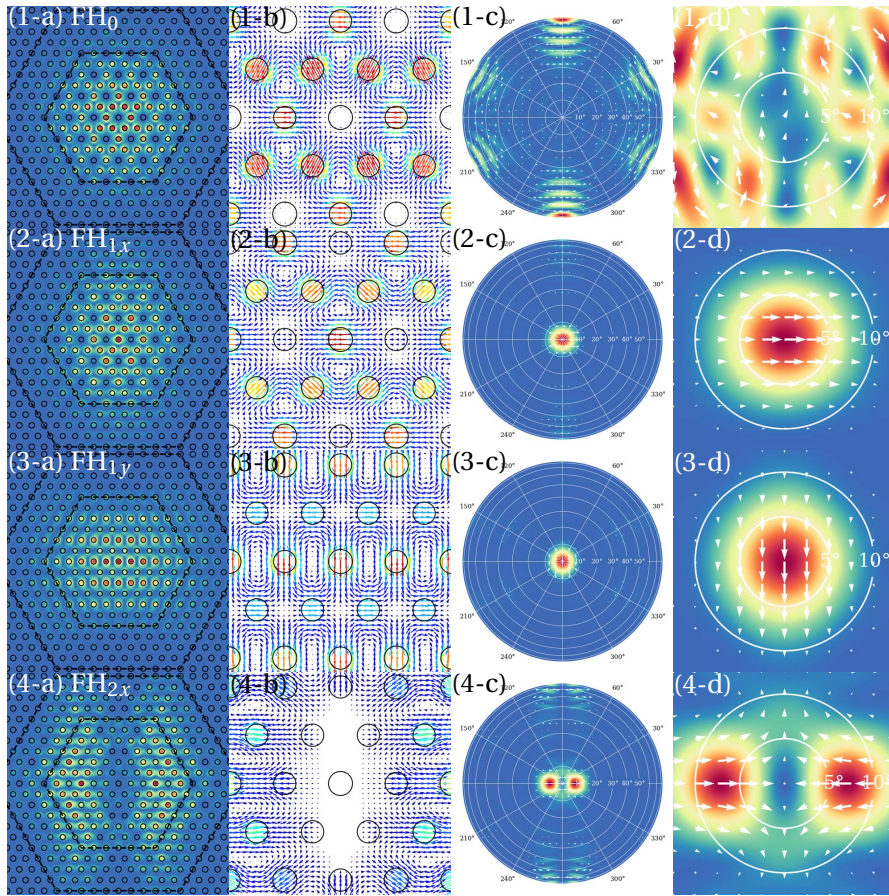


Figure 5.4: Fundamental modes at FH. The first column shows the near-field patterns. The color map shows the squared electric field,  $E_x^2 + E_y^2$ , at the center of the slab, and  $E_z = 0$ . The second column shows the vector map  $(E_x, E_y)$  of the electric field at the center of the slab. The color and the length of the arrows represent the norm of the electric field but are not necessarily normalized for all modes. The third column shows the full pattern of the far-field emission at the upper hemisphere of the slab. The color map and the white arrows show the intensity and the direction of the electric field. The center of the plots is at an emission angle of  $0^\circ$ , which is the normal direction of the slab, and the border is at an emission angle of  $90^\circ$ . The last column is a zoomed plot of the far-field emission, and the two white circles indicate the emission angle of  $5^\circ$  and  $10^\circ$ , respectively.

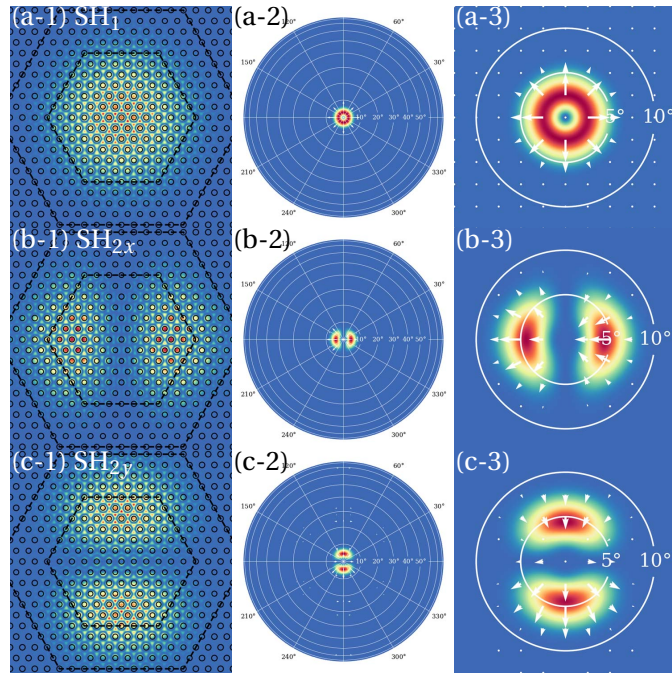


Figure 5.5: Fundamental modes at SH. The definition of the plots is the same as that for the plots for the FH range. The color map in the near-field patterns shows the squared electric field,  $E_z^2$ . The near-field vector maps are not shown because the modes are all TM, and the electric fields are perpendicular to the slab.

higher-order modes in the SH range are of less interest and are not discussed.

Note that, since the hexagonal lattice possesses 6-fold symmetry, the field patterns (both near- and far-field) exist equally when rotated by an integer number of  $60^\circ$  without changing the resonant frequency, and they are referred to as degenerate modes and are not necessarily orthogonal. However, if the symmetry of the cavity is destroyed, the degenerate modes can be separated in frequency, and this will be discussed later (see section 5.5).

### 5.3.2 Cavity Modes in Experiments

The experimental spectra generally differ from the simulated spectra because the intensity of the simulation spectra is the FFT amplitude, while the intensity of the experimental spectra is the intensity of the emission power collected by the microscope objective, where out-coupling efficiency should also be taken into account. The out-coupling efficiency is one-half (because the cavity emits to both sides of the slab) of the portion of the far-field emission pattern intensity inside the numerical aperture (NA) of the microscope objective. For  $FH_1$  and  $SH_1$  modes and a 20x objective with  $NA = 0.4$  ( $\theta \approx 23.6^\circ$ ), the out-coupling efficiency is close to 50%, which means almost all the emission in the upper hemisphere is collected. Obviously, it is not the case for the modes with intense side lobes in the far field.

The experimental spectra are sensitive to the positioning of the cavity with respect to the

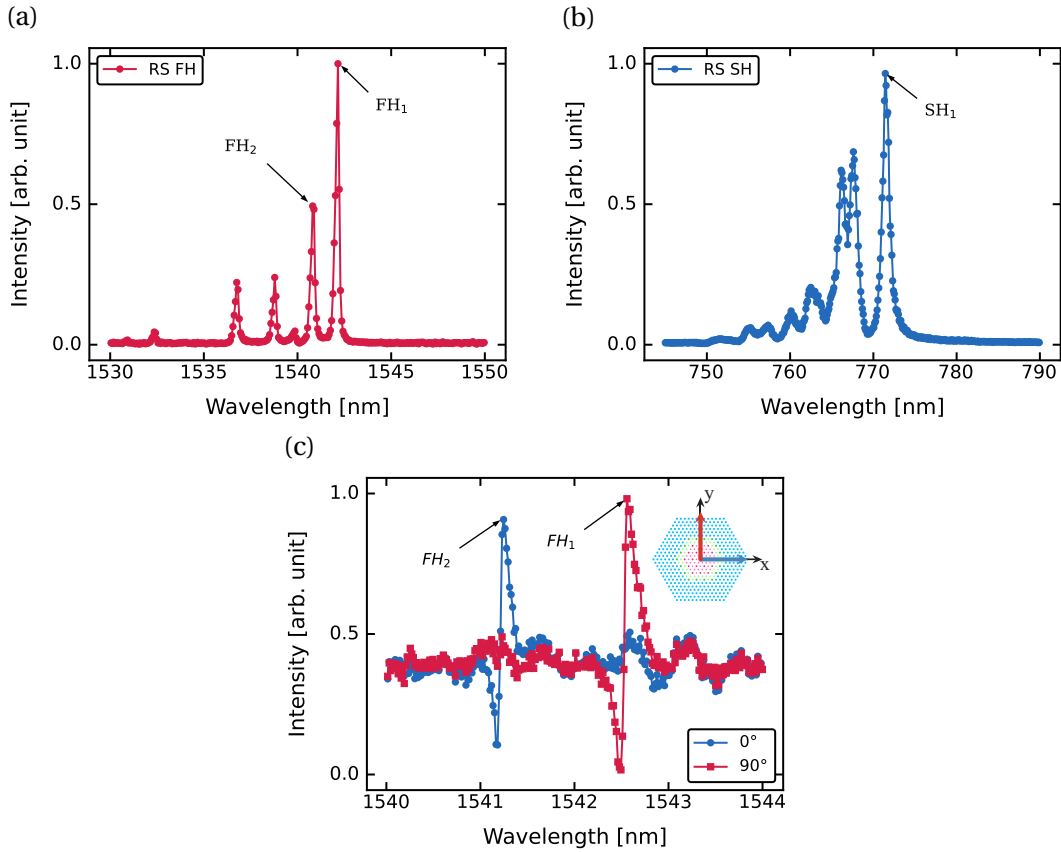


Figure 5.6: Examples of experimental spectra. (a) Normalized resonant scattering spectrum at FH range. (b) Normalized resonant scattering spectrum at SH range. (a) and (b) are taken by a spectrograph, so the line widths of the peaks are exaggerated. (c) FH mode polarization.

laser beam because the in- and out-coupling efficiencies are dependent on the overlap of the incident beam and the far-field patterns of the modes. The experimental spectra are usually optimized for the intensity of a certain peak by changing the relative position of the beam and the cavity. Because of practical difficulties, the orientation of the cavity is not changed, which means the cavity slab is always perpendicular to the incident laser beam, which may lower the coupling to certain modes like  $SH_1$ .

Examples of the experimental spectra in the FH and SH ranges are presented [Fig. 5.6 (a)-(b)]. The spectra were measured with the resonant scattering technique, which means the polarization of the incident beam is at  $45^\circ$ .

The spectra were taken while maximizing the intensity of the first peak (count from right to left for a wavelength  $x$ -axis). The first and the second peaks on the FH spectrum are easily excited by the  $45^\circ$ -polarized Gaussian beam, which means their far-field emission is intense in the normal direction, and the phase of the lobes matches the Gaussian beam, which are the features of the  $FH_{1x}$  and  $FH_{1y}$  peaks. The separation of these two peaks is around 0.5-2 nm, which is much smaller than the distance between the first and second excitable modes in



simulation (about 12 nm).

The polarizations of these two peaks are studied by a measurement modified from the resonant scattering measurement, in which the polarization of the incident beam is modified by a  $\lambda/2$  wave plate after the polarizer P1, and the analyzer P2 is removed. This configuration enables excitation of the cavity with  $x$ - ( $0^\circ$ ) and  $y$ - ( $90^\circ$ ) polarization but without the filtering of the excited signal. As a result, the signal collected by the power detector is dominated by the direct-reflected light rather than the light emitted from the cavity. Nevertheless, it is still possible to find the small peaks buried in a large background signal at the previous positions [Fig. 5.6 (c)]. The spectra show that the first peak is only excited by the  $y$ -polarized beam, and the second peak is only excited by the  $x$ -polarized beam. Then it can be concluded that the first and second peaks correspond to the  $FH_{1y}$  and  $FH_{1x}$  modes, respectively. The same conclusion can be given in the SHG experiments. The separation of the two modes could be due to symmetry breaking of the cavity (see section 5.5).

In the FH spectrum, a small peak could sometimes emerge on the right-hand side of the first peak described above. This peak has an intensity much smaller than the first and second peaks and is believed to be the  $FH_0$  mode.

The SH spectrum is similar to the simulated one and is much easier to understand. As revealed by the simulation, the mode  $SH_1$  is better excited when the Gaussian beam is shifted off the center of the cavity, and since the far field is a radially polarized donut, the polarization should match the shift direction. Although the mode is excitable, and thus the overlap between the Gaussian beam and the donut is nonzero, the numerical analysis of the overlap factor or the coupling efficiency could be rather complex. The experimental measurement of the coupling efficiencies is presented in section 6.3.4. The shape of the far-field emission pattern of the  $SH_1$  mode is also measured in the SHG experiment in section 6.3.5.

### 5.3.3 Redshift of Cavity Modes

During the measurements of the cavities over a long time, redshifts of both FH and SH peaks are observed [Fig. 5.7]. The spectra were measured on the same cavity at 5 points of time, not necessarily equally spaced, during 4 months. The separation between the two peaks in FH spectra remains unchanged. The average amounts of redshift with respect to the first spectrum are 0.416, 1.231, 1.512, and 2.324 nm for the FH range and 0.445, 1.077, 1.525, and 2.033 nm for the SH range, which means the detuning remains almost the same. It is also observed that the redshift is accelerated by strong excitation laser beams at FH or SH in a short period of time.

The reason for the redshift, after careful calibration of the wavelength reference, i.e., the OSA, could be strain relaxation of the suspended slab and the adsorption of gas molecules (e.g.,  $O_2$ ,  $H_2O$ ). Since there is a residual tensile strain in the slab inherited from the GaN/AlN thin film growth, and the cavity slab is suspended in air, the strain could be slowly released by changing

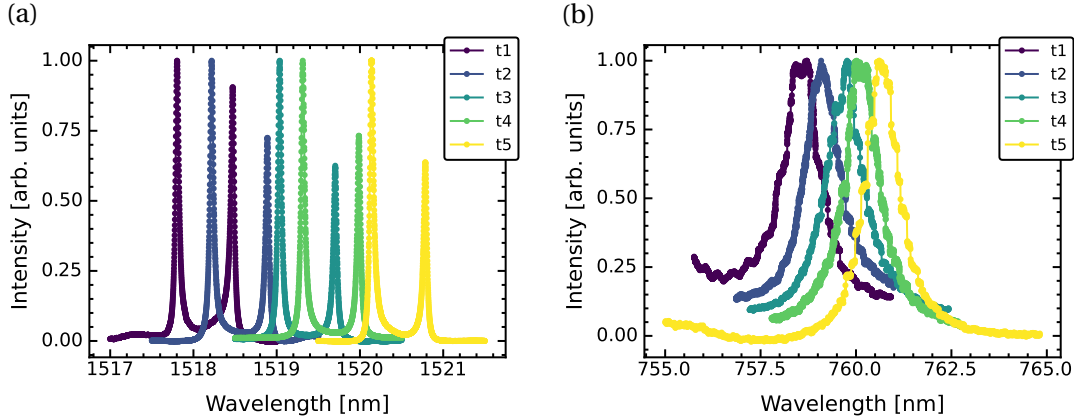


Figure 5.7: Redshift of modes in one cavity during 4 months.  $t_1$ - $t_5$  are points of time not necessarily equally spaced. (a) Redshift of  $FH_{1x}$  and  $FH_{1y}$ . In each spectrum, the separation between the two peaks remains the same. The average amounts of redshift with respect to  $t_1$  are 0.416, 1.231, 1.512, and 2.324 nm. (b) Redshift of  $SH_1$ . The amounts of redshift with respect to  $t_1$  are 0.445, 1.077, 1.525, and 2.033 nm.

the internal stress and the external geometry of the cavity. The expansion of the geometry results in a redshift, and the change in the inner stress could impact the refractive index of the slab and cause a peak shift.

Strain relaxation is confirmed by Raman spectroscopy (see the section below), while gas adsorption is not confirmed. Passivation tests were made by preparing the sample in an oxygen-saturated state with thermal oxidation but were not successful because the high temperature during the thermal oxidation deformed the cavity and destroyed the resonant modes. However, since the tests were quick tryouts without careful tuning of thermal oxidation parameters, the validity of the passivation is still to be explored. Alternatively, to prevent the potential issue of gas adsorption, the sample is stored and measured in  $N_2$  atmosphere (see section 5.3.5).

### 5.3.4 Raman Stress Analysis

The residual stress in the GaN layer is measured by Raman spectroscopy (Renishaw inVia). A 532 nm laser is used to excite the sample, and the beam spot size on the sample surface is about a few microns. A shorter laser wavelength is preferred because of higher absorption in GaN, resulting in larger GaN-featured phonon peaks. Low laser power is applied to ensure a nonsignificant heating effect. A 3000 gr/mm grating is used in the monochromator for the best available Raman shift resolution of  $0.8 \text{ cm}^{-1}$ .

The relation between the residual stress  $\sigma$  and the Raman shift  $\nu$  of the  $E_2^{high}$  phonon mode can be expressed as [168]:

$$\sigma = \frac{|\nu - \nu_0|}{\alpha}, \quad (5.1)$$

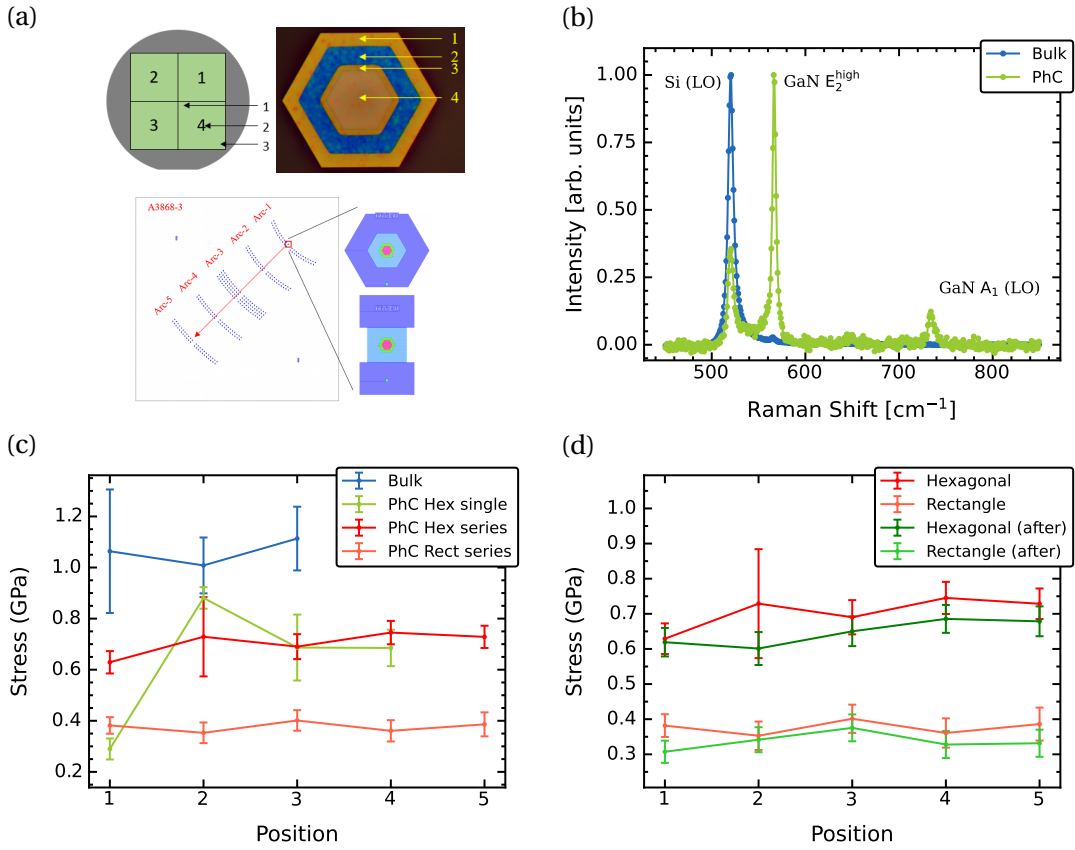


Figure 5.8: Stress measurement by Raman spectroscopy. (a) Positions measured with Raman spectroscopy on GaN/AlN/Si wafer, PhC cavity with hexagonal padding, and PhCs on 5 arcs with hexagonal and rectangular paddings. (b) Raman spectrum on bulk GaN sample and on PhC. (c) Measured stress on positions identified in (a). (d) Stress changes after one week for PhCs on 5 arcs with hexagonal and rectangular paddings.

where  $\nu_0 = 567.6 \text{ cm}^{-1}$  [169] is the unperturbed (relaxed) Raman shift of the  $E_2^{\text{high}}$  phonon mode of GaN,  $\alpha = 2.43 \text{ cm}^{-1}$  [170] is the biaxial pressure coefficient of GaN.

The measurement results are shown in Fig. 5.8. The Raman spectra were measured at different locations (i.e., different GaN film thicknesses) on a wafer, a doubly resonant cavity with hexagonal padding fabricated with the HSQ technique, and at the center of a series of cavities with hexagonal and rectangle padding at different locations on the sample (i.e., different slab thickness) [Fig. 5.8 (a)]. The Raman spectra were different at different locations [Fig. 5.8 (b)]: on the suspended GaN part, as in the case of locations 1, 3, and 4 on the cavity, the  $E_2^{\text{high}}$  peak of GaN is intense compared to the neighboring LO peak of Si; on the bulk (non-suspended) GaN film on Si substrate, as in the case of locations 1-3 on the wafer and location 2 on the cavity, the  $E_2^{\text{high}}$  peak of GaN is very weak compared to the LO peak of Si but is still visible. As for the stress [Fig. 5.8 (c)], the GaN bulk film on the wafer exhibits the highest inner stress of around 1.1 GPa. Location 1 on the cavity margin exhibits the lowest inner stress of around 0.3 GPa, because this location is close to the suspended border of the cavity. Location 2 on

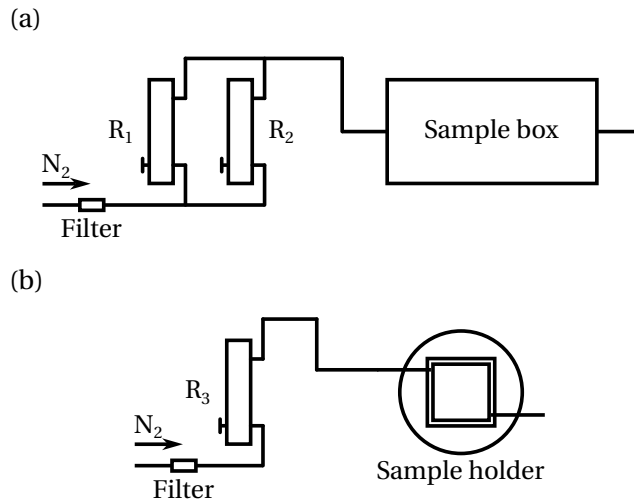


Figure 5.9: (a) Schema of the 2 L sample box with nitrogen protection for long period storage.  $R_1$  and  $R_2$  are flow regulators of 3-30 L/min and 10-100 mL/min for quick flush and small continuous flow, respectively. (b) Schema of the sample holder with nitrogen protection for measurement.  $R_3$  is a flow regulator of 10-100 mL/min for small continuous flow.

the cavity exhibits the highest stress in the cavity of around 0.9 GPa but is smaller than that on the wafer because this location is the same as the bulk (the blue hexagonal ring area is where the GaN slab has contact with the underneath Si substrate) except its width is very thin. Locations 3 and 4 on the cavity exhibit a lower stress of around 0.7 GPa because it is the PhC area full of holes and suspended in the air. The series of the center of cavities with hexagonal and rectangular paddings show no significant dependence of the stress on the slab thickness, while the stress on the center of cavities with rectangular padding is significantly smaller than the cavities with hexagonal padding. This could be because the PhC is more relaxed with rectangular padding since only two sides are constrained, and the other two sides are free to move and relax. The rectangular padding was originally introduced to create anisotropic strain in the cavity.

The same series of cavities were also measured after 1 week [Fig. 5.8 (d)], and the stress was found to be lowered by about 0.05 GPa. The lowering of inner stress could be evidence of self-relaxation during storage, which explains the continuous redshift of resonance peaks in the resonant scattering measurement. The light-induced enhancement of relaxation, observed in the resonant scattering measurement, could also play a role in the process.

### 5.3.5 Sample Protection with Nitrogen

Nitrogen systems are prepared for the AlN/GaN/Si substrates and devices for long-period protection during sample storage and for short-period protection during measurements [Fig. 5.9 (a)-(b)]. The adsorption of oxygen [104], water, etc., on the surface of the AlN/GaN/Si devices could potentially change their optical characteristics and degrade their performances.

## 5.4 Influence of Cavity Parameters and Lithographic Tuning

---

An intuitive way to avoid this is to put the samples in a vacuum or nitrogen atmosphere, while the latter is adopted for practical reasons. The sample box has a volume of 2 L and is connected to two flow regulators in parallel. One of the regulators provides a large flow of 3-30 L/min that is enabled to flush the box after opening, and the other one provides a small flow of 10-100 mL/min that is always enabled. The sample holder has a much smaller volume (about  $20 \times 20 \text{ mm}^2$  area with about 2 mm space between the sample and the glass lid) and is connected to a flow regulator of range 10-100 mL/min (see section 5.5).

### 5.4 Influence of Cavity Parameters and Lithographic Tuning

Although the numerical simulations took into account the GaN/AlN material dispersion, the geometrical parameters of the cavities are necessarily tuned and scanned on the fabricated chip, and typically there are more than 1000 cavities on a chip. The first thing to do is to find where exactly the resonances are located, i.e., their central wavelengths, and how good the cavities are, i.e., their Q-factors. Then, the second thing to do is to characterize how well the doubly resonant condition is matched, i.e., how well the FH and SH resonances match the 2-times frequency relation to enhance both the pump and the generated light.

The locations of the cavity modes are extracted by resonant scattering (see section 4.3). A convenient technique is to use a broadband source to excite all excitable modes simultaneously and then capture the spectrum with a spectrograph. The broadband source is typically a supercontinuum source (pulsed in the time domain), a superluminescent diode (broad Gaussian spectrum), or an incandescent light bulb (incoherent light, low coupling to fiber). A supercontinuum source is generally used. The spectrograph consists of a monochromator to generate the spectrum and a one-dimensional (1D) CCD array detector to capture the spectrum. The wavelength resolution of spectrographs is not as high as the scanning OSAs. Still, the advantage is the high speed of acquisition, which enables real-time spectra and is very helpful for optimizing the light coupling to the cavity.

After taking a spectrum by the combination of broadband source and spectrograph, a fine spectrum scan is followed at a smaller wavelength range around the desired cavity modes using the combination of a tunable laser and a photodetector. Conventionally, the fine scan is carried out in a point-by-point mode which gives a good wavelength accuracy but is very slow. During this work, a continuous sweep mode was developed. With good electrical synchronization and active wavelength calibration by the scanning OSA, the acquisition speed is approaching the broadband source and spectrograph combination while maintaining high wavelength accuracy.

To take a spectrum in the FH range (around 1550 nm), the cavity is excited by a linearly polarized Gaussian beam with the electric field at  $45^\circ$  from the  $x$ -axis of the cavity at normal incidence. On the main setup schema, the optical path for FH resonant scattering is C1-P1-BS5-BS4-Obj-Sample-Obj-BS4-BS5-BS6-P2-L15-F1-D1.

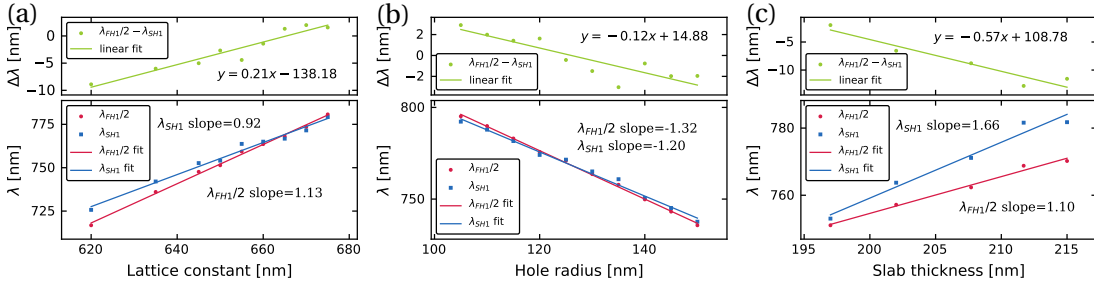


Figure 5.10: Lithographic tuning of doubly resonant cavities. (a)-(c) Dependence of  $\lambda_{FH}/2$ ,  $\lambda_{SH}$ , and  $\Delta\lambda$  on lattice constant  $a$ , hole radius  $r$ , and slab thickness  $d$ , respectively.

	$k_{a-\lambda_{FH}/2}$	$k_{r-\lambda_{FH}/2}$	$k_{d-\lambda_{FH}/2}$	$k_{a-\lambda_{SH}}$	$k_{r-\lambda_{SH}}$	$k_{d-\lambda_{SH}}$
Simulation	1.20	-1.54	0.83	1.08	-1.42	1.20
Experiment	1.13	-1.32	1.10	0.92	-1.20	1.66

	$k_{a-\Delta\lambda}$	$k_{r-\Delta\lambda}$	$k_{d-\Delta\lambda}$
Simulation	0.12	-0.11	-0.37
Experiment	0.21	-0.12	-0.57

Table 5.1: Parametric dependencies of FH and SH resonances.

In the SH range (around 775 nm), the cavity is excited with a similar configuration as for FH. On the main setup schema, the optical path for SH resonant scattering is C2-P3-BS7-BS4-Obj-Sample-Obj-BS4-BS7-BS8-P4-L14-F3-F2-D2. The quasi-TM mode at SH could be excited by a linear polarized Gaussian beam at normal incidence because of the nonzero overlap between the far-field donut pattern and the Gaussian shape at a nonconcentric configuration.

The matching of the doubly resonant condition is characterized by the detuning  $\Delta\lambda$  defined by:

$$\Delta\lambda = \lambda_{FH}/2 - \lambda_{SH}, \quad (5.2)$$

where  $\lambda_{FH}$  and  $\lambda_{SH}$  are the resonant wavelengths at FH and SH, respectively.

Since the dependencies of FH and SH resonant frequencies on the PhC parameters, such as the lattice constant  $a$ , the hole radius  $r$ , and the slab thickness  $d$ , are different, lithographic tuning of these parameters will help to achieve the doubly resonant condition [154]. In practice, the lattice constant  $a$ , the hole radii  $r$ , and the slab thickness  $d$  are scanned around the targeted values to verify the predicted dependencies and also to compensate for fabrication imperfections and uncertainty of the refractive index in the experiment compared with the values used in the simulation. The dependencies of FH and SH resonant wavelengths on these parameters are analyzed, and the results are in agreement with the FDTD simulations [Fig. 5.10, Table 5.1].

## 5.5 Influence of Anisotropy and Active Tuning

Although lithographic tuning is possible, the parameters of individual cavities are fixed after fabrication, and a large parameter space is required for the tuning, which results in a large number of cavities to fabricate and measure. If the parameters can be tuned actively, i.e., tuned repetitively and reversely by artificial controls during the measurements, then it could bring a great advantage.

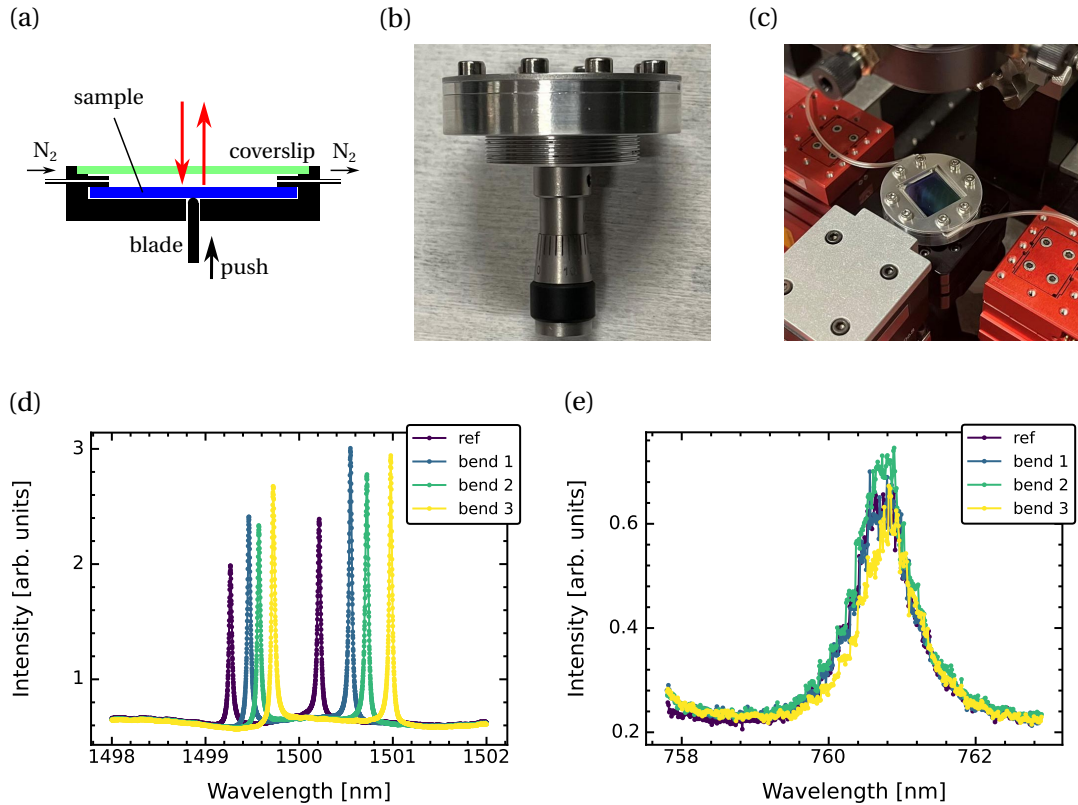


Figure 5.11: Active tuning by chip bending. (a) Schema of the stage for chip bending. The stage is also an enclosed chamber for N<sub>2</sub> protection of the sample. (b)-(c) Side view and top view of the stage. (d) Active tuning for FH peaks. (e) Active tuning for SH peaks.

The possible parameters to tune could be the geometric parameters, e.g., lattice constant  $a$  and slab thickness  $d$ , and the refractive indices, e.g., birefringence and refractive index change induced by stress or temperature change. The piezoelectric effect of GaN/AlN could be applied to change the geometric parameters. However, the piezoelectric effect is the strongest in the  $c$ -direction (i.e., perpendicular to the slab) of wurtzite GaN and much weaker in the  $a$ - and  $m$ -directions (i.e., in the plane of the slab). The Pockels effect [171, 172] could be applied to change the birefringence and, thus, the refractive indices, while the electric potential needed could be too large. The piezoelectric and Pockels effects require the fabrication of microelectrodes around the cavity. Temperature tuning could be applied to change the refractive indices and the geometry simultaneously, and the induced effect could be complex.

## Chapter 5. Doubly Resonant PhC Cavities

---

Temperature tuning was tested<sup>1</sup> for a tuning range of 80 K-400 K, but no effective tuning was observed.

Inspired by the split of the  $FH_{1x}$  and  $FH_{1y}$ , a simple stretch of the hexagonal lattice could change the strain and the geometry at the same time. An intuitive way to do that is to bend the chip mechanically, and this simple technique was tested and proven effective for tuning.

To bend the chip, a dedicated sample holder was designed and fabricated [Fig. 5.11 (a)-(c)]. The sample holder provides a framework that holds the square chip on the two sides from the top and a moveable blade to push the chip from the bottom up. The distance between the two contacting lines on the top side is 16 mm. Depending on the chip installation direction, the holder can bend a square chip of size 20 mm×20 mm in the  $x$ - or  $y$ -direction. The blade has a rounded surface of contact with the chip, so the pressure at the contact line can be mitigated. The blade is actuated by a micrometer screw, which is upgradable to piezoelectric actuators for higher precision. The bending is reversible because of the elasticity of the Si chip itself. The travel distance of the blade to break a Si chip of a thickness about 275  $\mu\text{m}$  was tested to be around 160  $\mu\text{m}$ , from which a travel distance under 100  $\mu\text{m}$  was generally considered safe for the chip. The holder is also designed to provide gas protection for the sample during measurements. A coverslip is put on the top side of the holder to form a chamber of a thickness around 2 mm, and thin pipes are installed on the sidewalls to provide the  $\text{N}_2$  flow (see section 5.3.5).

The tuning effects of the peaks are presented in Fig. 5.11 (c)-(d). For the 3 bending tests with blade travel distances within 100  $\mu\text{m}$ , the first peak in the FH range is redshifted by 0.34, 0.51, and 0.76 nm, the second peak in the FH range is redshifted by 0.20, 0.30, and 0.46 nm, and the first peak in the SH range is redshifted by 0.04, 0.01, and 0.11 nm. At the FH range, the redshift of the first peak is much larger than the second peak, which means the sensitivity of the two peaks is different for the induced anisotropy. This result also agrees with the assumption that the separation of the two degenerate modes is induced by the intrinsic anisotropy in the cavity. At the SH range, the smaller shifts suggest that the position of the TM mode is not sensitive to the in-plane anisotropy. Notice that the wavelength accuracy at SH is lower than FH, and the pump-enhanced relaxation could also play a role. Nevertheless, the tuning effect is recognizable and is shown to be more than 0.5 nm, which is comparable to one-half of the FWHM of the  $SH_1$  peak.

---

<sup>1</sup>in Dipartimento di Fisica, Università di Pavia, Italy



# 6 Nonlinear Frequency Conversion

## 6.1 Overview

Nonlinear frequency conversion is an essential aspect of nonlinear optics and has applications in various fields. SHG has already been demonstrated in resonant structures such as micro-ring resonators [142, 143, 173, 174] and others [175]. SPDC has already been demonstrated in micro-ring resonators with photon-pair generation at MHz rates [176].

In doubly resonant cavities, both up- and down-conversion benefit simultaneously from the enhancement of the pump through the amplification of the electric field strength and the enhancement of the signal through the Purcell effect [72, 73] (see appendix A.1 for Purcell effect). The increased conversion efficiency allows nonlinear photonic devices to work with low-power and continuous-wave light sources, which is promising for low-power integrated photonic devices. The small footprint of the cavity mode also adds value to Purcell's factor and the mass integration of on-chip photonic devices.

This chapter investigates up- and down-conversion in doubly resonant cavities, especially SHG and SPDC. Since SPDC is a pure quantum process [177–180], the mechanics are not exactly symmetric as SHG, which results in more difficulties measuring the signal. The main results of the SHG part in this chapter were published in [167].

## 6.2 Nonlinear Frequency Conversion in Doubly Resonant Cavities

Nonlinear frequency conversion processes in doubly resonant PhC slab cavities can be described by generalizing the dynamic equations of the coupled-mode theory [136, 137] [Fig. 6.1] (see section 2.1.4 for coupled-mode theory). The coupling ports for incoming and outgoing waves are on the top, bottom, and lateral sides of the slab. The top and bottom ports are symmetric, provided that the slab is symmetric about the bisection plane (the side walls of the PhC holes are vertical, etc.). The coupling through the lateral port is generally very small, provided that there are enough layers of holes in the outer region of the cavity and in the absence of side-coupling waveguides. Inside the cavity, the FH mode and the SH mode are coupled through SHG and PDC, which can be considered as a virtual port.

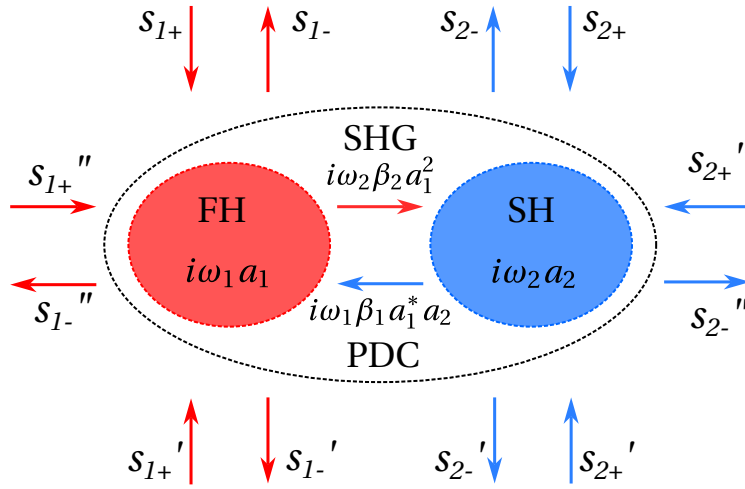


Figure 6.1: Schematic representation of the coupled-mode model for second-order nonlinear frequency conversion in the doubly resonant PhC slab cavity.

The dynamic equations of complex amplitudes in the doubly resonant PhC slab cavity with  $\chi^{(2)}$  processes (i.e., SHG and PDC) when pumped from the top side of the slab take the form:

$$\frac{da_1}{dt} = i\omega_1 a_1 - i\omega_1 \beta_1 a_1^* a_2 - \frac{1}{\tau_{10}} a_1 - \frac{1}{\tau_{1e}} a_1 + \kappa_1 s_{1+}, \quad (6.1)$$

$$\frac{da_2}{dt} = i\omega_2 a_2 - i\omega_2 \beta_2 a_1^2 - \frac{1}{\tau_{20}} a_2 - \frac{1}{\tau_{2e}} a_2 + \kappa_2 s_{2+}, \quad (6.2)$$

where the subscripts 1 and 2 indicate quantities at FH and SH ranges, respectively. For simplicity, only the degenerate case is considered, in which the frequencies are related as  $\omega_2 = 2\omega_1$ . The terms  $a_1/\tau_{10}$  and  $a_2/\tau_{20}$  represent the strength of material absorption. The terms  $a_1/\tau_{1e}$  and  $a_2/\tau_{2e}$  represent the strength of outgoing waves. The terms  $i\omega_1 \beta_1 a_1^* a_2$  and  $i\omega_2 \beta_2 a_1^2$  represent the strength of PDC and SHG, respectively.  $\beta_1$  and  $\beta_2$  are nonlinear

## 6.2 Nonlinear Frequency Conversion in Doubly Resonant Cavities

overlap factors, and their expressions can be deduced by perturbation theory as:

$$\beta_1 = \frac{1}{4} \frac{\lim_{V \rightarrow \infty} \int_V d\mathbf{r} \epsilon_0 \sum_{ijk} \chi_{ijk}^{(2)} (E_{1i}^* E_{2j} E_{1k}^* + E_{1i}^* E_{1j}^* E_{2k})}{\left( \lim_{V \rightarrow \infty} \int_V d\mathbf{r} \epsilon_0 \epsilon_1(\mathbf{r}) |\mathbf{E}_1(\mathbf{r})|^2 \right) \left( \lim_{V \rightarrow \infty} \int_V d\mathbf{r} \epsilon_0 \epsilon_2(\mathbf{r}) |\mathbf{E}_2(\mathbf{r})|^2 \right)^{1/2}}, \quad (6.3)$$

$$\beta_2 = \frac{1}{4} \frac{\lim_{V \rightarrow \infty} \int_V d\mathbf{r} \epsilon_0 \sum_{ijk} \chi_{ijk}^{(2)} E_{2i}^* E_{1j} E_{1k}}{\left( \lim_{V \rightarrow \infty} \int_V d\mathbf{r} \epsilon_0 \epsilon_1(\mathbf{r}) |\mathbf{E}_1(\mathbf{r})|^2 \right) \left( \lim_{V \rightarrow \infty} \int_V d\mathbf{r} \epsilon_0 \epsilon_2(\mathbf{r}) |\mathbf{E}_2(\mathbf{r})|^2 \right)^{1/2}}. \quad (6.4)$$

Due to energy conservation, i.e.,  $\frac{d}{dt} (|a_1|^2 + |a_2|^2) = 0$ ,  $\beta_1$  and  $\beta_2$  are related as  $\omega_1 \beta_1 = \omega_2 \beta_2^*$ .

Notice that since the cavity modes are standing waves, the phase-matching condition for SHG and PDC is not required. In the limit of a very large cavity, the nonlinear overlap factors recover the phase-matching condition [136].

Unlike in bulk materials or in nonresonant waveguides, the maximum conversion efficiency in doubly resonant cavities is achieved at a critical pump power [Fig. 6.2] [136, 137, 181]. This phenomenon is due to the fact that, in coupled-mode systems, to achieve a high transmission from an input port to an output port, the coupling rates to the two ports must be matched in order to minimize the back-reflected wave. In the present case, the coupling to the input port is characterized by the quality factor of the pump port, and the coupling rate to the output "port" (i.e., the nonlinear conversion to another frequency) is characterized by the nonlinear overlap factors (i.e.,  $\beta_1$  and  $\beta_2$ ).

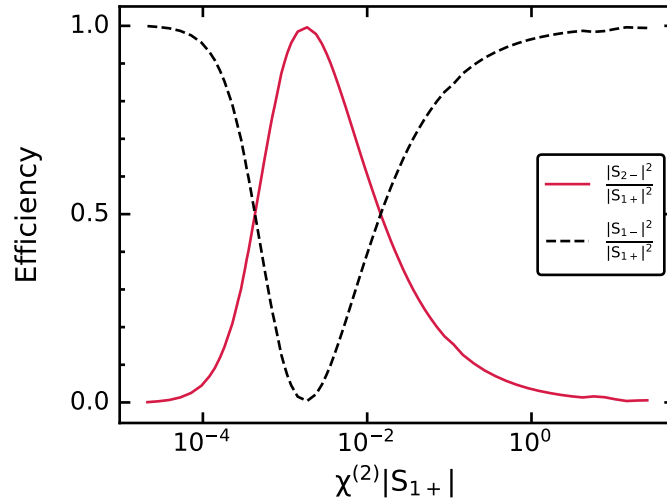


Figure 6.2: SHG efficiency versus pump strength (adapted from [136]). The red line represents the SHG efficiency, the black line represents the reflection efficiency of the pump. The calculation assumes an undepleted regime without absorption.

## Chapter 6. Nonlinear Frequency Conversion

In the case of SHG, the maximum conversion efficiency, the maximum normalized conversion efficiency, and the critical pump power can be respectively expressed as [137]:

$$\eta_{\max} = \frac{P_{2,\text{out}}}{P_{1,\text{in}}} = \left(1 - \frac{Q_1}{Q_{1,\text{rad}}}\right) \left(1 - \frac{Q_2}{Q_{2,\text{rad}}}\right), \quad (6.5)$$

$$\eta_{\text{norm,max}} = \frac{P_{2,\text{out}}}{(P_{1,\text{in}})^2} = \frac{8}{\omega_1} \left(\frac{\chi_{\text{eff}}^{(2)}}{\sqrt{\varepsilon_0 \lambda_1^3}}\right)^2 Q_1^2 Q_2 |\bar{\beta}|^2 \left(1 - \frac{Q_1}{Q_{1,\text{rad}}}\right)^2 \left(1 - \frac{Q_2}{Q_{2,\text{rad}}}\right), \quad (6.6)$$

$$P_{1,\text{crit}} = \frac{2\omega_1 \varepsilon_0 \lambda_1^3}{(\chi_{\text{eff}}^{(2)})^2 |\bar{\beta}|^2 Q_1^2 Q_2} \left(1 - \frac{Q_1}{Q_{1,\text{rad}}}\right)^{-1}, \quad (6.7)$$

where the subscripts 1 and 2 indicate quantities at FH and SH ranges, respectively,  $\chi_{\text{eff}}^{(2)}$  is the effective nonlinear susceptibility and  $Q = \left(\frac{1}{Q_{\text{rad}}} + \frac{1}{Q_c}\right)^{-1}$  is the quality factor incorporating the coupling to radiative decay (loss) channels ( $Q_{\text{rad}}$ ) and to an input/output channel ( $Q_c$ ). The nonlinear overlap factor  $\bar{\beta}$  can be expressed as:

$$\bar{\beta} = \frac{\int_V d\mathbf{r} \bar{\varepsilon}(\mathbf{r}) E_2^* E_1^2}{\left(\int_V d\mathbf{r} \varepsilon_1(\mathbf{r}) |\mathbf{E}_1|^2\right) \left(\int_V d\mathbf{r} \varepsilon_2(\mathbf{r}) |\mathbf{E}_2|^2\right)^{1/2}} \lambda_1^{3/2}, \quad (6.8)$$

where  $\bar{\varepsilon}(\mathbf{r}) = 1$  inside the material and zero elsewhere. This expression is a simplified dimensionless version of the nonlinear overlap factor for SHG as in Eq. (6.4), and it only takes into account the spatial overlap of the near-field patterns of FH and SH modes and same-polarization interactions.

In Eq. (6.5), the conversion efficiency is maximized to one at the critical pump power when  $Q/Q_{\text{rad}} \approx 0$ ,  $Q_{\text{rad}} \gg Q_c$ , which corresponds to the case when the coupling strength to the pump/detection channel is much larger than to the radiative decay channels. In Eq. (6.6), the normalized conversion efficiency is proportional to  $Q_1^2 Q_2 |\bar{\beta}|^2$ . In Eq. (6.7), the critical power is inversely proportional to the same term of  $Q_1^2 Q_2 |\bar{\beta}|^2$ , which suggests that the critical power can be engineered to a desired value by setting the value of  $Q_1^2 Q_2 |\bar{\beta}|^2$ . In the low-power regime, the quality factors and the nonlinear overlap factors are desired to be high enough to achieve a high normalized conversion efficiency at a low value of the critical pump power.

## 6.3 Frequency Up-Conversion

### 6.3.1 Frequency Up-Conversion in Doubly Resonant Cavity

According to Eq. (2.46) and Eq. (2.54) (see also Fig. 2.10), in the case of SFG, when assuming full permutation symmetry and Kleinman's symmetry (see section 2.2.1), the nonlinear polarization components can be explicitly expressed as:

$$P_x(\omega_3) = 2\varepsilon_0 \left[ \chi_{xzxx}^{(2)} E_z(\omega_1) E_x(\omega_2) + \chi_{xxz}^{(2)} E_x(\omega_1) E_z(\omega_2) \right], \quad (6.9)$$

$$P_y(\omega_3) = 2\varepsilon_0 \left[ \chi_{yzzy}^{(2)} E_z(\omega_1) E_y(\omega_2) + \chi_{yyz}^{(2)} E_y(\omega_1) E_z(\omega_2) \right], \quad (6.10)$$

$$P_z(\omega_3) = 2\varepsilon_0 \left[ \chi_{zxxx}^{(2)} E_x(\omega_1) E_x(\omega_2) + \chi_{zyyy}^{(2)} E_y(\omega_1) E_y(\omega_2) + \chi_{zzz}^{(2)} E_z(\omega_1) E_z(\omega_2) \right], \quad (6.11)$$

where we assume  $\omega_3 = \omega_1 + \omega_2$  (see section 2.2.2). In the doubly resonant cavity, since the FH mode is TE and the SH mode is TM, the only valid SFG process can be expressed as:

$$P_z(\omega_3) = 2\varepsilon_0 \left[ \chi_{zxxx}^{(2)} E_x(\omega_1) E_x(\omega_2) + \chi_{zyyy}^{(2)} E_y(\omega_1) E_y(\omega_2) \right]. \quad (6.12)$$

Notice that the electric fields  $E_x$ ,  $E_y$ , and  $E_z$  are those sensed by the wurtzite crystal of the material, so they should be the near field of the modes. On the other hand, the far field of the modes only determines the coupling between the incident Gaussian beam pump and the modes.

In SHG and in an isotropic doubly resonant cavity, i.e., when  $\omega_1 = \omega_2 = \omega_{\text{FH1x}} = \omega_{\text{FH1y}}$ , any combination of  $\text{FH}_{1x}$  and  $\text{FH}_{1y}$  contribute equally to the  $z$ -polarization that is resonant at  $\text{SH}_1$ , which means the process is not sensitive to the pump polarization.

In the case where  $\text{FH}_{1x}$  and  $\text{FH}_{1y}$  are split because of anisotropy, the pump can still be at either  $\text{FH}_{1x}$  or  $\text{FH}_{1y}$ , i.e.,  $\omega_1 = \omega_2 = \omega_{\text{FH1x}}$  or  $\omega_1 = \omega_2 = \omega_{\text{FH1y}}$ , for the SHG to happen independently, and the SHG intensity, at  $2\omega_1$ , depends on how much power is coupled to the  $\omega_{\text{FH1x}}$  and  $\omega_{\text{FH1y}}$  modes. This is the case in the experiment when two SHG peaks can be observed at  $\omega_{\text{FH1x}}$  and  $\omega_{\text{FH1y}}$  with a single frequency scan with a  $45^\circ$ -polarized pump.

However, the SFG between the  $\text{FH}_{1x}$  mode and the  $\text{FH}_{1y}$  mode, i.e.,  $\omega_1 = \omega_{\text{FH1x}}$  and  $\omega_2 = \omega_{\text{FH1y}}$ , could be very weak because of different frequencies with different polarizations in the near field. Since the near fields of  $\text{FH}_{1x}$  and  $\text{FH}_{1y}$  are close to orthogonal, although not exactly orthogonal, the product of the two fields is small.

### 6.3.2 Doubly Resonance and Detuning

The cavities in experiments are not always perfectly doubly resonant [Fig. 6.3 (a)]. In this case, the normalized conversion efficiency of the SHG process can be estimated by [182]:

$$\eta_{\text{norm}}(\lambda) = \frac{P_{2,\text{out}}}{(P_{1,\text{in}})^2} \quad (6.13)$$

$$= \frac{8}{\omega_1} \left( \frac{\chi_{\text{eff}}^{(2)}}{\sqrt{\epsilon_0 \lambda_1^3}} \right)^2 Q_1^2 Q_2 |\bar{\beta}|^2 \mathcal{L}_1^2(\lambda) \mathcal{L}_2(\lambda/2) \quad (6.14)$$

$$\propto Q_1^2 Q_2 \mathcal{L}_1^2(\lambda) \mathcal{L}_2(\lambda/2), \quad (6.15)$$

where the indices 1 and 2 indicate quantities at FH and SH ranges, respectively,  $\lambda$  is the excitation wavelength,  $\mathcal{L}_1(\lambda)$  and  $\mathcal{L}_2(\lambda)$  are the normalized Lorentzian functions of FH and SH resonances, respectively.

When the cavity is excited at the FH<sub>1</sub> resonance, i.e.,  $\lambda = \lambda_{\text{FH1}}$ , the detuning  $\Delta\lambda = \lambda_{\text{SH1}}/2 - \lambda_{\text{FH1}}$  determines the conversion efficiency  $\eta_{\text{conv}}$  via  $\mathcal{L}_2(\lambda_{\text{FH1}}/2)$ . Obviously, the smaller the detuning, the higher the conversion efficiency. Since the detuning can be changed by either passive lithographic tuning or active strain-induced tuning, the conversion efficiency can be changed and optimized accordingly.

### 6.3.3 Second-Harmonic Generation

After the doubly resonant condition is confirmed by the resonant scattering measurement [Fig. 6.3 (a)], the SHG is investigated<sup>1</sup> by exciting the doubly resonant cavity with a linearly polarized Gaussian beam at the normal incidence of the cavity slab. The polarization of the pump beam is either controlled by a  $\lambda/2$  waveplate or by simply rotating the collimator (with an attached PM fiber). The generated light (around 775 nm) is detected on the visible side by the APD without the analyzer P4. On the main setup schema, the optical path for SHG is C1-P1-BS5-BS4-Obj-Sample-Obj-BS4-BS4-BS8-L14-F3-F2-D2. The microscope objective (20 $\times$ , NA = 0.4) is selected to give a Gaussian beam for which the waist size is comparable to the core size of the cavity, and the divergence angle is comparable to the simulated far-field pattern of FH. Using the piezoelectric stage, the coupling is optimized by fine-translating the sample in the  $x$ ,  $y$ , and  $z$  directions. Assuming normal incidence is calibrated, the pitch and yaw of the sample stage and the objective are kept constant.

Because of the dichroic mirror and the wavelength filters in front of the APD, the signal observed is generally in the wavelength range of the transparent window (750-850 nm). Light leakage is possible due to imperfect wavelength blockade but should be very small. The Si APD is also not sensitive to the pump range at FH.

<sup>1</sup>The experiments were first carried out in Dipartimento di Fisica, Università di Pavia, Italy, and then repeated at EPFL.

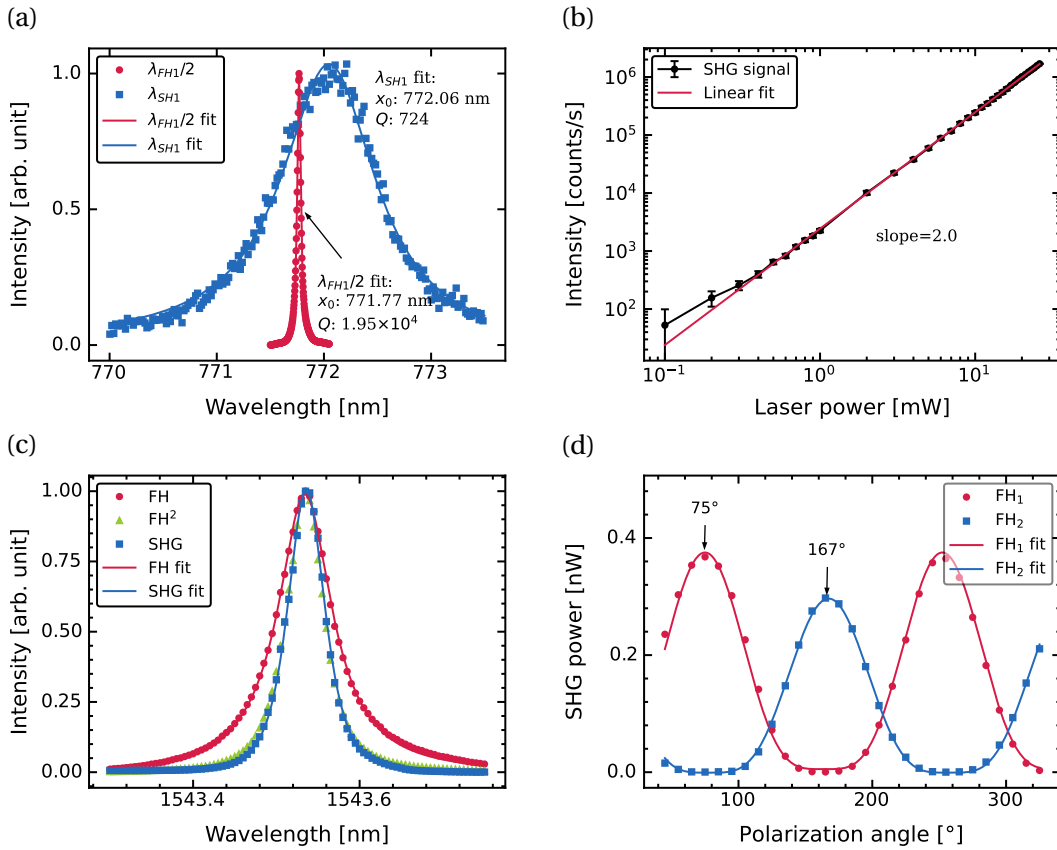


Figure 6.3: SHG in doubly resonant cavity (adapted from [167]). (a) Normalized resonant scattering intensity at FH and SH as a function of excitation wavelength for a cavity with  $-0.3$  nm detuning. Continuous lines show Lorentzian fits. (b) SHG intensity as a function of excitation power at resonance. (c) Normalized resonant scattering intensity at FH and SHG intensity as a function of excitation wavelength. Continuous lines show Lorentzian and Lorentzian squared fits for FH and SHG data, respectively. (d) SHG signal at FH<sub>1</sub> and FH<sub>2</sub> as a function of incident polarization angle. Continuous lines show  $\cos^4$  fits.

The SHG process is ascertained by power-dependent measurement: by fixing the excitation wavelength at FH<sub>1</sub>, the SHG intensity scaled quadratically with the excitation power [Fig. 6.3 (b)]. Alternatively, by fixing the excitation power and scanning the pumping wavelength, the SHG intensity exhibited Lorentzian-squared dependence and matched perfectly with the square of FH resonant scattering intensity, which also confirmed the quadratic nature of the SHG process [Fig. 6.3 (c)].

The polarization of the FH modes is also studied by a fine polarization scan of the excitation beam<sup>2</sup>. The results show that the SHG intensity is proportional to  $\cos^4(\theta_p)$ , where  $\theta_p$  is the incident polarization angle, and the curve for FH<sub>2</sub> is dephased from FH<sub>1</sub> by about 90° [Fig. 6.3 (d)]. Together with the previous resonant scattering experiment, this confirms that the polarization of mode FH<sub>1</sub> is around 90° (along the  $y$ -axis of the cavity) while the polarization of mode FH<sub>2</sub> is around 0° (along the  $x$ -axis of the cavity). The 180° period of both modes

<sup>2</sup>This measurement was performed by Andrea Barone from Dipartimento di Fisica, Università di Pavia, Italy

and the  $\cos^4$  dependence are consistent with the assumption of linear polarization of cavity modes at FH. The 2-fold symmetry for the FH modes instead of 6-fold suggests that the cavities investigated are anisotropic.

### 6.3.4 Efficiency Calibration

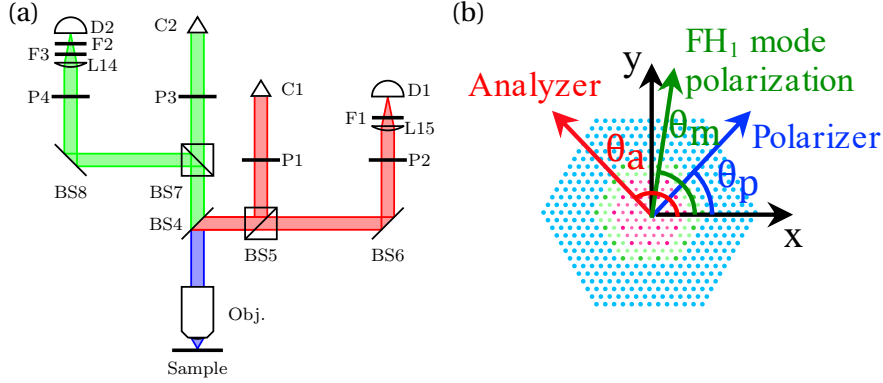


Figure 6.4: SHG efficiency calibration. (a) Core part of the optical setup. (b) Polarization of polarizer, analyzer, and FH<sub>1</sub> mode with respect to the cavity coordinate system Oxy.

The coupling efficiency to the cavity is calibrated with the help of a mirror reference at the same position as the sample [Fig. 6.4 (a)]. The incident power at FH ( $P_{in}$ ) is measured as a function of wavelength before the main objective by a free-space-coupled photodetector (power meter), while the output resonant scattered power (at FH) ( $P_{out}$ ) is measured after the analyzer with the same photodetector. These two power values are related by:

$$P_{out} = P_{in} T_{obj}^{FH} \cos^2(\theta_m - \theta_p) R_{cavity}^{FH} \times T_{obj}^{FH} T_{dichr}^{FH} R_{cube}^{FH} \cos^2(\theta_a - \theta_m) T_{A\parallel}, \quad (6.16)$$

where  $T_{obj}^{FH}$  is the transmittance of the main objective at FH;  $\cos^2(\theta_m - \theta_p)$  comes from the power projection from incident polarization ( $\theta_p$ ) to the resonant mode polarization ( $\theta_m$ ) [Fig. 6.4 (b)];  $R_{cavity}^{FH}$  is the reflectance of the cavity when the incident polarization is parallel to the polarization of the resonance mode;  $T_{dichr}^{FH}$  is the transmittance of the dichroic mirror,  $R_{cube}^{FH}$  is the reflectance of the splitter cube,  $T_{A\parallel}$  is the transmittance of the analyzer when the polarization is parallel to its axis (maximum transmission); the factor  $\cos^2(\theta_a - \theta_m)$  comes from the power projection from output polarization ( $\theta_m$ ) to the analyzer ( $\theta_a$ ). When replacing the sample with a mirror and resetting the analyzer to be parallel with the polarizer, a similar relation holds:

$$P_{out,mirror} = P_{in,mirror} T_{obj}^{FH} R_{mirror} T_{obj}^{FH} T_{dichr}^{FH} R_{cube}^{FH} T_{A\parallel}, \quad (6.17)$$

where  $P_{out,mirror}$  and  $P_{in,mirror}$  are the scattered and the excitation power at FH, respectively, for the reference mirror;  $R_{mirror}$  is the reflectance of the reference mirror, and it is close to



unity at FH. Comparing Eq. 6.17 to Eq. 6.16, we have:

$$R_{cavity\parallel}^{FH} = \frac{R_{mirror}}{\cos^2(\theta_m - \theta_p) \cos^2(\theta_a - \theta_m)} \frac{P_{out}}{P_{in}} \frac{P_{in,mirror}}{P_{out,mirror}}, \quad (6.18)$$

On the other hand,  $R_{cavity\parallel}^{FH}$  can be expressed as:

$$R_{cavity\parallel}^{FH} = \left(\frac{1}{2}\right) \eta_c (1 - \eta_{absorb}^{FH}) \eta_{cavity-obj}^{FH}, \quad (6.19)$$

where the factor 1/2 comes from the fact that the radiation of the cavity is symmetric to the bisection plane of the slab and the in-plane loss outside the cavity is negligible;  $\eta_c$  is the coupling efficiency, which is related to the overlap between incident beam pattern and cavity far-field radiation pattern;  $\eta_{absorb}^{FH}$  is the absorption of the material and is considered to be zero;  $\eta_{cavity-obj}^{FH}$  is the coupling efficiency from the cavity to the objective, which is related to the far-field emission pattern of the cavity at FH and the numerical aperture ( $NA = 0.4$  in practice) of the objective and is considered to be one since the FH emission is highly concentrated in the normal direction. Comparing Eq. 6.19 to Eq. 6.18, the coupling efficiency can be expressed as:

$$\eta_c = \frac{2}{\cos^2(\theta_m - \theta_p) \cos^2(\theta_a - \theta_m)} \times \frac{R_{mirror}}{(1 - \eta_{absorb}^{FH}) \eta_{cavity-obj}^{FH}} \frac{P_{out}}{P_{in}} \frac{P_{in,mirror}}{P_{out,mirror}}. \quad (6.20)$$

The SHG conversion (generation) efficiency is defined as:

$$\eta_{SHG,conversion} = \frac{P_{generated}}{P_{coupled}^2}, \quad (6.21)$$

where the coupled power can be expressed as:

$$P_{coupled} = P_{in} T_{obj}^{FH} \cos^2(\theta_m - \theta_p) \eta_c, \quad (6.22)$$

and the generated power can be expressed as:

$$P_{generated} = \frac{P_{out,SHG}}{T_{filter}^{SH} R_{dichr}^{SH} T_{obj}^{SH} \left(\frac{1}{2}\right) \eta_{cavity-obj}^{SH} (1 - \eta_{absorb}^{SH})}. \quad (6.23)$$

By inserting in Eq. 6.22 and Eq. 6.23 to Eq. 6.21 and replacing  $\eta_c$  by Eq. 6.20, the conversion

efficiency can be finally expressed as:

$$\eta_{SHG,conversion} = \frac{2P_{out,SHG}}{T_{filter}^{SH} R_{dichr}^{SH} T_{obj}^{SH} \eta_{cavity-obj}^{SH} (1 - \eta_{absorb}^{SH})} \times \left[ \frac{\cos^2(\theta_a - \theta_m)}{2} \frac{\eta_{cavity-obj}^{FH} (1 - \eta_{absorb}^{FH})}{T_{obj}^{FH} R_{mirror}} \frac{P_{out,mirror}}{P_{in,mirror}} \frac{1}{P_{out}} \right]^2, \quad (6.24)$$

where the power values can be extracted from the experimental spectra, and the other terms are (wavelength dependent) constant.

	$\Delta\lambda$ (nm)	$Q_{FH}$ ( $\times 10^4$ )	$Q_{SH}$	$\mathcal{L}_{SH}$ ( $\lambda_{FH}/2$ )	$\eta_c$ (%)	$P_c$ (mW)	$P_g$ (nW)	$\eta_{conv}$ ( $W^{-1}$ )
1	-0.9	1.49	804	0.23	19.6	0.541	1.120	$3.8 \times 10^{-3}$
2	-0.3	1.95	724	0.77	6.9	0.125	0.372	$2.4 \times 10^{-2}$

Table 6.1: Comparison of SHG in two cavities, where  $\Delta\lambda$  is the detuning,  $Q_{FH}$  and  $Q_{SH}$  are Q-factors for FH and SH resonances,  $\mathcal{L}_{SH}(\lambda_{FH}/2)$  is the normalized SH intensity at FH resonance,  $\eta_c$  is the coupling efficiency,  $P_c$  is the coupled power,  $P_g$  is the SHG power,  $\eta_{conv}$  is the intrinsic conversion efficiency (adapted from [167]).

Two cavities are shown as examples [Table 6.1]: one with large detuning (-0.9 nm) and the other with small detuning (-0.3 nm) [Fig. 6.3 (a)]. The ratio of the two conversion efficiencies is very close to the value predicted by Eq. 6.15. Moreover, the record intrinsic conversion efficiency in the cavity with small detuning,  $2.4 \times 10^{-2} W^{-1}$  ( $\pm 15\%$ , assuming 100% collection efficiency on the upper side of the slab, see supplement for the calibration details), is 10 times larger than that of singly resonant L3 and H0 cavities [151] ( $\eta_{conv} = 2.4 \times 10^{-3} W^{-1}$ ,  $Q = 3.3 \times 10^4$ ), even with a smaller Q-factor at FH, which confirms the great potential of this doubly resonant PhC cavity scheme for efficient nonlinear frequency conversion.

More calibrations suggest that the coupling efficiency is around 20% at FH, and the normalized conversion efficiency could also be larger than in the table because of higher quality factors at FH and SH and smaller detuning.

### 6.3.5 SH Far-Field Emission

Theoretical analysis and FDTD simulations predict that the far-field emission at SH frequency is a linearly polarized vortex beam with a donut-shaped intensity pattern and radial polarization. This is consistent with the topological nature of BICs in momentum space [157]. To verify this, the SHG far-field emission pattern was investigated by Fourier imaging (see section 4.4). On the main setup schema, the optical path for FH resonant scattering is C1-P1-BS5-BS4-Obj-Sample-Obj-BS4-BS7-L8-M4-M5-L11-M6-CCDVis. The SHG beam was focused by a lens (L8) to form an image of the back focal plane of the objective on a CCD array, and a donut-shaped pattern was directly captured [Fig. 6.5 (a)]. The donut-shaped far-field pattern is concentrated within a  $\pm 5^\circ$  angle in air, which is in perfect agreement with the simulation.

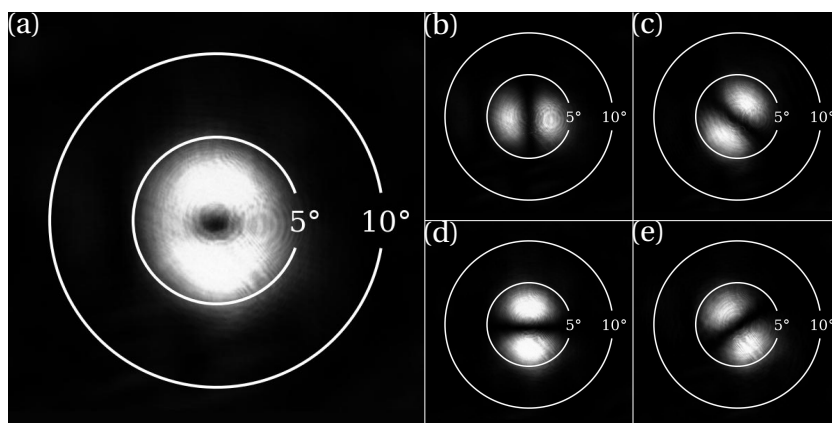


Figure 6.5: SH far-field emission pattern (reproduced from [167]). (a) Fourier imaging of SH far-field emission pattern. The grey scale represents the captured intensity as a function of the far-field emission angle. (b-e) Fourier imaging of SH far-field emission pattern with polarizer at  $0^\circ$ ,  $45^\circ$ ,  $90^\circ$ , and  $135^\circ$ , respectively.

Moreover, when placing a polarizer film in front of the CCD array, a pattern of two lobes always remains, and its axis, which crosses the centers of the lobes, is always aligned with the polarizer, which confirms the radially polarized nature of the beam [Fig. 6.5 (b-e)].

Note that the intensity of the vertically polarizing component in the donut is higher than that of the vertically polarizing component [Fig. 6.5 (a), (b), and (d)]. This could be an artifact of the optical measurement because of the lower transmission/reflection of the optical elements (especially the dichroic mirror BS4) for the  $p$ -polarization. The anisotropy of the cavity could also change the intensity distribution of the donut in a certain direction, while this effect is very weak, according to simulations.

## 6.4 Frequency Down-Conversion

### 6.4.1 Frequency Down-Conversion in Doubly Resonant Cavity

Similarly as in the up-conversion, according to Eq. (2.46) and Eq. (2.54) (see also Fig. 2.10), in the case of DFG, when assuming full permutation symmetry and Kleinman's symmetry (see section 2.2.1), the nonlinear polarization components can be explicitly expressed as:

$$P_x(\omega_2) = 2\varepsilon_0 \left[ \chi_{xzx}^{(2)} E_z(\omega_3) E_x(\omega_1) + \chi_{xxz}^{(2)} E_x(\omega_3) E_z(\omega_1) \right], \quad (6.25)$$

$$P_y(\omega_2) = 2\varepsilon_0 \left[ \chi_{yzy}^{(2)} E_z(\omega_3) E_y(\omega_1) + \chi_{yyz}^{(2)} E_y(\omega_3) E_z(\omega_1) \right], \quad (6.26)$$

$$P_z(\omega_2) = 2\varepsilon_0 \left[ \chi_{zxx}^{(2)} E_x(\omega_3) E_x(\omega_1) + \chi_{zyy}^{(2)} E_y(\omega_3) E_y(\omega_1) + \chi_{zzz}^{(2)} E_z(\omega_3) E_z(\omega_1) \right]. \quad (6.27)$$

And in the doubly resonant cavity, since the FH mode is TE and the SH mode is TM, the valid DFG processes can be expressed as:

$$P_x(\omega_2) = 2\varepsilon_0 \chi_{xzx}^{(2)} E_z(\omega_3) E_x(\omega_1), \quad (6.28)$$

$$P_y(\omega_2) = 2\varepsilon_0 \chi_{yzy}^{(2)} E_z(\omega_3) E_y(\omega_1). \quad (6.29)$$

In the case of DFG in an isotropic doubly resonant cavity, the SH pump is at  $\omega_3$  that is resonant in the TM SH<sub>1</sub> mode with  $z$ -polarization, the FH pump is at  $\omega_1$  that is resonant in the TE FH<sub>1</sub> mode that can be any combination of FH<sub>1x</sub> and FH<sub>1y</sub> with TE polarization. The DFG signal should be at  $\omega_2 = \omega_1 = 1/2\omega_3$  that is also resonant in the TE FH<sub>1</sub> mode with the same polarization as the FH pump.

The DFG signal and the FH pump are of the same frequency and polarization, so they can not be easily distinguished. The first solution to this issue could be modulating the SH pump, and the DFG signal should also be modulated with the same frequency and can be extracted from the strong background of the FH pump by lock-in detection. The second solution to this issue could be tracking the intensity at  $\omega_2$  while scanning the frequency of either the SH pump  $\omega_3$  or the FH pump  $\omega_1$  because some energy at  $\omega_3$  is eventually converted to  $\omega_2$  through the process. But the difference in intensity can be very small compared to the large background, especially when the DFG is very weak. The third solution could be carefully placing the FH pump frequency  $\omega_1$  on one side of the FH<sub>1</sub> resonance peak so that the DFG frequency  $\omega_2$  is at the other side, and the two frequencies can be identified by the frequency difference. However, this requires high-resolution spectrum analysis, possibly by a narrow linewidth bandpass filter, because the linewidth of the FH modes is very small.

In the case of DFG in an anisotropic doubly resonant cavity, the process could still happen at  $\omega_{FH1x}$  and  $\omega_{FH1y}$  independently, as described above. Interestingly, it could also be possible to have the FH pump at  $\omega_{FH1x}$  and the DFG signal at  $\omega_{FH1y}$  or vice versa at the same time, provided that the near fields of FH<sub>1x</sub> and FH<sub>1y</sub> are not exactly orthogonal. In this case, the FH pump and the DFG signal could be easily discriminated because they are orthogonal in the far

field. However, the efficiency could be low because of the small product of the near fields of  $FH_{1x}$  and  $FH_{1y}$ .

Notice that in DFG, the SHG of the SH pump at  $\omega_3$ , the SHG of the FH pump at  $\omega_1$ , and the SFG of the two pumps also exist with frequencies  $2\omega_3$ ,  $2\omega_1$ , and  $\omega_1 + \omega_3$ , respectively, although  $2\omega_3$  and  $\omega_1 + \omega_3$  are generally not resonant in the cavity.

In the case of SPDC where only one pump is provided at  $\omega_3$ , because the phase matching condition is not required, any combination of the signal and idler frequencies  $\omega_1$  and  $\omega_2$  are valid as long as the energy conservation,  $\omega_3 = \omega_1 + \omega_2$ , is fulfilled. However, only the combinations that are resonant in the cavity and possess significant nonlinear overlap factors with the pump mode  $SH_1$  play the main roles. The second requirement excludes some high-order modes of odd symmetry. Notice that the  $\chi_{xyz}^{(2)}$  element is zero for the wurtzite structure so that there is no process that locally involves the  $x$ ,  $y$ , and  $z$  polarizations at the same time, and thus the signal and the idler are always of the same polarization and never orthogonal, for a local piece of the material. However, as mentioned above, because of the non-zero product of the near fields of  $FH_{1x}$  and  $FH_{1y}$ , orthogonal far fields for signal and idler are still possible. Notice that the SHG of the pump also exists, with a frequency  $2\omega_3$ , although it is generally not resonant in the cavity.

In an isotropic doubly resonant cavity, The combination of  $\omega_1 = \omega_2 = \omega_{FH1x} = \omega_{FH1y}$  is valid, with the same polarization for the signal and the idler. Since all TE polarizations are valid, the collective beam of the signal and the idler is randomly polarized. The frequency scan around  $\omega_3$  results in one peak for the SPDC intensity.

In an anisotropic doubly resonant cavity, The combinations of  $\omega_1 = \omega_2 = \omega_{FH1x}$  and  $\omega_1 = \omega_2 = \omega_{FH1y}$  are valid, with the signal and the idler at the far field both  $x$ -polarized or  $y$ -polarized, respectively. The combination of  $\omega_1 = \omega_{FH1x}$  and  $\omega_2 = \omega_{FH1y}$  is also possible provided that the product of the near fields of  $FH_{1x}$  and  $FH_{1y}$  is non-zero, which result in orthogonal signal and idler at the far field. The frequency scan around  $\omega_3$  could result in three peaks for the SPDC intensity, with the middle peak smaller than the other two.

From a transient point of view, once an initial photon is spontaneously generated inside the cavity at the frequency of one of the FH modes, it possibly excites the mode and serves as a seed signal, and the process becomes DFG. The initial photons with different polarizations could be generated independently, and in an isotropic doubly resonant cavity, the superposition of the DFG processes results in a randomly polarized beam, while in an anisotropic doubly resonant cavity, only the initial photons with the same polarization of the split modes could exit the mode efficiently.

Notice also that the SPDC with the signal and the idler sharing the same polarization could result in type-I entangled photon pairs, and the SPDC with orthogonal signal and idler could result in type-II entangled photon pairs.

### 6.4.2 Difference Frequency Generation

The DFG was investigated before the SPDC because the DFG can be regarded as the stimulated version of SPDC. Since the anisotropy of the cavity is verified, the FH pump is placed at either  $FH_{1x}$  or  $FH_{1y}$ , and the SH pump is placed at  $SH_1$ .

Because of the radially polarized donut in the far field of the  $SH_1$  mode, the Gaussian pump is placed off the center of the cavity with appropriate polarization, i.e., with  $x$ -polarization when the pump beam is moved in the  $x$ -axis of the cavity, and with  $y$ -polarization when the pump beam is moved in the  $y$ -axis of the cavity. The pump beam at SH is still in the normal direction of the cavity slab because of the complexity of adjusting the incident angle. With this configuration, the coupling efficiency of the SH pump is tested to be also around 20%, using a similar technique as in section 6.3.4, which is comparable to the coupling efficiency at the FH range. The FH pump is also a Gaussian beam at normal incidence, centered in the cavity, and with a  $45^\circ$ -polarization. The coupling of the two pump beams is optimized by a similar technique as the resonant scattering. The coupling of the SH pump is optimized first by moving the sample in  $x$ ,  $y$ , and  $z$  directions by the piezoelectric actuator, and then the coupling of the FH pump is optimized by changing the pitch and yaw of the FH beam. Although the microscope objective used is chromatic, the coupling to the FH mode is found not sensitive to the focus. As a comparison, the coupling to the SH mode is more sensitive to the focus and the position.

Because the DFG signal generally has the same polarization and frequency as the FH pump, to discriminate the DFG signal by lock-in detection, the SH pump is modulated by an optical chopper at 2 kHz, which is the bandwidth of the NIR PD. The DFG signal is collected by the NIR PD with the same configuration as resonant scattering but without the analyzer. The signal contains a large constant background, as expected, because of the direct reflection of the FH pump. However, the modulation of the signal can be easily identified with the oscilloscope with the same frequency and line shape as the modulation at FH. Since the SH pump beam is filtered out by the long pass filter before the NIR PD, the signal is for certain the NIR signal. However, when slightly changing the frequency of the FH pump, the signal on the NIR PD not only changed the amplitude but also occasionally shifted the phase by  $\pi$ . This phenomenon is not expected in a DFG process.

To investigate the origin of the phase shift of the signal, the FH pump beam is placed at 5 frequencies around the first resonance peak at FH [Fig. 6.6 (a)], and the SH pump is scanned in frequency around the SH peak without modulation. The corresponding spectra of the NIR PD signal versus the SH wavelength show that when the FH pump is placed at wavelength points 1, 2, and 3, the signal with the SH pump is smaller than that without the SH pump, while when the FH pump is placed at wavelength points 4 and 5, the signal with the SH pump is larger than that without the SH pump [Fig. 6.6 (b)-(f)]. This suggests the FH resonance peak might be redshifted when the SH pump is on.

To verify this assumption, the SH pump is fixed at 3 frequencies around the SH resonance

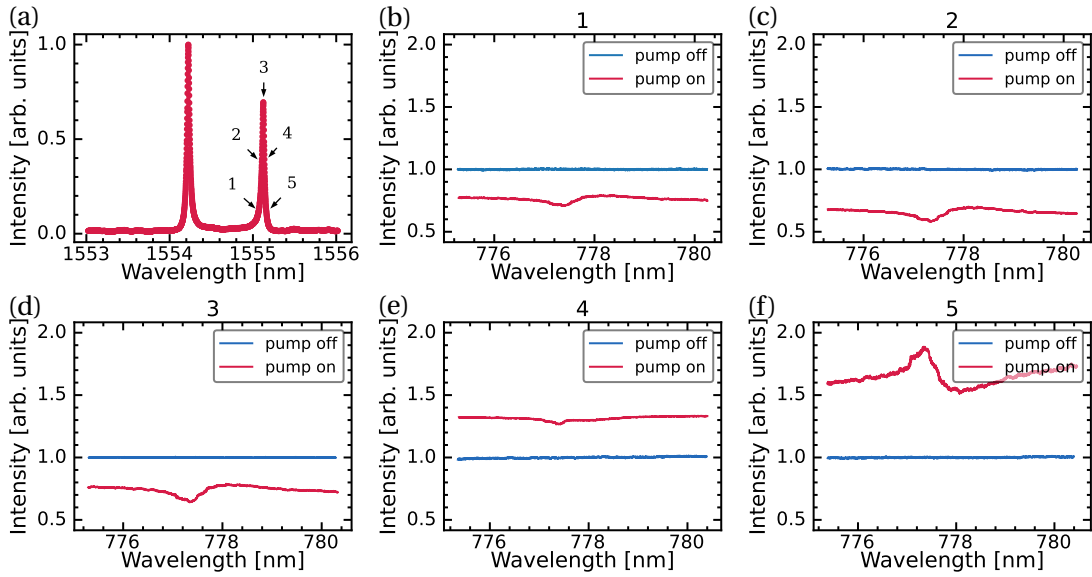


Figure 6.6: Pump-induced shift of FH resonance with SH scan. (a) Resonant scattering spectrum of the  $FH_{1x}$  and  $FH_{1y}$  peaks for reference. The FH pump is placed at 5 wavelengths around the  $FH_{1y}$  peak. (b)-(f) Intensity measured on the NIR PD when scanning the wavelength of the SH pump, with the FH pump fixed at positions 1-5 as indicated in (a).

peak [Fig. 6.7 (a)], and the FH pump is scanned in frequency around the FH peak without modulation. The corresponding spectra of the NIR PD signal versus the FH wavelength are basically the same as the resonant scattering spectrum, however, by comparing the off and on states of the SH pump, each with 3 repetitions [Fig. 6.7 (d)-(f)], a small redshift of only about 5 pm can be identified, accompanied with a slight decrease in the Q-factors. [Fig. 6.7 (b)-(c)]. The redshift is also reversible as the peak positions and Q-factors recover when the SH pump is turned off again. Now it can be concluded that the SH pump at SH induces a small and reversible redshift of about only 5 pm for the FH peak, which is responsible for the signal perturbation and phase shift with SH modulation.

The reason for the SH pump-induced redshift might be the thermal effect because the SH pump is at a relatively high power of several tens of milliwatts, compared to below 10 milliwatts power for the FH pump. Notice that the effect is reversible at a modulation frequency of 2 kHz, so the process for the origin of the redshift is reversible and fast.

Since the Q-factors of the FH peaks are as high as  $4 \times 10^4$ , the linewidth of the peaks is as small as about 40 pm, so that even if the redshift is only about 5 pm, the induced perturbation of the NIR PD signal is significant. Because of this effect, the idea of identifying the DFG signal by SH modulation is no more valid. As mentioned before, the alternatives could be tracking the intensity change of the FH signal or fine-adjusting the FH pump frequency on one side of the FH peak so that the DFG signal is on the other side. However, these alternatives require fine resolution in either intensity or frequency, which is rather challenging using the currently available setups.

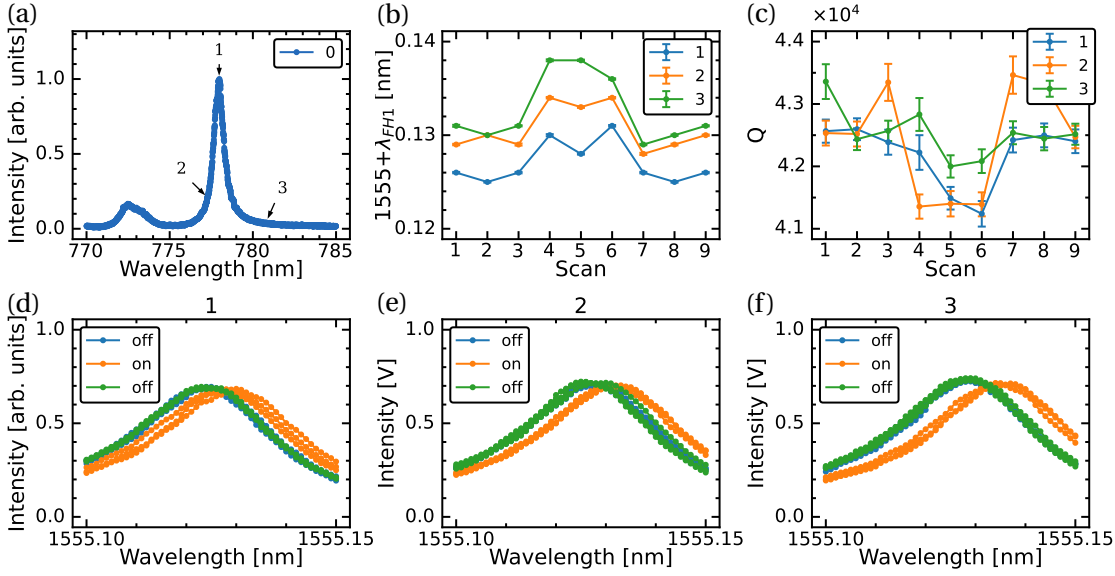


Figure 6.7: Pump-induced shift of FH resonance with FH scan. (a) Resonant scattering spectrum of the SH<sub>1</sub> peak for reference. The SH pump is placed at 3 wavelengths around the SH<sub>1</sub> peak. (d)-(f) Intensity measured on the NIR PD when scanning the wavelength of the FH pump around the FH<sub>1y</sub> peak, with the SH pump fixed at positions 1-3 as indicated in (a). Blue, orange, and green lines, each repeated three times for reliability, represent the status of the SH pump in sequential order. (b) Peak locations of the 9 lines for the SH pump at wavelengths 1-3. (c) Q-factors of the 9 lines for SH pump at wavelengths 1-3.

### 6.4.3 Spontaneous Parametric Down Conversion

The DFG is an intermediate step for investigating SPDC. If the SPDC signal is already observed, then it is no more necessary to test the DFG. However, the challenge for SPDC is that the signal could be very weak and below the detectable power of the PDs.

The SPDC is directly investigated on the main setup with a pump at FH of power about 100 mW measured after the collimator. The coupling to the cavity is the same as described in DFG, with about 20% coupling efficiency, and the FH signal is collected with the NIR PD without the analyzer. The detector NIR PD has a noise-equivalent power (NEP) of  $1.5 \times 10^{-14} \text{W}/\sqrt{\text{Hz}}$  at around 1550 nm and a bandwidth of 2 kHz, which results in a minimum detectable power of about 0.67 pW with lock-in detection. Since the FH peaks are very sharp (with the FWHM about 40 pm) and the wavelength resolution for the Ti:sapphire laser is limited (about 4 pm at maximum, with large fluctuations, plus the mode-hopping effect at certain wavelength ranges), the SH pump is either scanned continuously with the slowest speed or point by point with the minimum step. However, several measurements on doubly resonant cavities with different detunings and at different wavelength ranges were carried out, but no SPDC signal was observed.

The reason for the absence of SPDC could be technical issues with the measurement setup or the fact that the conversion efficiency is too low to be observed by the setup. The issues with the setup could be: firstly, the wavelength resolution of the Ti:sapphire laser is too low for



the linewidth of FH peaks, and the peak is missed; secondly, the mode-hopping happened occasionally at the FH peak positions so that the peak is missed; thirdly, the power collection on the NIR PD is not well aligned, and the SPDC power is not fully measured by the NIR PD; fourthly, the NEP of the NIR PD degraded so that the sensitivity is decreased. For the possibility that the conversion efficiency is too low to be observed by the setup, the solution could be using a more sensitive detector, e.g., a single photon detector, higher pump power or even pulsed pump, and smaller power losses through the optical elements.

Although SPDC can be regarded as the inverse process of SHG, the conversion efficiency of SPDC is much smaller than SHG. In SHG, the generated signal is at a fixed frequency that is determined by the pump, while in SPDC, the signal and the idler can be a series of combinations that fulfill the energy conservation. Although the requirement of phase matching and nonlinear overlap factor put more strict constraints on the combinations, the combinations are still more than that in SHG, which is only one. The conversion to combinations competes with each other and eventually limits the efficiency of a certain combination. Nevertheless, in doubly resonant cavities, because of the enhancement of both the pump and the signal extraction, the conversion efficiency of SPDC should be much higher than in bulk materials. However, the quantitative analysis of the process could be rather complex, and the theoretical conversion efficiency is still being debated.

Another reason for the lower efficiency of SPDC than SHG in the doubly resonant cavity is that the Q-factor of the SH resonance is more than one order of magnitude lower than that of the FH resonance. The enhancement factor, for either SHG or SPDC, turns out to be proportional to  $Q^2$  on the pump side and to  $Q$  on the extraction side. As a result, the enhancement factor of the doubly resonant cavity is proportional to  $Q_{\text{FH}}^2 Q_{\text{SH}}$  for SHG, and  $Q_{\text{FH}} Q_{\text{SH}}^2$  for SPDC, which results in a decrease factor of  $Q_{\text{FH}}/Q_{\text{SH}}$  for SPDC compare to SHG. Numerically, taking  $Q_{\text{FH}} = 4 \times 10^4$  and  $Q_{\text{SH}} = 800$ , the enhancement for SPDC could be  $Q_{\text{FH}}/Q_{\text{SH}} = 50$  times less efficient than that for SHG.



## 7 Conclusions and Perspectives

In the fabrication part, the existing fabrication processes are further developed. The strain engineering by spring tethers is demonstrated and proved effective for suspending waveguides and PhCs, which improved the stability of devices with an end-fire design. The deep etching technique improves the fabrication repeatability of the waveguide terminals. The HSQ technique for EBL is demonstrated to be effective, but because of the much longer exposure time in the case of 2D PhC, it is not widely adopted. The AlN etching recipe is developed, although with a larger sidewall inclination than GaN.

In the optical measurement part, the main optical setup is redesigned, and the stability and functionality are improved. Dedicated LabVIEW scripts for measurement controls are developed from scratch, which provides not only the conventional point-by-point measurement scheme but also the fast continuous sweep mode with active wavelength calibration. The scripts significantly improve the measurement efficiency and wavelength reliability.

In the doubly resonant cavity part, the first doubly resonant PhC slab cavity has been experimentally demonstrated. The Q-factors at FH (around 1550 nm) and SH (around 775 nm) ranges are around  $2.0 - 4.3 \times 10^4$  and 700-1000, respectively. The small detuning between the two resonant modes is realized by lithographic tuning. Although the optimization of material quality and Q-factors were not the main targets during the fabrication process, the Q-factors are comparable with the predicted values. This shows the robustness of the cavity design and suggests great potential for improvement in the Q-factors. Alternative doubly resonant cavity designs have been proposed based on topology optimization of microposts and microrings [137, 183]. However, these designs contain very fine structural features that make them less robust to fabrication imperfections in practice. Further design based on cylindrical dielectric structures has also been demonstrated [175], characterized by a high degree of compactness and sustaining relatively high excitation powers. However, the measured Q-factors and conversion efficiencies are much lower than the ones shown in the present work.

The two fundamental degenerate modes at the FH range are observed to have polarizations

along the  $x$ - and  $y$ -axis, respectively, in the far field, which is in agreement with FDTD simulations. However, the 0.5-2 nm split of the modes is observed, and the mode with  $y$ -polarization has a lower frequency than the mode with  $x$ -polarization. FDTD simulations suggest that the split could be due to anisotropic refractive index or cavity geometry deformation. Inspired by the mode split, active tuning by applying anisotropic stress is demonstrated, and up to 0.5 nm reversible tuning is realized, which adds a great degree of freedom to tune the performance of the doubly resonant cavity.

In the nonlinear frequency conversion part, the SHG is successfully demonstrated in the cavity. An experimental intrinsic SHG conversion efficiency of  $2.4 \times 10^{-2} \text{ W}^{-1}$  is achieved, which is 10 times larger than the previously shown result for a singly resonant cavity with an even higher Q-factor at FH [151]. This result is in agreement with the higher efficiency of nonlinear frequency conversion in doubly resonant cavities predicted by theory. Significant room for improvement is left for further developments, both at the level of nonlinear overlap factor design and experimental Q-factors, and thus the SHG conversion efficiency could be ultimately increased in the future. Active tuning could also be investigated in the SHG process.

It is confirmed that the SHG far-field emission pattern is tightly concentrated ( $\pm 5^\circ$ ) around the normal direction with donut shape and radial polarization, as a result of the BIC confinement at SH, which is in agreement with FDTD simulations. The far field of the BIC mode confirms the topological charge description [157]. Although the BIC resonant mode is not the only way of generating a radially polarized beam [184], the highly normal-direction concentration of the beam is peculiar and takes advantage of beam out-coupling. The implementation of the BIC and the heterostructure put forward a practical realization of the long-standing challenge of designing PhC slab cavities fulfilling the doubly resonant conditions. The BIC confinement mechanism also provides a natural way to generate a highly concentrated and radially polarized vortex beam through the SHG process.

Unfortunately, SPDC is not observed in the cavity. This may be because, even with the enhancement mechanisms of the doubly resonant cavity, the intrinsic efficiency of the process is too low and is beyond the capability of the current experimental setup (100 mW pump at around 775 nm, 0.67 pW nominal minimum detectable power). Limited wavelength resolution (4 pm), occasional mode-hopping, and small collection efficiency could also be the reason. In DFG, the lack of  $\chi_{xyz}^{(2)}$  element of the wurtzite crystal, combined with the TM pump and TE extraction configuration, results in the same polarization of the signal and idler beams, which adds difficulties for discriminating the generated idler signal. The SH pump-induced shift at FH hinders the pump modulation for idler discrimination. In order to achieve SPDC in the doubly resonant cavity, the efficiency needs to be carefully analyzed, and potentially a photodetector with higher sensitivity, e.g., a single photon detector, is required for the low-power continuous-wave pump. Alternatively, pumping by a tunable pulsed laser can also be investigated.

# A Appendices

## A.1 Purcell Effect

Purcell's factor, i.e., the factor by which the spontaneous emission rate is enhanced by a cavity, can be expressed as [72, 73]:

$$F_P = \frac{3}{4\pi^2} \left(\frac{\lambda}{n}\right)^3 \frac{Q}{V}, \quad (\text{A.1})$$

where  $\lambda$  is the wavelength in vacuum,  $n$  is the refractive index,  $Q$  is the quality factor, and  $V$  is the effective volume.

### Derivation

The probability density (per unit of time) of spontaneous emission into a prescribed mode in a cavity is given by [71]:

$$p_{\text{sp}} = \frac{c}{V} \sigma(\nu), \quad (\text{A.2})$$

where  $V$  is the volume of the cavity,  $\sigma = \sigma_{\text{max}} \cos^2 \theta$  is the transition cross-section, and  $\theta$  is the angle between the dipole moment of the atom and the field direction of the mode.

The density of modes, i.e., the number of modes per unit volume per unit bandwidth around the frequency  $\nu$ , in a large (size much larger than the wavelength) three-dimensional (3D) cavity in a vacuum is given by [71]:

$$\rho_{\text{cav}}(\nu) = \frac{8\pi\nu^3}{c^3}, \quad (\text{A.3})$$

where  $\nu$  is the optical frequency,  $c$  is the light speed in vacuum.

The total probability density (per unit of time) of spontaneous emission into all modes in a

large cavity can be expressed as:

$$P_{\text{sp}} = \int_0^{\infty} \left[ \frac{c}{V} \bar{\sigma}(\nu) \right] [V \rho_{\text{cav}}(\nu)] d\nu, \quad (\text{A.4})$$

where  $\bar{\sigma} = \langle \sigma_{\text{max}} \cos^2 \theta \rangle = \frac{1}{3} \sigma_{\text{max}}$  is the average transition cross section in space.

Similarly, the total probability density (per unit of time) of spontaneous emission into all modes in a microcavity can be expressed as:

$$P_{\text{cav}} = \int_0^{\infty} \left[ \frac{c}{V} \sigma_{\text{max}}(\nu) \right] \left[ \frac{2Q}{\pi\nu} \right] d\nu, \quad (\text{A.5})$$

where  $\frac{2Q}{\pi\nu}$  is the mode density (number of modes per unit frequency) of the microcavity at resonance. It is assumed to be the maximum value of the Lorentzian function of the mode density:

$$\mathcal{L}(\nu) = \frac{1}{\pi} \frac{\frac{\delta\nu}{2}}{\left(\frac{\delta\nu}{2}\right)^2 + (\nu - \nu_0)^2}, \quad (\text{A.6})$$

where  $Q = \nu_0 / \delta\nu$  is the quality factor.

Finally, the spontaneous emission rate is enhanced by a factor of:

$$F_{\text{P}} = \frac{P_{\text{cav}}}{P_{\text{sp}}} = \frac{\frac{2Q}{\pi\nu} \frac{c}{V} \int_0^{\infty} \sigma_{\text{max}}(\nu) d\nu}{\frac{1}{3} \frac{8\pi\nu^3}{c^3} V \frac{c}{V} \int_0^{\infty} \sigma_{\text{max}}(\nu) d\nu} = \frac{3}{4\pi^2} \left(\frac{c}{\nu}\right)^3 \frac{Q}{V} \quad (\text{A.7})$$

## A.2 Doubly Resonant Cavity Design by Gdspy

The following Python code is a minimized example for generating a doubly resonant cavity using the Python package **gdspy** [106]. The first function is the core function for generating a doubly resonant cavity with band-folding extractors. It implements a list of vectors and a three-layer loop to create cavity holes from the core region to the outer region in an anti-clock spiral order (Fig. A.1). It is independent of gdspy and is also used to create simulation models. The second function is an example of creating a GDS file using the gdspy package. The example code generates a GDS file containing a doubly resonant cavity.

The implemented code is an object-oriented version that also manages the parameter scan, the layout arrangement, etc., on a larger scale. It is much longer and thus not shown here.

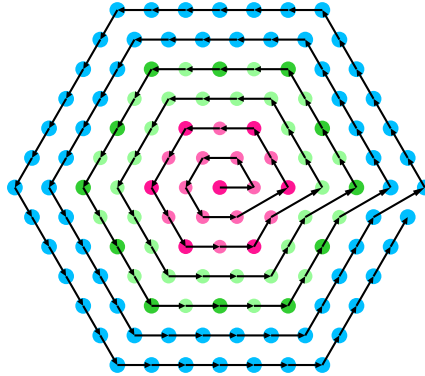


Figure A.1: Schema of the writing order of holes in a doubly resonant cavity. The EBL exposure follows the same order by default.

```

1  import numpy as np
2  import gdspy
3
4
5  def doubly_resonant_cavity_nodes(a, n_c, n_t, n_o):
6      nodes = []
7
8      # the hexagonal vectors, for drawing as hexagonal rings
9      v1 = np.array([-1 / 2, +np.sqrt(3) / 2])
10     v2 = np.array([-1, 0])
11     v3 = np.array([-1 / 2, -np.sqrt(3) / 2])
12     v_list = [v1, v2, v3, -v1, -v2, -v3]
13
14     # the main loop to generate the lattice nodes
15     nodes.append(dict(x=0, y=0, mark='c_ext')) # the center hole
16     for rn in range(1, n_c + n_t + n_o + 1):
17         # rn: the radius of hexagonal rings in unit of a
18         vi = np.array([rn, 0])
19         for j in range(0, 6):
20             for i in range(0, rn):
21                 if rn <= n_c: # the core region
22                     mark = 'c_ext' if rn % 2 == 0 and i % 2 == 0 else 'c'
23                 elif rn <= n_c + n_t: # the transition region
24                     mark = 't_ext' if rn % 2 == 0 and i % 2 == 0 else 't'
25                 else: # the outer region
26                     mark = 'o'
27                 nodes.append(dict(x=vi[0]*a, y=vi[1]*a, mark=mark))
28                 vi = vi + v_list[j]
29
30     return nodes # a list of dictionaries [{'x':, 'y':, 'mark':},]
31
32
33 def doubly_resonant_cavity_example():

```

```

34     # define the base parameters for a doubly resonant cavity
35     a, n_c, n_t, n_o, r_c, r_t, r_o, r_c_ext, r_t_ext = \
36         [650, 6, 4, 14, 130, 137, 150, 135, 142]
37
38     # define the parameters for the hole instances
39     params_holes = [
40         dict(name='c', r=r_c, layer=1),
41         dict(name='t', r=r_t, layer=2),
42         dict(name='o', r=r_o, layer=3),
43         dict(name='c_ext', r=r_c_ext, layer=4),
44         dict(name='t_ext', r=r_t_ext, layer=5)
45     ]
46
47     # define a gdspy library
48     lib = gdspy.GdsLibrary(unit=1e-9, precision=1e-11)
49
50     # create a dictionary of hole instances
51     holes = {}
52     for params in params_holes:
53         cell = lib.new_cell(params.get('name'))
54         poly = gdspy.Round(
55             center=(0, 0),
56             radius=params.get('r'),
57             number_of_points=199,
58             layer=params.get('layer'),
59             datatype=3,
60         )
61         cell.add(poly)
62         holes.update({params.get('name'): cell})
63
64     # generate the hole coordinates and fill holes in the lattice
65     nodes = doubly_resonant_cavity_nodes(a, n_c, n_t, n_o)
66     cell = lib.new_cell('doubly_resonant_cavity_example')
67     for node in nodes:
68         cell.add(gdspy.CellReference(holes.get(node.get('mark')),
69                                     (node.get('x'), node.get('y'))))
70
71     # write the cells to a GDS file
72     lib.write_gds('doubly_resonant_cavity_example.gds')
73
74
75     if __name__ == "__main__":
76         doubly_resonant_cavity_example()

```

### A.3 Main Optical Setup Drawing and Element List

The schematic drawing of the main optical setup is presented [Fig. A.2], together with the elements used [Table A.1, A.2]. The drawing was prepared with the LaTeX package **pst-optexp**.



### A.3 Main Optical Setup Drawing and Element List

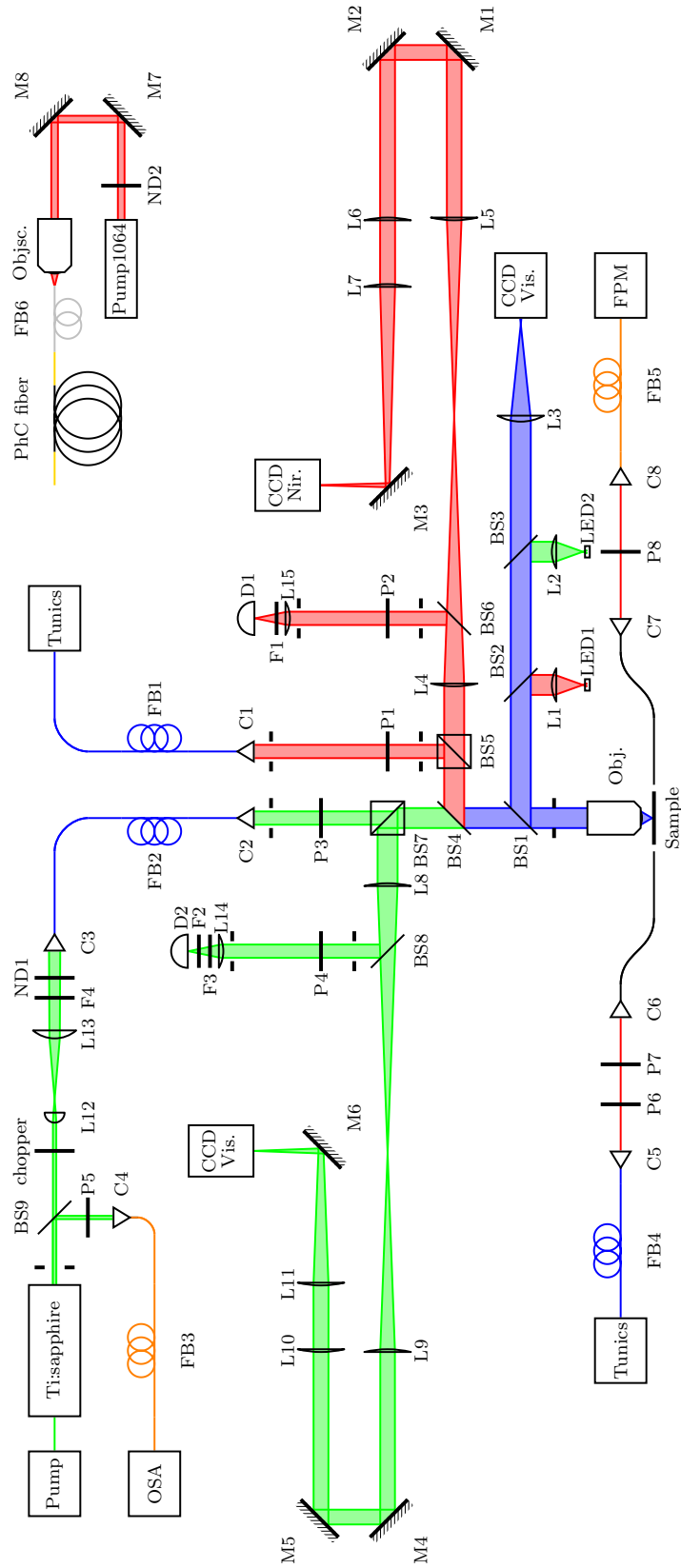


Figure A.2: Schematic drawing of the main optical setup.

## Appendix A. Appendices

Label	Model	Description
BS1	TL BP145B1	pellicle beam splitter
BS2	TL BP145B3	pellicle beam splitter
BS3	TL EBS1	economy beam splitter
BS4	TL DMSP1000R	dichroic mirror, short pass, 1000 nm
BS5	EO 47-236	beam splitter cube for 1550 nm
BS6	TL BP245B3	pellicle beam splitter
BS7	EO 47-236	beam splitter cube for 775 nm
BS8	TL BP245B1	pellicle beam splitter
BS9	TL BSF10-B	beam sampler
C1	TL F280APC-1550	fixed collimator, 1550 nm
C2	TL F280APC-780	fixed collimator, 775 nm
C3	TL RC08APC-P01	reflective collimator
C4	TL CFC-8X-B	adjustable collimator, 775 nm
C5, C6	TL PAF-X-5-1550	Fiber ports
C7, C8	TL PAF-X-2.6A-1550	Fiber ports
D1	Eosystems DSS-IGA020TC	InGaAs photodiode
D2	Hamamatsu C4777-01	Avalanche Photodiode
F1	TL FELH1400	long-pass filter, 1400 nm
F2	TL FESH0850	short-pass filter, 850 nm
F3	TL FELH0750	long-pass filter, 750 nm
F4	TL FELH0550	long-pass filter, 550 nm
FB1, FB4	TL P3-1550PM-FC-2	polarization maintaining fiber
FB2	TL P3-780PM-FC-5	polarization maintaining fiber
FB3	TL M42L05	multimode fiber
FB6	TL P5-1064HE-2	single mode fiber, end-capped
L1, L2	-	lens
L3	-	lens A400, f=400 mm
L4	-	lens A400C, f=400 mm, IR coating
L5, L6	-	lens A300C, f=400 mm, IR coating
L7	-	lens A500C, f=500 mm, IR coating
L8	TL AC508-400-A	lens f=400 mm, VIS coating
L9, L10, L11	TL AC508-300-A	lens f=300 mm, VIS coating
L12, L13	-	lens
L14	TL AC254-050-B	lens f=50 mm
L15	TL AC254-050-C	lens f=50 mm
LED1	TL M1550L3	LED, 1550nm
LED2	-	white or blue LED
M1, M2, M3	TL PFSQ20-03-M01	protected gold mirror
M4, M5, M6	TL PFSQ20-03-P01	protected silver mirror

Table A.1: List of optical elements used (TL: Thorlabs, NP: Newport, EO: Edmund Optics) (1/2).

Label	Model	Description
Obj	-	main objective, 20x NA=0.45
Objsc	-	
P1, P2	NP 10LP-NIR	Linear polarizer, 1100-1750 nm, 1000:1
P3	NP 05P108AR.16	Linear polarizer, 740-860 nm, 10000:1
P4	TL LPNIR050-MP2	Linear polarizer, 650-2000 nm, 10000:1
P5	-	linear polarizer film
P6	OFR RZB-1/2-1550	$\lambda/2$ wave plate, 1550 nm
P7	OFR PCB-1550-1.5	linear polarizer, 1550 nm
P8	-	linear polarizer, 1550 nm

Table A.2: (List of optical elements used (TL: Thorlabs, NP: Newport, EO: Edmund Optics) (2/2).

### A.4 Alignment of the Main Setup

Since 1550 nm light is invisible and 775 nm light is also difficult to see, fiber-coupled laser pointers (also called visual fault locators) at around 650 nm are used for coarse alignment. These lasers are especially convenient when combined with optical fibers and fiber collimators. Because of dispersion issues, the alignment is fine-tuned with 1550 nm and 775 nm lasers afterward, with laser viewing cards or CCD sensors.

The main microscope objective should be aligned in the vertical direction so that the sample can be positioned in a horizontal stage. To do this, an alignment laser is connected to C2, the silver mirror between BS1 and the main objective is changed to a plate beam splitter, the main objective is covered with a small iris at its axis, and a mirror is placed on the sample stage. The light beam reflected by the mirror passes through the main objective, the small iris, and the beam splitter and goes vertically up. This beam is aligned to be vertical with a plumb by changing the tilt of the mirror and the objective.

When aligning the NIR part with the alignment laser, a higher power is needed because of the low reflectivity of the dichroic mirror for the visible range. In practice, an 80 mW laser at 650 nm is used, and the beam spot at the detector position is barely visible in the dark<sup>1</sup>.

When 1550 nm and 775 nm wavelengths are involved simultaneously, it is generally required that these two beams spatially coincide. To do this, two alignment lasers are connected to C1 and C2, respectively, and BS1 is replaced with a mirror module that redirects the light to a screen at a long distance (the CCD Vis can also be used for this purpose while ND filters should be installed to avoid any damage). By adjusting BS4 and BS5, the two spots on BS4 as well and the two spots on the screen coincide at the same time, which ensures the coincidence of the two beams.

<sup>1</sup>This issue is considered at the beginning of the setup design, and the configuration with a long-pass dichroic mirror is not adopted for practical reasons

### A.5 Ti:sapphire Laser Wavelength Nonlinearity Analysis

Although the relation between the output wavelength and the actuator position appears linear for large tuning ranges, a small wavelength nonlinearity can be observed during experiments. An example can be given by analyzing the transmission spectrum of an optical element possessing Fabry-Pérot interference.

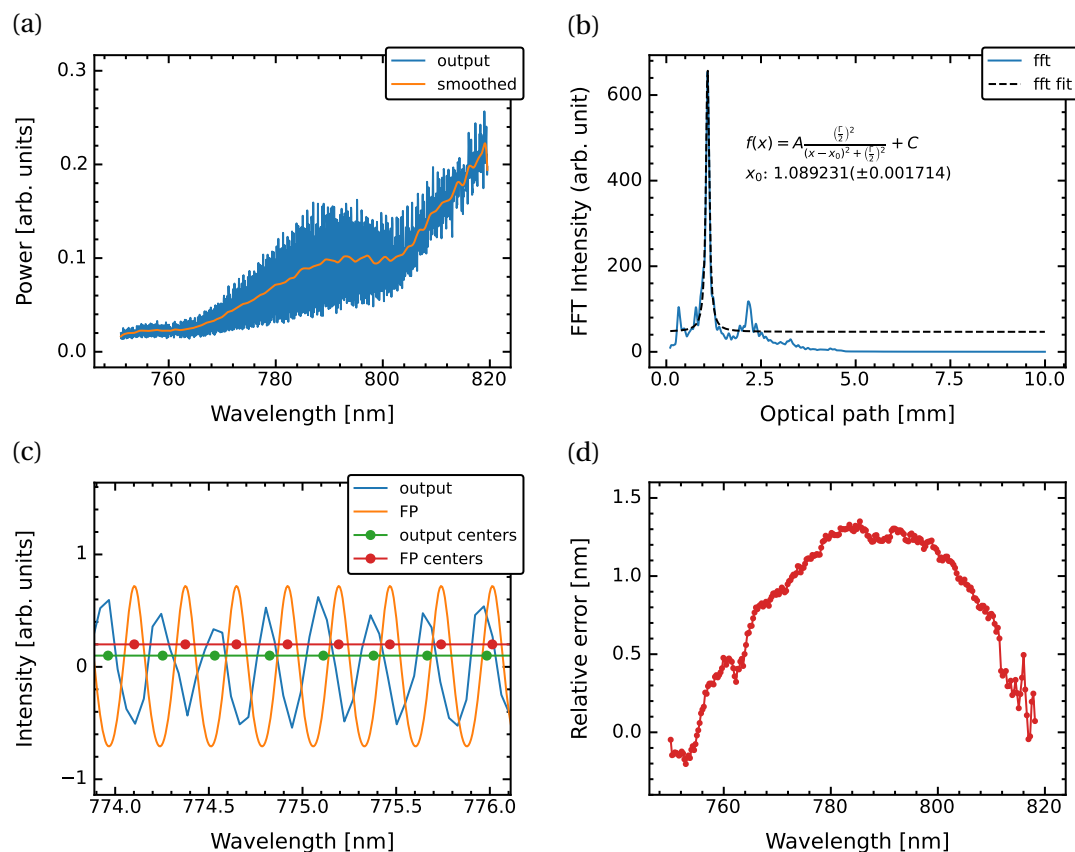


Figure A.3: (a) Ti:sapphire laser output spectrum. Fringes are due to interference of filter elements. b) FFT to extract the optical path of the involved cavity, according to Fabry-Pérot interference relations. (c) Comparison of peak locations of the measured output and the calculated output. (d) Relative wavelength error spectrum of the Ti:sapphire laser.

First, a transmission spectrum of a long-pass filter (edge at 600 nm and slightly reflective in the NIR range) is measured using the Ti:sapphire laser [Fig. A.3 (a)]. The transmission spectrum is full of interference fringes, and the wavelength is given by a linear interpolation according to the actuator position. Then, the optical path of the long-pass filter is extracted from the transmission spectrum by fast Fourier transform (FFT) according to Fabry-Pérot interference [Fig. A.3 (b)]. Next, a theoretical FP transmission spectrum is calculated and compared to the measured spectrum [Fig. A.3 (c)]. Finally, The difference between the corresponding fringe peaks of the two spectra is calculated and plotted with respect to the peak wavelength [Fig. A.3 (d)]. The result shows that there is as much as 1.5 nm for the error in wavelength

between the center and the edge of the scanned wavelength range when assuming a linear relation between wavelength and actuator position. This difference arises from the geometric configuration of the birefringent tuner and the actuator. Alternatively, direct wavelength measurements with the OSA give similar results but are much more time-consuming.

## A.6 Lock-in Amplification

Lock-in amplifiers use phase-sensitive detection to filter alternating current (AC) signals whose frequencies are very close to the reference frequency and to reduce noise in the frequency domain. The applied lock-in amplifier (Stanford Research Systems SR510 or SR830) is used together with an optical chopper (Thorlabs MC1000) or an acousto-optic modulator (see section 4.2.3) that modulates the light source with a fixed reference frequency [Fig. 4.2 (a)]. The reference modulation frequency should be, in general, smaller than the bandwidth of the photodetector, which is usually defined as the frequency at which the photosensitivity is attenuated by 3 dB (i.e., a factor of 2).

Inside the lock-in amplifier, a multiplier (phase sensitive detector, PSD) takes the signal and the reference as the inputs and gives the product of the two as the output.

$$V_{out} = \tilde{V}_{sig} \cdot \tilde{V}_{ref} \quad (\text{A.8})$$

$$= V_{sig} \sin(\omega_{sig} t + \theta_{sig}) \cdot V_{ref} \sin(\omega_{ref} t + \theta_{ref}) \quad (\text{A.9})$$

$$= \frac{1}{2} V_{ref} V_{sig} \cos[(\omega_{sig} - \omega_{ref}) t + (\theta_{sig} - \theta_{ref})] \quad (\text{A.10})$$

$$- \frac{1}{2} V_{ref} V_{sig} \cos[(\omega_{sig} + \omega_{ref}) t + (\theta_{sig} + \theta_{ref})] \quad (\text{A.11})$$

where  $\tilde{V}_{sig}$  is the small signal to be measured,  $\tilde{V}_{ref}$  is the reference with large enough amplitude. The output of the multiplier contains two terms with two frequency components. The frequency component  $(\omega_{sig} - \omega_{ref})$  is ideally zero and experimentally small, and the first term is a low-frequency (ideally DC) component. The frequency component  $(\omega_{sig} + \omega_{ref})$  is large, and the second term is a high-frequency component. The second term is filtered out by a low-pass filter, i.e., signal averaging, and the attenuation of the noise frequencies is determined by the bandwidth of the low-pass filter, i.e., the averaging time.

A lock-in amplifier usually contains one or two multipliers. For a lock-in amplifier with a single multiplier (e.g., SR510), the phase of the reference is adjusted to be the same as the signal,  $(\theta_{sig} - \theta_{ref}) = 0$ , and the resulting output is a DC signal with the amplification gain of  $V_{ref}/2$ :

$$V_{out} = \frac{1}{2} V_{ref} V_{sig}. \quad (\text{A.12})$$

For a lock-in amplifier with two multipliers (also called 2-channel or vector lock-in amplifier, e.g., SR830), the dependencies on the phase difference  $(\theta_{sig} - \theta_{ref})$  can be eliminated by

analyzing the two outputs,  $X$  and  $Y$ , with  $\pi/2$  constant phase delay:

$$X = \frac{1}{2} V_{sig} V_{ref} \cos(\theta_{sig} - \theta_{ref}), \quad (\text{A.13})$$

$$Y = \frac{1}{2} V_{sig} V_{ref} \cos\left(\theta_{sig} - \theta_{ref} + \frac{\pi}{2}\right), \quad (\text{A.14})$$

$$R = \frac{1}{2} V_{ref} V_{sig} = \sqrt{X^2 + Y^2}, \quad (\text{A.15})$$

$$\theta = (\theta_{sig} - \theta_{ref}) = \arctan\left(\frac{Y}{X}\right), \quad (\text{A.16})$$

where  $R$  is the phase-independent amplitude, and  $\theta$  is the phase difference between the signal and the reference.

The relation between the average time  $t_{avg}$  and the low-pass filter bandwidth  $f_{bw}$  is given by the Nyquist–Shannon sampling theorem, which states that if a function  $P(t)$  contains no frequencies higher than  $f_{bw}$  hertz, it is completely determined by giving its ordinates at a series of points spaced apart by  $t_{avg}$  seconds, where  $t_{avg}$  can be expressed as:

$$t_{avg} = \frac{1}{2f_{bw}}. \quad (\text{A.17})$$

The minimum detectable power is related to the filter bandwidth  $f_{bw}$  by:

$$P_{min} = NEP(\lambda) \times \sqrt{f_{bw}}, \quad (\text{A.18})$$

where  $NEP(\lambda)$  is the noise-equivalent power (in unit of  $W/\sqrt{Hz}$ ) of the photodetector.

When the reference or the signal is not perfectly sinusoidal, the output of the multiplier only contains the first term of the Fourier expansion, which results in a smaller amplitude of the output. On the signal side, the optical chopper modulates the light signal only into a square-like wave, while the acousto-optic modulator gives variable waveforms, including sinusoidal waves. On the reference side, the amplifier SR510 directly takes the external reference (square wave from the optical chopper or others from the function generator), while the amplifier SR830 internally generates a perfect sinusoidal signal with the same frequency and phase as the external reference for better performance.

## **A.7 High Order Modes of Doubly Resonant Cavity**

## A.7 High Order Modes of Doubly Resonant Cavity

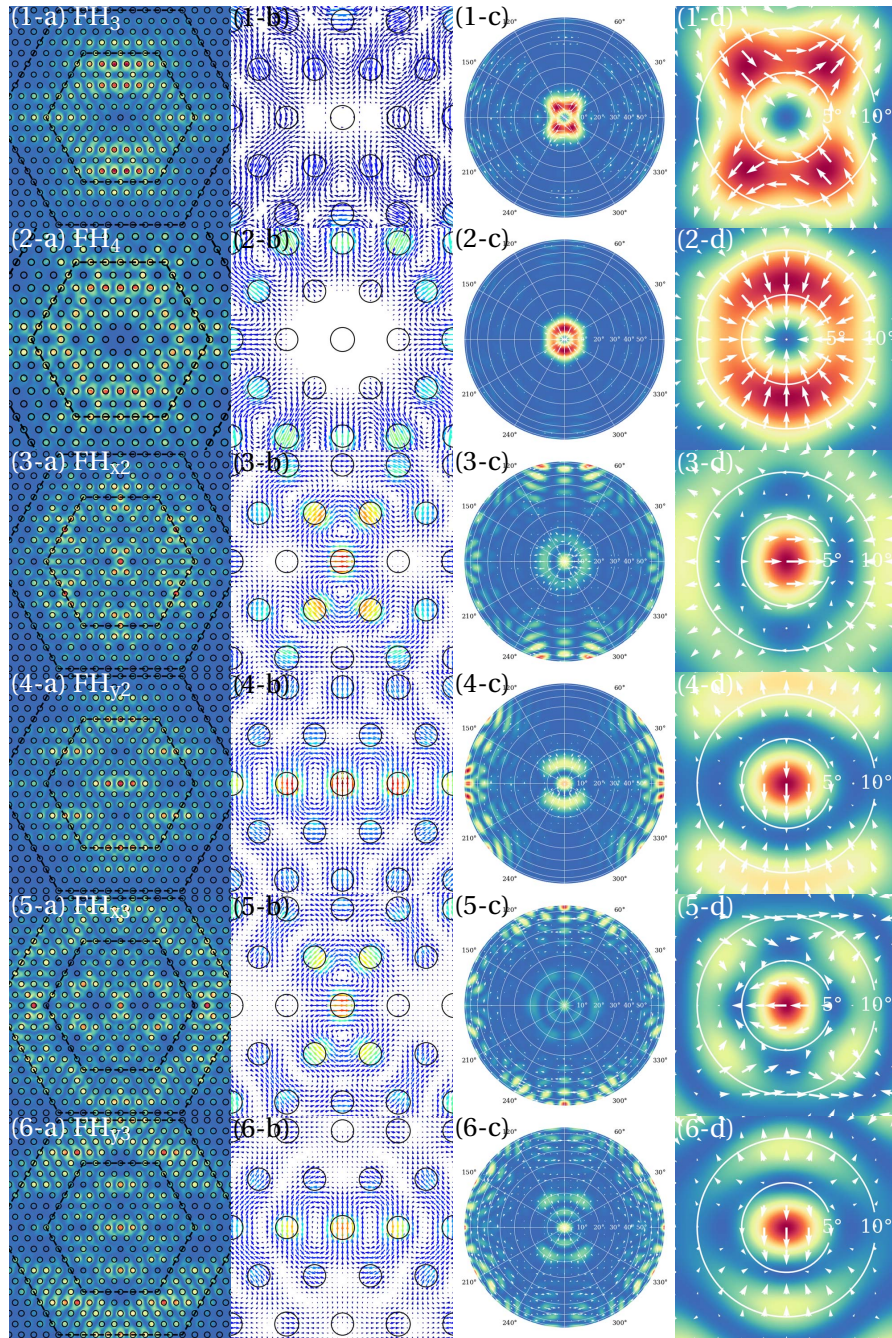


Figure A.4: High order modes at FH. The first column shows the near-field patterns. The color map shows the squared electric field,  $E_x^2 + E_y^2$ , at the center of the slab, and  $E_z = 0$ . The second column shows the vector map  $[E_x, E_y]$  of the electric field at the center of the slab. The color and the length of the arrows represent the norm of the electric field but are not necessarily normalized for all modes. The third column shows the full pattern of the far-field emission at the upper hemisphere of the slab. The color map and the white arrows show the intensity and the direction of the electric field. The center of the plots is at an emission angle of  $0^\circ$ , which is the normal direction of the slab, and the border is at an emission angle of  $90^\circ$ . The last column is a zoomed plot of the far-field emission, and the two white circles indicate the emission angle of  $5^\circ$  and  $10^\circ$ , respectively.





# Bibliography

- [1] P. B. Deotare, M. W. McCutcheon, I. W. Frank, M. Khan, and M. Lončar. “High quality factor photonic crystal nanobeam cavities”. In: *Applied Physics Letters* 94.12 (2009), p. 121106.
- [2] S. G. Johnson, S. Fan, P. R. Villeneuve, J. D. Joannopoulos, and L. Kolodziejski. “Guided modes in photonic crystal slabs”. In: *Physical Review B* 60.8 (1999), p. 5751.
- [3] E. Chow, S. Lin, S. Johnson, P. Villeneuve, J. Joannopoulos, J. R. Wendt, G. A. Vawter, W. Zubrzycki, H. Hou, and A. Alleman. “Three-dimensional control of light in a two-dimensional photonic crystal slab”. In: *Nature* 407.6807 (2000), pp. 983–986.
- [4] Y. Akahane, T. Asano, B.-S. Song, and S. Noda. “High-Q photonic nanocavity in a two-dimensional photonic crystal”. In: *nature* 425.6961 (2003), pp. 944–947.
- [5] T. A. Birks, J. C. Knight, and P. S. J. Russell. “Endlessly single-mode photonic crystal fiber”. In: *Optics letters* 22.13 (1997), pp. 961–963.
- [6] J. C. Knight. “Photonic crystal fibres”. In: *nature* 424.6950 (2003), pp. 847–851.
- [7] P. Russell. “Photonic crystal fibers”. In: *science* 299.5605 (2003), pp. 358–362.
- [8] C.-C. Cheng, V. Arbet-Engels, A. Scherer, and E. Yablonovitch. “Nanofabricated three dimensional photonic crystals operating at optical wavelengths”. In: *Physica Scripta* 1996.T68 (1996), p. 17.
- [9] S.-y. Lin, J. Fleming, D. Hetherington, B. Smith, R. Biswas, K. Ho, M. Sigalas, W. Zubrzycki, S. Kurtz, and J. Bur. “A three-dimensional photonic crystal operating at infrared wavelengths”. In: *Nature* 394.6690 (1998), pp. 251–253.
- [10] P. V. Braun, S. A. Rinne, and F. García-Santamaría. “Introducing defects in 3D photonic crystals: state of the art”. In: *Advanced Materials* 18.20 (2006), pp. 2665–2678.
- [11] E. Armstrong and C. O’Dwyer. “Artificial opal photonic crystals and inverse opal structures—fundamentals and applications from optics to energy storage”. In: *Journal of materials chemistry C* 3.24 (2015), pp. 6109–6143.
- [12] J. D. Joannopoulos, S. G. Johnson, J. N. Winn, and R. D. Meade. *Photonic Crystals: Molding the Flow of Light*. 2nd. Princeton University Press, New Jersey, 2008. ISBN: 9780691124568.

## Bibliography

---

- [13] E. Yablonovitch. “Inhibited spontaneous emission in solid-state physics and electronics”. In: *Physical review letters* 58.20 (1987), p. 2059.
- [14] S. John. “Strong localization of photons in certain disordered dielectric superlattices”. In: *Physical review letters* 58.23 (1987), p. 2486.
- [15] D. Lindley. “Landmarks—the birth of photonic crystals”. In: *Physics* 6 (2013), p. 94.
- [16] L. Rayleigh. “XXVI. On the remarkable phenomenon of crystalline reflexion described by Prof. Stokes”. In: *The London, Edinburgh, and Dublin Philosophical Magazine and Journal of Science* 26.160 (1888), pp. 256–265.
- [17] V. P. Bykov. “Spontaneous emission in a periodic structure”. In: *Soviet Journal of Experimental and Theoretical Physics* 35 (1972), p. 269.
- [18] E. Yablonovitch, T. Gmitter, and K.-M. Leung. “Photonic band structure: The face-centered-cubic case employing nonspherical atoms”. In: *Physical review letters* 67.17 (1991), p. 2295.
- [19] T. F. Krauss, R. M. D. L. Rue, and S. Brand. “Two-dimensional photonic-bandgap structures operating at near-infrared wavelengths”. In: *Nature* 383.6602 (1996), pp. 699–702.
- [20] California Institute of Technology, Mineral Spectroscopy Server. *SEM image of a gem-quality opal from Australia*. URL: <http://minerals.caltech.edu/> (visited on 01/01/2023).
- [21] Musée de Minéralogie, Mines Paris - PSL, photography Eloïse GAILLOU. *Opal from Tenel Wega, Wollo, Ethiopia (#83317; 3.8 x 5 x 2.7 cm)*. URL: <https://www.musee-minesparis.psl.eu/Gifts/Gifts-2015/> (visited on 01/01/2023).
- [22] J. M. Medina, J. A. Díaz, and P. Vukusic. “Classification of peacock feather reflectance using principal component analysis similarity factors from multispectral imaging data”. In: *Optics express* 23.8 (2015), pp. 10198–10212.
- [23] R. O. Prum, T. Quinn, and R. H. Torres. “Anatomically diverse butterfly scales all produce structural colours by coherent scattering”. In: *Journal of Experimental Biology* 209.4 (2006), pp. 748–765.
- [24] J. Teyssier, S. V. Saenko, D. Van Der Marel, and M. C. Milinkovitch. “Photonic crystals cause active colour change in chameleons”. In: *Nature communications* 6.1 (2015), p. 6368.
- [25] J. Sanders. “Colour of precious opal”. In: *Nature* 204 (1964), pp. 1151–1153.
- [26] V. Astratov, V. Bogomolov, A. Kaplyanskii, A. Prokofiev, L. Samoilovich, S. Samoilovich, and Y. A. Vlasov. “Optical spectroscopy of opal matrices with CdS embedded in its pores: Quantum confinement and photonic band gap effects”. In: *Il Nuovo Cimento D* 17 (1995), pp. 1349–1354.
- [27] J. P. Vigneron and P. Simonis. “Natural photonic crystals”. In: *Physica B: Condensed Matter* 407.20 (2012), pp. 4032–4036.

- [28] E. J. Denton and M. Land. “Mechanism of reflexion in silvery layers of fish and cephalopods”. In: *Proceedings of the Royal Society of London. Series B. Biological Sciences* 178.1050 (1971), pp. 43–61.
- [29] F. Ollivier, D. Samuelson, D. Brooks, P. Lewis, M. Kallberg, and A. Komáromy. “Comparative morphology of the tapetum lucidum (among selected species)”. In: *Veterinary ophthalmology* 7.1 (2004), pp. 11–22.
- [30] M. Land. “A multilayer interference reflector in the eye of the scallop, *Pecten maximus*”. In: *Journal of Experimental Biology* 45.3 (1966), pp. 433–447.
- [31] J. Zi, X. Yu, Y. Li, X. Hu, C. Xu, X. Wang, X. Liu, and R. Fu. “Coloration strategies in peacock feathers”. In: *Proceedings of the National Academy of Sciences* 100.22 (2003), pp. 12576–12578.
- [32] V. Saranathan, S. Narayanan, A. Sandy, E. R. Dufresne, and R. O. Prum. “Evolution of single gyroid photonic crystals in bird feathers”. In: *Proceedings of the National Academy of Sciences* 118.23 (2021), e2101357118.
- [33] G. S. Smith. “Structural color of *Morpho* butterflies”. In: *American Journal of Physics* 77.11 (2009), pp. 1010–1019.
- [34] A. R. Parker, V. L. Welch, D. Driver, and N. Martini. “Opal analogue discovered in a weevil”. In: *Nature* 426.6968 (2003), pp. 786–787.
- [35] J. W. Galusha, L. R. Richey, J. S. Gardner, J. N. Cha, and M. H. Bartl. “Discovery of a diamond-based photonic crystal structure in beetle scales”. In: *Physical Review E* 77.5 (2008), p. 050904.
- [36] B. D. Wilts, K. Michielsen, J. Kuipers, H. De Raedt, and D. G. Stavenga. “Brilliant camouflage: photonic crystals in the diamond weevil, *Entimus imperialis*”. In: *Proceedings of the Royal Society B: Biological Sciences* 279.1738 (2012), pp. 2524–2530.
- [37] D. J. Griffiths. *Introduction to Electrodynamics*. 4th. Pearson Education, Glenview, 2013. ISBN: 9780321856562.
- [38] H. A. Haus. *Waves and fields in optoelectronics*. Prentice-Hall, Inc., Englewood Cliffs, New Jersey, 1984. ISBN: 0139460535.
- [39] C. Kittel and P. McEuen. *Introduction to solid state physics*. 8th. John Wiley & Sons, Inc., Hoboken, 2005. ISBN: 047141526X.
- [40] N. W. Ashcroft and N. D. Mermin. *Solid State Physics*. Harcourt, Inc, Orlando, 1976. ISBN: 0030839939.
- [41] K. Sakoda. *Optical properties of photonic crystals*. 2nd. Springer-Verlag Berlin Heidelberg, 2005. ISBN: 3540206825.
- [42] K. Busch, S. Lölkes, R. B. Wehrspohn, and H. Föll. *Photonic crystals: advances in design, fabrication, and characterization*. WILEY-VCH Verlag GmbH & Co.KGaA, Weinheim, 2004. ISBN: 3527404325.

## Bibliography

---

- [43] J.-M. Lourtioz, H. Benisty, V. Berger, J.-M. Berard, D. Maystre, and A. Tcheltnokov. *Photonic crystals: towards nanoscale photonic devices*. 2nd. Springer-Verlag Berlin Heidelberg, 2008. ISBN: 9783540783466.
- [44] K.-M. Leung and Y. Liu. “Full vector wave calculation of photonic band structures in face-centered-cubic dielectric media”. In: *Physical Review Letters* 65.21 (1990), p. 2646.
- [45] Z. Zhang and S. Satpathy. “Electromagnetic wave propagation in periodic structures: Bloch wave solution of Maxwell’s equations”. In: *Physical review letters* 65.21 (1990), p. 2650.
- [46] M. Minkov, I. A. Williamson, L. C. Andreani, D. Gerace, B. Lou, A. Y. Song, T. W. Hughes, and S. Fan. “Inverse design of photonic crystals through automatic differentiation”. In: *ACS Photonics* 7.7 (2020), pp. 1729–1741.
- [47] M. Minkov. *Legume project*. URL: <https://github.com/fancompute/legume> (visited on 01/01/2023).
- [48] L. C. Andreani and D. Gerace. “Photonic-crystal slabs with a triangular lattice of triangular holes investigated using a guided-mode expansion method”. In: *Physical Review B* 73.23 (2006), p. 235114.
- [49] D. Englund, I. Fushman, and J. Vuckovic. “General recipe for designing photonic crystal cavities”. In: *Optics express* 13.16 (2005), pp. 5961–5975.
- [50] V. Zabelin. “Numerical Investigations of Two-Dimensional Photonic Crystal Optical Properties, Design and Analysis of Photonic Crystal Based Structures”. In: *EPFL thesis* 4315 (2009).
- [51] M. Minkov. “Numerical study and optimization of photonic crystals”. In: *EPFL thesis* 6857 (2016).
- [52] Z. Zhang and M. Qiu. “Small-volume waveguide-section high Q microcavities in 2D photonic crystal slabs”. In: *Optics express* 12.17 (2004), pp. 3988–3995.
- [53] H.-Y. Ryu, M. Notomi, and Y.-H. Lee. “High-quality-factor and small-mode-volume hexapole modes in photonic-crystal-slab nanocavities”. In: *Applied physics letters* 83.21 (2003), pp. 4294–4296.
- [54] M. Notomi, A. Shinya, S. Mitsugi, E. Kuramochi, and H. Ryu. “Waveguides, resonators and their coupled elements in photonic crystal slabs”. In: *Optics express* 12.8 (2004), pp. 1551–1561.
- [55] E. Kuramochi, M. Notomi, S. Mitsugi, A. Shinya, T. Tanabe, and T. Watanabe. “Ultra-high-Q photonic crystal nanocavities realized by the local width modulation of a line defect”. In: *Applied physics letters* 88.4 (2006), p. 041112.
- [56] B.-S. Song, S. Noda, T. Asano, and Y. Akahane. “Ultra-high-Q photonic double-heterostructure nanocavity”. In: *Nature materials* 4.3 (2005), pp. 207–210.
- [57] Y. Tanaka, T. Asano, and S. Noda. “Design of Photonic Crystal Nanocavity With Q-Factor of  $\sim 10^9$ ”. In: *Journal of Lightwave Technology* 26.11 (2008), pp. 1532–1539.

- [58] C. Jamois, R. Wehrspohn, L. Andreani, C. Hermann, O. Hess, and U. Gösele. “Silicon-based two-dimensional photonic crystal waveguides”. In: *Photonics and Nanostructures-Fundamentals and Applications* 1.1 (2003), pp. 1–13.
- [59] A. Chutinan and S. Noda. “Waveguides and waveguide bends in two-dimensional photonic crystal slabs”. In: *Physical review B* 62.7 (2000), p. 4488.
- [60] H. S. Dutta, A. K. Goyal, V. Srivastava, and S. Pal. “Coupling light in photonic crystal waveguides: A review”. In: *Photonics and Nanostructures-Fundamentals and Applications* 20 (2016), pp. 41–58.
- [61] Y. A. Vlasov, M. O’boyle, H. F. Hamann, and S. J. McNab. “Active control of slow light on a chip with photonic crystal waveguides”. In: *nature* 438.7064 (2005), pp. 65–69.
- [62] T. F. Krauss. “Slow light in photonic crystal waveguides”. In: *Journal of Physics D: Applied Physics* 40.9 (2007), p. 2666.
- [63] T. Baba. “Slow light in photonic crystals”. In: *Nature photonics* 2.8 (2008), pp. 465–473.
- [64] B. Corcoran, C. Monat, C. Grillet, D. J. Moss, B. J. Eggleton, T. P. White, L. O’Faolain, and T. F. Krauss. “Green light emission in silicon through slow-light enhanced third-harmonic generation in photonic-crystal waveguides”. In: *Nature photonics* 3.4 (2009), pp. 206–210.
- [65] C. Monat, M. Ebnali-Heidari, C. Grillet, B. Corcoran, B. J. Eggleton, T. White, L. O’Faolain, J. Li, and T. F. Krauss. “Four-wave mixing in slow light engineered silicon photonic crystal waveguides”. In: *Optics express* 18.22 (2010), pp. 22915–22927.
- [66] N. Matsuda, T. Kato, K.-i. Harada, H. Takesue, E. Kuramochi, H. Taniyama, and M. Notomi. “Slow light enhanced optical nonlinearity in a silicon photonic crystal coupled-resonator optical waveguide”. In: *Optics express* 19.21 (2011), pp. 19861–19874.
- [67] H. Takesue, N. Matsuda, E. Kuramochi, W. J. Munro, and M. Notomi. “An on-chip coupled resonator optical waveguide single-photon buffer”. In: *Nature communications* 4.1 (2013), p. 2725.
- [68] N. Matsuda, H. Takesue, K. Shimizu, Y. Tokura, E. Kuramochi, and M. Notomi. “Slow light enhanced correlated photon pair generation in photonic-crystal coupled-resonator optical waveguides”. In: *Optics express* 21.7 (2013), pp. 8596–8604.
- [69] H. Takesue, N. Matsuda, E. Kuramochi, and M. Notomi. “Entangled photons from on-chip slow light”. In: *Scientific reports* 4.1 (2014), p. 3913.
- [70] M. Sabry. “Light Confinement and Nonlinear Light-Matter Interaction in Semiconductor Photonic Crystal Cavities”. In: *EPFL thesis* 8562 (2018).
- [71] B. E. Saleh and M. C. Teich. *Fundamentals of photonics*. 2nd. John Wiley & Sons, Inc., Hoboken, New Jersey, 2007. ISBN: 9780471358329.
- [72] E. M. Purcell. “Spontaneous emission probabilities at radio frequency”. In: *Physical Review* 69 (1946), p. 681.

## Bibliography

---

- [73] E. M. Purcell. “Spontaneous emission probabilities at radio frequencies”. In: *Confined Electrons and Photons*. Springer, 1995, pp. 839–839.
- [74] L. Collot, V. Lefevre-Seguin, M. Brune, J. Raimond, and S. Haroche. “Very high-Q whispering-gallery mode resonances observed on fused silica microspheres”. In: *EPL (Europhysics Letters)* 23.5 (1993), p. 327.
- [75] L. C. Andreani, G. Panzarini, and J.-M. Gérard. “Strong-coupling regime for quantum boxes in pillar microcavities: Theory”. In: *Physical Review B* 60.19 (1999), p. 13276.
- [76] P. T. Kristensen, C. Van Vlack, and S. Hughes. “Generalized effective mode volume for leaky optical cavities”. In: *Optics letters* 37.10 (2012), pp. 1649–1651.
- [77] K. Lee, P. Leung, and K. Pang. “Dyadic formulation of morphology-dependent resonances. I. Completeness relation”. In: *JOSA B* 16.9 (1999), pp. 1409–1417.
- [78] S. Fan, W. Suh, and J. D. Joannopoulos. “Temporal coupled-mode theory for the Fano resonance in optical resonators”. In: *JOSA A* 20.3 (2003), pp. 569–572.
- [79] W. Suh, Z. Wang, and S. Fan. “Temporal coupled-mode theory and the presence of non-orthogonal modes in lossless multimode cavities”. In: *IEEE Journal of Quantum Electronics* 40.10 (2004), pp. 1511–1518.
- [80] S. Combrié, A. De Rossi, et al. “Directive emission from high-Q photonic crystal cavities through band folding”. In: *Physical Review B* 79.4 (2009), p. 041101.
- [81] S. L. Portalupi, M. Galli, C. Reardon, T. Krauss, L. O’Faolain, L. C. Andreani, and D. Gerace. “Planar photonic crystal cavities with far-field optimization for high coupling efficiency and quality factor”. In: *Optics express* 18.15 (2010), pp. 16064–16073.
- [82] R. W. Boyd. *Nonlinear Optics*. 3rd. Academic Press, Cambridge, Massachusetts, 2008. ISBN: 9780123694706.
- [83] P. N. Butcher and D. Cotter. *The Elements of Nonlinear Optics*. Cambridge Studies in Modern Optics. Cambridge University Press, Cambridge, United Kingdom, 1990. ISBN: 0521341833.
- [84] F. Zernike and J. E. Midwinter. *Applied nonlinear optics*. Dover Publications, New York, 2006. ISBN: 048645360X.
- [85] H. Schulz and K. Thiemann. “Crystal structure refinement of AlN and GaN”. In: *Solid State Communications* 23.11 (1977), pp. 815–819.
- [86] C. Hammond. *The basics of crystallography and diffraction*. 4th. Oxford University Press, Oxford, United Kingdom, 2015. ISBN: 9780198738671.
- [87] S. Committee et al. “Standards on Piezoelectric Crystals, 1949”. In: *Proceedings of the IRE* 37.12 (1949), pp. 1378–1395. DOI: 10.1109/JRPROC.1949.229975.
- [88] H. Zhang, X. He, Y. Shih, M. Schurman, Z. Feng, and R. Stall. “Study of nonlinear optical effects in GaN: Mg epitaxial film”. In: *Applied physics letters* 69.20 (1996), pp. 2953–2955.

- [89] S. Shokhovets, M. Himmerlich, L. Kirste, J. Leach, and S. Krischok. “Birefringence and refractive indices of wurtzite GaN in the transparency range”. In: *Applied Physics Letters* 107.9 (2015), p. 092104.
- [90] D. Brunner, H. Angerer, E. Bustarret, F. Freudenberg, R. Höpler, R. Dimitrov, O. Ambacher, and M. Stutzmann. “Optical constants of epitaxial AlGaIn films and their temperature dependence”. In: *Journal of applied physics* 82.10 (1997), pp. 5090–5096.
- [91] M. Abe, H. Sato, I. Shoji, J. Suda, M. Yoshimura, Y. Kitaoka, Y. Mori, and T. Kondo. “Accurate measurement of quadratic nonlinear-optical coefficients of gallium nitride”. In: *JOSA B* 27.10 (2010), pp. 2026–2034.
- [92] Y. Fujii, S. Yoshida, S. Misawa, S. Maekawa, and T. Sakudo. “Nonlinear optical susceptibilities of AlN film”. In: *Applied Physics Letters* 31.12 (1977), pp. 815–816.
- [93] D. Blanc, A. Bouchoux, C. Plumereau, A. Cachard, and J. Roux. “Phase-matched frequency doubling in an aluminum nitride waveguide with a tunable laser source”. In: *Applied physics letters* 66.6 (1995), pp. 659–661.
- [94] J. Miragliotta and D. Wickenden. “Optical third-harmonic studies of the dispersion in  $\chi^{(3)}$  for gallium nitride thin films on sapphire”. In: *Physical Review B* 50.20 (1994), p. 14960.
- [95] I. Skinner and S. Garth. “Reconciliation of esu and mksa units in nonlinear optics”. In: *American Journal of Physics* 58.2 (1990), pp. 177–181.
- [96] N. Vico Triviño, U. Dharanipathy, J.-F. Carlin, Z. Diao, R. Houdre, and N. Grandjean. “Integrated photonics on silicon with wide bandgap GaN semiconductor”. In: *Applied Physics Letters* 102.8 (2013), p. 081120.
- [97] A. Dadgar, M. Poschenrieder, J. Bläsing, O. Contreras, F. Bertram, T. Riemann, A. Reiher, M. Kunze, I. Daumiller, A. Krtschil, et al. “MOVPE growth of GaN on Si (1 1 1) substrates”. In: *Journal of Crystal Growth* 248 (2003), pp. 556–562.
- [98] A. Dadgar. “Sixteen years GaN on Si”. In: *physica status solidi (b)* 252.5 (2015), pp. 1063–1068.
- [99] K. J. Chen, O. Häberlen, A. Lidow, C. lin Tsai, T. Ueda, Y. Uemoto, and Y. Wu. “GaN-on-Si power technology: Devices and applications”. In: *IEEE Transactions on Electron Devices* 64.3 (2017), pp. 779–795.
- [100] S. Figge, H. Kröncke, D. Hommel, and B. M. Epelbaum. “Temperature dependence of the thermal expansion of AlN”. In: *Applied Physics Letters* 94.10 (2009), p. 101915.
- [101] C. Roder, S. Einfeldt, S. Figge, and D. Hommel. “Temperature dependence of the thermal expansion of GaN”. In: *Physical Review B* 72.8 (2005), p. 085218.
- [102] Y. Okada and Y. Tokumaru. “Precise determination of lattice parameter and thermal expansion coefficient of silicon between 300 and 1500 K”. In: *Journal of applied physics* 56.2 (1984), pp. 314–320.
- [103] W. Yim and R. Paff. “Thermal expansion of AlN, sapphire, and silicon”. In: *Journal of Applied Physics* 45.3 (1974), pp. 1456–1457.

## Bibliography

---

- [104] I. Rousseau, G. Callsen, G. Jacopin, J.-F. Carlin, R. Butté, and N. Grandjean. “Optical absorption and oxygen passivation of surface states in III-nitride photonic devices”. In: *Journal of Applied Physics* 123.11 (2018), p. 113103.
- [105] *GDSII format specifications*. URL: <https://boolean.klaasholwerda.nl/interface/bnf/gdsformat.html> (visited on 01/01/2023).
- [106] *GdsSpy project*. URL: <https://github.com/heitzmann/gdsSpy> (visited on 01/01/2023).
- [107] T. Chang. “Proximity effect in electron-beam lithography”. In: *Journal of vacuum science and technology* 12.6 (1975), pp. 1271–1275.
- [108] E. Seo, B. K. Choi, and O. Kim. “Determination of proximity effect parameters and the shape bias parameter in electron beam lithography”. In: *Microelectronic Engineering* 53.1-4 (2000), pp. 305–308.
- [109] R. Therisod. “Resonant optical trapping in hollow photonic crystal cavities and its potential use for bacterial characterization”. In: *EPFL thesis* 9661 (2019).
- [110] K. Nojiri. *Dry etching technology for semiconductors*. Springer International Publishing, Switzerland, 2015. ISBN: 9783319102955.
- [111] M. Lin, B. Sverdlov, S. Strite, H. Morkoc, and A. Drakin. “Refractive indices of wurtzite and zinblend GaN”. In: *Electronics Letters* 29.20 (1993), pp. 1759–1760.
- [112] J. Pastrňák and L. Roskovcová. “Refraction index measurements on AlN single crystals”. In: *physica status solidi (b)* 14.1 (1966), K5–K8.
- [113] L. V. Rodríguez-de Marcos, J. I. Larruquert, J. A. Méndez, and J. A. Aznárez. “Self-consistent optical constants of SiO<sub>2</sub> and Ta<sub>2</sub>O<sub>5</sub> films”. In: *Optical Materials Express* 6.11 (2016), pp. 3622–3637.
- [114] K. Adachi, H. Ogi, A. Nagakubo, N. Nakamura, M. Hirao, M. Imade, M. Yoshimura, and Y. Mori. “Elastic constants of GaN between 10 and 305 K”. In: *Journal of Applied Physics* 119.24 (2016), p. 245111.
- [115] W. M. Haynes and D. R. Lide. *CRC handbook of chemistry and physics*. 95th. CRC Press, Boca Raton, 2014. ISBN: 978-1-4822-0868-9.
- [116] P. Agaskar, V. Day, and W. Klemperer. “A new route to trimethylsilylated spherosilicates. Synthesis and structure of [Si<sub>12</sub>O<sub>18</sub>](OSiMe<sub>3</sub>)<sub>12</sub>, D<sub>3h</sub>-[Si<sub>14</sub>O<sub>21</sub>](OSiMe<sub>3</sub>)<sub>14</sub>, and C<sub>2v</sub>-[Si<sub>14</sub>O<sub>21</sub>](OSiMe<sub>3</sub>)<sub>14</sub>”. In: *Journal of the American Chemical Society* 109.18 (1987), pp. 5554–5556.
- [117] H. Namatsu, T. Yamaguchi, M. Nagase, K. Yamazaki, and K. Kurihara. “Nano-patterning of a hydrogen silsesquioxane resist with reduced linewidth fluctuations”. In: *Microelectronic Engineering* 41 (1998), pp. 331–334.
- [118] A. Grigorescu and C. Hagen. “Resists for sub-20-nm electron beam lithography with a focus on HSQ: state of the art”. In: *Nanotechnology* 20.29 (2009), p. 292001.



- [119] X. Liu, C. Sun, B. Xiong, L. Niu, Z. Hao, Y. Han, and Y. Luo. "Smooth etching of epitaxially grown AlN film by  $\text{Cl}_2/\text{BCl}_3/\text{Ar}$ -based inductively coupled plasma". In: *Vacuum* 116 (2015), pp. 158–162.
- [120] M. Skorobogatiy, G. Bégin, and A. Talneau. "Statistical analysis of geometrical imperfections from the images of 2D photonic crystals". In: *Optics Express* 13.7 (2005), pp. 2487–2502.
- [121] J. Canny. "A computational approach to edge detection". In: *IEEE Transactions on pattern analysis and machine intelligence* PAMI-8.6 (1986), pp. 679–698.
- [122] D. Sliney. "What is light? The visible spectrum and beyond". In: *Eye* 30.2 (2016), pp. 222–229.
- [123] P. F. Moulton. "Spectroscopic and laser characteristics of  $\text{Ti: Al}_2\text{O}_3$ ". In: *JOSA B* 3.1 (1986), pp. 125–133.
- [124] K. Wall and A. Sanchez. "Titanium sapphire lasers". In: *The Lincoln laboratory journal* 3.3 (1990), pp. 447–462.
- [125] D. E. Spence, P. N. Kean, and W. Sibbett. "60-fsec pulse generation from a self-mode-locked  $\text{Ti: sapphire}$  laser". In: *Optics letters* 16.1 (1991), pp. 42–44.
- [126] D. Strickland and G. Mourou. "Compression of amplified chirped optical pulses". In: *Optics communications* 55.6 (1985), pp. 447–449.
- [127] C. Raman and N. Nagendra Nathe. "The diffraction of light by high frequency sound waves: Part I." In: *Proceedings of the Indian Academy of Sciences-Section A*. Vol. 2. Springer. 1935, pp. 406–412.
- [128] C. Burckhardt. "Diffraction of a plane wave at a sinusoidally stratified dielectric grating". In: *JOSA* 56.11 (1966), pp. 1502–1508.
- [129] M. Moharam and L. Young. "Criterion for Bragg and Raman-Nath diffraction regimes". In: *Applied optics* 17.11 (1978), pp. 1757–1759.
- [130] *N-BK7, SCHOTT*. URL: <https://refractiveindex.info/?shelf=glass%5C&book=BK7%5C&page=SCHOTT> (visited on 01/01/2023).
- [131] M. Galli, S. Portalupi, M. Belotti, L. Andreani, L. O’Faolain, and T. Krauss. "Light scattering and Fano resonances in high-Q photonic crystal nanocavities". In: *Applied Physics Letters* 94.7 (2009), p. 071101.
- [132] U. Fano. "Effects of configuration interaction on intensities and phase shifts". In: *Physical Review* 124.6 (1961), p. 1866.
- [133] P. Drummond, K. McNeil, and D. Walls. "Non-equilibrium transitions in sub/second harmonic generation". In: *Optica Acta: International Journal of Optics* 27.3 (1980), pp. 321–335.
- [134] R. Paschotta, K. Fiedler, P. Kürz, and J. Mlynek. "Nonlinear mode coupling in doubly resonant frequency doublers". In: *Applied Physics B* 58.2 (1994), pp. 117–122.

## Bibliography

---

- [135] V. Berger. “Second-harmonic generation in monolithic cavities”. In: *JOSA B* 14.6 (1997), pp. 1351–1360.
- [136] A. Rodriguez, M. Soljačić, J. D. Joannopoulos, and S. G. Johnson. “ $\chi$  (2) and  $\chi$  (3) harmonic generation at a critical power in inhomogeneous doubly resonant cavities”. In: *Optics express* 15.12 (2007), pp. 7303–7318.
- [137] Z. Lin, X. Liang, M. Lončar, S. G. Johnson, and A. W. Rodriguez. “Cavity-enhanced second-harmonic generation via nonlinear-overlap optimization”. In: *Optica* 3.3 (2016), pp. 233–238.
- [138] M. Liscidini and L. C. Andreani. “Second-harmonic generation in doubly resonant microcavities with periodic dielectric mirrors”. In: *Physical Review E* 73.1 (2006), p. 016613.
- [139] K. Rivoire, S. Buckley, and J. Vučković. “Multiply resonant photonic crystal nanocavities for nonlinear frequency conversion”. In: *Optics express* 19.22 (2011), pp. 22198–22207.
- [140] S. Buckley, M. Radulaski, J. L. Zhang, J. Petykiewicz, K. Biermann, and J. Vučković. “Multimode nanobeam cavities for nonlinear optics: high quality resonances separated by an octave”. In: *Optics express* 22.22 (2014), pp. 26498–26509.
- [141] L. Scaccabarozzi, M. Fejer, Y. Huo, S. Fan, X. Yu, and J. S. Harris. “Enhanced second-harmonic generation in AlGaAs/Al<sub>x</sub>O<sub>y</sub> tightly confining waveguides and resonant cavities”. In: *Optics letters* 31.24 (2006), pp. 3626–3628.
- [142] W. H. P. Pernice, C. Xiong, C. Schuck, and H. Tang. “Second harmonic generation in phase matched aluminum nitride waveguides and micro-ring resonators”. In: *Applied Physics Letters* 100.22 (2012), p. 223501.
- [143] A. W. Bruch, X. Liu, X. Guo, J. B. Surya, Z. Gong, L. Zhang, J. Wang, J. Yan, and H. X. Tang. “17 000%/W second-harmonic conversion efficiency in single-crystalline aluminum nitride microresonators”. In: *Applied Physics Letters* 113.13 (2018), p. 131102.
- [144] M. Celebrano, X. Wu, M. Baselli, S. Großmann, P. Biagioni, A. Locatelli, C. De Angelis, G. Cerullo, R. Osellame, B. Hecht, et al. “Mode matching in multiresonant plasmonic nanoantennas for enhanced second harmonic generation”. In: *Nature nanotechnology* 10.5 (2015), pp. 412–417.
- [145] M. W. McCutcheon, J. F. Young, G. W. Rieger, D. Dalacu, S. Frédérick, P. J. Poole, and R. L. Williams. “Experimental demonstration of second-order processes in photonic crystal microcavities at submilliwatt excitation powers”. In: *Physical Review B* 76.24 (2007), p. 245104.
- [146] K. Rivoire, Z. Lin, F. Hatami, W. T. Masselink, and J. Vučković. “Second harmonic generation in gallium phosphide photonic crystal nanocavities with ultralow continuous wave pump power”. In: *Optics express* 17.25 (2009), pp. 22609–22615.
- [147] M. Galli, D. Gerace, K. Welna, T. F. Krauss, L. O’Faolain, G. Guizzetti, and L. C. Andreani. “Low-power continuous-wave generation of visible harmonics in silicon photonic crystal nanocavities”. In: *Optics express* 18.25 (2010), pp. 26613–26624.

- [148] S. Yamada, B.-S. Song, S. Jeon, J. Upham, Y. Tanaka, T. Asano, and S. Noda. “Second-harmonic generation in a silicon-carbide-based photonic crystal nanocavity”. In: *Optics letters* 39.7 (2014), pp. 1768–1771.
- [149] S. Buckley, M. Radulaski, J. Petykiewicz, K. G. Lagoudakis, J.-H. Kang, M. Brongersma, K. Biermann, and J. Vuckovic. “Second-harmonic generation in GaAs photonic crystal cavities in (111) B and (001) crystal orientations”. In: *Acs Photonics* 1.6 (2014), pp. 516–523.
- [150] Y. Zeng, I. Roland, X. Checoury, Z. Han, M. El Kurdi, S. Sauvage, B. Gayral, C. Brimont, T. Guillet, M. Mexis, et al. “Resonant second harmonic generation in a gallium nitride two-dimensional photonic crystal on silicon”. In: *Applied Physics Letters* 106.8 (2015), p. 081105.
- [151] M. S. Mohamed, A. Simbula, J.-F. Carlin, M. Minkov, D. Gerace, V. Savona, N. Grandjean, M. Galli, and R. Houdré. “Efficient continuous-wave nonlinear frequency conversion in high-Q gallium nitride photonic crystal cavities on silicon”. In: *APL Photonics* 2.3 (2017), p. 031301.
- [152] B.-S. Song, T. Asano, S. Jeon, H. Kim, C. Chen, D. D. Kang, and S. Noda. “Ultrahigh-Q photonic crystal nanocavities based on 4H silicon carbide”. In: *Optica* 6.8 (2019), pp. 991–995.
- [153] M. Clementi, K. Debnath, M. Sotto, A. Barone, A. Z. Khokhar, T. D. Bucio, S. Saito, F. Y. Gardes, D. Bajoni, and M. Galli. “Cavity-enhanced harmonic generation in silicon rich nitride photonic crystal microresonators”. In: *Applied Physics Letters* 114.13 (2019), p. 131103.
- [154] M. Minkov, D. Gerace, and S. Fan. “Doubly resonant  $\chi$  (2) nonlinear photonic crystal cavity based on a bound state in the continuum”. In: *Optica* 6.8 (2019), pp. 1039–1045.
- [155] C. W. Hsu, B. Zhen, A. D. Stone, J. D. Joannopoulos, and M. Soljačić. “Bound states in the continuum”. In: *Nature Reviews Materials* 1.9 (2016), pp. 1–13.
- [156] C. W. Hsu, B. Zhen, J. Lee, S.-L. Chua, S. G. Johnson, J. D. Joannopoulos, and M. Soljačić. “Observation of trapped light within the radiation continuum”. In: *Nature* 499.7457 (2013), pp. 188–191.
- [157] B. Zhen, C. W. Hsu, L. Lu, A. D. Stone, and M. Soljačić. “Topological nature of optical bound states in the continuum”. In: *Physical review letters* 113.25 (2014), p. 257401.
- [158] L. Carletti, K. Koshelev, C. De Angelis, and Y. Kivshar. “Giant nonlinear response at the nanoscale driven by bound states in the continuum”. In: *Physical review letters* 121.3 (2018), p. 033903.
- [159] L. Carletti, S. S. Kruk, A. A. Bogdanov, C. De Angelis, and Y. Kivshar. “High-harmonic generation at the nanoscale boosted by bound states in the continuum”. In: *Physical Review Research* 1.2 (2019), p. 023016.

## Bibliography

---

- [160] L. Xu, K. Zangeneh Kamali, L. Huang, M. Rahmani, A. Smirnov, R. Camacho-Morales, Y. Ma, G. Zhang, M. Woolley, D. Neshev, et al. “Dynamic nonlinear image tuning through magnetic dipole quasi-BIC ultrathin resonators”. In: *Advanced Science* 6.15 (2019), p. 1802119.
- [161] X. Ge, M. Minkov, S. Fan, X. Li, and W. Zhou. “Low index contrast heterostructure photonic crystal cavities with high quality factors and vertical radiation coupling”. In: *Applied Physics Letters* 112.14 (2018), p. 141105.
- [162] H. M. Doleman, F. Monticone, W. den Hollander, A. Alù, and A. F. Koenderink. “Experimental observation of a polarization vortex at an optical bound state in the continuum”. In: *Nature Photonics* 12.7 (2018), pp. 397–401.
- [163] Q. Zhan. “Cylindrical vector beams: from mathematical concepts to applications”. In: *Advances in Optics and Photonics* 1.1 (2009), pp. 1–57.
- [164] J. Ng, Z. Lin, and C. T. Chan. “Theory of optical trapping by an optical vortex beam”. In: *Physical review letters* 104.10 (2010), p. 103601.
- [165] K. Kitamura, K. Sakai, N. Takayama, M. Nishimoto, and S. Noda. “Focusing properties of vector vortex beams emitted by photonic-crystal lasers”. In: *Optics letters* 37.12 (2012), pp. 2421–2423.
- [166] J. Wang. “Advances in communications using optical vortices”. In: *Photonics Research* 4.5 (2016), B14–B28.
- [167] J. Wang, M. Clementi, M. Minkov, A. Barone, J.-F. Carlin, N. Grandjean, D. Gerace, S. Fan, M. Galli, and R. Houdré. “Doubly resonant second-harmonic generation of a vortex beam from a bound state in the continuum”. In: *Optica* 7.9 (2020), pp. 1126–1132.
- [168] R. Loudon. “The Raman effect in crystals”. In: *Advances in Physics* 50.7 (2001), pp. 813–864.
- [169] V. Y. Davydov, Y. E. Kitaev, I. Goncharuk, A. Smirnov, J. Graul, O. Semchinova, D. Uffmann, M. Smirnov, A. Mirgorodsky, and R. Evarestov. “Phonon dispersion and Raman scattering in hexagonal GaN and AlN”. In: *Physical Review B* 58.19 (1998), p. 12899.
- [170] F. Demangeot, J. Frandon, P. Baules, F. Natali, F. Semon, and J. Massies. “Phonon deformation potentials in hexagonal GaN”. In: *Physical Review B* 69.15 (2004), p. 155215.
- [171] X.-C. Long, R. Myers, S. Brueck, R. Ramer, K. Zheng, and S. Hersee. “GaN linear electro-optic effect”. In: *Applied physics letters* 67.10 (1995), pp. 1349–1351.
- [172] M. Li, J. Ling, Y. He, U. A. Javid, S. Xue, and Q. Lin. “Lithium niobate photonic-crystal electro-optic modulator”. In: *Nature Communications* 11.1 (2020), p. 4123.
- [173] X. Guo, C.-L. Zou, and H. X. Tang. “Second-harmonic generation in aluminum nitride microrings with 2500%/W conversion efficiency”. In: *Optica* 3.10 (2016), pp. 1126–1131.
- [174] J.-Q. Wang, Y.-H. Yang, M. Li, X.-X. Hu, J. B. Surya, X.-B. Xu, C.-H. Dong, G.-C. Guo, H. X. Tang, and C.-L. Zou. “Efficient frequency conversion in a degenerate  $\chi$  (2) microresonator”. In: *Physical Review Letters* 126.13 (2021), p. 133601.

- 
- [175] K. Koshelev, S. Kruk, E. Melik-Gaykazyan, J.-H. Choi, A. Bogdanov, H.-G. Park, and Y. Kivshar. “Subwavelength dielectric resonators for nonlinear nanophotonics”. In: *Science* 367.6475 (2020), pp. 288–292.
- [176] X. Guo, C.-I. Zou, C. Schuck, H. Jung, R. Cheng, and H. X. Tang. “Parametric down-conversion photon-pair source on a nanophotonic chip”. In: *Light: Science & Applications* 6.5 (2017), e16249–e16249.
- [177] C. Couteau. “Spontaneous parametric down-conversion”. In: *Contemporary Physics* 59.3 (2018), pp. 291–304.
- [178] M. Schubert and B. Wilhelmi. “Nonlinear optics and quantum electronics”. In: *New York* (1986).
- [179] C. Hong and L. Mandel. “Theory of parametric frequency down conversion of light”. In: *Physical Review A* 31.4 (1985), p. 2409.
- [180] M. H. Rubin, D. N. Klyshko, Y. Shih, and A. Sergienko. “Theory of two-photon entanglement in type-II optical parametric down-conversion”. In: *Physical Review A* 50.6 (1994), p. 5122.
- [181] M. Soljačić, C. Luo, J. D. Joannopoulos, and S. Fan. “Nonlinear photonic crystal microdevices for optical integration”. In: *Optics letters* 28.8 (2003), pp. 637–639.
- [182] S. Zanotti, M. Minkov, S. Fan, L. C. Andreani, and D. Gerace. “Doubly-resonant photonic crystal cavities for efficient second-harmonic generation in III–V semiconductors”. In: *Nanomaterials* 11.3 (2021), p. 605.
- [183] Z. Lin, M. Lončar, and A. W. Rodriguez. “Topology optimization of multi-track ring resonators and 2D microcavities for nonlinear frequency conversion”. In: *Optics Letters* 42.14 (2017), pp. 2818–2821.
- [184] R. Camacho-Morales, M. Rahmani, S. Kruk, L. Wang, L. Xu, D. A. Smirnova, A. S. Solntsev, A. Miroshnichenko, H. H. Tan, F. Karouta, et al. “Nonlinear generation of vector beams from AlGaAs nanoantennas”. In: *Nano letters* 16.11 (2016), pp. 7191–7197.



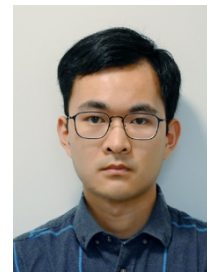
**First name :** Jun

**Last name :** WANG

Address: Chemin des Triaudes 4,  
Ecublens, 1024, Switzerland.

E-mail: jun.wang@epfl.ch  
wangjun.crst@gmail.com

Tel: (+41) 07 79 65 03 39



## PROFESSIONAL EXPERIENCES

- 2018 - 2023** **Doctoral Assistant**, “Nonlinear Frequency Conversion in III-Nitride Doubly Resonant Photonic Crystal Cavities” at Photonic Crystals Group, Institute of Physics, EPFL, with Prof. Romuald Houdré.  
Keywords: photonic crystals, nonlinear optics, doubly resonant cavities, GaN, AlN, BIC, SHG, SPDC, clean-rooms, nano-fabrication, integrated photonics.
- 2017 - 2017** **Internship**, “Nano-film Nucleation and Growth Observed by High Precision Stress Measurements” at Saint-Gobain Recherche (Paris), with Dr. Sergey Grachev.  
Keywords: Ag nano-film, sputtering, stress generation in thin film growth, *in-situ* stress measurement, digital image correlation, ray tracing simulation, AFM, profilometer.
- 2016 - 2016** **Internship**, “Development of SiGe Nanowire-based Core-shell Radial Junction Solar Cells” at LPICM (Laboratory of Physics of Interfaces and Thin Films), Ecole Polytechnique, with Prof. Pere Roca i Cabarrocas.  
Keywords: solar cells, SiGe nanowires, VLS, PECVD, SEM, Raman spectroscopy, thermal evaporation.

## EDUCATION

- 2018 - 2023** Ph.D., Physics, EPFL, Lausanne, Switzerland.
- 2015 - 2017** Master, Optics and Nanosciences, École Polytechnique, Université Paris-Saclay, Paris, France.
- 2013 - 2015** Bachelor, Physics, Université Claude Bernard Lyon1, Lyon, France.
- 2011 - 2013** Bachelor, Physics, Wuhan University, Wuhan, China.

## LANGUAGE AND SOFTWARE

- Language** English (advanced), French (intermediate), Chinese (native)
- Software** COMSOL, Lumerical, SOLIDWORKS, Blender.
- Coding** Python, C/C++, MATLAB, LaTeX, LabVIEW.